University of Udine

Polytechnic Department of Engineering and Architecture

Doctorate School in
Industrial and Information Engineering
- XXXIII Cycle -

Doctoral Thesis

Development of Particle Reinforced Metal Matrix Composite Materials for Selective Laser Melting Applications

Supervisor:
Prof. Marco Sortino

Candidate:
Dott. Christian Pfeifer

Year 2021

Author's e-mail: pfeifer.christian@spes.uniud.it

Author's address:

Dipartimento Politecnico di Ingegneria e Architettura
Università degli Studi di Udine
Via delle Scienze, 206
33100 Udine
Italia

This dissertation is dedicated to
my wife Sandra who always encourages me to pursue my dreams and supports me on my journeys and adventures
and to
my parents who always believed in me and my goals in life, and for being my first teachers.

Abstract

Maraging steels are often used for high temperature applications, like forging dies, casting dies, or parts which are used in harsh environments. They are based on Fe with a relatively high amount of Ni (i.e. 17 - 19 %) and were developed for the aero, space and tooling industry. Maraging steels feature a high strength and toughness, but lack of resistance against wear, which limits their applications in some areas. Due to the weak tribological behaviour, parts made out of maraging steel sometimes do not last very long, if they are involved in an abrasive movement.

In this thesis work, the metal matrix of maraging steel MS1 was reinforced with different volume contents of either vanadium carbide or titanium carbide. The goal was to improve the hardness values and the tribological behaviour of the created metal matrix composite (MMC). As traditional manufacturing methods like casting are often not applicable, a powder processing route had to be chosen. For this, mechanical mixing of the MS1 and the composite material was chosen for the first step of the process route. After mechanical mixing, the powders were processed with a selective laser melting (SLM) machine to additively manufacture solid parts. Computer aided design (CAD) files were used to laser weld contours of the metal powder and layer by layer, parts were built three dimensional.

The first investigation was about the influence of the initial particle size of the composite material. As vanadium carbide has a significantly higher melting temperature, the ability to melt these particles in a SLM machine had to be analyzed. Furthermore, the tendency of agglomerations due to Van der Waals forces had to be considered. After performing a Design of Experiments to find the optimal parameters for SLM processing, specimens with improved hardness were manufactured, but had some design flaws. To further improve the results and to better understand the effects of vanadium carbide on the matrix material, different volume contents were analyzed. However, after these first investigations it was found that solely mixing is insufficient for a homogeneous particle distribution, which is why mechanical alloying (MA) was performed as a post-powder processing technique. MA allowed to crack the agglomerations of the carbides and to embed the particles into the metal matrix material. This processing step was important for the stability of the SLM process and significantly improved the results. The metal matrix composite system of MS1 and TiC was the most promising and achieved the best results. A higher energy density η improved the part density and lead to the complete melting of VC and TiC particles, which then solidified as primary carbides.

While designing advanced materials with metal matrix composites, it is important to understand the phase formations and the mechanical properties of the new material. Several metallurgical, mechanical and tribological tests were performed after SLM processing the mechanically alloyed powders. To find the optimal mechanical alloying parameters, various milling times were applied. Afterwards, the morphology and the particle size distribution was investigated. It was found that the addition of carbides through mechanical alloying can significantly influence not just the mechanical properties, but also the phase formation. Some chemical transformations were observed in the VC and TiC particles, which influenced the solidification of the melt and the phase transformation of the γ-Fe into α-Fe. Future scientific work is suggested in the optimization of SLM parameters for higher part densities and as a result, higher mechanical properties. Electron

backscatter diffraction and transmission electron microscopy could furthermore, help to understand the microstructures of metal matrix composites.

Acknowledgments

This dissertation was written and carried out during my time at the Laboratory for Advanced Mechatronics of Friuli-Venezia-Giulia (LAMA FVG) in Udine, Italy. I hereby want to thank Prof. Marco Sortino for supervising this thesis and Prof. Giovanni Totis for the scientific support. They both gave me the opportunity for my PhD studies and trusted me enough to carry out research in a more independent way. Furthermore, I want to thank Davide, Emanuele, Federico and Thomas, which were not just colleagues, but also became friends. Most of my research work was financed by the European Strategy for the Alpine Region (EUSALP) and therefore, I want to thank the EUSALP institution of the European Union for the financial support.

A large portion of my research was carried out at Joanneum Research Materials in Niklasdorf, Austria. The equipment and materials provided were essential and I appreciate the scientific discussions in late evening hours with Dr. Wolfgang Waldhauser and Dipl. Ing. Elmar Brandstätter. I also want to thank the whole team of Joanneum Research Materials for having me and the welcoming atmosphere.

During my PhD studies I also collaborated with some other institutions. First of all, I want to thank Dr. Dariusz Grzesiak and Dr. Pawel Figiel from the Technical University of Szczecin, Poland. They provided me access to their high energy ball mill, the X-ray diffractometer and the selective laser melting laboratory. I really enjoyed my several visits, the work with them and getting to know the history of Szczecin and the cuisine of Poland.

I also want to thank Dipl. Ing. Udo Rabe, Ing. Bettina Hübsch and Mag. Marcus Fasching from the Austrian Gold and Silver Refinery (ÖGUSSA) for their support and for letting me use their equipment. Especially Dipl. Ing. Udo Rabe has to be acknowledged as he pointed me into the right directions in the beginning of my thesis work.

On a final note, my visit as a research scholar at the Center for Additive Manufacturing and Logistics (CAMAL) at the North Carolina State University in Raleigh, USA was very informative. Dr. Ola Harrysson was a great and professional host and I truly enjoyed my time at the laboratory. I further want to thank Sullivan Figurskey, Carter Keough and Matt White for the warm welcoming.

My research stays in Europe and the United States of America not just helped me scientifically, they also expanded my personal horizon and therefore, I want to finish these acknowledgements with the motto of the European Union: *United in diversity*!

Contents

List of Figures

List of Tables

Introduction

Inventions become perfect by slow improvement, and each step is itself an invention

Josep Jastrow

Motivation and Background

Todays manufacturing plants are more than ever forced to consider the factor "time to market" to create products and parts which are financially able to succeed. In some cases it might be reasonable to exceed planned budgets for research and development just to make sure that a product can be delivered to the market "in time" and maybe before a competitor does. To decrease developing times and manufacturing costs, new processes had to be developed. Especially the production of prototypes was a time consuming process, which caused high costs during product developments. The first rapid prototyping (RP) technologies have been invented. These technologies had the goal to decrease development times and to produce prototypes from computer aided design (CAD) models. Whereas in the beginning of RP technologies the focus laid solely on design prototypes, to review the CAD model and their design, these days RP is capable of creating functional parts with very similar mechanical properties like the final product. Because of an early usage during product development of rapid prototyping technologies, product recalls, which are not just cost intense but also bad for a brands reputation, can be avoided.

Another huge demand of todays industry is the possibility to economically produce customized parts and to manufacture parts which are designed for their function rather than designed for their manufacturing process. It can be seen that industries are shifting away from mass produced standardized parts to mass customized parts. In these fields additive manufacturing (AM, or commonly also called 3D-printing) can show-off it's core strengths. In traditional methods, such as casting or subtractive machining, customization of products can not be achieved that easily in most cases. As the name suggests, parts are additively built layer-by-layer, rather than subtractively removed from a solid block. AM is a cost effective production technique, which allows a direct production of complex parts even from lot size one. AM techniques are able to produce nearly net-shaped or even full net-shaped parts by slicing CAD models into lots of thin sections, which are then passed to the 3D printer. The printer then produces the desired part layer-by-layer [45, 46]. Additive manufacturing can not just decrease the costs for part production or part development, but also decrease the lead times, as there is no need for casting molds or tools. Another advantage is the fact, that AM technologies are producing parts in a more lean-philosophy friendly way than wasteful subtractive processes do. In theory, AM technologies have the capability to produce with zero wastage, because the feedstock material can be recycled. As a matter of fact this consequently reduces emissions due to a lower amount of feedstock material which has to be produced. In subtractive processes there are often toxic chemicals used for lubrication and/or cooling. These liquids are not needed in most AM machines as they are working with another principle of manufacturing.

At the time of writing this thesis, the most common AM technologies can be named as fused deposition modeling (FDM), selective laser sintering (SLS) and stereolithography for the production of - or with - plastics and laser metal deposition (LMD), selective laser melting (SLM) and electron beam melting (EBM) for the production of metals. Each of these technologies works with a raw material like a wire, a liquid resin, a printing ink, a thermoplastic filament which is extruded, a thermoplastic powder or a metal powder which is sintered, respectively molten by a laser or electron beam. Currently, one of the most promising AM technologies for metals is SLM. Even though SLM has its roots in a sintering process, these days the technology is able to produce fully dense parts. Improvements in laser sources, laser powers, focus diameters and feedstock powder morphology drastically influenced the achievable part density and surface quality. SLM is a powder bed fusion technology to manufacture solid parts from metal feedstock powder. The aforementioned CAD file is sliced and transferred to an SLM printer, which melts the coated powder selectively with a laser. The resulting melt pool experiences rapid solidification with a very high cooling rate, which gives this technology some unique metallurgical properties. The main applications for SLM parts are found in aerospace, dental, medical and tooling industries and it has proven its capabilities in numerous industries and areas [16, 47–55]. Even though some materials and their according processing parameters have been undergone a lot of research, there are still many materials which have not been processed yet or need further investigations to achieve higher density or crack resistance. The complex metallurgical and atomic mechanisms during SLM processing and the involved heat absorption have a huge effect on microstructures, mechanical properties, cracks, surface quality, residual porosity and dimensional accuracy. [56–59].

Research Problem and Approach

Every year about 2 billion parts are manufactured in Germany through solid forming processes [60]. Most of these parts are made for the automotive industry and about a third of them is produced for machinery and industrial applications. 67 % of all these parts are manufactured using solid forming processes [61]. For the process of forging there are dies used, which should give the final form and shape to a part. These dies can have a negatively shaped form of the final part, but might also be designed as a forging inlay for holes depending on the application. The lifetime of a die is mostly influenced by mechanical, tribological and thermal strains. During the forging process of complex steel parts, like connecting rods or crankshafts, temperatures are exceeding 1000 ° C and simultaneously, there are huge mechanical forces involved to get the parts into shape. Because of these influences, some of the most stressed forging dies have a lifetime of less than 1500 cycles [62]. To decrease the costs of the forging process, dies which are lasting longer are desired by the industry. Ocylok [62] analyzed the possibilities of using LMD to repair or initially weld a reinforcing protective layer by adding nanoparticular elements. As LMD has its process related disadvantages in terms of freedom of design compared to the SLM process, in the following study various powder based alloys for SLM applications were analyzed. The focus was set on materials not just suitable for forging dies, but which are also used in other industries. Industries like the tooling, aircraft and oil industry, or the nuclear industry, which uses high strength materials for the production of enriched uranium, are constantly looking for better and longer lasting materials. A core technology, beside the additive manufacturing with SLM, in this study is mechanical alloying (MA). The process parameters for MA were investigated to produce powders with a fitting morphology for SLM. As the influence of some of the reinforcing particles and their melt point significantly influences the melt pool during SLM processing, a design of experiments (DoE) was used to get adequate parameters for the production of SLMed specimens.

The present study set out to develop new innovative particle-reinforced metal matrix composites (MMC) based on maraging steel (MS). Maraging steels have superior toughness and strength derived from precipitations of intermetallic nickel compounds. Maraging steels are used in areas in which a high strength-to-weight ratio is needed, as it offers an unusual preferrable combination of a high tensile strength, a good resistance to cracks and a high elongation at break. One of the biggest advantages of MS is their capability to be machined even at temperatures of up to 500 °C without warpage. Typically, MS contains about 17 - 19 wt. % of nickel which acts as the main alloying element and some amounts of cobalt, molybdenum and titanium. Even though the carbon content is under 0.03 wt. % in most maraging steels, they do not compromise lower ductility levels. The martensitic phase almost contains no carbon, but it is a supersaturated solution of Ni in α-ferrite.

MMCs offer promising mechanical properties, but are limited in their usage with traditional manufacturing methods [12]. Because of these limitations their applications in engineering fields are limited. In this study a different route was chosen to develop these particle reinforced MMCs. The powders were mechanically mixed, mechanically alloyed and then processed in SLM machines. The effects of ball milling and different initial particle reinforcement sizes were analyzed in detail. As there is a high amount of parameters in SLM that can be changed, it was important to understand the relationships between the SLM processing, the microstructure and the resulting mechanical properties, but also the build behaviour of the material. The most important investigation tools for the reinforcing content and the microstructure were X-ray diffraction (XRD), scanning electron microscopy (SEM) and electron backscattering diffraction (EDX). The mechanical properties have been investigated through micro hardness testing, ultimate tensile strength testing, Charpy impact tests and hot tensile strength tests.

Ideally, materials for forging dies, rocket motor cases, gas centrifugal components and landing gears for aircrafts have to withstand high stresses. The three main desired characteristics are:

- shape retention
- toughness
- wear resistance

A more specific overview of the most desired material properties can be found in table 1. Of course, not all of these characteristics can be fully achieved in one single material. For example, it can be said that toughness has an inverse proportional effect on the resistance against abrasion in high temperature environments. Furthermore, it can be said that usually a harder material is more brittle than a softer material as it features a higher ductility. Through alloying elements some of these properties can be increased, but the potential of classical methodologies is limited. This is the reason why todays researchers are focusing on MMCs to further improve material properties and to create advanced materials, which are able to outperform currently available alloys.

Table 1: Characteristics of an ideal material for high performance applications [36]

Requirement	mechanical & metallurgical characteristics
shape retention	hardness strength
toughness	ductility resistance against stress from repeated temperature changes
wear resistance	surface hardness abrasion resistance caused from high temperatures

Scope of the Thesis

Chapter 1 is about additive manufacturing in general. A quick historical background information is provided and then the selective laser melting process with the laser system and the according the laser physics are explained. To understand the effects during laser melting, information about material processing is provided as well.

Chapter 2 talks about mechanical mixing and mechanical alloying, which are powder processing techniques for metal matrix composites. A historical overview, some physics and a technological explanation is given.

In Chapter 3 metal matrix composites are explained and examples of other investigations are listed. The used materials in this thesis work are listed in Chapter 4. Furthermore, the theoretical shift

of melting points is explained.
To process and to analyze the used materials, several machines and different equipment was used in this work, which is shown in Chapter 5.
In the Chapters 6 to 10 the scientific research is described. In the beginning, the effects of different initial particle sizes and different volume contents of the metal matrix composite were investigated. Some difficulties were found while processing mixed MMC powders, which is why mechanical alloying was used as an alternative powder processing route. While Chapter 8 and 9 are about maraging steel with an addition of vanadium carbide, Chapter 10 was about the investigation of maraging steel with reinforcing titanium carbide powder.

In the beginning, it was desired to reinforce maraging steel with carbides simply by mechanically mixing the two powders together and then processing them in a selective laser melting machine. Metal matrix composite materials should have been produced with outstanding mechanical properties. Especially the wear resistance and hardness were aimed to be improved. However, the mixing process had some significant difficulties and drawbacks, which is why the processing route of mechanical alloying had to be performed. This step, between mixing and SLM processing the powders, allowed to embed the hard carbide materials into the softer and more ductile matrix material. Bigger VC particles were cracked into smaller ones and then formed coalescences with the maraging steel powder.

1

Additive Manufacturing

> I think there is a need for something completely new. Something that is too different, too unexpected, to be accepted as yet
>
> Anton Zeilinger

In this chapter an overview of the current state of the art technology shall be given. In the beginning some of the historical background is given. The main technology to additively manufacture metal parts used for this thesis work was selective laser melting (SLM), which will be described in detail. The technology and its biggest influencing parameters will be explained and the technique will be compared to traditional manufacturing techniques in terms of impact on the environment, energy efficiency, microstructure and morphology. Even though SLM is a widely known process these days, a general introduction will be given.

1.1 Introduction to Additive Manufacturing

As mentioned before, in modern production plants the "time to market" principle is becoming more and more relevant. The first additive manufacturing (AM) technologies had the goal to decrease development times of new products. As the name suggests, additive manufacturing technologies are creating parts from bulk materials, like powders, wires or liquids by giving them a new shape. In contrast, subtractive manufacturing technologies start with a solid block and cut the desired part shape out of the block. One of the greatest advantages of AM is the freedom of designing a product according to the needs of a customer, rather than designing a product according to the manufacturing capabilities. These days, AM technologies can provide products with outstanding mechanical properties and new levels of customizations for customers with a lot size of only one single piece. The more complex a product is, the better it fits for additive manufacturing. Additive manufacturing is also referred to as *Rapid Prototyping*, because in the beginnings of this relatively new production method, mainly prototypes were manufactured. And compared to their traditionally manufactured counterparts, these prototypes were manufactured a lot faster, hence the name.

The term rapid prototyping describes a fast method of producing prototypes or models with a CAD model. It allows a much quicker scrutiny of the design and, if there are corrections necessary, the model can be changed very quickly. Modifications of models prepared for traditional manufacturing methods are often very complex and critical, as most products have a complex structure and a change of the product often leads to necessary changes of other parts and tools. The later a modification is necessary in the product development process, the higher are the resulting costs, since these increase exponentially with the degree of product development and become substantially more time consuming. Prominent examples for cost intensive and prestige damaging cases are recall actions in the automotive industry. Additive manufacturing can help to identify inevitable modifications in parts. Prototypes can be manufactured faster and sometimes even cheaper than traditional methods could. These prototypes can be built as proof-of-concept prototypes, geometry or functional prototypes, and technical prototypes. But also final production parts are becoming more and more interesting for additive manufacturing techniques.

The various AM technologies for rapid prototyping, rapid tooling and rapid manufacturing are powerful tools for modern companies. With these methods, highly flexible products can be produced and a fast reaction to individual customer demands and requirements is possible. The technologies are relevant for aerospace technology, military, motor sports, automotive industry, tools and machine tools, medical technology, dentistry, art and jewellery, consumer products, household appliances, and many more. Additive manufacturing is the right tool for companies to keep pace with the constantly changing world market and increasing competitive pressure.

1.2 Historical Overview of Laser and Powder-Bed-Based AM

The earliest known technique, which can be considered as an additive manufacturing technology, or at least an approach, was back in the days of the end of the 19th century. Layer-based maps for topographical purposes were produced layer by layer. In 1951, Otto John Munz invented a system similar to modern stereolithography technologies. He used photosensitive emulsion and printed transparent photographs. Then, a system for selective light exposure was used to harden the emulsion. The finished part was a transparent cylinder with a 3D image of the desired object [7]. The first developments regarding powder based technologies were done by Ciraud in 1971 and in 1979 by Housholder. Housholders patent described a layer based system, which used a controlled heat source for solidifying areas of each layer.

For laser based additive manufacturing, an even earlier important date can be named. Back in the days of 1926, the Austrian scientist Erwin Schrödinger developed one of the main equations for todays quantum mechanics. Various modern technologies are based on his equation, like lasers, scanning electron microscopes and many others. Lasers are essential for most additive manufacturing technologies and some machines even use multiple laser sources these days.

In the early years of 1990 selective laser sintering (SLS) of metals was invented and had a few minor fields in which it was used. A laser source sintered or partially melted metal powder, which was the only cause for a rapid consolidation. The main problem with this process was the relatively low density and ductility that was achieved. Today it is still used for thermoplastics, but the principle is not used for metals anymore. The differences can be seen in figure 1.1, but it has to be mentioned that the SLS layers are usually bonded very well, but not fully melted. In the image Klocke [1] tried to show the improvements that were made in the technologies. SLS is a sintering process, in which the layers and particles are not perfectly melted together. The selective laser sintering process was improved and refined to a process in which metal powder is not just sintered, but rather fully melted and this process was them named Selective Laser Melting (SLM). SLS machines for thermoplasts are still very common and use CO_2 lasers, whereas SLM devices use high-energy-density fibre lasers, which emit short-wavelength infrared light that is necessary to melt thin layers of metal powder.

1.3 Selective Laser Melting Process

In this thesis work, selective laser melting was used to fabricate specimens for further analysis. It is one of the most common techniques to additively produce metal parts during writing this thesis and it is based on the similar process of selective laser sintering. However, powders in SLM are not

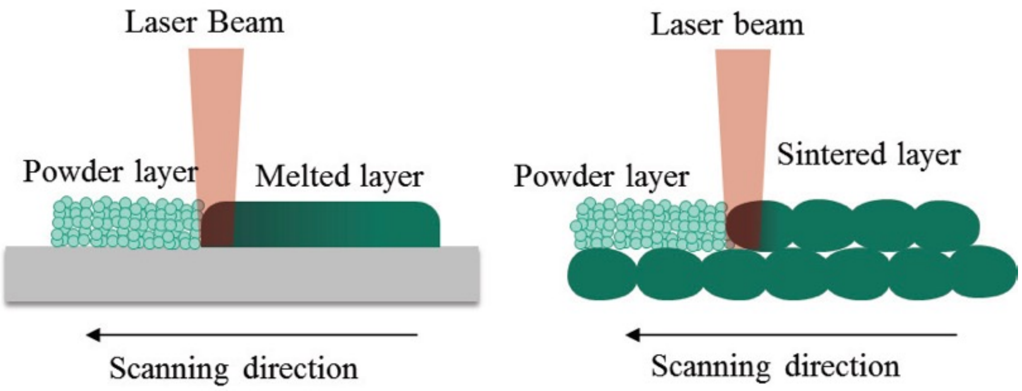

Figure 1.1: Differences between SLM (left) and SLS (right). [1]

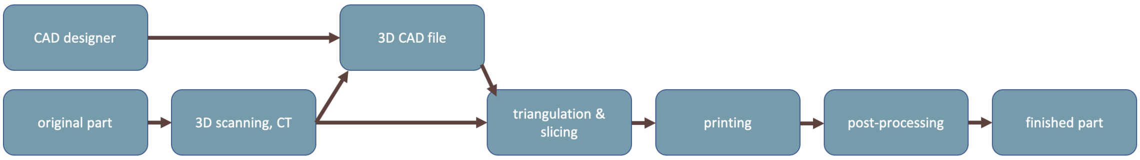

Figure 1.2: Processing route of additively manufactured parts.

sintered anymore, they are melted completely and rapidly solidified afterwards. Materials available for selective laser melting are increasing as industries demand ever improving material properties.

Various materials can be processed with SLM. Basically, all metals, ceramics and carbides that can be molten with the laser and will solidify while cooling down can be processed. In the beginning of each printing job, there is always a CAD file of the desired part necessary. These CAD files can be either created based on technical drawings, or on reverse engineered files acquired by computed tomography scanning, 3D scanning or other techniques. In Figure 1.2 the processing route from the design to the finished printed product is shown. Usually, a CAD designer creates a CAD file for the 3D printing process. However, if reverse engineering is necessary, an original part can be 3D scanned with computer tomography to create voxel data, which can then be transformed into a CAD file or directly triangulated. Triangulation and slicing is the next necessary step for each file to create a suitable file for the printer. After printing the part it has to be post-processed in most cases to create a smooth surface and to remove support structure.

1.3.1 Triangulation

As mentioned before, an additive process is the exact opposite of a subtractive process, as parts are built layer by layer in additive manufacturing. The part is created by fusing together small volumetric elements. In the case of selective laser melting these elements are powders. To get a suitable file for the SLM machine, a *Standard Triangulation Language* (STL) file is necessary. The CAD file is triangulated, which means that the surface model is interpolated in triangles. The more triangles used, the higher the resolution of the final part. In any case, it has to be understood that every volumetric model is changed into a surface model and all surfaces have to be closed to be able to be triangulated. The surface of the part is approximated by triangles of different sizes that perfectly fit the shape of the surface. The triangle patches contain the coordinates of the three corner points and the normal vector in positive outward direction. The STL format is de facto an industry standard of additive manufacturing and thus, usable in almost every system. The quality of a part depends not just on the type of production and the SLM parameters, but also on the quality of the CAD design and the triangulation into an STL format. As a matter of

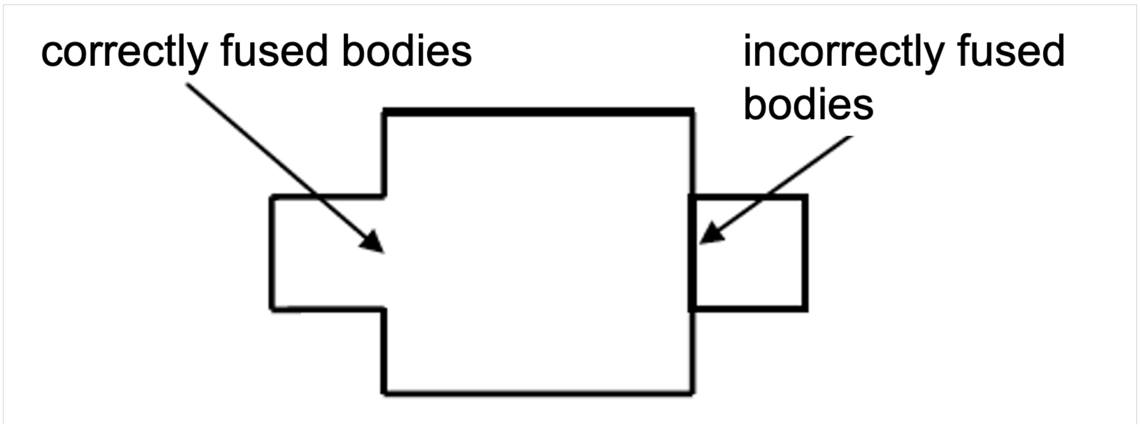

Figure 1.3: Joining of two bodies (based on [2]).

fact, a triangulated component can never be of a higher quality than the CAD model on which it is based on. If there are errors or inaccuracies in a CAD or STL component, they will also have a negative impact on the construction process. State of the art rapid prototyping software, e.g. Magics (Materialise, Belgium) checks these models for errors and can even correct them if necessary. However, defects or baldy designed CAD files should be avoided in any case.

The three categories of errors are:

- design errors,
- execution errors,
- and description errors.

Design errors are about redundant data inside of a body and are caused by an incorrect combination of bodies in the CAD program. Usually, these errors are relatively irrelevant in powder bed fusion processes. The part might be melted by the laser more often than necessary in some areas and this causes a longer build time. However, if the bodies are overlapped in most parts, the additional laser exposure can cause residual stress, which is very unwanted. An example is given in Figure 1.3 for a correctly and an incorrectly fused body.

Conversion errors and round-shaped edges with reduced quality are caused by the STL formulation. The surface of the component is approximated by flat triangles. This is absolutely no problem on flat surfaces and slopes, but sharp edges do occur on curves. An example for the problem of triangulation is given in Figure 1.4.

Unfortunately, perfectly rounded edges are impossible with the process of triangulation. However, it is possible to increase the resolution of the shape through varying the amount of triangles in the STL file. A higher number of triangles will increase the accuracy of a round contour as the round shape is more precisely approximated. But as a matter of fact, the higher the resolution of the STL file, the more data has to be handled. The computational effort is strongly increased and the process time of the STL file will be much longer. In Figure 1.5 three spheres with the same diameter (i.e. 10 mm), but with different amounts of triangles are given. One can see that the file size significantly increases. The first sphere is made out of 80 triangles and has a very rough surface, but features a file size of only 4 kB. The second sphere is triangulated with 320 triangles and has 16 kB. The third sphere has the highest resolution with 5120 triangles and is almost perfectly spherical. However, the file has a size of 251 kB.

Errors in the triangulation process can be characterized by three types:

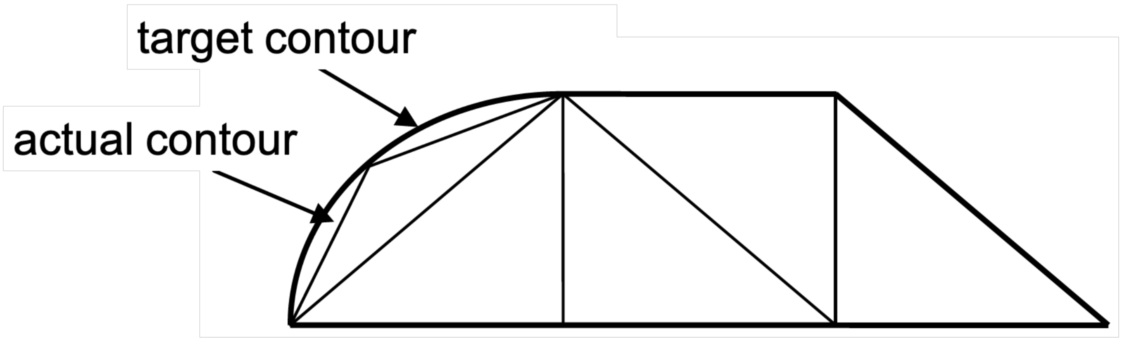

Figure 1.4: Triangulation of round-shaped edges (based on [3]).

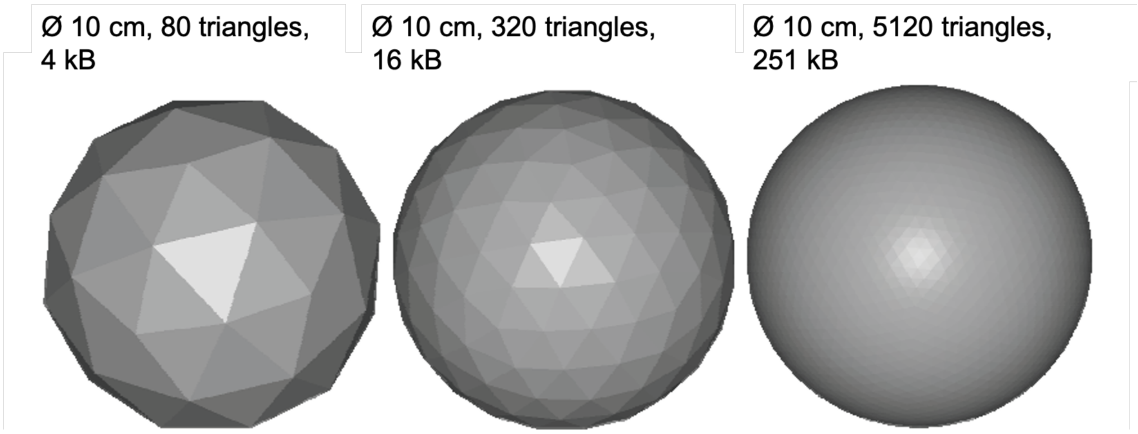

Figure 1.5: Triangulation of spheres and their respective file size (based on [3]).

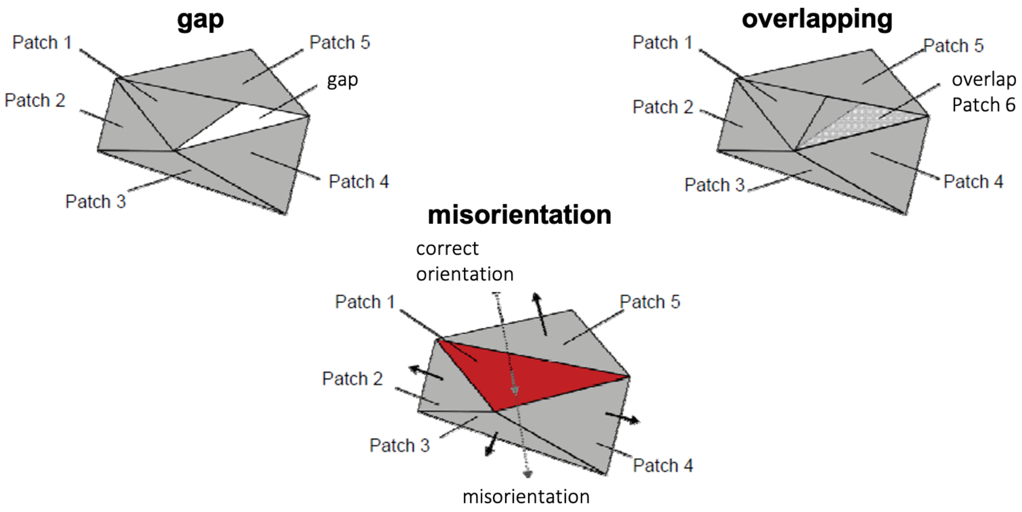

Figure 1.6: Triangulation errors (based on [4]).

- Boundary errors, which are gaps between triangular patches.
- Overlapping errors, which are double triangular patches in the same place.
- Misorientation errors, which are incorrectly oriented patches.

Triangulation errors, in contrast to design and implementation errors, can have significant negative effects on the building process of a part. Under certain circumstances, the production process is only possible with restrictions, or not at all. If patches are calculated imprecisely, gaps can occur and the model will not be completely closed. An incorrect orientation is characterized by the orientation of the vector points. If the vector points to the inside of the model - not to the outside - the software cannot distinguish what is inside and what is outside of the body. This can lead to unmelted layers in the construction process, which in turn can cause defects in the component, such as layer separation and the associated loss of material strength [3]. Examples for boundary errors, overlapping errors and misorientation errors are given in Figure 1.6.

1.3.2 Slicing

After triangulation, the STL file has to be sliced into layers to be readable in an SLM machine. Through the slicing process, the layer thickness for the SLM process is defined. The software preparation process chain is shown in Figure 1.7. While slicing a file the used powder already has to be taken into account. Especially the average particle size distribution has to be known. If the particles used for the SLM process have a size distribution of 30 to 60 microns, it is advisable to set the layer height t to approximately 40 microns. If one uses a layer height of 25 or even less microns, the SLM process will be more unstable and the coating of the powder will be critical. The thinner the layer thickness in the construction process, the finer the details and the less ”stairs” will be visible. The stair effect refers to the layer height and occurs because the building in the z-direction is done by joining individual layers of a certain thickness. If there are more layers available to describe or build a contour, the resolution will be finer. However, the finer the layer thickness, the longer the overall build time will be.

After slicing the part and loading it into the SLM machine, the SLM processing parameters have to be set. Especially the hatching is important for the contour calculation. The laser has

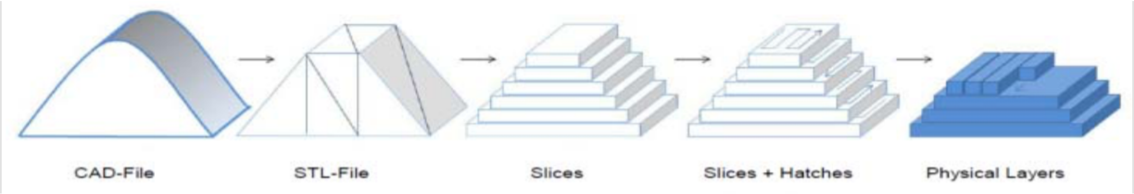

Figure 1.7: Process chain of the cad preparation, slicing and printing [5].

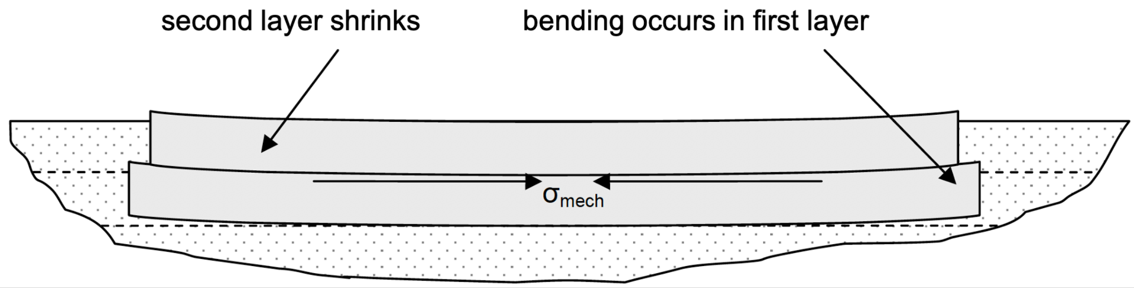

Figure 1.8: Shrinking and bending caused by mechanical tension (based on [6]).

to know which paths it has to follow. Other parameters include, but are not limited to, the laser energy in watts, the overlapping described by the hatch distance in microns and the scanning speed given in mm/s.

1.3.3 Geometry

One of the biggest advantages in powder bed fusion additive manufacturing compared to conventional manufacturing technologies is the fact, that the geometry of the parts is of little importance. The layer based manufacturing allows the construction of complex bodies with cavities and undercuts. Even though support structure is necessary in SLM processing, the surrounding powder during manufacturing is a natural support for the melted part and geometries are possible to be manufactured, which would be very difficult or impossible to manufacture with other techniques.

The production of thin walls is only limited by the laser beam diameter d_L in the focus point w_0. However, the melt pool and therefore, the solidified material will usually be slightly bigger. The challenge of producing thin walls, is the warping during the fast solidification. This is particularly noticeable at the beginning of flat surfaces, for example in the first layers of a component and overhangs. The very first layer is not very critical and does not have any major effects. The area ist just subject to a normal shrinkage after solidification. However, the following layer is welded to the first layer and the volume reduction is hindered at the border of the two layers. Mechanical tension σ_{mech} occurs, which can lead to distortion and cause bending of the part.

Some of these problems can be solved through variation of the placement in the building chamber. A different angle or position affects how the part is built and also changes the requirements for support structure. Support structure can not just help to keep a part in place, it is also an effective way to get rid of excessive heat in a part. Especially large massive parts can face a lot of thermal stress and they can bend, if there is too much heat in the part. A support structure can dissipate heat from these critical massive areas.

1.3.4 Dimensions

The maximum possible size of a component that has to be printed, is limited to the volume of the building chamber of the SLM machine. Large objects have a correspondingly long printing time. In order to keep this time as short as possible, the dimensions in x, y and z direction should be limited, if realizable. The height in the z-direction determines the number of layers that have to be printed. The sum of the laser exposure time, the material coating time and the number of layers extends the SLM processing time and therefore, increases costs.

Components with a large mass can also store a lot of heat during the building process. The parts cool down very slowly and the stored heat leads to an excessive attaching of surrounding powder material, as adjacent powder particles melt to the contour of the part. Components with small dimensions cool down very fast and might warp in the cooling process.

1.3.5 Parameters

As soon as the parameters are set for each part that should be produced, the machine can be flooded with an inert gas like argon or nitrogen, to prevent the metal powders from oxidation and to provide good welding conditions. Once an oxygen level of approximately 0.4 % is reached, the print job can be started. The first step is the coating of the building platform with powder. The coating of the powders is done by a coater equipped with a brush made out of carbon fibre. Another possibility is the use of rubber coaters, depending on the processed material. After coating the powder material, a laser beam controlled by various motorized scanning mirrors, is melting the powder exactly at the geometries given by the sliced CAD file. An overview of the SLM process is given in Figure 1.9. To minimize stress through thermal energy, some SLM machines offer the possibility to heat the process chamber. For some materials, this can be advisable, but it is not necessary for all of them. After the laser beam has molten all parts of the layer, the coater will apply the next layer of powder and the process is repeated. During the coating process, the building platform will be slightly lowered to avoid unwanted movements caused by the coater. Layer by layer the part will be printed and only the powder that will be formed to a solid part will be melted. The time needed for the whole print job depends mostly on the slices and the time needed to exposure one layer. The rest of the unmelted powder can be recycled and reused for the next print job. However, during the SLM process there are spatters formed and powder in the laser heat affected zone can be sintered with other surrounding particles. Because of this, sieving as a post-printing-process is necessary. But as a matter of fact, not all spatters are large enough to be able to be sieved out of the powder, which is why the quality and the properties of the powder will decrease after each use. Fresh powder can be added after each print job for dilution.

The quality of the finished product depends on several factors. It can be differentiated between process related and material related influencing factors [7].

Process Related Influencing Factors

The laser system depends on:

- the energy,
- the intensity,
- the wave length,
- and the spot diameter.

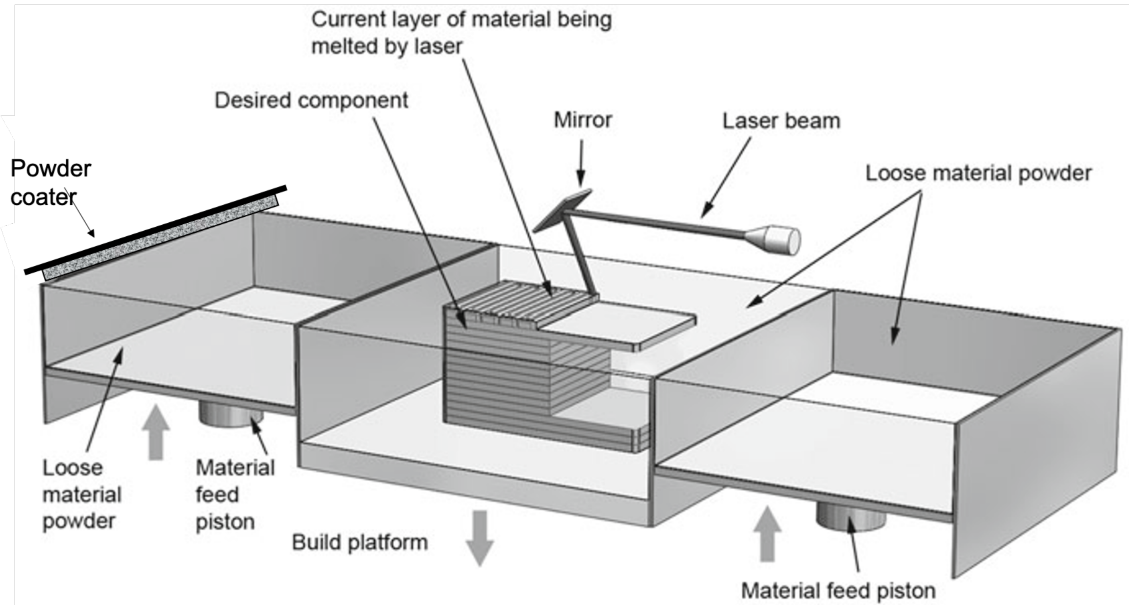

Figure 1.9: Powder bed fusion additive manufacturing (based on [7]).

The exposure with the laser depends on:

- the hatch distance,
- the scanning speed,
- the number of scan iterations,
- the scanning strategy,
- and the compensation settings.

The mentioned factors are machine related and some can be better manipulated than others. The produced part is dependent of other factors, which are related to the preparation in the CAD and slicing software [5]. These influencing parameters are:

- the layer thickness,
- the way the part is positioned in the building chamber,
- the orientation of the part,
- the support structure design, quality and quantity,
- the geometry and the dimensions,
- and the scaling factor.

As one can see, there are factors which can be used to improve the part quality and reduce the risk of a failing print job. To determine which factors should be changed accordingly requires a lot of experience of the machine user. Preliminary work showed, that even though some parts are in theory printable, it is not advisable to print them. If the geometry or the dimension of a part is too thick, there might be too much energy in the building chamber, causing an excessive heat and extreme stress in the part. This stress can even cause damage in the SLM machine in some rare occasions. In some cases, printing might not be the right technology, or the process parameters have to be adjusted accordingly and a longer print time has to be calculated to let cool down the chamber after each layer. But also the environment, in which the selective laser melting process is performed, can be seen as an influencing factor. For example the pre-heating phase can lead to lower stress and the selected inert gas can react with the powder material if not chosen properly. Furthermore, the oxygen level has to be kept very low (i.e. < 0.4 %). One major influencing factor, which is important to actually produce weldings right in the beginning of the process, is the used base plate material. If the base plate is manufactured out of a material that is hard to weld to in combination with the desired end product, the print job will very likely fail.

Material Related Influencing Factors

Of course, the used material for the SLM process can also significantly influence the results. There are factors which are powder related, material property related and ones which are related to the laser physics [5].

The thermal influencing factors are:

- the thermal heat flux,
- the heat capacity of a material,
- the thermal expansion,
- and the viscosity.

As selective laser melting relies, as the name suggests, on a laser to melt the powder, the optical properties of the material can influence the outcome. Therefore, the influencing factors in terms of optics are:

- the absorption,
- the reflexion,
- the transmission,
- the index of absorption,
- and the index of refraction.

And lastly, one must not forget the powder itself, which depends on various factors:

- the state of the powder in terms of dryness,
- the particle size,
- the particle morphology,
- the particle size distribution,
- the packing density in the SLM machine,
- and the pourability.

1.4 The Laser Source

1.4.1 Laser Physics

The laser is the main tool for the whole melting and production process. It is responsible to provide enough energy to heat up the powder material up to its melting point and therefore, to provide enough thermal energy. The name *laser* is an acronym for *light amplification by stimulated emission of radiation.* The principle of a laser is based on Albert Einstein's theory of light from 1916 and the work of Gordon Gould from 1959. Gould published a paper about lasers and was the first person who suggested the term. However, a patent from April 1959 was denied and instead, a patent was awarded to the Bell Labs in 1960. Theodore H. Maiman was the first person who actually built a working laser, which was based on a flash lamp pumped ruby crystal, in May 1960.

Today it is known that there are three working principles of lasers, which are different interactions between the electron in the laser medium and the photons:

- stimulated absorption,
- spontaneous emission,
- and stimulated emission.

In the stimulated absorption, a nucleus, that is made of protons and neutrons with a positive charge, is needed. Usually, electrons are most likely found in a ground state as it is easier for them to exist in this level. However, it is possible to excite electrons by external means. If a photon of light, which is one unit of light, comes across an electron in a low energy ground state, it can sacrifice itself and push the electron to a higher excited state. The photon is inhaliated, but the energy is now part of the excited electron. At this point, it should be noted that each material has different levels of energy and the photon has to have the exact necessary energy to push the electron form the ground state to the excited state, that is required in this excited state. If the energy is too low, the electron will not jump into the excited state. If the energy of the photon is too high, the electron will be pushed out and the atom will be ionized.

The next mechanism is called spontaneous emission and is the following mechanism after an electron was excited. As commonly known, the excited state is more unstable than the ground state for an electron. The electron would stay in the higher state, if the energy levels would be perfectly balanced. However, due to vacuum energy perturbations, a quantum mechanical effect, the electron will become out of balance. Because of this, the electron will fall back to the ground state after approximately 100 nano seconds. During this process, the electron will release a photon with an energy equal to the difference in energy levels. The higher the fall from the excited state to the ground state, the higher the energy of the photon will be. If the energy is in the visible range to the human eye, it can be seen as a colour. As a result of the spontaneous emission, the lasers have different colours.

The most important mechanism for lasers is the stimulated emission. This mechanism occurs, when a photon interacts with an electron that is already in an excited state. This photon can act as a type of perturbation and will also cause the electron to fall down to a lower energy state. As a result, two photons are emitted at the same time. These emitted photons now have the same phase, frequency and polarisation and are coherent with each other. This is exactly what *light amplification by stimulated emission radiation* is about.

The time frame for the stimulated emission is very short (i.e. 100 nano seconds). However, there are materials available with meta stable states in which photons have more time to interact with electrons in an excited state. The electrons can stay in these meta stable states for a longer period of time (i.e. several milli seconds) and therefore, chances for an interaction are increased.

The transformation from a stable to a metastable state is radiationless, but some energy becomes heat. To increase the total number of electrons in an excited state, a population inversion is required. For example, if there are only two energy levels in a nucleus, chances are 50 % to 50 % that half of the electrons are in an excited state and the other half is is a ground state. By introducing the metastable state by pumping, there are significantly more electrons in an excited state than usual.

It is not practical to build lasers that are extremely long, which is why the laser medium is put into a cavity. Since light is a wavelength, it is subject to destructive and constructive interference. In order to get a high intensity laser beam, a constructive interference between all photons is desired. For this, the laser cavity containing the laser medium is put between two mirrors. Some lightwaves will travel through the medium irregularly through spontaneous emission. Others will travel perpendicularly back and forth between the mirrors as they are reflected. At the first stage, emissions are spontaneously emitted followed quickly by stimulated emitted photons. As photons can also be seen as waves, they will travel with the same phase and frequency towards the mirror and will be reflected. Two waves are now traveling through the laser medium. One from the left and one from the right. The amplitude will increase, because of the constructive interference between the mirrors. In this case, a standing wave is produced to they eye of an observer. To understand what modes can exist in a specific cavity, Equation 1.1 is given.

$$f = n * \frac{v}{2 * L} \tag{1.1}$$

In the equation, f is the frequency that exists in the cavity, n is the mode, which is always an integer, v is the velocity of the wave, and L is the length of the cavity. The velocity is always equal to the speed of light c (i.e. 299,792,458 ms^{-1} in vacuum). In the cavity, some modes can produce standing waves, others cannot and not all frequencies can exist in this cavity. All waves can just exist, because the photons are coherent with each other [63, 64]. A schematic overview of a laser with its mirrors and the cavity is given in Figure 1.10.

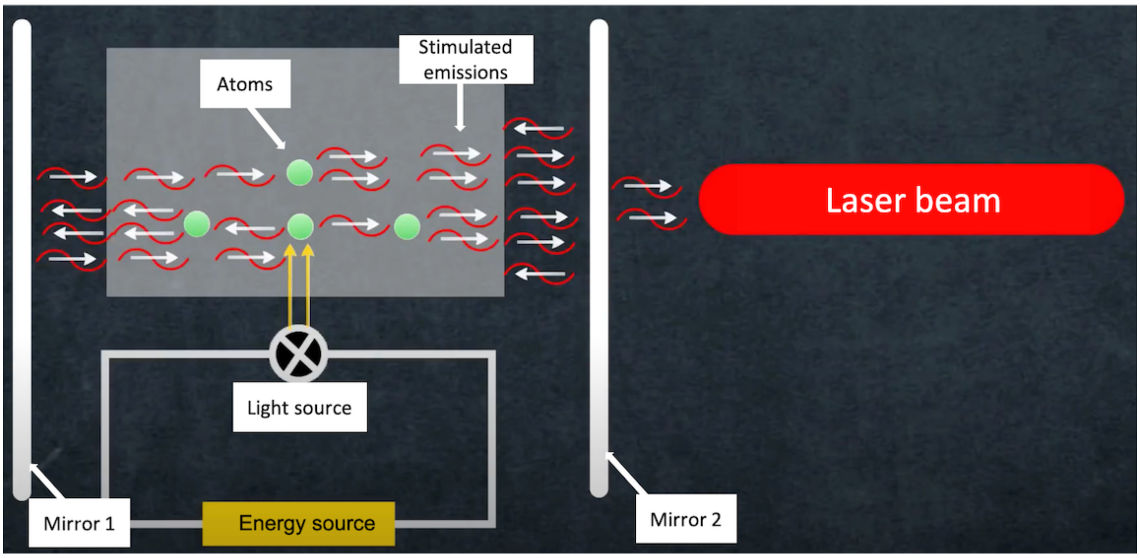

Figure 1.10: Overview of a simple laser with mirrors and a pumping source.

In laser sintering machines for the production of plastics, CO_2 lasers are used. The gas in these lasers consists of a mixture of carbon dioxide, nitrogen and helium. Their emitting wavelength is at approximately 10600 nm. For metal applications however, shorter wavelengths are necessary due to their absorptivity. For metals, usually a wavelength of 0.2 and 0.5 microns is advisable, as these materials have an absorption rate of approximately 10 to 90 % in this range. This is the reason why SLM machines use solid-state lasers like Yb:YAG or Nd:YAG lasers. In both cases, the laser beam can be guided through glass fibre optics, which is not possible with CO_2 lasers. The CO_2 laser sources are furthermore somewhat limited in their minimum spot size. Figure 1.11 gives an overview of the different laser types and the absorption rate of some selected materials.

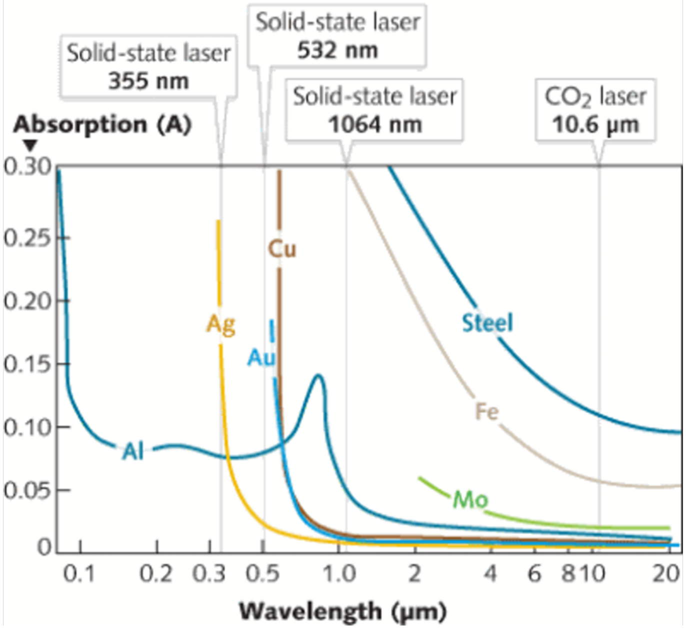

Figure 1.11: Overview of the different wavelengths of lasers and the absorption of some materials [8].

1.4.2 Laser Power

The laser beam power P always has to be chosen according to the material that has to be processed. It is one of the main influencing parameters to put energy into a system in SLM processing. The overall energy has to exceed a certain minimum in powder bed fusion and other laser based systems, to be sufficiently high to melt the powders completely. This always depends on the material used in the SLM machine. Melting temperatures are a key factor, but also the reflectivity and the thermal conductivity has to be taken into account. Obviously, the energy has to be high enough, to reach or exceed the melting temperature of the used material. But the reflectivity influences the amount of energy that can be absorbed by the material. Furthermore, the thermal conductivity increases the minimum required amount of energy density, as energy and heat can diffuse faster, if the material has a higher heat flux density. Aluminium and copper are relatively complex to process with laser based technologies, to name two critical materials. Of course, the spot size should be relatively small, not just for geometry purposes, but also to put a higher energy into a smaller area. The laser beam is focused through a lens and the laser spot represents the smallest spot of the laser beam. Yb:YAG fibre lasers feature such small spot diameters d_L due to their short wavelengths. Figure 1.12 explains the laser beam and the spot diameter accordingly.

It has to be understood that the energy density, defined by hatch distance h, laser power P, scanning speed v, and layer thickness t, have a significant influence on the melt pool and also the heat affected zone (HAZ). Therefore, the surrounding material of a melt pool is influenced and things like a consequent remelting of layers underneath the melt pool, the cool down speed (quenching), and nucleation are influenced. Furthermore, too much energy can cause the vaporization of material. Apart from that, too little energy will result in lack of fusion, pores and a low

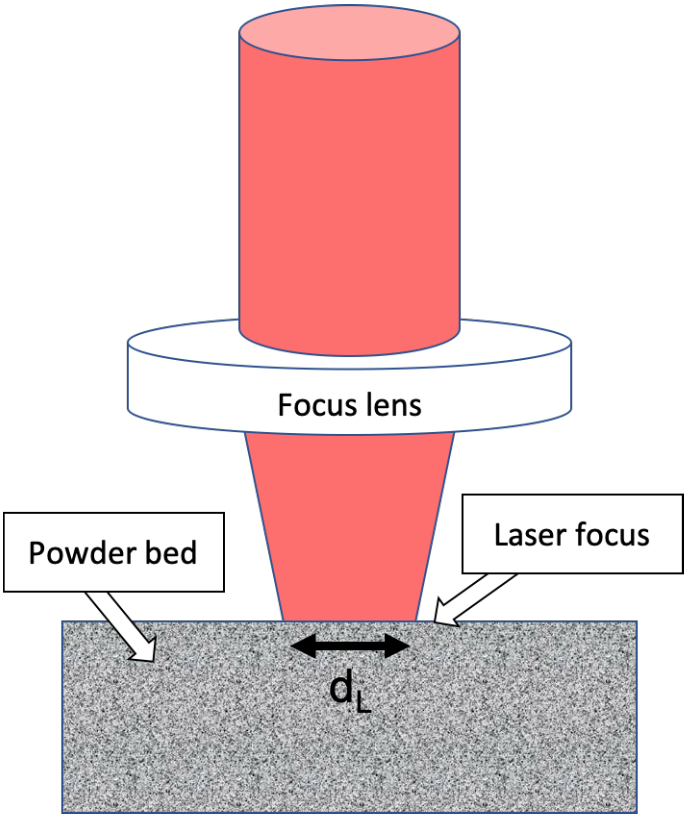

Figure 1.12: Focussing of the laser beam (based on [3]).

part density [65]. Equation 1.2 shows how the energy density E_v, given in J/mm^3 is calculated. However, the energy density is just an indicator for the approximate melting process, as they do not take into account all the physical phenomenons happening during SLM processing.

$$E_v = \frac{P}{v * t * h} \tag{1.2}$$

1.4.3 Scanning Strategy

Another important parameter in SLM processing is the scanning strategy. To achieve a full melting and a well welded part with the powder material in SLM, the layers are remelted repeatedly. The heat energy of the laser beam is sufficiently high to remelt parts of the previously solidified material. Therefore, parts with a high relative density are possible, but the scanning strategy influences the quality of each layer and the stress in the system. The path the laser is guided to from the controlling software, is critical for the heat distribution and different scanning strategies cause different effects in the material. While printing a model with an SLM machine, there are often different settings chosen for the contour and for the infill. The contour mode defines how the laser has to scan the hull, respectively the outline of the part. Furthermore, the laser power can be adjusted to achieve better surface finishes and less powder satellites attached to the solid part. The rest of the part is then scanned differently [9]. In Figure 1.13 the most common infill strategies, namely *meander, stripes, chess* and *contour* are shown.

The right choice for a scanning strategy always depends on the material, the energy density and other factors. What can be said for certain, is that the rotation of the scanning strategy after each layer definitely improves the results of the selective laser melting. Most studies recommend

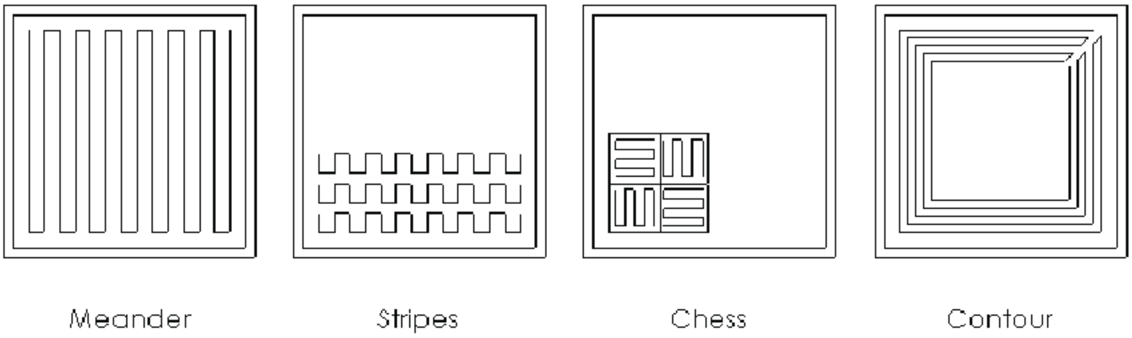

Figure 1.13: Some common scanning strategies for SLM applications [9].

a rotation of 67 ° after each layer for the best results [9]. While rotating the scanning strategy for 67 °, the scheme will be repeated after 180 layers. A schematic of the scanning pattern rotation is given in Figure 1.14. The figure shows a rotation for 90 degrees on the left side and a 67 degree rotation on the right side of the picture. Some SLM devices allow to set the direction of scanning. It is possible to choose, if the laser scanning should be done in the direction of the gas flow or away from the gas flow. In a processing chamber in an SLM device, an inert gas is usually flooding the chamber, to prevent oxidation. Fumes are sucked away to improve the part quality and to avoid too much metal dust on the laser optics. In most cases it is advisable to follow the gas stream of the metal dust, as the laser beam will not be diffracted as much as vice versa.

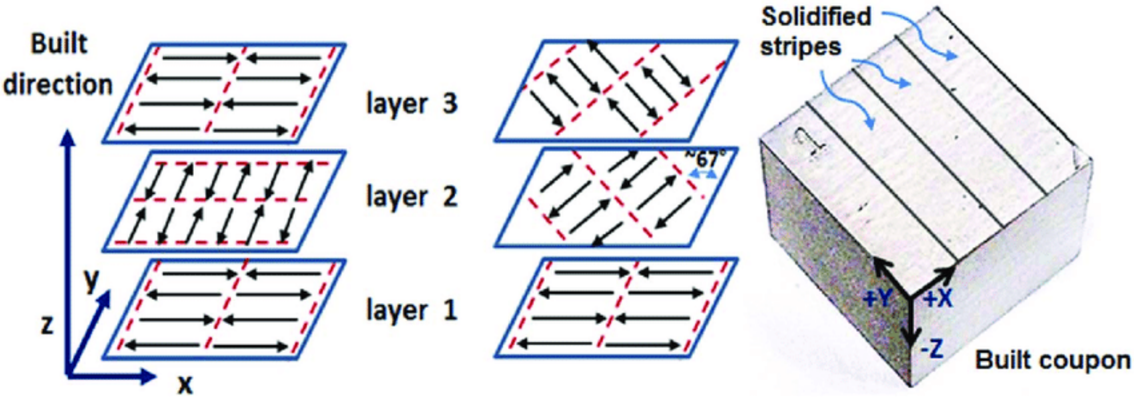

Figure 1.14: Stripe scanning pattern with 90 degree (left) and 67 degree (right) rotation after each layer. [10].

1.4.4 Laser Spot Considerations

The slicer fill scan spacing or hatch distance is the distance between each scanning track. One strategy is, to consequently overlap each laser track to ensure a full melting of the powder. However, another strategy is to use more laser power to completely melt the powder. There is always a heat affected zone which is significantly larger than the laser spot itself. To give a schematic explanation for the hatch distance, Figure 1.15 is provided. It shows the laser focus spot d_L scanning each line and overlapping the previous layer with the hatch distance h. The higher the hatching distance h, the faster the printing process.

Of course, if one considers the true focus of a laser beam, it becomes obvious that the focus

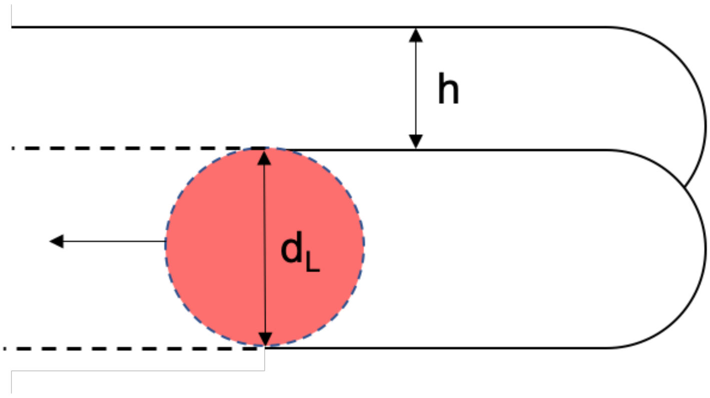

Figure 1.15: Hatching distance h between the laser tracks (based on [3]).

spot is a tiny spot in the middle. At this spot, the focus is perfectly centered and the theoretical maximum energy density available. However, the further the distance from this focus point w_0, the lower the energy density. The laser beam around the focus w_0 was described by Rayleigh. The Rayleigh length of a laser spot can be defined as the length from the laser beam waist radius and the wavelength λ. A laser beam is in most cases approximated by the Gaussian beam, even though a laser in any real life application cannot be perfectly described by a Gaussian distribution. In Figure 1.16 a three dimensional heat distribution of a 50 W laser source is shown from the work of Teng et al. [11].

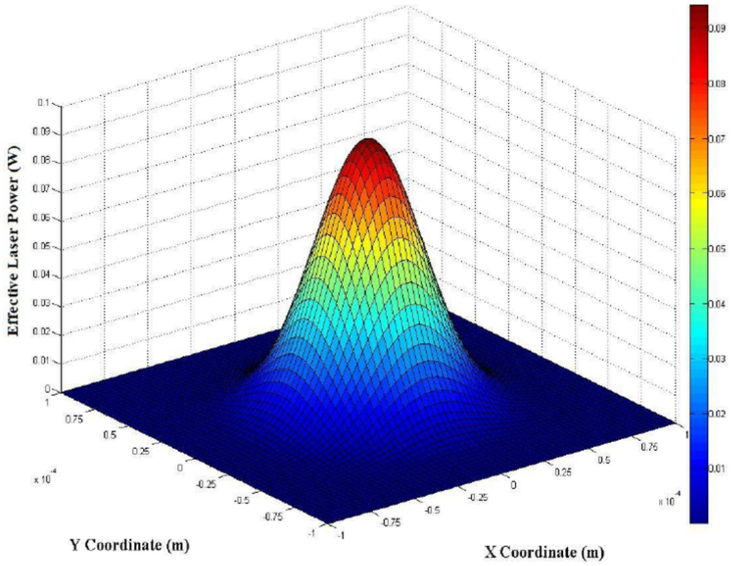

Figure 1.16: Laser beam energy heat distribution of a 50 W laser source [11].

While printing parts with a round shaped laser, it is obvious that edges in a part cannot be printed perfectly. The smaller the laser spot, the higher the possible achievable resolution. Some SLM devices feature adjustable laser spot diameters. Most larger SLM machines have minimum spot sizes of approximately 80 microns, whereas research machines can have smaller diameters like approximately 35 microns. The laser track width can never be smaller than the laser spot diameter. In Figure 1.17a a typical limitation in the parts geometry is shown. The round laser spot is not able to melt the edge of the CAD drawing and therefore, the edge will be manufactured with a slightly rounded shape. This problem only occurs in outwards facing edges. In inwards facing edges, the laser track is intersecting itself with an X - and Y - movement as shown in the image. The image also indicates the areas, which cannot be molten by the laser. Furthermore, some geometrical details cannot be printed, or will be printed too large as Figure 1.17b and 1.17c shows.

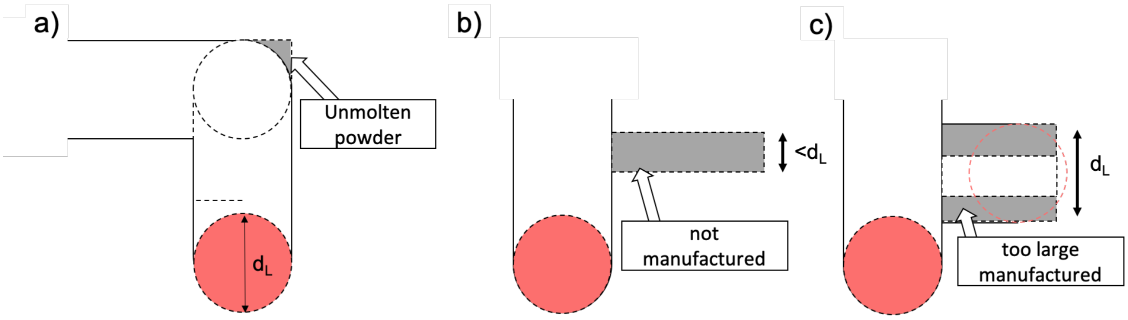

Figure 1.17: Limitations during SLM processing with a round shaped laser beam (based on [3]).

1.4.5 Track Width Compensation

In the SLM machine controlling software, the laser beam is usually guided according to the contour of the part and its according infill. At the outwards facing contour of every part, this would lead to parts manufactured too large, because the half width of the laser beam would melt powder outside of the contour. Contours which are facing outwards, would be manufactured too large and inwards facing contours would be built too small. In Figure 1.18 a simple plate is shown for demonstration reasons. In the middle of the plate, there is a rectangular hole. The laser beam would usually melt too much powder material on the outwards facing contour and therefore, the plate would be too large. The same happens with the hole in the middle of the plate and the hole would be manufactured too small. At each contour, the error would be w_0 or $d_L/2$ respectively. At the right edge of the shown part, an incision is shown. Without any kind of compensation, the incision would be gone and the plate would be printed as an enclosed rectangle. If the laser beam has a spot diameter of 80 microns, the error would be 40 microns.

To manufacture parts as precisely as possible, an intelligent software to calculate a correct track width compensation at each contour is inevitable. In some SLM machine softwares, this is called beam offset. The software usually calculates a new path in parallel to the original contour (nominal value). This offset contour considers the laser beam spot size and changes the nominal value and the path accordingly. Of course, the new calculated path always has to be facing the inner part, which has to be printed. Otherwise, the calculated new path would double the error according to $2 * w_0$ or d_L.

1.5 Material Processing

1.5.1 Preparation of the Feedstock Powder and Characteristics

The powder used for SLM processing has to be chosen with the correct properties and characteristics to achieve the best possible results. Some of the most important properties were listed by Al Mangour [12] and are given in Table 1.1. The flow rate, for example, is significantly influenced by the size of the used powder and the particle size distribution. Thereby, the melt pool viscosity

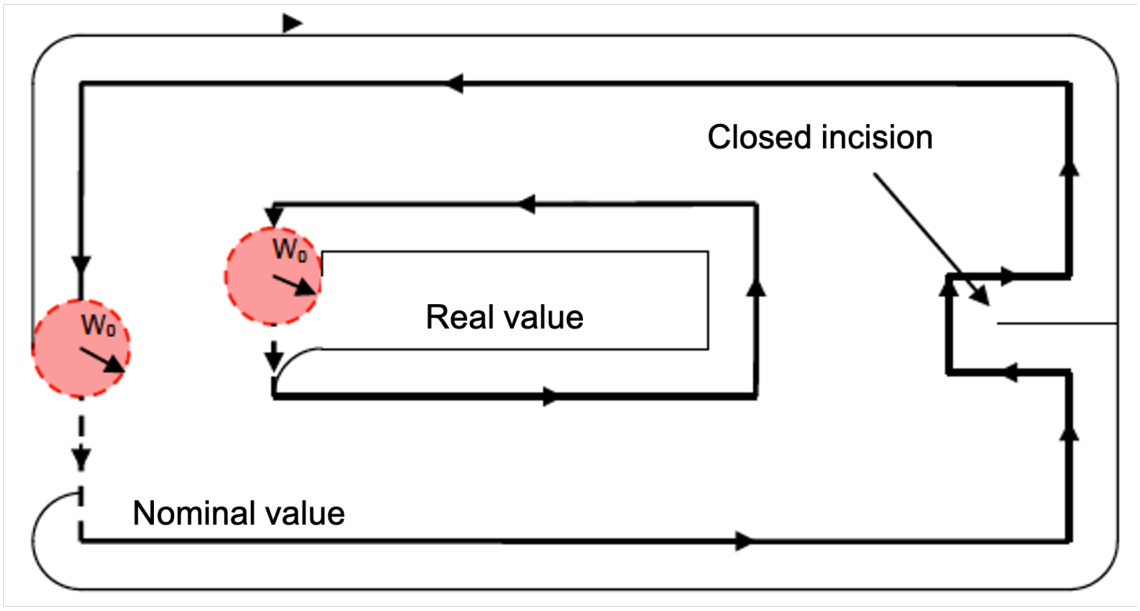

Figure 1.18: Overhangs of SLM parts without track width compensation (based on [3]).

is influenced too. As one can imagine, a smaller particle - especially, if the particle diameter is smaller than the diameter of the laser spot - tends to absorb more energy and therefore, the particle temperature is increased. The mechanisms of densification are influenced and are different than the mechanisms of bigger particles. Coarse particle cannot fill voids as good as small particles can and depending on the average particle size and the particle size distribution, the packing density of the feedstock powder can be very different from batch to batch. Furthermore, the solidification rate is different and therefore, the microstructure can be more coarse or finer, depending on the feedstock powder material [66]. However, if the particles are relatively small, large Van der Waals forces can increase the formation of huge agglomerates, which is especially the case with sub-micron and nanoparticles [67]. These agglomerations negatively influence the homogenisation and the flowability of a powder [68]. Also, depending on the materials used, agglomerations can increase the solidification rate and therefore, the microstructure formation is influenced [12].

Table 1.1: Influencing powder characteristics for the SLM process [12].

Property type	**Examples**
Metallurgical and chemical properties	alloy composition, oxygen and carbon concentration, reaction enthalpy, oxidation potential
Granulomophometric characteristics	particle morphology, particle size distribution, powder flowability, surface roughness of the powder particle
Rheological properties	viscosity and surface tension
Mechanical properties	elastic modulus, tensile strength, yield point
Thermal properties	conductivity, melting temperature, thermal expansion, specific heat
Optical properties	optical penetration, reflection and absorption ratio

1.5.2 Solidification Physics of the Melt Pool and Microstructure

Melt Pool Physics

The selective laser melting process features not just rapid solidification after melting the powder, it also rapidly heats the powder and melts it, due to the high scanning speed and the high laser power. This leads to short interaction times between the laser and the powder material. Several physical phenomena are happening during SLM processing, which are very complex. This is schematically shown in Figure 1.19. The laser melts the powder with a near-Gaussian energy distribution and moves along the contour given by the software. A melt pool is formed very rapidly due to absorption of the material, followed by rapid solidification and, depending on the material, dendrite forming. Heat and mass are transferred and in some cases, a phase formation appears, which is, again, depending on the material and the process parameters. Furthermore, chemical reactions can change the chemical composition of the material and surface tension gradients influence the formation of spatters and the homogenization of the melt [69]. The shape and the size of the melt pool influence, just like the cooling rate does, the microstructure formation and the grain growth. Through the Hall-Petch grain refinement, caused by such a high cooling rate and fine microstructure, the material properties can be improved. However, effects like the Marangoni flow, which is generated through a temperature gradient between the middle point of the melt pool and the outer periphery (near-Gaussian energy distribution), causing surface tension gradients to incline, significantly influence the results of homogenization of elements in the final part [70]. In the Marangoni flow, the melt flow will first flow in the outward direction, but due to surface energy decreases, the melt flow can change its direction and will then flow into the center of the melt pool. This can, on one hand, cause the formation of spatters and defects, but can on the other hand lead to a refined microstructure and metastable phases [71].

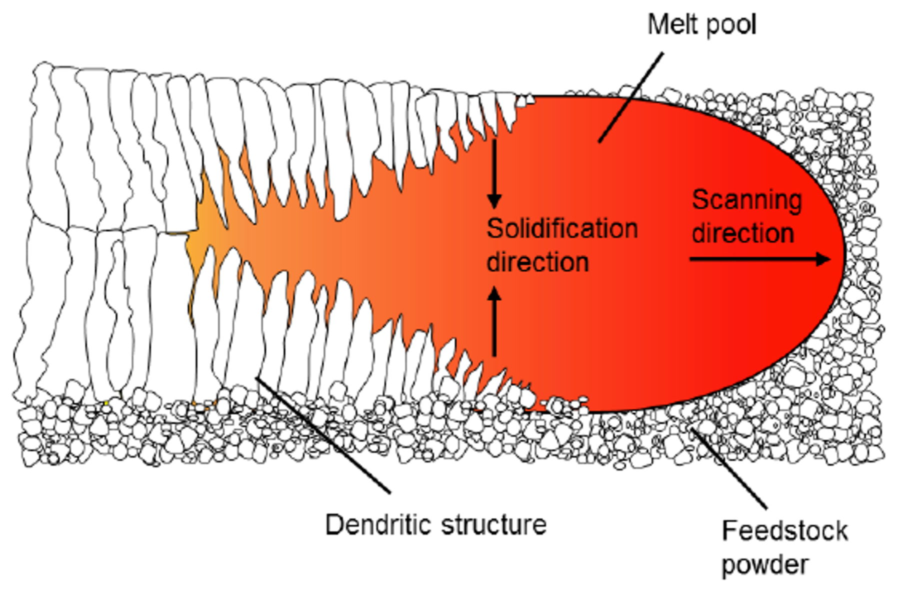

Figure 1.19: Process of solidification during SLM processing [12].

It can be said that the Marangoni flow is formed due to the surface gradient and the direction of the flow depends on a negative or positive gradient. If the surface gradient is positive, the formed melt pool has a small diameter, the depth is relatively deep and the flow is directed from the periphery to the center point. However, if the surface gradient is negative, the melt pool is comparably wide, but not very deep and the Marangoni flow is directed from the center to the edge of the melt pool [72]. To calculate the surface tension, Equations 1.3 are needed.

$$\frac{d\gamma_{LV}}{dT} < 0, \qquad \frac{d\gamma_{LV}}{dT} > 0 \tag{1.3}$$

In the given equations, γ_{LV} is the surface tension of the liquid and T the temperature. Therefore, if $\frac{d\gamma_{LV}}{dT} < 0$ then the flow is facing outwards, like shown in Figure 1.20a (upper part) and in contrary, if $\frac{d\gamma_{LV}}{dT} > 0$, then the flow changes its direction and faces to the center point of the melt pool, which is shown in Figure 1.20a (bottom part) [13, 72].

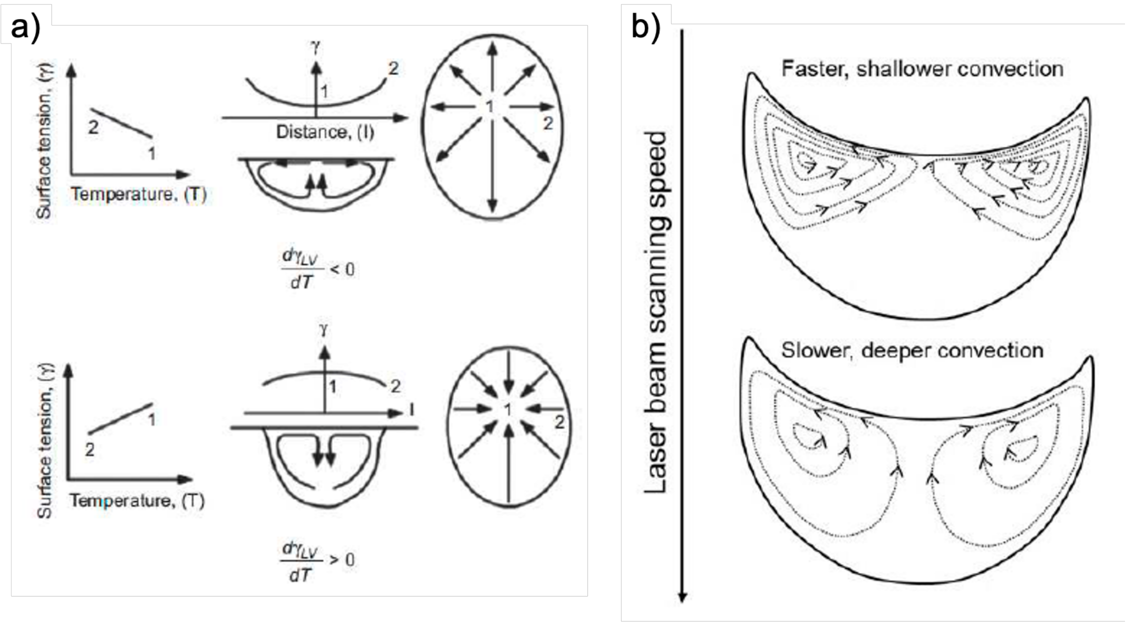

Figure 1.20: Effects of the a) surface tension gradient [13] and b) the scanning speed on the Marangoni flow during SLM processing [12].

In Figure 1.20b the Marangoni flow with a negative surface gradient is shown, but with different laser scanning speeds. The melt pool can have a different shape and different convection flows, but with the same direction of Marangoni flow [12]. The depth of the melt pool can be used, to influence the microstructure and homogeneity of the phases.

Microstructure Mechanisms

Two categories of microstructure growth mechanisms can be named in selective laser melting, which are the *epitaxial growth mechanism* and the *irregular solidification front mechanism*. In the first mechanism, grains are growing in the direction of the maximum thermal gradient [12]. The grains are forming, if the solidification temperature is uniformly decreasing in all directions. The forming grains are also called globulites. In SLM processing, previously processed and already solidified layers of the part are subsequently remelted with the laser and therefore, the crystals will have the same orientation as the ones in previous layers. Large grains can form through this mechanism, which are mostly arranged in columns. The second mechanism happens, if the melt pool induces unstable solidification fronts. This usually happens through inconsistencies in the melt pool front. A very fine grain structure grows away from the periphery of the melt pool to the center point of it. If long and fine prismatic crystal grains are formed, the melt does not cool evenly in all directions. The crystals grow preferentially in one direction, but less rapidly in the other two directions. Uneven directed heat dissipation will cause elongated crystal growth against the preferred direction of heat dissipation. In any case, the mechanisms can be influenced through variation of the energy density (i.e. the laser power and the scanning speed). Starr et al. [14] studied the control of the phase composition in selective laser melted steels and found a very unique microstructure. In Figure 1.21 images of a stainless steel 17-4 specimen is shown, in Figure 1.21a the image was taken with an optical microscope (OM) and in Figure 1.21b with a scanning electron microscope (SEM). In the image taken with the OM, a typical microstructure of an SLM processed sample is shown. The laser melted the material and after solidification and polishing the specimen, the laser tracks became visible. These laser tracks are overlapping and are shaped like a bowl. In the SEM image, columnar grains are shown, which have a clearly visible grain orientation. In a cubic crystal structure, which is also the crystal system of stainless steel 17-4, the grain tends to grow more rapidly perpendicularly to the cubic surface than in other directions [12]. Interestingly, both microstructures - columnar grains and fine equiaxed grains - can be found in the specimen of Starr et al. [14].

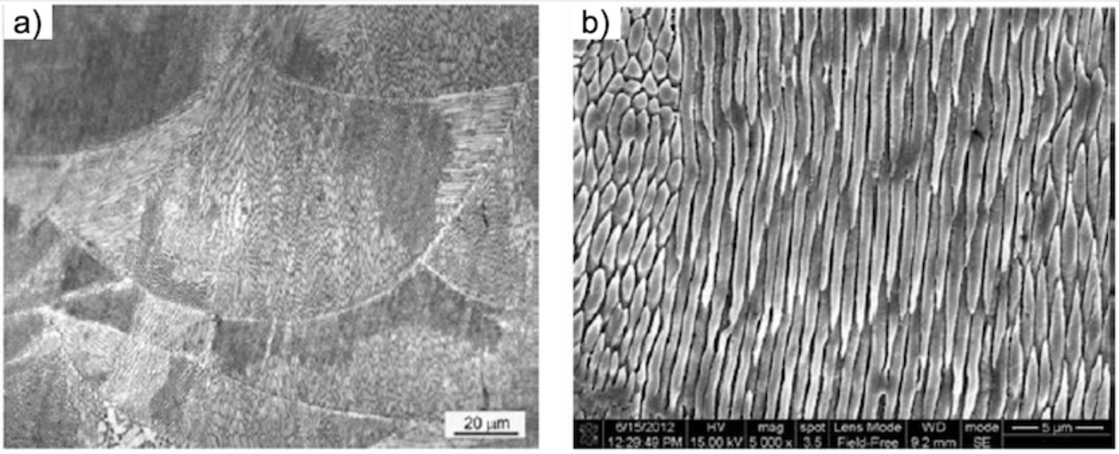

Figure 1.21: Images of stainless steel 17-4 of a) optical microscopy and b) scanning electron microscopy [14].

1.5.3 Crystallographic Textures

A crystallographic texture is the sum of the crystalline orientations in a multi-crystalline solid material. It describes the anisotropy of the material and it can be measured through electron backscatter diffraction. Selective laser melting usually experiences a cyclic thermal history based on each layer [15]. The texture is influenced by the type and speed of solidification. The scanning method can change the texture by changing the scanning vector. The <001> crystallographic texture is developed in the build direction and therefore, against the route of the heat dissipation. The maximum thermal gradient for cubic metals follows the <100> direction, which is why this the typical texture form in steel based materials. This columnar crystal orientation, respectively the columnar crystal growth, can be broken, if a zigzag pattern in a bidirectional scanning strategy is applied and the laser beam is directed with a 90 ° rotation along the contour [12]. Sun et al. [15] investigated the possibilities of in-situ tailoring of the crystallographic texture of 316L stainless steel. Specifically, it was desired to change the <100> crystal orientation of the face-centered cubic metal to a more favourable finer <011> texture, by changing the scanning strategy. In Figure 1.22 their theoretical approach for specimens with higher stress resistance processed by SLM is shown. First, the scanning strategy, including the scanning vector rotation and alternation, and the laser power can be varied. Resulting of these influencing factors, the melt pool geometry will be changed in width, depth and rear length. These geometrical changes are directly correlated with the grain growth and the crystallographic texture. To reinforce a material, the two prevailing deformation mechanisms have to be considered, which are twinning and dislocation movements. Finally, an enhanced strength and ductility can be expected according to Sun et al. [15].

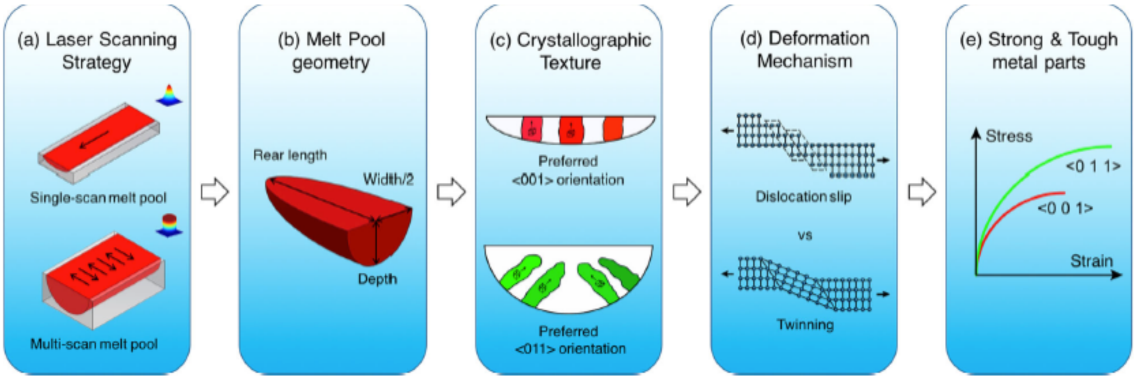

Figure 1.22: Flowchart of texture optimized SLM processing. a) A different laser scanning strategy. b) Grain growth affection by variation of the width, depth and rear length. c) Orientation of different crystal textures. d) Deformation mechanisms in metals. e) Expected outcome through texture variation [15].

1.5.4 Grain Size and Homogenization

Monolithic parts manufactured by traditional technologies like casting usually have a more coarse microstructure than their SLM processed counterparts. The significantly higher cooling rate of SLM processed parts limits the time a grain can evolve and grow. In Figure 1.23 some AlSi10Mg samples after T6 heat treatment can be seen. It is very obvious that the casted specimen of Figure 1.23a and 1.23b have a more coarse and a less homogeneous microstructure than the SLM processed specimen of Figure 1.23c and 1.23d. The casted specimen has lots of dendritical crystal growth and precipitations of silicon along the dendrite borders, whereas the Si precipitations in the SLM processed specimen are very homogeneously distributed in the microstructure [16].

1.5.5 Densification Level and Laser-Based Defects

A quite common problem while selective laser melting metals and alloys is balling. It occurs, if the wettability of the laser melted material is insufficient and it cannot wet the powder or solid material underneath [73, 74]. Therefore, the melted material forms balls and furthermore, porosities are generated, as material is missing in these areas. The quality of the surface decreases and the mechanical properties are lower, due to these defects. One way to increase the wettability is the sufficient and even supply of inert gas in the processing chamber to avoid oxidation. It is also important, to handle the powder as quick as possible under standard environment atmospheres to avoid oxide layers on the powder. Moisture has to be avoided with drying agents in the powder containers. The wettability of some materials can also be improved by adding different alloying additions to the powder material [47].

Another type of porosity can form due to insufficient melting, because of energy density that is too low. If the powder feeding with the coater faces problems, an uneven powder layer can also cause porosities. Furthermore, gas can be trapped in the solidified material after SLM processing. This gas can either come from oxidation, SLM process related effects (Marangoni convection), or

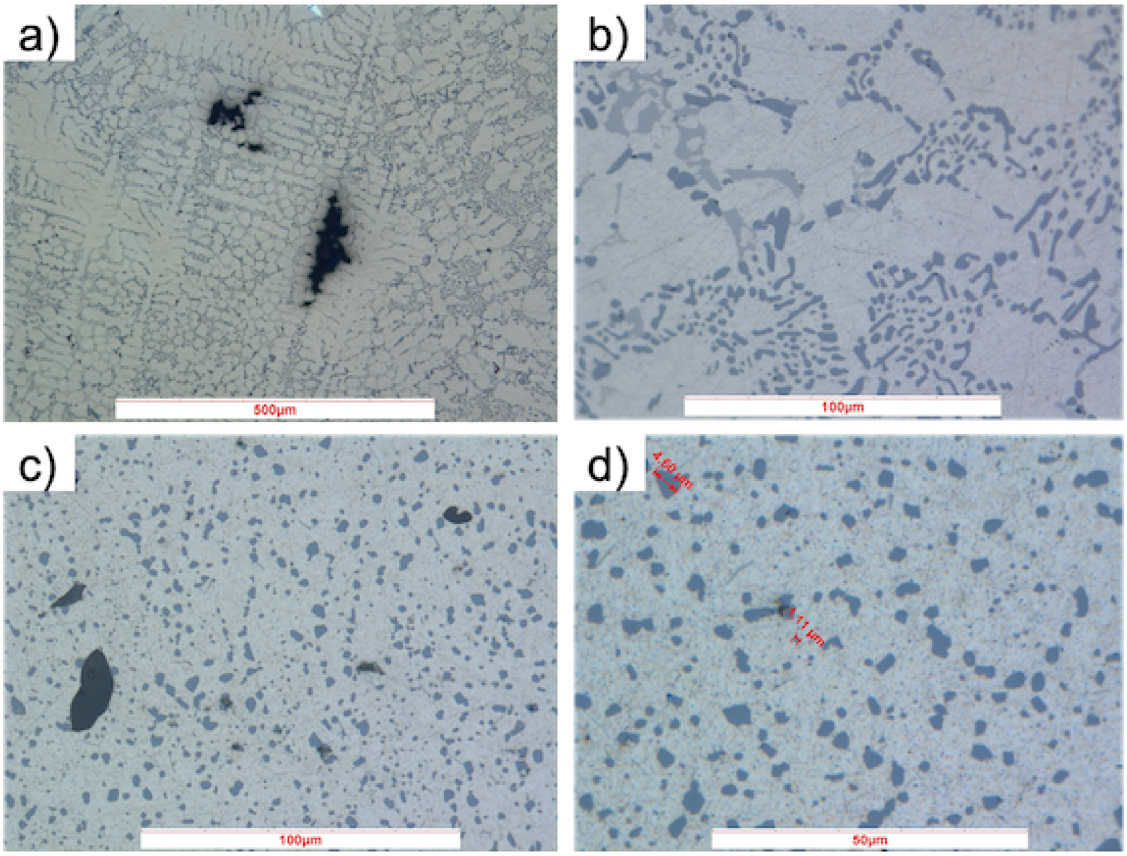

Figure 1.23: OM images of AlSi10Mg of a) and b) a casted sample and c) and d) an SLM processed sample [16].

from the gas atomization process while manufacturing the powder in the gas atomizer.

Every laser based melting technology introduces stress in a small area of the part. Therefore, residual stresses occur as the thermal gradients change quickly. After melting the powder, rapid solidification takes place and this is repeated in every layer several times as the laser usually remelts each layer for two - three times. The higher the cooling rate, the finer the microstructure, but the more residual stresses are brought into the part and therefore, the material properties are weakened. If the energy density in an SLM process is lowered, the residual stresses are lowered, but other errors might occur, like a poor wetting, spheroidization or unstable melt pools. A higher energy density however, can cause the vaporization of liquid metal and keyholes can be formed. In general it can be said, that a stable melt pool is very important for a high part quality. Further, finding the optimal parameters is challenging, but inevitable for highly dense parts without cracks.

Another variable that is subject to fluctuations during the printing process is the laser power that is available at the powder bed level. Variations of the optical output power at the laser itself, as well as the additional expansion and scattering of the laser radiation due to deposited condensates and dirty and worn optical elements in the laser beam lead to changed process conditions. In most cases, a lower optical power is available in the process zone, so that the heat balance and the resulting component properties change. In addition, the formation of smoke above the process zone and its influence by the existing inert gas flow contribute to this effect. Further variations in the process itself are caused by the user or machine operator. The cleaning of the construction chamber in general and the removal of condensate residues, before each building process in particular, as well as the manual powder recycling, are subject to certain fluctuations which cannot be easily quantified. The repeated processing of the unconsolidated powder can also lead to a changed particle size distribution and to a contamination of the powder with other substances.

2

Mechanical Alloying

> Invention is a process; you don't get there overnight
>
> Louis Foreman

2.1 Historical Overview of Mechanical Alloying

The powder processing technique of mechanical alloying was developed in 1966 by John Benjamin et. al. of the INCO, the International Nickel Company [75, 76]. Mechanical alloying (MA) is able to produce homogenous mixtures of different bulk powder materials, but can also form coalescences of elements added to the mill, through repeated cold welding and fracturing of the powder particles. Initially, the technology was developed to create nickel-based superalloys for gas turbines. INCO was working on a technique to inject nickel coated oxides into nickel-based alloys. That way, the oxide particles should get wettable by a nickel chromium alloy. But as these tests failed and other attempts did not prove to be successful, attention was brought to the ball milling process. In previous tests, ball milling was used for coating of hard tungsten carbide particles with softer nickel or cobalt. Researchers also knew, that metal powder could be cracked and fractured with extreme plastic deformation techniques. Benjamin decided to create composite powders with the use of a high energy ball mill and he was even able to produce thoria dispersed nickel, which is used in high temperature applications. In further tests, encouraged by his success, an alloy of Ni-Cr-Al-Ti containing thoria dispersion was created. These successful tests were the birth of MA as a production technique to process oxide dispersion strengthened alloys [17]. The term of *mechanical alloying* was suggested by Ewan C. MacQueen, who was a patent attorney at INCO and this term has become the most common term in literature these days.

Since then, MA has become a useful production technique to process materials both for industry and for scientific sectors. In 1981 Ermakov et al. investigated the magnetic properties of amorphous Y-Co alloys (i.e. YCo_3, Y_2Co_7, YCo_5 and Y_2Co_{17}) using a high energy ball mill [77] and Koch et al. observed the formation of amorphous $Ni_{60}Nb_{40}$ during mechanical alloying in 1983 [78]. Koch compared amorphous liquid quenched with mechanically alloyed $Ni_{60}Nb_{40}$ and proved the achievable similarities of these two processing techniques. These studies brought attention to MA and were the basis for further investigations, as they showed the potential of MA being a non-equilibrium technique. Further research was performed including amorphous alloys, stable and metastable phases and supersaturated solid solutions [17, 79–82]. Due to all these investigations, this relatively simple technology has been applied to composite materials, polymers, ceramics and of course metals [17, 37]. Even conferences have been organized, which were focused on the topic of MA and its proceedings, but also books and journals have been published [83–87]. To name a few examples:

- Rapidly Quenched Metals (now known as Rapidly Quenched and Metastable Materials) [88–91]
- International Symposia on Mechanically Alloyed, Metastable, and Nanocrystalline Materials (ISMANAM)
- Materials Science Forum of Tech Publications [92–95]
- Mechanical Alloying [81]
- Literature collection of MA between 1970 and 1994 [79]
- Journal of Mechanochemistry and Mechanical Alloying

Today there are many researcher worldwide performing investigations in the topics of MA and advanced materials. These results are mostly published in well recognized journals. Two terms are mostly used in todays scientific world: *Mechanical Alloying* and *Mechanical Milling.* When two different powders are mixed together and the goal is to transfer one element into the other respectively to form coalescences with a homogeneously distributed alloy, the commonly used nomenclature is *mechanical alloying.* Whereas the terminology of *mechanical milling* is more likely used solely for homogenization of different elements without any material transfer, but this is not a common rule, as the terms are used in different applications..

2.2 General Mechanical Alloying Process

Todays high performance applications in the aerospace, rocket and the nuclear industry, just to name a few, are striving to get ever-increasing material properties. In the last few decades significant improvements have been achieved in physical, chemical and mechanical material properties. Traditional metals become more resistant to abrasion and corrosion, were improved in terms of lightness, stiffness and increasingly became stronger. However, as technologies improve and human mankind strives for higher limits, materials scientists designed and developed the new field of advanced materials.

Advanced materials can outperform traditional materials and they provide precisely tailored properties which are demanded by a specific application [96]. It is well known these days, that the constitution and the structure of materials in general can be controlled in a better way, while these materials are processed under non-equilibrium respectively far-from-equilibrium conditions [97]. One of the first attempts to control materials in a far-from-equilibrium way and to get supersaturated materials was the rapid solidification of melted alloys [98,99]. Since then, other technologies have evolved like plasma processing, vapour deposition and mechanical alloying [79–82,100,101]. The goal or principle of all these technologies is basically the same. A material has to be brought into a metastable non-equilibrium state by the use of external forces like evaporation, melting or plastic deformation [17,102] and might also involve the change of the state of matter (i.e. solid, liquid, gas). After reaching the aforementioned non-equilibrium state the material has to be quenched into a frozen status.

Turnbull et. al. defined the departure from equilibrium as an indicator of efficiency for the different processing technologies to create metastable structures, which can either be calculated or estimated [17, 102, 103]. The principle, which is illustrated in Figure 2.1 of "energizing and quenching" is based on storing as much excess energy as possible in a system and furthermore, to keep this energy in the system. The resulting departure from the equilibrium or stable status to the metastable phase is expressed in kJ/mol for the excess energy [103,104]. The schematic figure shows how the Gibbs free energy (G) can be increased thru temperature (T), pressure (P) and

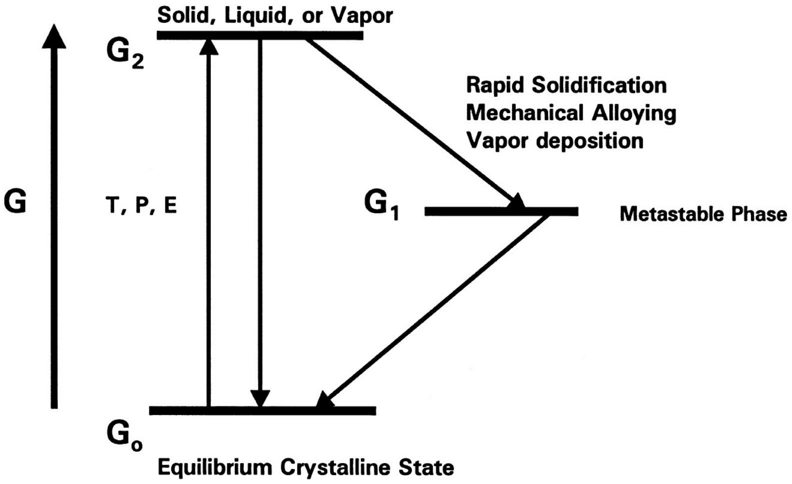

Figure 2.1: schematic concept of energizing and quenching non-equilibrium materials. [17]

internal energy (E).

To todays understanding it is clear, that ion implantation and vapour deposition technologies have an effective quenching rate respectively have a large departure from the stable equilibrium state. But it is also clear, that rapid solidification cannot process material as far from equilibrium as mechanical alloying can, even though rapid solidification has proven its tremendous potential [96, 97].

The process of MA actually always starts with with a mixture of different powders, which are poured into the mill. As there also has to be a grinding medium involved, in most cases balls made out of steel, ceramics or tungsten carbide are added - except the goal is to solely mix the powders homogeneously. After closing the milling container, it sometimes might be advisable to use an inert gas to prevent oxidation during the milling process. After the setup process, the actual MA process can be started. The powders are milled for the desired duration, whereas the jar can get quite hot due to the high energy brought into the system. Depending on the process parameters and the desired outcome, breaks to cool-off the equipment must take place.

2.2.1 Raw Materials

The initial bulk powder for MA can have a size distribution of 1-200 μm and can be brittle, ductile, soft or hard. Even though the initial particle size is not that important in most cases, as the particles tend to decrease in size after only a short amount of time, it depends on the application. If the MA powder should keep its morphological properties, the particle size will not change as dramatically, due to a lower energy input during milling. This can be done through lower rotational speeds, or a different ball-to-powder weight ratio. After longer milling periods however, some of the particles tend to increase in their size, even with lower energy levels. This happens because of the constant fracturing and cold-welding of the particles involved in the process mechanics of MA. Initial powder mixtures can be made with ductile - ductile, brittle - brittle or ductile - brittle materials, whereas ductile matrix materials with some added brittle particles might be the easiest route to get coalescences. In some milling experiments there might be a liquid additive involved, which can reduce the surface energy of the newly formed particles to obtain finer material [17]. MA with a liquid grinding additive is called *wet grinding* and MA without these additives is referred to as textitdry grinding.

As mentioned before, the process of MA is a repeated sequence of fracturing, flattening and cold welding of the involved particles. This happens every time a ball-powder-ball collision occurs, as the powder is trapped in-between the balls, as can be seen in Figure 2.2. Another option is the ball-powder-vial collision, which can also happen. In the first phase of the process, some fracturing and cold-welding occurs and forces the different powders compositions (i.e. metal A and metal B - or component B) together (Figure 2.3a). This process is permanently repeated and produces a constant exchange of elements between the particles, which ensures a high mixing rate [105]. In the second phase, the different elements start to form dispersoids and precipitations during solidification (Figure 2.3b). This obviously just occours, if enough power is used for the MA process. Next, some intermetallic compounds can be discovered and the two starting powders have formed a solid coalescence while the microstructure gets finer in the particles (Figure 2.3c). In the last phase the particles have formed a metastable structure in a steady-state period. The particles can still contain precipitations of intermetallic compounds or dispersoids (Figure 2.3d) [18]. One key factor for MA is the thermal activation of the surface areas of the grinded powders. With high energy ball milling the elements of the particles tend to be mixed on an atomic level, whereas the formation of coalescences without chemical reactions or phase formations is the goal with low energy ball milling.

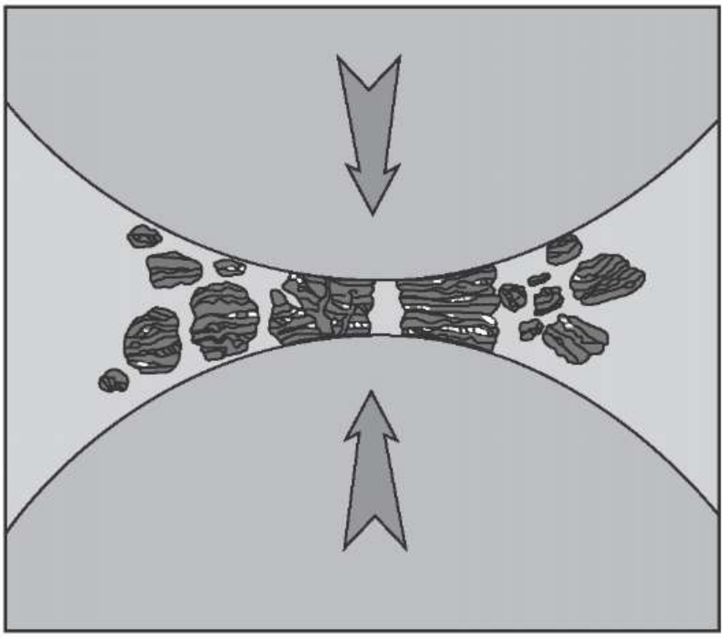

Figure 2.2: Balls crushing particles and force them together. [18]

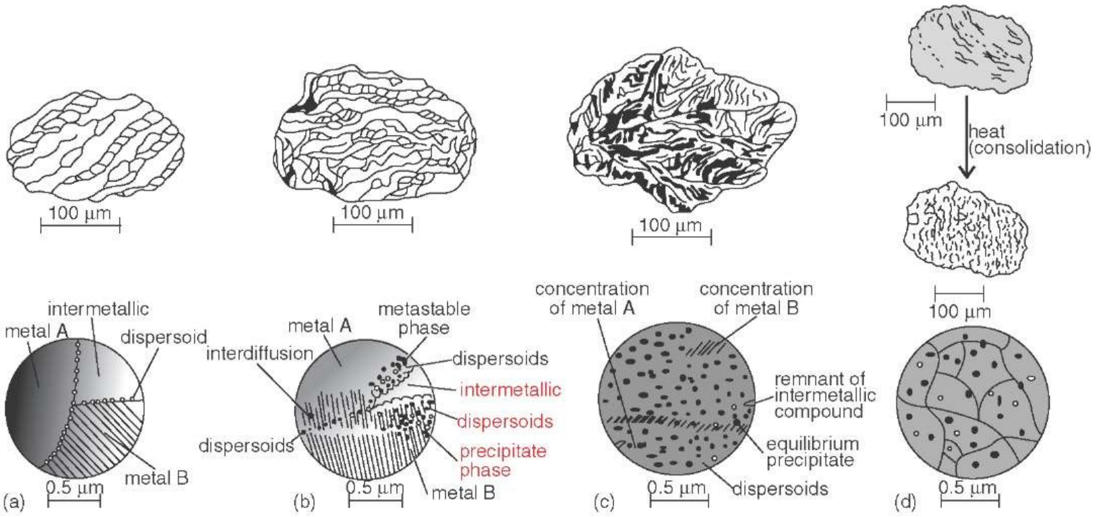

Figure 2.3: Stages of mechanical alloying. [18]

2.2.2 Types of Mills

These days various types of mills for mechanical allying exist. They differ in their general design, way of operation, capacity and some can even be equipped with cooling or heating additions.

Planetary Ball Mills

One of the most popular mills for powder processing is probably the planetary ball mill. The biggest and most well known manufacturers for ball mills are the Fritsch GmbH (Figure 2.4a) and the Retsch GmbH, both located in Germany.

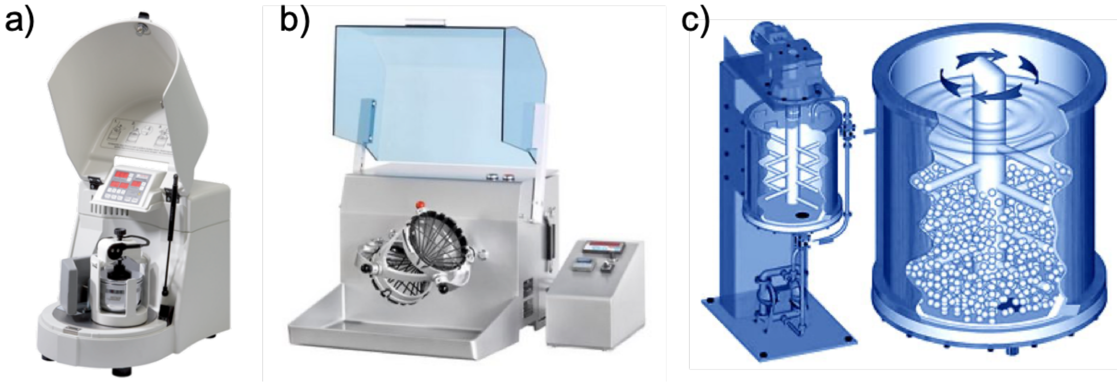

Figure 2.4: Photos of a) Fritsch Pulverisette 4 [19], b) Turbula shaker mixer [20], c) Attritor ball mill [21].

As the name suggests the mill has a planet-like movement of its jars, which are mounted on a support disk. The support disk moves with an adjustable rotational speed and because of a special drive mechanism also the vial itself rotates around its own axis. The occurring centrifugal forces act on the jar and its containing balls and powders. As the supporting disc and the jar rotate in the opposite direction, the centrifugal forces act in like and in the opposite direction depending on their position in the cycle. Due to this change of rotational direction respectively the change of the direction of the force, the grinding balls travel freely through the jar and collide with the opposing wall. This is the time, when the balls will crush some of the powder material and induce force to the powder particles. An overview of the process is given in Figure 2.5 in which a planetary ball mill with 4 jars is shown.

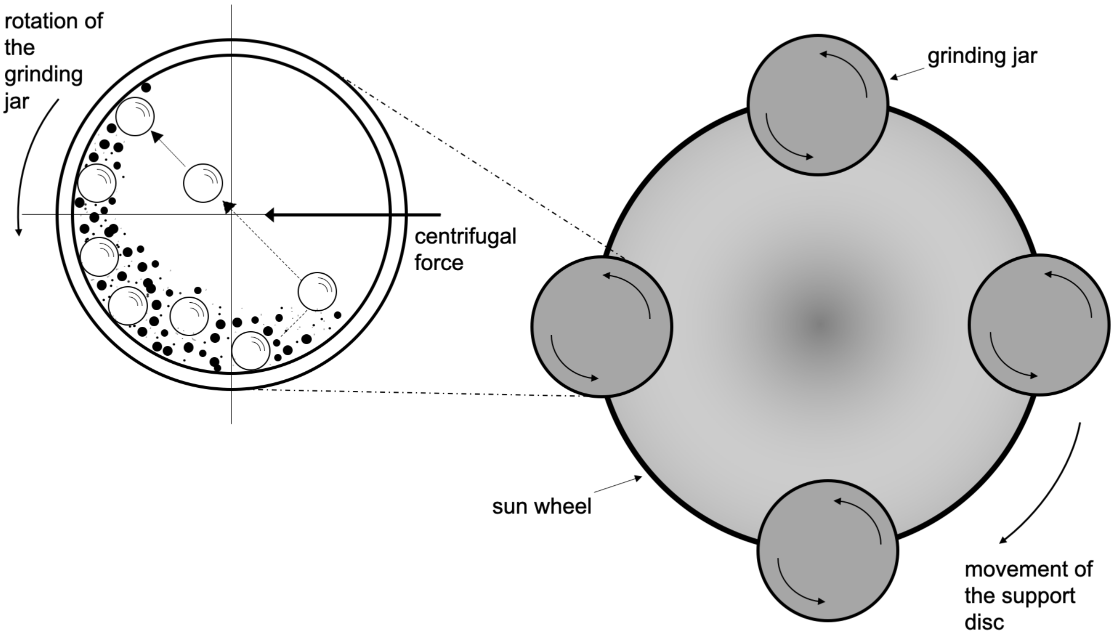

Figure 2.5: Schematic image of a planetary ball mill with 4 vials.

There are also mills available with only two or even one jar for research applications in laboratories. The image also shows the free travelling balls and the friction effect, which occurs when the balls run from one side to the other side of the jar. Some modern mills let the operator adjust not just the rotational speed of the supporting disc, but also the rotational speed of the grinding jars. The grinding vials are available in various materials - hardened steel, stainless steel, tungsten carbide, agate, sintered aluminium oxide (corundum), silicon nitride, zirconium oxide, polypropylene. The sizes of the milling containers can be up to 500 mL each.

Attritor Mills

Horizontal mixing mills, similar to the ones used on construction sites, are limited in their maximum milling speed, as they are relying on the principle of gravity and centrifugal force. As soon as the milling container rotates too fast, the centripetal and the centrifugal forces are equal and therefore none of the material inside will fall down. To induce higher energies into a system, the principle of *stirred ball milling* was invented and the machines are commonly known as *Attritor Mills*. One of the advantages of an Attritor is the fact, that the power input is used for agiatating the powder thru a rotating impeller instead of rotating a large and heavy jar [106]. They are built in a vertical setup and the rotating impeller energizes the balls. Therefore, the process of milling is started and the mean powder size is decreased. The powder gets impacted between the milling balls, the container wall and the impeller shafts. In Figure 2.4c a schematic overview is given. This induces shearing and impact forces to the powder material. Attritors are built to handle large quantities of powder, as they are designed to work with 0.5 - 40 kg of material. Commercial units are designed and manufactured by Union Process in Akron, Ohio. Even though they can work with higher speeds than their predecessors (i.e. horizontal mixing mills), their overall energy input

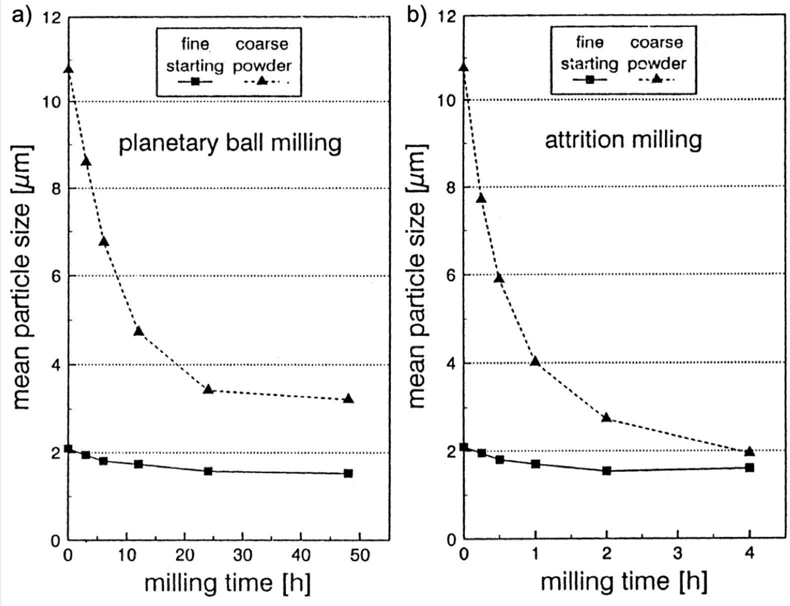

Figure 2.6: Time to decrease particle size distribution of TiB_2 powder in a) planetary ball mill and b) Attritor.

is comparably lower than in planetary ball mills due to the lower grinding medium velocities. The grinding jars are mostly made out of stainless steel and can be coated with rubber, polyurethane, aluminum, silicon carbide, silicon nitride or zirconia. A great plus, is the possibility to heat or cool the grinding jars, which is often not possible with other techniques [17, 106].

Others

Lots of other designs have been developed in recent years like vibrating mills, rod mills, jaw crushers, cutting mills, knife mills, morat grinders, disc mills and cryo mills. Cryo mills use liquid nitrogen to cool down the powder material to make it more brittle and then perform an axial movement to crush the powder with the grinding balls. One type of device, which was intentionally not designed for milling, but can easily be used for this purpose is a Turbula shaker mixer. Shaker mixers are mostly known for their outstanding capability to homogeneously mix powders, which is achieved by an interaction of translation, rotation and inversion. They are designed to rotate in a three-dimensional motion. They mostly work with plastic containers which can be completely closed and therefore work dust-free. If one adds steel balls to the powder material, a similar effect like in other mills can be achieved, even though the energy input is not as high. Tests showed, that the milling time has to be increased accordingly, but the results are comparable to planetary ball milling. They were brought to the market in the early 1990s by Willy A. Bachofen AG, Switzerland (Figure 2.4b). The efficiency of the mills always depends on the starting material and the desired outcome. For example, Figure 2.6 shows, that an Attritor mill can decrease the particle size faster for a TiB_2 powder than a planetary ball mill, but due to the lower energy input it might not always be that suitable for mechanical alloying of the bulk powder [107].

2.2.3 Process Variables

For the technique of mechanical alloying there are lots of parameters influencing the process. These parameters can be quite complex if there is a specific desired outcome of the particle size, phase and microstructure. As mentioned before, there are lots of different mills. So choosing the right mill for the application is mostly the first step. Next, the material for the milling container and the grinding balls has to be chosen. On one hand the material depends on the budget that can be spent, on the other hand it is important to understand the effects of a material which is too weak or soft for an application. Due to the high impact forces of the balls against the inner jar walls, some of the material might get dislodged and can cause contaminations. With some applications this must not happen, while in other applications it might not be such a problem, as the milled powder might contain similar elements just as the grinding jar does. Another possibility is, that fine and hard particles of a powder sample could get stuck in a jar or in the balls, if the used material is too soft. Therefore, the percentual amount of these elements might decrease. One of the most influencing process variable is the milling speed. The higher the milling speed, the higher the energy input into the powder system. This is true up to a certain maximum speed, which depends on the design of the mill. In a conventional high energy ball mill an increased rotational speed will effect the balls linearly. The higher this rotational speed is set, the more energy will be transferred into the powder, but if the speed gets too high, the balls will be pinned to the jar and will not fall down anymore. This is the critical point which must not be exceeded for this type of mill. The milling speed also affects the temperature during ball milling. This is somehow also a limitation factor, as the vials are not supposed to get too hot and therefore could get damaged. However, in some applications a high temperature might be desired, because it is necessary for a particular system to form alloys or special phase changes. In other cases, a high temperature during MA might cause problems. Kaloshkin et. al. reported, that an increasing mechanical intensity, due to an increasing temperature inside the vial, accelerated the diffusion processes while mechanically alloying Fe-Cu powder. The face centered cubic (f.c.c.) Fe-Cu solution contained random Fe and Cu atoms in the lattice and decomposed into Fe-rich and Cu-rich solutions, instead of homogenous f.c.c. Fe-Cu. The positive enthalpy of the Fe-Cu solution formation and therefore, its endothermic reaction, resulted in less free energy [108].

2.2.4 Temperature Rise during Ball and Powder Impacts

To avoid temperatures that can cause damage to the grinding jar it is necessary to understand the temperature rise during ball milling. But also, it is of importance to understand the powder surface temperatures occurring during every impact to predict the mechanisms during MA. Due to the dynamic behaviour of the process it is very difficult to measure temperatures in-situ. Furthermore, the temperatures changes only on a microscopic size level. To face these challenges, one can choose from three different approaches: theoretical calculations, indirect measurements and observations on a microstructural level. [109]. As the goal for the materials in this study was to form coalescences with low energy ball milling and to keep a near spherical shape after the MA process, the temperatures during the procedure had to be kept as low as possible. An estimation for the peak temperature of a particle, which is trapped between two balls, can be approximately estimated based on calculations of Schwarz and Koch [110]. In their research they assume that a particle is deformed by localized shear and the bulk temperature increases:

$$\Delta T = \frac{F}{2}\sqrt{\left(\frac{\Delta t}{\pi k_0 \rho_p c_p}\right)} \tag{2.1}$$

where F = the energy flux which dissipated on the glide plane. F equals to $\sigma_n v_r$ in which σ_n = normal stress caused by a head-on collision. It is assumed that a particle deforms by shear under this stress [109]. v_r = the relative velocity of the ball before impacting the particle. In this study, tungsten carbide and stainless steel 440C were the materials used for high energy ball milling. Both, the jar and the balls were either made out of 440C or WC and were not mixed up. As there were different bulk powder materials processed, case scenarios have to be considered for the correct calculations.

First, the volume of the 10 mm balls had to be calculated which was 0.523 cm^3. Based on the specific density of 440C ($\rho_{b_{440C}}$) and WC ($\rho_{b_{WC}}$) the mass m_{440C} and m_{WC} can be calculated. This gives $m_{440C} = 4.02$ g and $m_{WC} = 8.12$ g respectively. Then, the two centrifugal forces had to

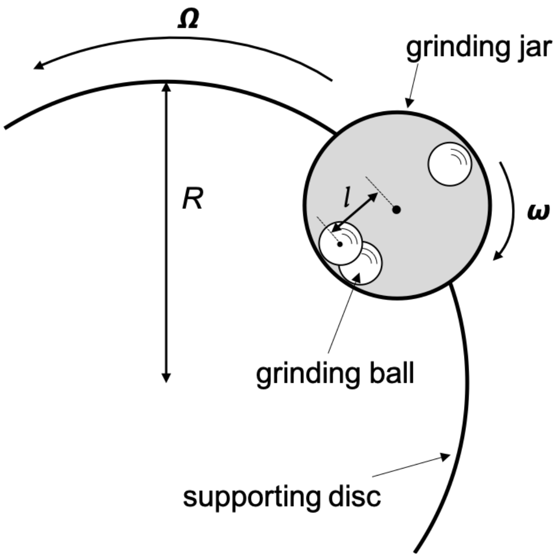

Figure 2.7: Rotation and revolution of the supporting disc and the grinding jar in a planetary ball mill.

be calculated, because on one hand the supporting disc has a revolutionary speed, which rotates the grinding jar on its outside. On the other hand, the jar itself has a rotational speed, spinning around its own axis. The rotational speed of the jar and the revolution speed of the supporting disc are linked with a -2:1 ratio.

To calculate the centrifugal forces the equations

$$F_j = m * l * \omega^2 \tag{2.2}$$

$$F_{sd} = m * (R - l) * \Omega^2 \tag{2.3}$$

are needed [111]. In these equations m is the mass of the used balls (i.e. WC or 440C steel), R is the radius of the supporting disc, l denotes the radius minus the diameter of one ball as it is the distance of the rotational center of the jar to the centroid of a ball which is in contact with the jar wall and ω and Ω are the angular velocities respectively the angular frequency for the jar rotation and the supporting disc revolution. A schematic is given in Figure 2.7.

This angular frequency is the product of 2π and the frequency f. Based on 200 rpm for the supporting disc f is equal to 3.332 rps and based on 400 rpm for the grinding jar it is 6.667 rps. As there are case differentiations, the centrifugal force of the supporting disc with steel balls ($F_{sd_{440C}}$), for the grinding jar with steel balls ($F_{j_{440C}}$), for the supporting disc with tungsten carbide balls ($F_{sd_{WC}}$) and for the grinding jar with tungsten carbide ($F_{j_{WC}}$) had to be calculated separately. If one uses the values for Equation 2.2 and Equation 2.3, the results are

$$F_{sd_{440C}} = 0.0879 \text{ N}, F_{j_{440C}} = 0.7837 \text{ N}, F_{sd_{WC}} = 0.1602 \text{ N and } F_{j_{WC}} = 0.388 \text{ N.} \tag{2.4}$$

Furthermore, the acceleration of the balls can be calculated. Because of the unique design of a planetary ball mill at a certain point during a circle, the two centrifugal forces have to be added and at another point, the forces have to be subtracted. The latter is the point, in which the balls will fall freely through the vial and crush the powder. It is therefore given:

$$a_{440C} = \frac{F_{sd_{440C}} + F_{j_{440C}}}{m_{440C}} \text{ and } a_{WC} = \frac{F_{sd_{WC}} + F_{j_{WC}}}{m_{WC}} \tag{2.5}$$

Thus, the results for the acceleration of steel balls are $a_{440C} = 116.21$ m s^{-2} and $a_{WC} = 116.24$ m s^{-2}, which are interesting results considering the different forces and masses involved. Finally, the velocity of the balls can be understood with:

$$v_r = \sqrt{a * 2l + v_0^2} \tag{2.6}$$

If one fills in the numeric results and values for Equation 2.6, in which v_0 is the initial speed, a is the acceleration of the steel, respectively the tungsten carbide balls and l is the way the balls travelled through the vial, the results for the velocities are $v_{r_{440C}} = 3.2340$ m s^{-1} and $v_{r_{WC}} = 3.2344$ m s^{-1}, which is not a big difference, but reasonable due to the fact of the small differences in the acceleration of the balls and the short travelling distance from one end of the vial to the other end. Nevertheless, it is therefore proven, that the velocity and the acceleration during MA is, at least in this case, not dependent of the material of the balls. To keep the further calculations simple, the value for $v_r = 3.23$ m s^{-1} will be used for Equation 2.1.

To solve Equation 2.1 it shall be deemed that $\sigma_n = \rho_b v_s v_r$, in which $\rho_b = 7.67$ g cm^{-3} for 440C steel and $\rho_b = 15.63$ g cm^{-3} for tungsten carbide. This state of stress lasts for a certain amount of time which is expressed through Δt and this equals to $2d/v_s$ where $d = 1$ cm and is the diameter of all used balls and v_s is the speed of a longitudinal wave running through the used solid material of the balls (i.e. steel or WC), which has to be distinguished accordingly. In 440C steel $v_s = 5390$ m s^{-1} and in tungsten carbide $v_s = 6220$ m s^{-1}. The values for the powder density ρ_p and specific heat capacity c_p are based on the manufacturers data. Therefore equations 2.7 have to be considered:

$$V_{MS1_{90}VC_{10}} = \frac{m_{MS1}}{\rho_{MS1}} + \frac{m_{VC}}{\rho_{VC}} \tag{2.7}$$

The typical density value for MS1 is 8.0 g/cm^3 and 5.77 g/cm^3 for VC. The ratio for MS1 and VC was 90:10 wt% so it can be therefore calculated:

$$V_{MS1_{90}VC_{10}} = \frac{90}{8.0} + \frac{10}{5.77} = 12.98 \text{ cm}^3 \tag{2.8}$$

With equation 2.9 the relative density of the combined material can be estimated:

$$\rho_{MS1_{90}VC_{10}} = \frac{100}{V_{MS1_{90}VC_{10}}} = 7.734 \ \frac{\text{g}}{\text{cm}^3} \tag{2.9}$$

The same approach can now be adopted to the MS1 and TiC mixtures, which had the same composition. Pure TiC has a density of typically 4.93 g/cm^3:

$$V_{MS1_{90}TiC_{10}} = \frac{90}{8.0} + \frac{10}{4.93} = 13.28 \text{ cm}^3 \tag{2.10}$$

$$\rho_{MS1_{90}TiC_{10}} = \frac{100}{V_{MS1_{90}TiC_{10}}} = 7.53 \ \frac{\text{g}}{\text{cm}^3} \tag{2.11}$$

To calculate the specific heat capacity c_p for MS1 and VC respectively MS1 and TiC the following equation was used:

$$c_{p(mixture)} = \sum_i c_{p(i)} x_i \tag{2.12}$$

where x_i is the mole fraction of each component. From equation 2.12 can be obtained

$$c_{p(mixture)} = (\frac{m_1}{m_{mixture}})C_{p1} + (\frac{m_2}{m_{mixture}})C_{p2} + ... + (\frac{m_n}{m_{mixture}})C_{pn} \tag{2.13}$$

Based on the data of EOS MS1 and Treibacher VC the equation can be formed accordingly to:

$$c_{p(MS1_{90}VC_{10})} = (\frac{90}{100}) \cdot 450 + (\frac{10}{100}) \cdot 519 \tag{2.14}$$

respectively for EOS MS1 and Treibacher TiC:

$$c_{p(MS1_{90}TiC_{10})} = (\frac{90}{100}) \cdot 450 + (\frac{10}{100}) \cdot 569 \tag{2.15}$$

which results in a heat capacity of 456.9 J/kgK for MS1 and 10 wt% VC and 461.9 J/kgK for MS1 and 10 wt% TiC. As mentioned above, the energy heat flux, that dissipates on the glide plane, can be calculated with $F = \rho_n v_r$, but a case differentiation has to be considered according to the used balls for MA. Two new formulas can be generated:

$$F_{440C} = \rho_{b_{440C}} v_{s_{440C}} v_r^2 \tag{2.16}$$

and

$$F_{WC} = \rho_{b_{WC}} v_{s_{WC}} v_r^2. \tag{2.17}$$

If one puts the previously mentioned values into these equations, the results are:

$$F_{440C} = 7670 * 5390 * 3.23^2 = 431.31 \text{ MJ/m}^2\text{s} \tag{2.18}$$

$$F_{WC} = 15630 * 6220 * 3.23^2 = 1014.27 \text{ MJ/m}^2\text{s} \tag{2.19}$$

Furthermore, it can now be calculated that $\Delta t_{440C} = 3.71\ \mu$s and $\Delta t_{WC} = 3.22\ \mu$s. To finally calculate ΔT with equation 2.1 the thermal conductivity k_0 is assumed by EOS for maraging steel at 0.15 W/cmK and therefore, the resulting irradiated temperature rise per impact for maraging steel and vanadium carbide with 440C steel balls for the time Δt is:

$$\Delta T_{VC_{440C}} = \frac{431310000}{2} \sqrt{\frac{3.71 * 10^{-6}}{\pi * 15 * 7734 * 456.9}}$$

$$\Delta T_{VC_{440C}} = 32.19 \text{ K} \tag{2.20}$$

The irradiated temperature for maraging steel and vanadium carbide with tungsten carbide balls is:

$$\Delta T_{VC_{WC}} = \frac{1014270000}{2} \sqrt{\frac{3.22 * 10^{-6}}{\pi * 15 * 7734 * 456.9}}$$

$$\Delta T_{VC_{WC}} = 70.52 \text{ K} \tag{2.21}$$

And eventually for maraging steel and titanium carbide with tungsten carbide balls is:

$$\Delta T_{TiC_{WC}} = \frac{1014270000}{2} \sqrt{\frac{3.22 * 10^{-6}}{\pi * 15 * 7734 * 456.9}}$$

$$\Delta T_{TiC_{WC}} = 71.08 \text{ K} \tag{2.22}$$

The results of the average temperature rises lies substantially below the melting temperatures of the used powders, but the heat might be sufficient for transformation processes which are thermally activated. As these temperatures occur only with direct ball-to-ball head-on impacts and only affect a very small surface, they do not affect the whole powder or jar. But after longer milling times, temperature may rise and therefore cooling-off breaks are advisable during the process of mechanical alloying. While the melting of surfaces with these temperature increasings are quite unlikely, it is possible that the occurring temperatures cause enhanced micro-diffusion or enhanced deformation [109].

2.3 Mechanical Mixing

In mixing processes, the constituents of at least two separate mixture components are repositioned by a relative movement in such a way that a new arrangement pattern is created. This produces a mixture (also called batch) and, under certain conditions, a new substance. The so-called main phase is present as a continuous phase, while the so-called additional phase is initially discontinuous. In distributive mixing, two substances that are soluble in each other are mixed at low shear forces, but as there were just solid un-soluble one-phase powders (solid-solid) used in this thesis, the focus was set on diffusive mixing.

In the first attempts to produce composite powders in this work, mechanical mixing was used. It was furthermore used as a preliminary step in each powder batch, to achieve homogeneous powder mixtures. This is, where the core strength of the procedure lies. It is capable of fast and efficient mixing of different constituents. One very common tool to mix powders is a Turbula shaker mixer. The powders are poured into a plastic container and mixed for 10 to 20 minutes. While mixing solid-solid batches together, it is important to introduce as much relative motion as possible into the material that has to be mixed. A Turbula shaker mixer is performing several of these relative motions due to its unique design. The mixing procedure can be done with or without solid additives. Additives can prevent the formation of agglomerations and therefore, a finer dispersion can be achieved. While mixing powders one has to consider the energy in the mixing system. Especially, if additives are added, the energy can lead to unwanted coalescences and deformation of the particles due to excess heat and plastic deformation.

Mechanical mixing is a promising technique for large spherical powders that have to be coated with a second element, which is significantly smaller. The second constituent should have a submicron or nano size distribution [17]. In the work of Gu et al. [23] the capabilities of mechanical mixing are presented, just to name one example. Nano-TiC powder was coated to spherically shaped Ti without the use of any additives. Two flaws of mechanical mixing however, are the possible inhomogeneities due to agglomerations and the low Van-der-Waals forces, which hold the elements together.

3

Metal Matrix Composites

> The task is not to see what has never been seen before, but to think what has never been thought before about what you see everyday.
>
> Erwin Schrödinger

As mentioned in the chapter of *Mechanical Alloying*, todays research focus lies on advanced materials. These materials are a relatively new, but promising research field. Research groups all over the world are investigating alternative processing technologies to manufacture these advanced materials. One may have heard from high entropy alloys (HEA) which are alloys that do not have a base element, but rather have five or more components which are synthesized in an almost equal amount. Another route to advanced materials are so called metal matrix composites (MMCs). MMCs consist of two or more chemically and physically distinct phases, which are distributed in a suitable way. These phases shall give properties to an advanced material, which would not be obtainable with only one phase individually [37]. The two phases consist of the matrix material, which is the bulk material, and at least one reinforcing material in a particulate, fibrous or laminate shape [112].

3.1 Introduction

Composite materials are made out of two or more elements and while designing a composite material, it is usually desired to combine the positive aspects of each element into one composite material. In most cases, the mechanical properties are the main reason, why one would try to create a new advanced material. But the economical aspects are factors that must be considered too. The availability and the price of an element can be critical and the production costs of a composite material might be too high for some applications. Krainer [113] mentions the following potentials of composites:

- the increase of ultimate tensile strength and the elongation at break,
- the increase of the fatigue strength in high temperature environments,
- a higher wear resistance
- a lower thermal expansion coefficient
- and an increase of the Young's modulus.

Hamilton [112] categorizes the enhancements in *mechanical properties*, *thermal capabilities* and *fatigue behaviour*. Through the increase of the frequency of dislocations in a matrix material

Table 3.1: Types of reinforcing elements for MMCs [37].

Type	Aspect ratio	Diameter	Examples
Particle	1 - 4	1 - 25 μm	SiC, Al_2O_3, BN, B_4C, WC
Short fiber or whisker	10 - 10,000	1 - 5 μm	C, SiC, Al_2O_3, Al_2O_3 + SiO_2
Continuous fiber	> 1,000	3 - 150 μm	SiC, Al_2O_3, C, B, W, Nb-Ti, Nb_3Sn
Nanoparticle	1 - 4	< 100 nm	C, Al_2O_3, SiC
Nanotube	> 1,000	< 100 nm	C

caused by the reinforcing composite, the mechanical properties can be better than the properties of unreinforced materials. The thermal capability is influenced, because of the constraint of the matrix flow properties and therefore, MMCs can have a higher creep resistance. Lastly, the fatigue resistance can be increased with ceramic reinforcing particles as shown by Chawla and Chawla [37].

Arth [114] furthermore mentions, that the magnetic properties and the bio-compatibility can be increased. Polymers, ceramics and metals are the three main material groups and they all can be combined together. In this thesis, the focus was set on metal matrix composites, as they are the most promising for casting tools and selective laser melting.

However, some material properties can be improved, but there are some drawbacks of MMCs. For example, the machinability of MMCs is often complicated due to the low ductility and resistance against fracture. Furthermore, stress caused by different coefficients of thermal expansion between the matrix material and the composite material can create a comparably low fracture toughness [112] . Especially, environmental temperature changes can cause part failure, due to stresses in the MMC. It was also discovered by Jayalakshmi and Gupta [115] that some MMCs have a lower ductility and a higher brittleness. Another very well known critical aspect of composite materials are agglomerations and inhomogeneities of the reinforcing elements in the matrix material, caused by Van der Waals forces between the sub-micron and nano-particles [115].

Typically metal matrix composites have improved mechanical properties compared to traditional unreinforced metal alloys. Because of the better mechanical properties, in some cases there can be less material used, while achieving similar results in performance. Other advantages are higher temperature capabilities and resistances, higher wear resistances and in some cases improved fatigue characteristics. During the time of writing this thesis there are four main types of MMCs known, which are, according to Chawla and Chawla [37], the following:

- Particle reinforced metal matrix composites
- Short fibre- or whisker-reinforced metal matrix composites
- Continuous sheet- and fibre-reinforced metal matrix composites
- Layered or laminated metal matrix composites

The different types of MMCs are given in figure 3.1. Typically, there are particles in the micron, sub-micron or nanometer scale used for metal matrix composites. However, there are other forms sometimes used and an overview is given in Table 3.1.

To produce MMCs there are different processing routes available. Evans et al. [116] differentiate between.

- liquid - phase processes (e.g. in the melt pool),
- solid - phase processes (e.g. powder metallurgy),
- two - phase processes (e.g. rheo-casting),
- gas - phase processes (e.g. coatings).

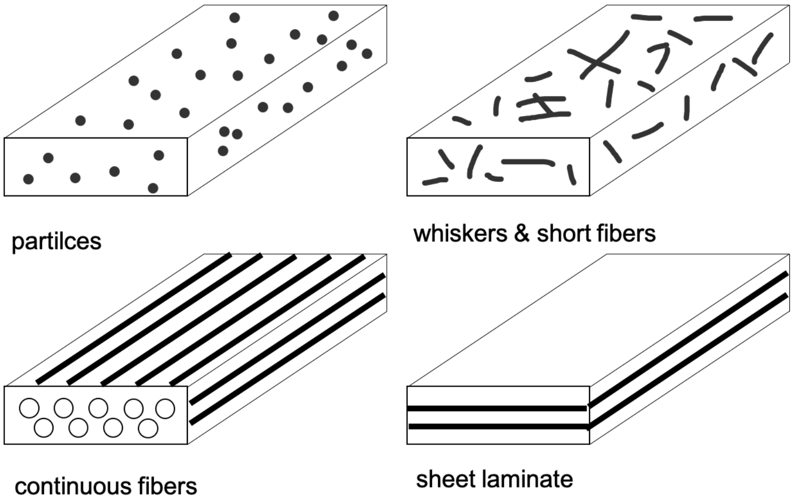

Figure 3.1: Different ways to create reinforcing composite materials.

As gas - phase processes were not relevant for this thesis work, the topic will not be discussed in detail. In liquid-phase processes for example ceramic particles are infiltrated into a melt. Another variant includes a vortex mixer, which mixes the ceramic particles into a melt for a better homogenisation. In solid - phase processes, the components will be mixed together, whereas the amount and the particle size can be varied as required. Powder metallurgy is the most known example for a solid - phase process. One method for the powder metallurgical route is mechanical mixing followed by sintering. Another way to fabricate MMCs within a solid - phase is mechanical alloying, in which a mill is used to form coalescences of the different elements. It is mostly used for elements, which are impossible or very hard to create an alloy with.

3.2 Grain Refinement

While designing a steel based alloy, it is very common to use carbide-forming elements like Ta, Ti, V or Nb as they will form mono-carbides with carbon during solidification [117]. These precipitations at the grain borders will hinder the further growth of grains and therefore, the grains will exist in a smaller form. Each of these grains is a border for dislocation movements and they will act against stress. The lattice structure of the grains differs in orientation and if a force acts against a grain, there is more energy required to dislocate adjacent grains, as they are oriented differently and the force has to change directions. This is called the Hall-Petch grain strengthening. The grain strengthening effect is expressed in a dislocation-dislocation interaction and the stress field around these grains is given by:

$$\sigma \propto \frac{G * b}{r}, \tag{3.1}$$

in which σ is the stress, G is the shea modulus of the material, r is the distance of the dislocation and b is the Burgers vector. Therefore, stress is inversely proportional to the distance between the precipitations [112]. It can be said that the more homogeneous and the finer the reinforcing particles are distributed in the matrix, the shorter is the distance r. Therefore, if one assumes a fixed weight percentage of reinforcing composite particles, the higher the resistance is against dislocation movements.

In any case, it has to be understood that through the introduction of carbide-forming elements, these elements will bind carbon with them and therefore, the phase formation will be significantly influenced. For example, the martensite starting temperature will be increased, if there is less carbon in the steel matrix. Furthermore, there will be less C available for a formation of martensite and therefore, the hardening effects of martensite will be decreased [118]. Another effect of grain refinement is the introduction of particles for potential nucleation starting points. These particles should not be melted during the melting process due to their significantly higher melting temperature. They should not be soluble in an iron matrix and should have a similar crystal structure to the matrix material crystal structure [62]. To act as a nucleation starting point, the particle has to act as a point of a new solidification wave. For this, an interaction between melt and particle surface is necessary, which requires a good wettability of the particle and therefore, a contact angle of less than 90 ° [62, 119].

Oxide ceramics, like aluminum oxide and yttrium oxide, do not dissolve very well in an iron melt [119] and their wettability is also relatively poor (contact angle $> 90°$). The elements furthermore have a tendency to agglomerate and will separate from the metal matrix. Carbides however, have a good solutability at higher temperatures in an iron matrix, but are depending on the carbide forming alloying element [120]. Therefore, mono-carbide forming elements like titanium, vanadium and tungsten are potential candidates for a reinforcing component in a metal matrix composite.

3.2.1 Correlation of the Mechanical Properties to the Grain Size

Grain refinement is usually performed with ultra high strength steels. The correlation is described by the Hall-Petch relationship [62]. Specifically, a correlation between the yield stress σ_y of a material with a large grain size and the yield stress σ_0 of a material with a small grain size is given. Furthermore, k_{HP}, the Hall-Petch strengthening constant of a material, and d, the average grain diameter, is needed [121]. The Hall-Petch relationship is mathematically described as:

$$\sigma_y = \sigma_0 + \frac{k_{HP}}{\sqrt{d}}. \tag{3.2}$$

The relationship of the yield stress σ_y of a material with a fine grain size and the yield stress σ_0 of a material with a large grain size is given in Figure 3.2. It has to be mentioned that the Hall-Petch effect has its limits. If the grains become finer than approximately 10 nm, the grain boundaries will begin to slide past each other and there will be no strengthening effects anymore [112].

3.3 Particle Strengthening

As mentioned before, the Hall-Petch effect can increase the mechanical properties of a material through finer grains. Grain refinement causes natural borders for stress and dislocation movements. The same effect can be caused through precipitation hardening and coherent, semi-coherent and incoherent precipitated particles. If the precipitated particles have a similar lattice constant as the matrix material has (difference less than 2 %), the lattice structure of the matrix material can blend into the precipitation. If the precipitation and the matrix material just have a few similar lattice planes, it is called semi-coherence. Incoherence describes precipitates with no similarity to the matrix material and in this scenario, a theoretical dislocation movement cannot cut through the lattice structure of such a precipitation. The force has to change its direction and is therefore weakened (Orowan force) [122, 123]. As a result, the material properties are increased, due to the higher force necessary for dislocation movements [123].

The extension of the dislocation line can be geometrically defined as semicircles with the radius R:

$$R = \frac{l - 2r}{2} \tag{3.3}$$

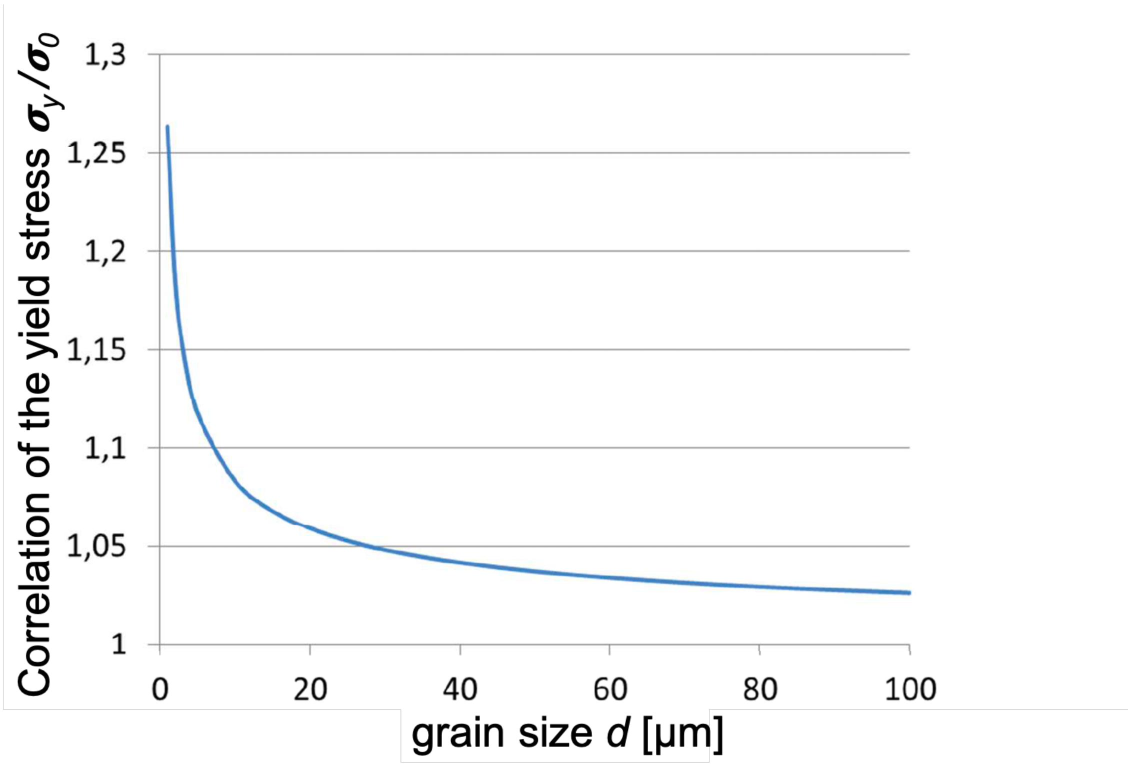

Figure 3.2: The correlation of yield stresses and the grain size explained through the Hall-Petch relationship.

in which $2r$ is the diameter of the particle and l is the average distance of the particles from the center to the center point. Therefore, $l - 2r$ is the dislocation line. For the mechanism, a critical configuration, respectively a critical maximum is reached, if the stress Δ_τ exceeds the value:

$$\Delta_\tau = \frac{G * b}{l - 2r} \tag{3.4}$$

and in which G is the shear modulus and b the magnitude of the Burgers vector. If the critical stress is exceeded, the particles are either cut or the force for the dislocation movement changes its direction.

In Table 3.2 the information about the crystal structure of all materials used in this thesis work are provided. The martensitic phase, which was the matrix material, did not show any similarity to the intermetallic phases $FeNi_3$, Ni_3Ti, $MoFe_2$ nor to the carbides TiC, VC, V_8C_7, V_2C or V_6C_5. Because of this, the intermetallic phases precipitated incoherently and so did the carbides, if they were melted completely. Therefore, the intermetallic phases and the carbides can potentially hinder dislocation movements and increase the strength of the material. Some carbides, which did not melt completely, had a bigger particle size and also acted as dislocation movements, but were also potential starting points for micro-cracks, due to their size and shape in the solidified matrix material. Such particles are never perfectly embedded into a matrix and therefore, cracks can potentially start from these spots. However, unmolten carbides are usually also starting points for nucleation and crystal growth and therefore, a finer crystal structure, which increases the material properties of a material.

Table 3.2: Crystallographic data for the materials used in this study [38].

Phase	**Pearson Symbol**	**Space Group Designation**	**Prototype**
(α-Fe)	$cI2$	$Im\bar{3}m$	W
$FeNi_3$	$cP4$	$Pm\bar{3}m$	$AuCu_3$
Ni_3Ti	hP16	194	$TiNi_3$
$MoFe_2$	hP12	194	$MgZn_2$
TiC	cF8	225	NaCl
VC	cF8	225	NaCl
V_8C_7	cP60	213	V_8C_7
V_2C	oP12	60	$Fe_2N_{0.94}$
V_6C_5	hP33	151	V_6C_5

3.4 Wear

In recent years some scientific work showed the capabilities of ceramic particle reinforced materials [124–128]. The materials used for the reinforcing phase included Al_2O_3, SiC and TiO_2. Of course, an inevitable requirement for reinforcing particles is a higher hardness and wear resistance than the matrix material. Especially ceramic particles and carbides are interesting candidates as composite materials, due to their relatively high hardness of > 1000 HV. There are two different mechanisms of how a reinforcing phase can act in the matrix material:

- The reinforcing particles are not melted and just act as a starting point for nucleation and will act against dislocations or
- the particles will be melted and dissolved, but will form primary precipitations after solidification.

In the first case, the particle will not be molten and it will be intracrystallinely (within a crystal) or intercrystallinely (along the borders of the crystals) integrated. The morphology of the particles will not change dramatically. The second mechanism describes a full dissolvement of the reinforcing particles and therefore, the morphology is changed completely. In most cases, the primary formed precipitated particles will be more homogeneously distributed in the solidified matrix material. In traditional casting methodologies, the materials should be quenched or at least cooled down more rapidly, as a slow solidification process can increase the particle size of these elements. However, in selective laser melting the cooling rates are significantly higher and therefore, the reinforcing particles will precipitate relatively small [62, 129].

3.5 Additive Manufacturing of Metal Matrix Composites

The addition of ceramic particles to achieve a grain refinement is a common technique and has been known for many years, especially in the casting industry. Even in welding processes, the addition of ceramic reinforcing particles was successful and it was possible to achieve a heterogeneous nucleation and equiaxed grain growth [112, 130]. Sokoluk et al. [131] investigated aluminum metal matrix composites with nano-sized TiC particles, to get crack-free welds in an unweldable Al7075. In recent years, research started to apply nano-ceramic refinement particles in additive manufacturing technologies, to mitigate phase segregation and to resolve cracking in Al based alloys [132].

Research is more and more focusing on metal matrix composites (MMC) for selective laser melting applications, but particle reinforced advanced materials have a very particular tailoring process. One has to take into account the particle size distribution and the particle morphology during powder processing and SLM processing. Furthermore, the melt pool is affected during laser scanning the powders and the Marangoni convection in a melt pool can cause segregation and therefore, an inhomogeneous distribution in the solidified part. Because of some drawbacks while designing metal matrix composites for additive manufacturing and because of the complex effects happening during the process route, MMCs in AM are a relatively new research field.

Overall, there is a huge demand from various industries for advanced materials, due to the better mechanical properties, thermal properties and wear resistances. There were several MMCs developed for laser beam melting, with very good results. However, for powder bed based technologies, there were less studies performed and the powder preparation and SLM parameters have to be optimized and investigated. In the future, more composite materials will be developed, but research has to focus on the particle morphology, the particle size distribution, the homogeneous distribution of the composite materials and the investigation of phase formations during SLM processing.

3.6 MMC Powder Fabrication for SLM

Usually, powders for selective laser melting or other powder bed fusion based techniques, are produced via gas, water or plasma atomization. Water and plasma atomization are limited in terms of powder oxidation and more expensive than gas atomization, which is why the production of powders is mostly done in a gas atomizer.

For the atomization process a solid block, wire or powder is molten and then rapidly cooled down by an inert gas. A schematic overview of two gas atomizers is given in Figure 3.3. In Figure 3.3a the raw material exists as melt or powder and in Figure 3.3b a solid metal block is processed. In both cases the raw material is transformed to metal powder through gas atomization. Through the rapid solidification and the gas, spherical powders are formed, which is the perfect morphology and shape for powder bed fusion processes. The process is hard to control, as there are many different particle sizes produced during the solidification. Usually, the right particle sizes are sieved for each application. In some cases, there are many satellites formed in the powders. Satellites are smaller undesired particles which attach to bigger ones and significantly influence the spreadability in the SLM coating process. During the cooling phase in the gas atomizer, a matching inert gas has to be chosen to control the microstructure of the spherical powders and to prevent oxidation.

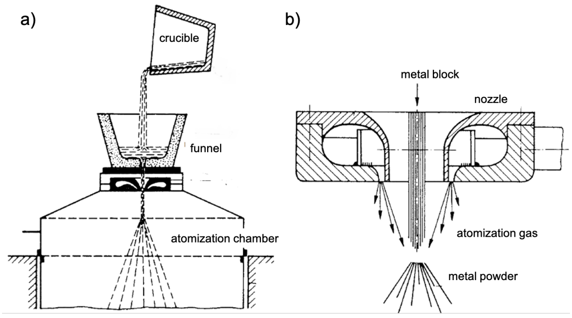

Figure 3.3: Schematic of a gas atomizer for powder production (based on [22]).

The gas atomization process is suitable for most conventional alloys, but is limited for the production of MMCs. The reinforcing particles have to be spray injected into the matrix material during the atomization process into the molten spray stream. The particles have to be precisely injected to guarantee a homogeneous distribution. This is particularly hard to achieve, the smaller the reinforcing particles get. Sub-micron and nano-particles have a high tendency to form agglomerations, due to large Van der Waals forces and are hard to inject. Due to these problems and the high equipment costs, a small batch production is not advisable.

Another route of reinforcing formation is an in-situ reaction synthesis during melting the matrix material and the composite particles. In selective laser melting, the capabilities of controlling the heat input and the speed of solidification are relatively flexible, which makes SLM an optimal processing technique for the formation of MMCs. Al Mangour [133–135] in-situ formed TiC in a 316L stainless steel matrix with a laser-induced reaction. 99 % purity Ti powder and graphite powder were mechanically alloyed with 316L powder. The mixture was then SLM processed and it was discovered that the Ti and C elements formed a TiC phase [12]. Chang et al. [68] investigated AlSi10Mg with the addition of coarse or fine SiC in a laser beam melting process. They discovered a formation of Al_4C_3 and an increase of microhardness and a decrease of the wear rate. However, some reactions can cause troubles and are not desirable. Cormier et al. [136] analyzed the possibilities of mechanically alloyed γ-TiAl compounds from Ti alloys using electron beam melting. Ti and Al powders were used in a planetary high energy ball mill, but a less preferable $TiAl_3$ phase was synthesised. An in-situ synthetisation of MMCs has proven in several scientific investigations its capabilities, however, the production is still challenging. The feedstock powder preparation and the laser process parameters significantly influence the results and the phase formations and therefore, further work should be performed for a deeper understanding of the mechanisms.

Surface coating is another way how researchers have successfully produced metal matrix composites. There were several studies found in the literature, like excessive mechanical mixing or mechanical alloying. If the composite powder is in a sub-micron or nano size range, it can be sufficient to just mix the powders, for example in a planetary ball mill, without any grinding medium. Gu et al. [23] distributed nano-TiC on spherically shaped Ti powders in a planetary ball mill without grinding balls. The result of their work is given in Figure 3.4.

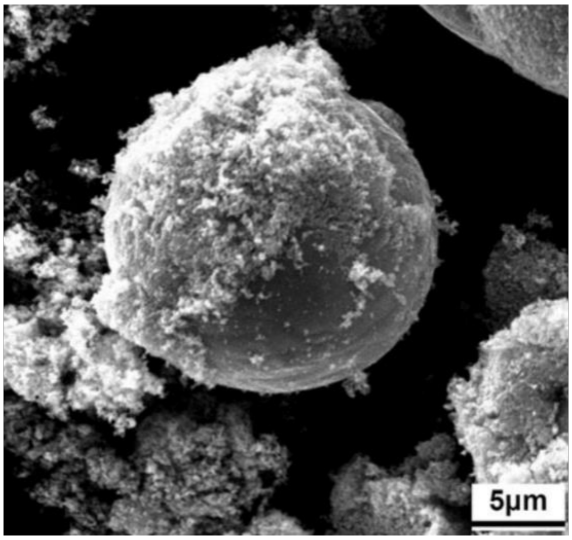

Figure 3.4: Nano-TiC distributed on Ti fabricated with mechanical mixing [23].

The biggest advantage of a mixing process is, that particles will stay spherical, and this is beneficial for the coatability in selective laser melting applications. However, in some studies, the reinforcing elements did not stick very well to the matrix material. Agglomerations were caused and as a result, inhomogeneous distribution after SLM processing. Mechanical alloying in high energy planetary ball mills with grinding balls has proven to successfully combat these issues [17].

4

Materials

> The most rewarding researches are those which, inasmuch as they are a joy to the thinker, are at the same time of benefit to mankind.
>
> Christian Doppler

4.1 The Base Material: Maraging Steel Grade 300

Maraging steels (MS) are a group of high performance steels which have superior toughness and strength, derived from precipitations of intermetallic nickel compounds, without compromising lower ductility levels [137]. They are almost carbon free and are alloyed with a high amount of nickel. Typically the weight percentage of nickel in maraging steels is greater than 12 percent. The name is a portmanteau of *maternsite* and *aging*, in which the latter refers to the heat treatment process in which a solutionized metal allows its alloyed elements to diffuse through the microstructure and therefore, form intermetallic particles. In maraging steels these particles are most likely Fe_3Ni intermetallics and will fall out of the solution. They then act as a reinforcing phase and increase the materials strength. The main alloying elements are Ni, Mo, Co and Ti. The carbon content has to be kept low in these types of steels. Even at low cooling rates, maraging steels will form a soft type of nickel-martensite, which can be age hardened at 435 - 510 ° C for 1 - 6 h. During this aging process, the mentioned intermetallic precipitations form and make the steel very hard. Microstructures of maraging steels impart in excellent tensile strength, high elongation at break, impact strength, resistance to cracks, a good thermal conductivity plus great machinability at temperatures of up to 500 ° C. These steels are used in the tooling, aircraft and oil industry, but are also used for gas centrifuges in the nuclear industry. Maraging steel fabrication with SLM and its mechanical properties has been investigated by various researchers and these days, maraging steel powder for SLM is commercially available. For example German SLM manufacturer EOS offers maraging steel powder called *MS1*, but also Austrian based steel manufacturer Böhler Edelstahl offers MS powder for SLM processing called *W722* just to name a few. These days, most maraging steels have a nickel content of around 18 %. Commercial MS is available with different tensile strengths and they are named with their ultimate tensile strength in ksi (kilo pound force per square inch) and their nickel content. Variants between 200 ksi (1380 MPa) and 350 ksi (2400 MPa) are available [138]. Therefore, 18Ni300 has a nickel content of 18 % and an ultimate tensile strength of 300 ksi, to name an example. The MS1 from EOS has a chemical composition corresponding to US classification 18 % Ni Maraging 300, European 1.2709 and German X3NiCoMoTi 18-9-5. After the SLM building process, it can be easily post-hardened to more than 50 HRC by age-hardening at 490 ° C for 6 hours. The ultimate tensile strength can be expected at around 1100 MPa respectively at 2050 MPa after age hardening.

4.1.1 Properties and Applications

Typically, maraging steels are used for applications which demand high ductility levels, a high tensile strength and a good resistance to stress in high temperature environments. Maraging steels are able to deliver these characteristics. The promising material properties often find usage in rocket and space parts, motorsports, the military environment, nuclear power plants and the forging industry. Especially dies for the solid forming industry and the injection molding industry often are manufactured out of maraging steels. These dies and molds are influenced by a number of external forces and therefore, they often have a lifetime of less than 1500 cycles. Injection molding dies made out of MS often face complex cavities and cooling channels. To further improve lifetimes of dies, space exploration parts and uranium centrifugal plants, carbides can be added to the MS matrix material.

One way to increase the material properties of maraging steel is to form particle-reinforced metal matrix composites, for example with tungsten carbide, like the work of Yan et al. [139] shows. While designing MMCs the main aim is to combine the high toughness of the metal matrix material and the superior hardness of the added composite particles to produce parts with excellent wear resistance, mechanical properties and isotropic behaviour. Furthermore, they can be processed with similar technologies as for monolithic materials. Nevertheless some material properties can be increased, others like the fracture toughness of steel MMCs is comparably lower than that of the original matrix material. Studies of Pagounis [140] and Bacon [141] suggested, that stress caused by strain can crack up the reinforcing particle respectively cause the matrix interface to form cracks starting from the primary hard particle. Another factor for possible failures is the difference in thermal expansion coefficients of the metal matrix component and the reinforcing composite component, which can deviate cracks during solidification, but also can be a source of errors during high temperature usage of a MMC part.

As promising as the material properties of these MMCs are, their usage is limited due to the geometrical limitations of traditional manufacturing methods. Because of this, engineering applications of particle-reinforced metal matrix composites are limited these days. In this study, a unique approach of powder processing and manufacturing was applied, after some preliminary experiments revealed the drawbacks of mechanical mixing compared to mechanical alloying.

4.1.2 Microstructure and Chemical Properties

Martensite is the main phase of maraging steels and is an α-Fe which forms out of austenite without the diffusion of atoms. It is named after German metallurgist Adolf Martens. To form martensite in carbon-steels, they have to be quenched from the γ-austenite phase with a very high cooling rate to start a phase formation, plus the quenching has to be fast enough to prevent the diffusion of atoms out of the crystal structure to form Fe_3C cementite. This differs from steels with a very low amount of carbon respectively in maraging steels. Especially nickel, but also other alloying elements (i.e. Co) can stabilize the γ-Phase down to temperatures of 200 ° C. The temperature at which the martensite starts to form (M_S) is underneath the equilibrium temperature T_0, in which austenite and martensite have an identical level of Gibbs free energy and therefore are in an equal state. Quenching the face-centered cubic (f.c.c.) austenite under T_0 forms body-centered tetragonal (b.c.t.) martensite, which is supersaturated with carbon. To start the transformation from austenite into the non-equilibrium phase martensite, a minimum level of Gibbs free energy $\Delta G_{(T_0-M_S)}$ for nucleation is necessary, which is dependent of the alloying elements. As soon as the temperature reaches T_0 the process of martensite formation starts [142]. A schematic is given in Figure 4.1. Martensite can reach hardness values of more than 900 HV, whereas cementite is limited to 800 HV. The more carbon in an alloy the higher the retained-austenite, which leads to lower hardness levels, but might increase the ductility.

The chemical composition of the MS1 powder, which acts as the metal matrix in this study, is shown in Table 4.1 [24].

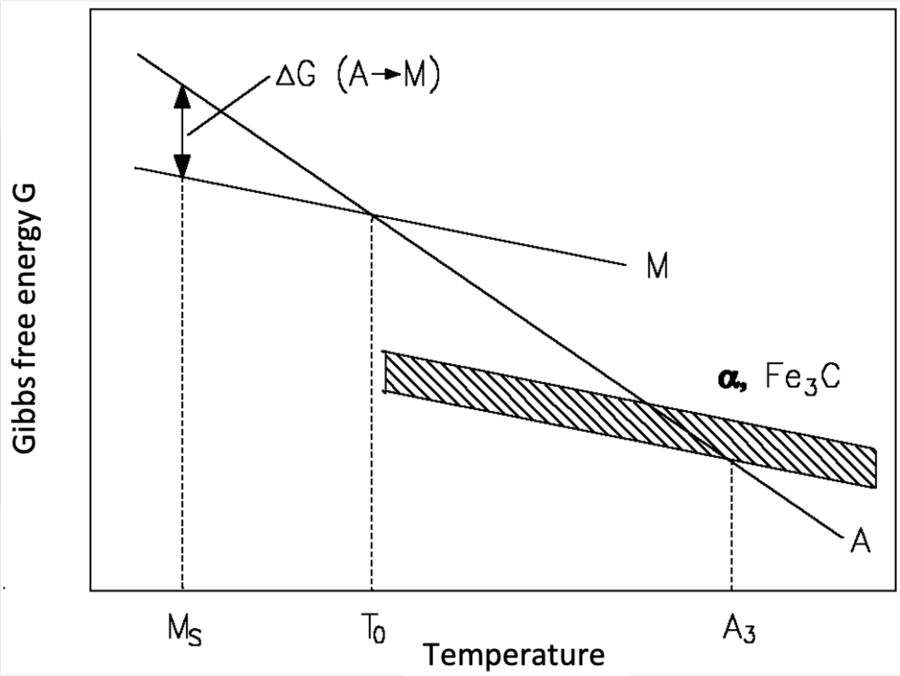

Figure 4.1: Influence of the temperature on the Gibbs free energy G of austenite A, ferrit α, iron carbide Fe_3C and martensite M (based on [24]).

Table 4.1: Chemical composition of MS1 powder [24].

Element	Fe	Ni	Co	Mo	Ti	Al	Cr, Cu	C	Mn, Si	P, S
wt%	Rest	17-19	8.5-9.5	4.5-5.2	0.6-0.8	0.05-0.15	≤ 0.5	≤ 0.03	≤ 0.1	≤ 0.01

Figure 4.3 shows as-purchased gas atomized EOS MS1 powder analyzed with (X-ray diffraction) XRD by Thotakura et. al [26]. The constituent phases were evaluated in a Rigaku 600 Miniflex diffractometer with Cu Kα radiation. The 2θ values were recorded from 40 ° to 100 ° with a stepping of 0.02 °. The Miller indices h, k and l of the $2\theta_{hkl}$ planes were fitted to the corresponding diffraction peaks with a pseudo-Voigt function, which is a typical function to describe diffraction peaks in XRD analysis and is a combination of Gauss and Lorentz functions. Then the phases were identified by comparison of the diffraction angles and intensities of the different diffraction peaks with standard x-ray diffraction patterns from the literature. Their analysis showed that the powder particles consisted mostly out of α-martensite (b.c.c. structure) and some small amounts of retained-γ-austenite (f.c.c. structure). Retained-austenite was found in akin analyses [27, 143] and depends on the carbon content and the speed of solidification. The phase diagram for the Fe-Ni system can be found in Figure 4.2, which not just shows the various phases and intermetallic compounds, but also the change of the Curie temperature. The crystallographic data is given in Table 4.2.

The microstructure of commercially available MS1 has been investigated by Kempen et. al. [27]. In their study they found a cellular and dendritic grain growth in their SLMed specimens. The crystals had homoepitaxial grain growth perpendicular to the laser track build sequence. Figure 4.4b shows their results under the scanning electron microscope. Depending on the temperature and the elements in an alloy, the grains of a martensitic material can change. Lath martensite is formed at very high temperatures (temperatures close to the martensite start temperature) and low amounts of carbon (i.e. 0.4 - 0.5 %). Typically, lath martensite has portions of parallel laths which are < 1 μm wide. Plate martensite is formed at lower temperatures and higher carbon contents

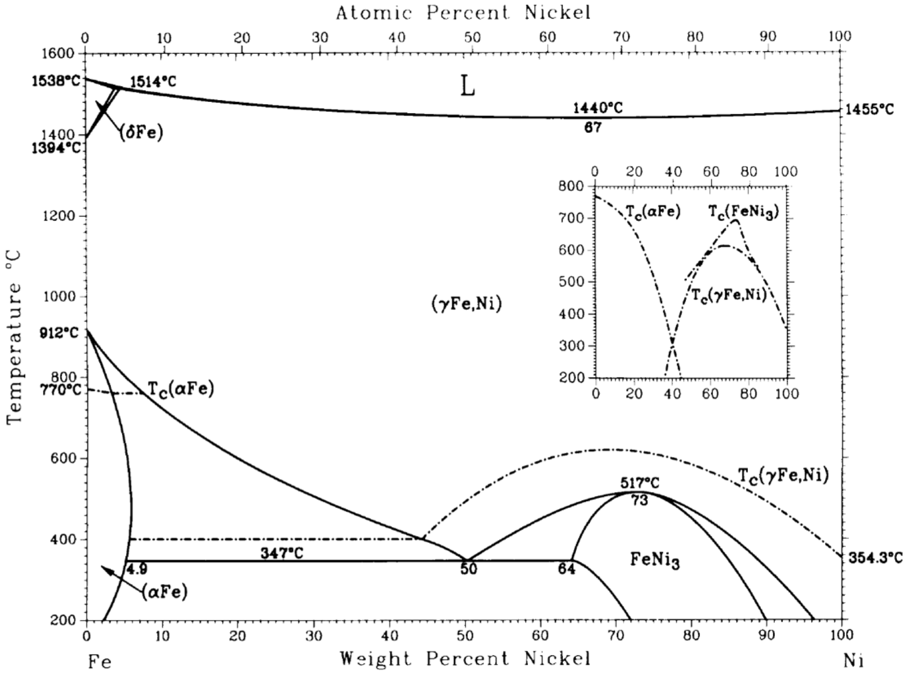

Figure 4.2: Phase diagram of the Fe-Ni system [25].

Table 4.2: Crystallographic data for the Fe-Ni system [25].

Phase	Composition, wt% Ni	Pearson Symbol	Space Group Designation	Prototype
(δ-Fe)	0 to 3.7	$cI2$	$Im\bar{3}m$	W
(γ-Fe, Ni)	0 to 100	$cF4$	$Fm\bar{3}m$	Cu
(α-Fe)	0 to 5.8	$cI2$	$Im\bar{3}m$	W
$FeNi_3$	64 to ~90	$cP4$	$Pm\bar{3}m$	$AuCu_3$

of about 0.8 - 1.0 %. The plates are not formed parallel, but are formed in different angles to each other. Their growth is stopped due to retained-austenite or other plates. This means, that the longer the solidification can last, the shorter these plates are. Plate martensite is not as easily formed and shaped as lath martensite is. In the study of Kempen the intercellular spacing was < 1 μm indicating lath martensite, but due to the very rapid solidification rates during SLM, lath formation can be prevented, respectively the laths can be very short. Figure 4.4a is a maraging steel sample fabricated with a Farsoon SLM printer with 94 J/mm^3 resulting from a layer thickness of 40 μm, a scanning speed of 600 mm/s, a laser power of 180 W and a hatching distance of 80 μm. The density of this specimen was measured at 97.91 %. The cylindrical sample manufactured with the Farsoon SLM printer was cross-sectioned, polished and etched in a solution of 10 ml 65 % HNO_3 and 100 ml 96 % ethanol also known as nital. It can be seen, that the laser remelted every layer about two to three times, which can help to increase the density of a SLMed part and decrease porosity.

4.1.3 Powder Morphology

The scanning electron microscope revealed that there were lots of very small particles distributed in the maraging steel powder used for mechanical alloying and selective laser melting. Also, in

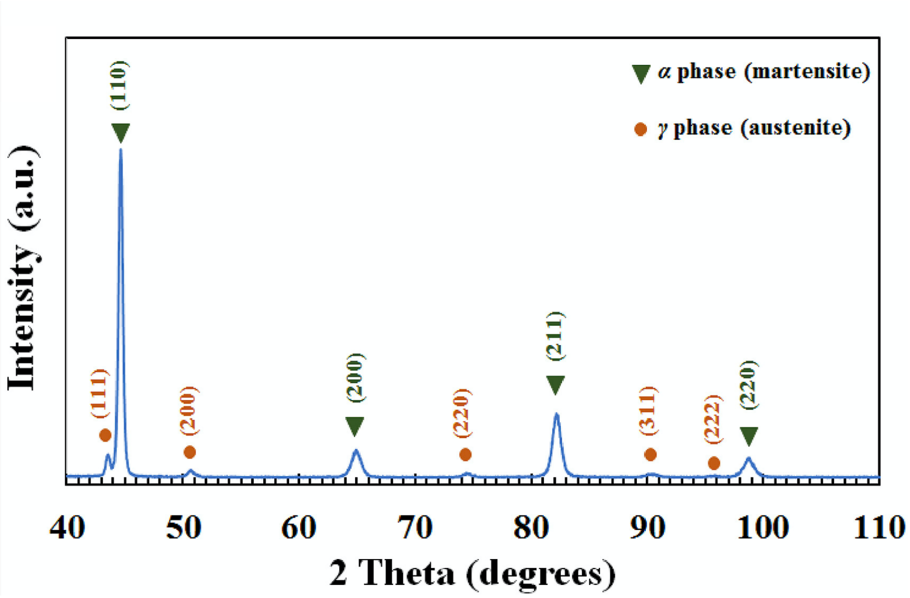

Figure 4.3: XRD analysis of pure MS1 powder. [26]

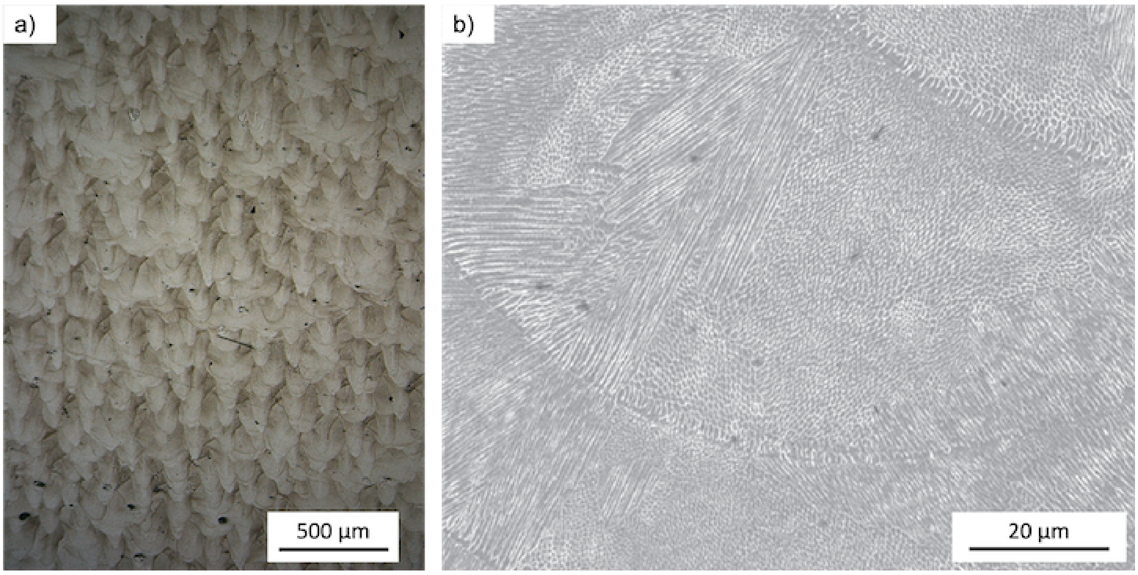

Figure 4.4: Microstructure of maraging steels in a) an optical microscope and b) in a scanning electron microscope showing very short lath martensite [27].

some of the bigger particles were smaller satellites found, which adhered to primary particles in the gas atomization process when particles collided and the temperature was already too low to let the bigger particle absorb the satellite particle [144]. In Figure 4.5 two SEM images of MS powder are given. Figure 4.5a shows some spherical particles, which would be the optimal outcome of gas atomized powder. However, there are some irregular solidified particles attached to the spherical powders, which will affect the flowability of the powder during the coating process in a SLM machine. Another defect that can occur are so called satellites. An example is given in Figure 4.5b. Furthermore, the martensitic grains are visible in the MS particle, but again, some irregular solidified material is sticking to the bigger spherical particle.

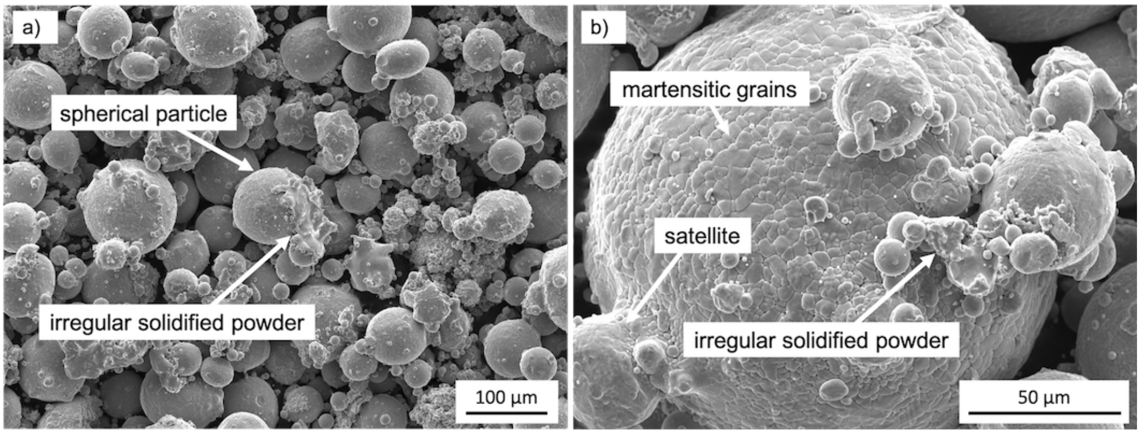

Figure 4.5: SEM images of MS powder a) showing spherical and irregular solidified powder and b) with satellites, irregular shaped solidified MS and the visible grain boundaries of the martensitic phase.

4.1.4 Aging Process

Maraging steels can have outstanding hardness values, but right after selective laser melting their hardness is limited to around 33 - 37 HRC. Nevertheless, these steels are easily thermally ageable and hardness values of up to 50 - 54 HRC are possible, if the as-built parts are heated to 480 - 500 ° C for several hours [28]. During this time a fine dispersion of hard precipitates can form within the softer martensite matrix, which will hinder the material from motions of dislocations. The respective diagram for 18Ni300 can be found in Figure 4.6a which shows the achievable Rockwell hardness. The main types of precipitates in maraging steels are Ni_3Mo, Ni_3Al, Ni_3Ti and Fe_3Mo. Due to the low amount of carbon in the chemical composition, the formation of carbide precipitations is very unlikely. Due to the precipitations and some retained austenite the yield strength and ultimate tensile strength is also very high in maraging steels. Figure 4.6b gives an example of the performance of heat treated 18Ni300 in an ultimate tensile strength test including the reduction of area measurement [28].

4.2 Carbides

Carbides usually are described as a compound of carbon and another element. There are four types of carbides defined according to Tulhoff et. al. [39], which are:

- Saltlike carbides of metallic elements (i.e. CaC_2)
- Metal-like carbides of metallic elements (i.e. WC)
- Diamond-like carbides (i.e. SiC)
- Carbides of non-metallic elements (i.e. CO)

In this thesis the focus is set on metal-like carbides, which are not soluble in water. These carbides have a comparably high electrical and thermal conductivity. Alkaline, acids and organic liquids are not able to attack metal-like carbides.

4.2.1 Tungsten Carbide

In the hexagonal tungsten carbide system, there are the monocarbides α-WC and the subcarbides W_2C known to be of industrial significance [39]. Additionally, a substoichiometric face-centered

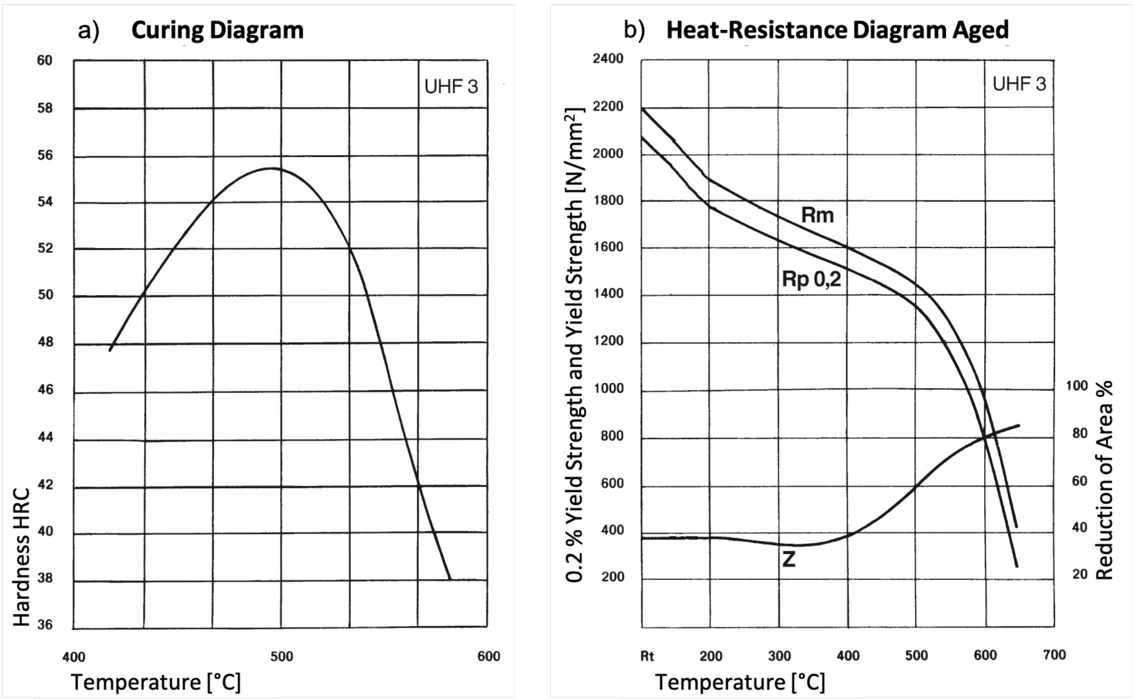

Figure 4.6: Diagrams of 18Ni300 maraging steel showing a) the achievable hardness over the temperature and b) yield strength at various temperatures [28].

Table 4.3: Physical properties of TiC, VC and WC [39].

Properties	**VC**	**WC**	**TiC**
CAS Registry Number	[12070-10-9]	[12070-12-1]	[12070-08-5]
Molecular mass M_r	62.96	195.87	59.91
Carbon content (theory), wt%	19.08	8.13	20.05
Crystal structure	fcc, B1	hex., Bh	fcc, B1
Lattice constants, pm	416.5	*a* 291 / *c* 284	432.8
Density, g/cm^3	5.36	15.7	4.93
Melting point mp,°C	2650	2776	3067
Microhardness, kg/mm^2	2900	1200-2000	$\approx$ 3000
Modulus of elasticity, GPa	422	696	451
Specific heat, J mol^{-1} K^{-1}	32.3	39.8	47.7
Heat of formation ΔH_{289}, kJ/mol	-100.8	-40.5	-183.7
Coefficient of thermal conductivity, Wm^{-1}K^{-1}	38.9	121	21
Coefficient of thermal expansion, 10^{-6}K^{-1}	7.2	*a* 5.2 / *c* 7.3	7.74
Electrical resistivity, $\mu\Omega \cdot cm$	60	22	68
Superconductive transition temp., K	> 1.2	10.0	1.15
Hall constant 10^{-4}cm^{3}A^{-1}s^{-1}	-0.48	-21.8	-15.0
Magnetic suspectibility, 10^{-6} emu/mol	+26.2	+10.0	+6.7

cubic WC_{1-x} (β-WC) exists, but has only be found above 2530 °C and is unstable at room temperature. The properties of WC can be found in Table 4.3. Tungsten carbide is a gray metallic powder and is one of the basic components for very hard metal alloys. Tungsten carbide tends to oxide above 600 °C, which might be a problem, if particles are used for the reinforcement of forging dies. This is one of the reasons, why WC was not used for particle reinforcement in this work, even though the material properties are very good and especially the hardness is a key advantage of WC. In this study tungsten carbide is mentioned for comparison reasons and because the vial and the grinding balls were made out of WC in some of the performed tests. Even though WC offers high performance material properties, some grit was found in the powder samples due to mechanical wear of the equipment.

4.2.2 Vanadium Carbide

Vanadium Carbide is an intermetallic compound and one of the most thermally stable carbides. It has a melting temperature of 2650 ° C and a hardness of around 2800 HV. VC is often used in alloys for grain refinement and therefore, to strengthen the alloy through the Hall-Petch grain boundary strengthening effect. It is furthermore commercially used in workshop tools and cutting tools.

Various forms of vanadium carbide are known. A very common form is the face-centered cubic monocarbide VC, which exists from 43 to 49 mol% C [39]. At very high temperatures VC can transform to the subcarbide V_2C which can exist in a low-temperature α phase and in a high-temperature β phase, but the latter decomposes on melting. In todays industries, especially stoichiometric VC is used, as it has a higher shear modulus, bulk modulus, hardness and Young's modulus than other forms of VC. However, in the study of Wang et. al. [29] it was found that due to the different symmetry of VC ($Fm3m$) and V_8C_7 ($P4_332$) the latter is more stable. The unit cell of VC has a body centered cubic form. As V_4C_3 is missing one C atom, the form changes to a face centered cubic unit cell. V_8C_7 also has a cubic symmetry, but it crystallizes in the space group $P4_332$. The vanadium atoms are occupying positions slightly off the ideal fcc positions and therefore, the carbon atoms have an ordered arrangement on the interstitial sites [29, 145, 146]. A tabular overview is given in Table 4.4 and the phase diagram for vanadium carbide can be found in Figure 4.7d.

Table 4.4: Crystallographic data for the V-C system [30, 40–42].

Phase	Pearson Symbol	Space Group	Strukturbericht Designation	Prototype
V (bcc)	$cI2$	$Im\bar{3}m$	$A2$	W
VC	$cF8$	$Fm\bar{3}m$	$B1$	$NaCl$
V_2C	$hP3$	$P63/mmc$	$L'3$	Fe_2N
V_4C_3	$hR20$	$R\bar{3}m$	...	$HoAl_3$
V_6C_5 (monoclinic)	$hP33$	$C2/m$ or $C2$	...	...
V_6C_5 (trigonal)	$hP33$	$P3_1$	...	...
V_8C_7	$cP60$	$P4_332$ or $P4_332$	...	...
C	$hP4$	$P63/mmc$	$A9$	$C(graphite)$

The physical properties of the vanadium carbide acquired from Treibacher Industrie AG are shown in the Table 4.3 and a SEM picture of the powder with a particle size distribution of approximately sub-micron levels to maximum 2.5 μm (according to Treibacher Industrie AG) can be found in Figure 4.8. In Figure 4.8a there is a VC powder particle, that is clearly bigger than the maximum of 2.5 μm that should be in this powder. Unfortunately, there were more of these particles found and it is not clear, how they found their way into this mixture. As this particle was obviously formed during consolidation, it should be sieved out from the manufacturer. In

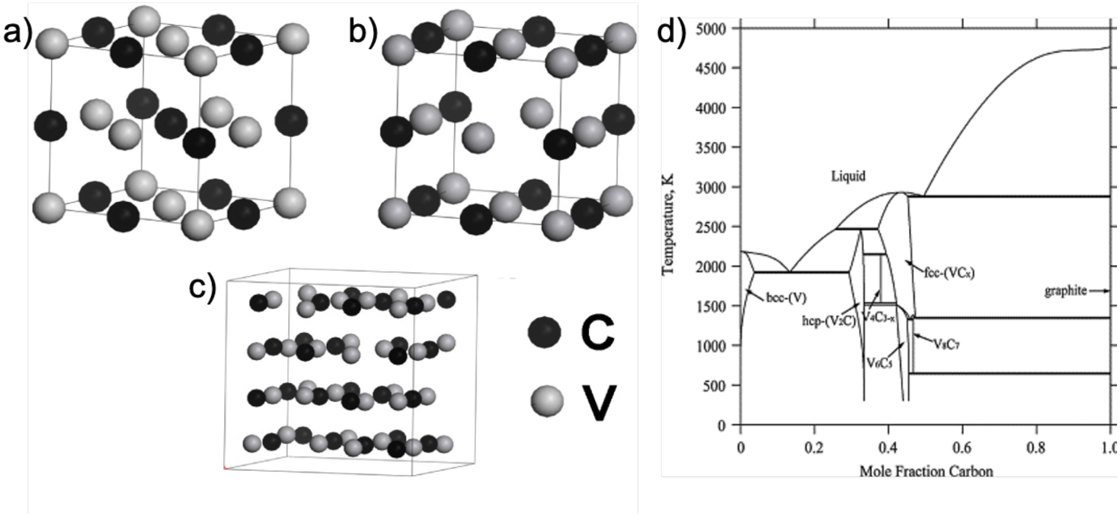

Figure 4.7: Schematic of the crystallographic unit cell structure of a) VC, b) V_4C_3 and c) V_8C_7 [29]; and d) the phase diagram for the V-C system [30].

Figure 4.8b there is also a bigger particle visible, which did not form out of the melt pool, but rather formed due to finer particles forming an agglomeration. Agglomerations in fine particle size distributions are a common effect. Fine particles have much larger surface to volume ratio, which means that the surface free energy versus bulk free energy is much higher than in larger particles. Therefore, these fine particle can stick together, because of simple mechanical connections or Van der Waals forces. These particles can be easily cracked up again, as their bounding forces are relatively low.

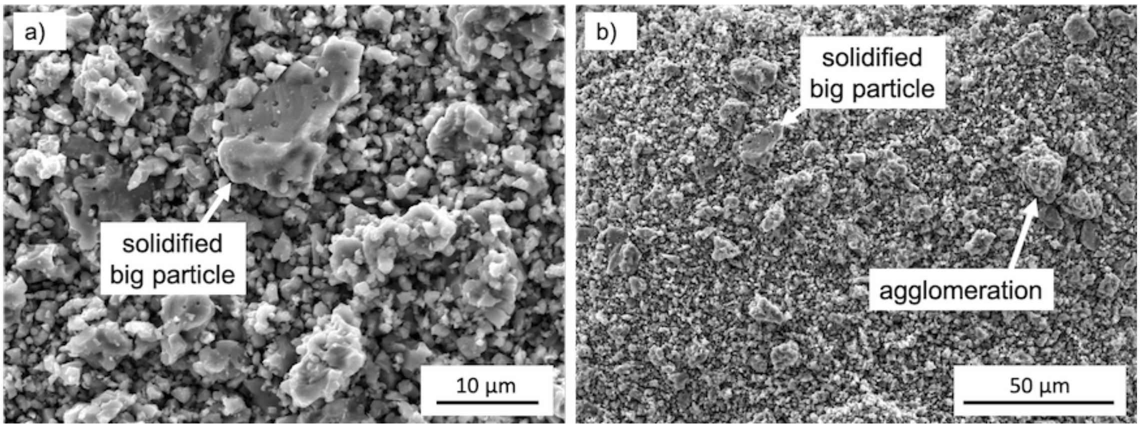

Figure 4.8: SEM images of the Treibacher VC powder with a) a big solidified powder particle and b) an overview and an agglomerated powder particle.

4.2.3 Titanium Carbide

As the name suggests, TiC consists of titanium and carbon. Pure titanium can exist in a hexagonal crystal structured α - phase up to 882 °C and will transform into a body centered cubic crystal β - phase above this temperature. Nevertheless, TiC typically forms a face-centered cubic system and crystallizes in the rock salt (NaCl-type) lattice structure [147]. Like most other carbides, Titanium Carbide (TiC) offers a very high hardness. TiC is often used in very low amounts (i.e. < 0.2 wt%)

in steels for grain refinement and therefore, to increase the steels yield strength values through the Hall-Petch grain boundary effect [62, 118]. TiC only exists as a refractory monocarbide and has a greyish or blackish colour. There are, however, sub-stoichiometric forms of γ-TiC, like $TiC_{0.50}$ to $TiC_{0.97}$, but they are defined through vacancies in the crystal structure. It precipitates faster than other carbides and prevents the formation of austenite. Titanium carbide is often used in CVD and PVD coated tools [148]. In Table 4.3 the physical properties of the Treibacher Industrie AG TiC powder is given. In Figure 4.9a the average TiC particles are visible under the SEM with an SE detector. The particle size distribution was specified as < 2 μm. The image clearly shows the small size distribution at sub-micron level. However, Figure 4.9b shows a big agglomeration. Van der Waals forces and mechanical effects hold this fragile metastable structure together. The involved forces of a high energy ball mill will easily break up these particles.

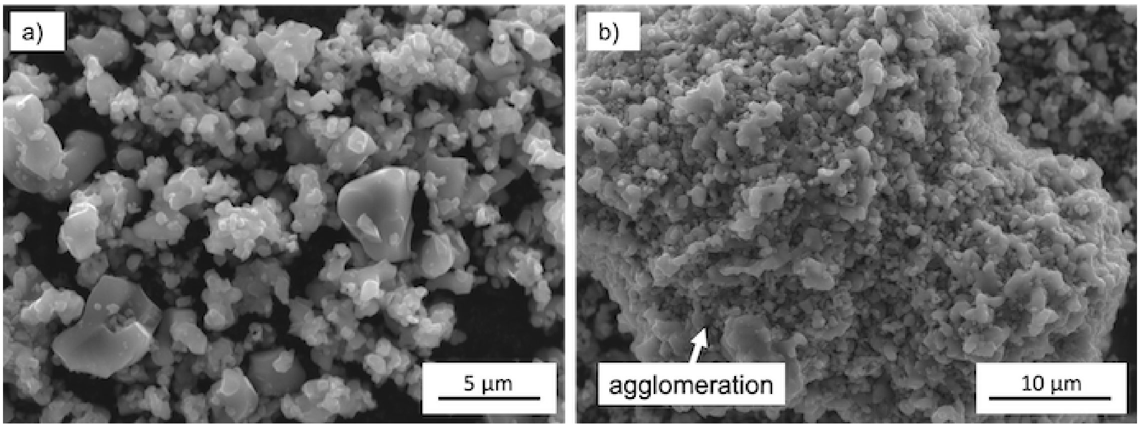

Figure 4.9: SEM images of the Treibacher TiC powder in a) a detailed image and b) an agglomerated powder particle.

The phase diagram of TiC consists of α - Ti, β - Ti, monocarbide TiC, liquid phases and C - phases. It can be found in Figure 4.10b. One peritectoid at 920 °C and two eutectic reactions at 1646 and 2776 °C can be found in the TiC phase diagram. There is a tendency of carbon ordering below stoichiometric concentrations in this intermetallic compound, which is why there is no Ti_2C phase in the phase diagram [31, 149]. The crystal structure data is given in Table 4.5 [43].

Table 4.5: Crystallographic data for the Ti-C system [43].

Phase	**Composition (at. %C)**	**Pearson Symbol**	**Space Group**	**Strukturbericht Designation**	**Prototype**
(α-Ti)	0 - 1.6	$hP2$	$P63/mmc$	$A3$	Mg
(β-Ti)	0 - 0.6	$cI2$	$Im\bar{3}m$	$A2$	W
TiC	$\sim$ 32 - 48.8	$cF8$	$Fm\bar{3}m$	$B1$	$NaCl$
Ti_2C	$\sim$ 32 - 36	$cF48$	$Fd\bar{3}m$	...	...
(C)	100	$hP4$	$P63/mmc$	$A9$	$C(graphite)$

The phase stabilities of sub-stoichiometric TiC_{1-x} were studied by Hugosson et al. [32]. They used a model of a 16 atom TiC supercell and four planes of the crystal to understand the vacancies of the lattice structure. The results of their work are given in Figure 4.11.

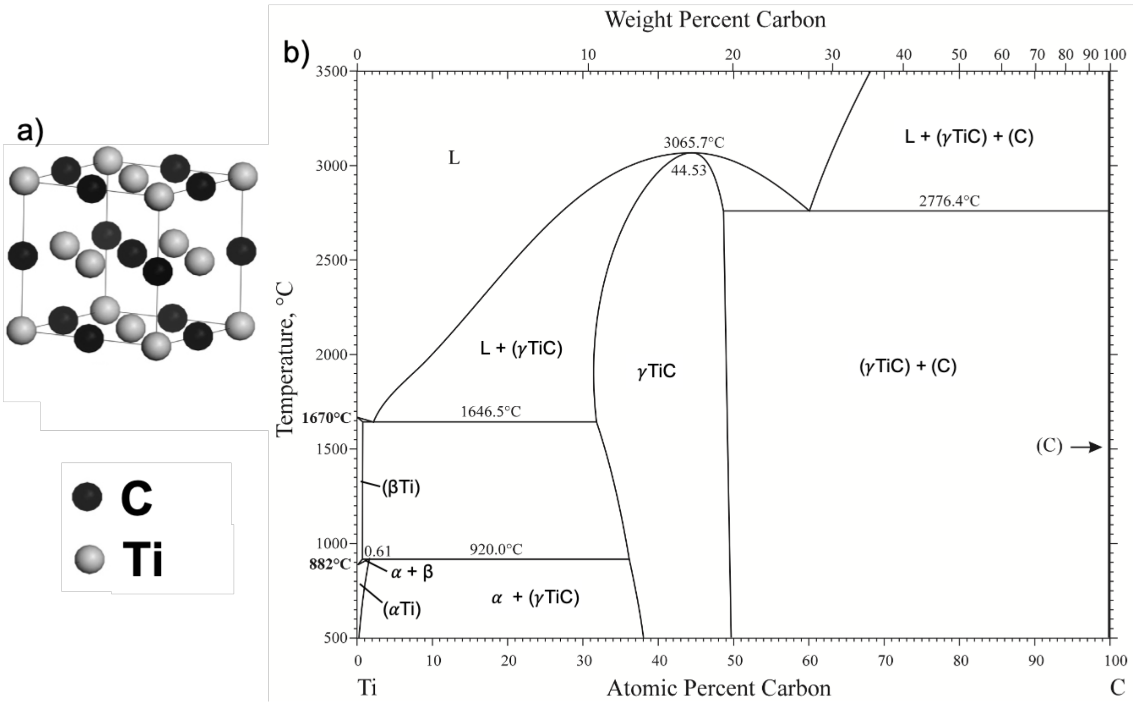

Figure 4.10: Schematic of a) the crystallographic unit cell structure of TiC and b) the phase diagram for the Ti-C system [31].

4.3 Shift of Melting Points

In 1886 German physicist Robert von Helmholtz observed a higher vapour pressure of finely dispersed liquids [150] which lead to predictions in 1906 of German chemist Friedrich Wilhelm Küster, that the melting point of fine powders must be lower that the bulk solid [151]. After years of research, in 1920 two scientists independently developed the Gibbs-Thomson equation. German physical chemist Friedrich Meissner and Austrian physicist Gustav Tammann from the University of Vienna first derived the modern form of the equation [152]. However, it was not called Gibbs-Thomson equation back then, but it was based on their work. In todays common physics usage, it is about the dependence of the vapour pressure across a curved surface. Due to the existence of positive interfacial energies caused by a change in bulk free energy, there is a higher need of energy to form small particles with a high curvature [153]. According to the Gibbs-Thomson effect, these particles will exhibit an increase in vapour pressure [154].

Based on the early model to describe the shift of the melting points of fine particles, three main hypotheses were developed. The hypothesis of homogenous melting describes the melting of the particles from solid to liquid without any kind of pre-melting phase. They are named *Homogeneous Melting (HM)*, *Liquid Skin Melting (LSM)* and *Liquid Nucleation Growth (LNG)*. The schematic process flows of these theories are given in Figure 4.12. In the theory of homogeneous melting, the particle heats up and as soon as the temperature reaches the melting point T_{pm} the particle instantly melts as a whole. According to the liquid skin theory the surface of the particle melts faster than the core of the particle. As soon as the temperature T_1, which lies under T_{pm}, the surface starts to melt and transforms to a liquid state around the inner core. The LSM theory also assumes that, even though the temperature increases, the thickness of the liquid layer does not increase until T_{pm} is reached. The thickness of the melted boundary layer is increasing until the particle melting temperature is reached and the whole particle liquifies. Only then, the particle melts completely and liquifies. The third hypothesis also considers that particles will first melt

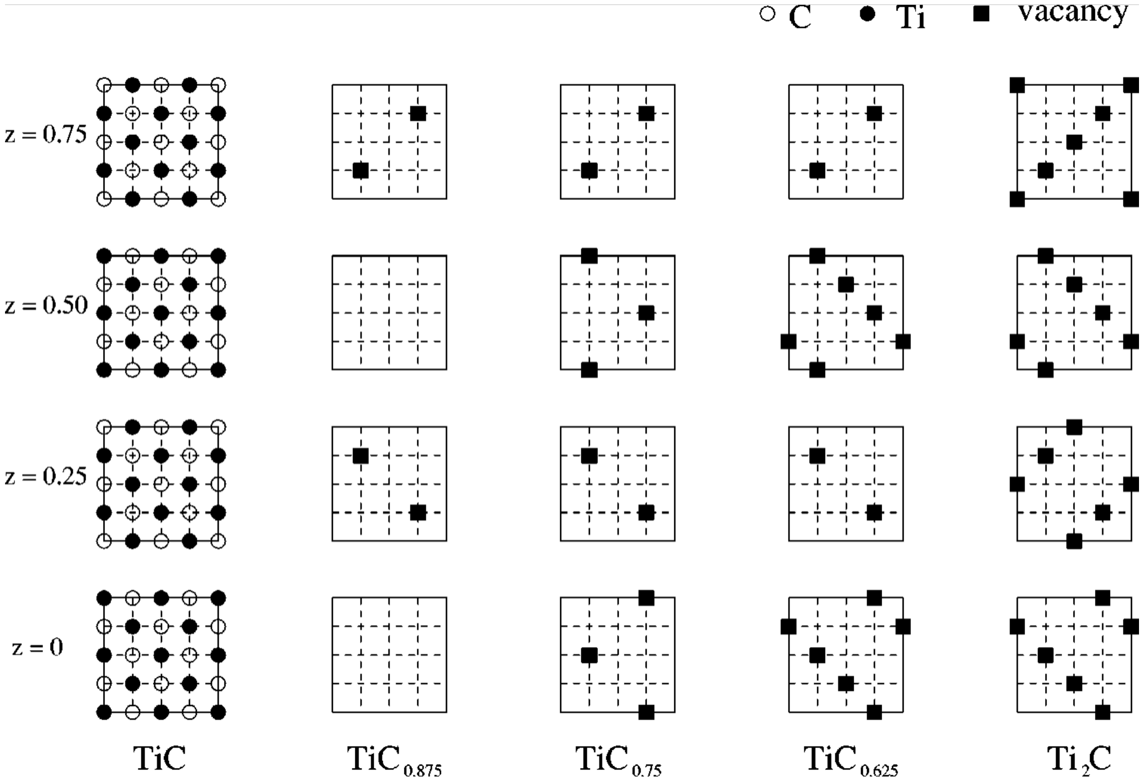

Figure 4.11: Structures of TiC in a stoichiometric and sub-stoichiometric form in a 16 atom supercell in which z represents the different planes [32].

a thin boundary layer after reaching a temperature T_1, which is lower than the melting temperature T_{pm} of the bulk solid. But in contrast to the LSM theory, the liquid nucleation growth theory assumes a continued and consistent growth of the liquid layer until the whole particle is smelted [62, 155].

The particle melting temperature T_{pm} can be calculated with Equation 4.1. The value of T_M is referring to the melting temperature of the bulk solid material. The particle diameter is given in d_p and the values z, β and δ are operating numbers. Furthermore, δ and z are constants in the various smelting hypotheses [155].

$$T_{pm} = T_M * (1 - \frac{z\beta}{d_p - 2\delta}) \tag{4.1}$$

To calculate β the Equation 4.2 is needed.

$$\beta = 2 * \frac{\vartheta}{\Delta H_f}(\gamma_{sv} - \gamma_{lv}) \tag{4.2}$$

For the hypotheses of HM and LSM the value for $z = 3$ in Equation 4.1, whereas in the hypothesis of LNG z is considered as 2 [155]. δ equals to zero in the cases of homogenous melting and liquid nucleation growth, which means, that the calculated shift of the melting point T_{pm} is linearly dependent of the inversive particle diameter d_p^{-1} [62, 155].

To calculate the figure of β the specific volume ϑ, the latent heat of fusion (or melting enthalpy) ΔH_f and the gamma surface energies of solid-vapour (γ_{sv}) and liquid-vapour (γ_{lv}) are needed. The δ value is positive for LSM only and is zero for HM and LNG. To solve the equation for β, in LSM and HM $z = 3$ and for LNG $z = 2$. All of the three theories describe a decrease of

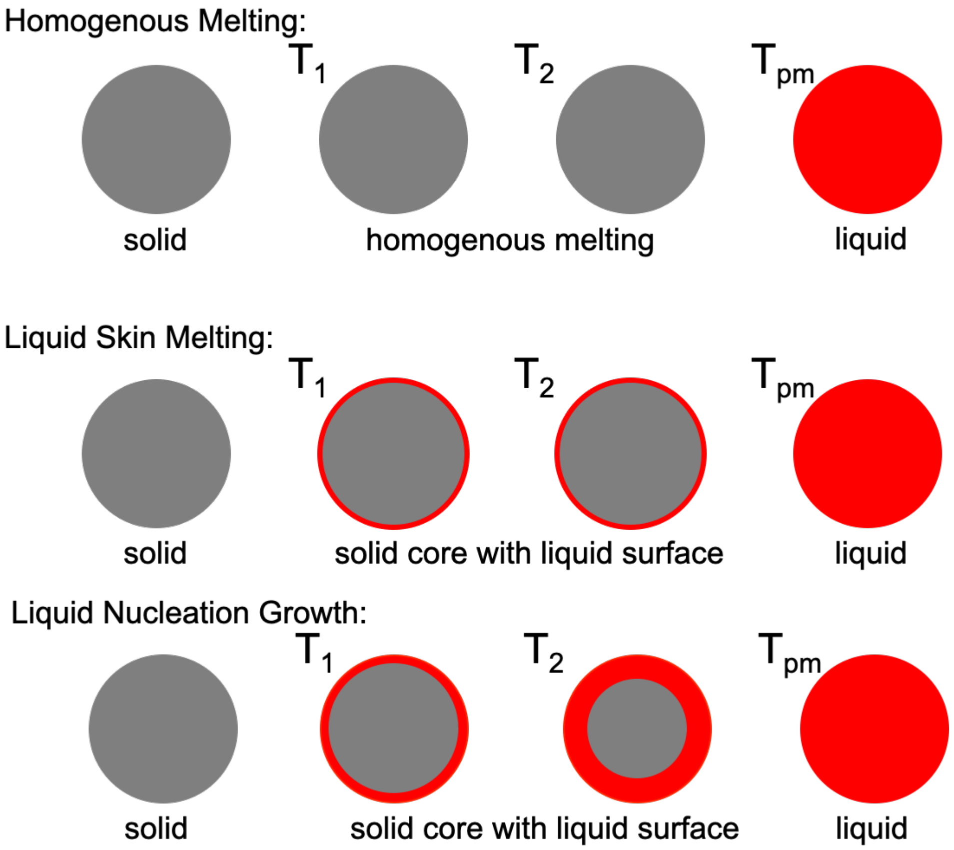

Figure 4.12: Schematic of the different melting hypotheses HM, LSM and LNG.

the melting temperature of small particles in comparison to bulk solid material. The smaller the particles, the lower the melting point. This effect is potentially present for nanoparticles, but also affects sub-micron or even micron sized particles. In Figure 4.13 the different melting hypotheses are shown. The values for the diagram are based on tungsten carbide and shall give a schematic overview of the hypotheses. To get all the needed values, some physical experiments have to be performed. Calverley for example used a tungsten rod in an apparatus to find out the surface tension of bulk and liquid particles with the drop weight theory [156]. Another experimental procedure was performed by Skripov et. al. to verify their theory. They used Sn, Bi, Pb and In in an electron diffractometer to measure the integral intensity of reflection [157]. Other studies have been done for aluminum nanoparticles [158], small tin particles [159,160], gold [161,162] and lead [163]. Furthermore, various studies were done to verify the LSM, HM and LNG hypotheses [164–167].

It was found, that in most scientific papers the shift of the melting point was at about 5 - 15 % lower for small sized particles. As in this study powders with a very fine particle size distribution were used - some of them as low as some tens of nanometers - the respective lower melting point has to be considered. Based on these percental values the an approximation for the materials used in this study are given in Table 4.6. The calculation is based on a decrease of 5 % for particles $>$ 5 μm and a decrease of 12 % below 5 μm, as these values tended to be reasonable and common in LNG, HM and LSM calculations.

Of course, it has to be mentioned that a significant particle size refinement took place during high energy ball milling. As the experiments were based on ductile-brittle materials, the particles mostly formed coalescences and therefore their size is not measurable anymore. An approximation

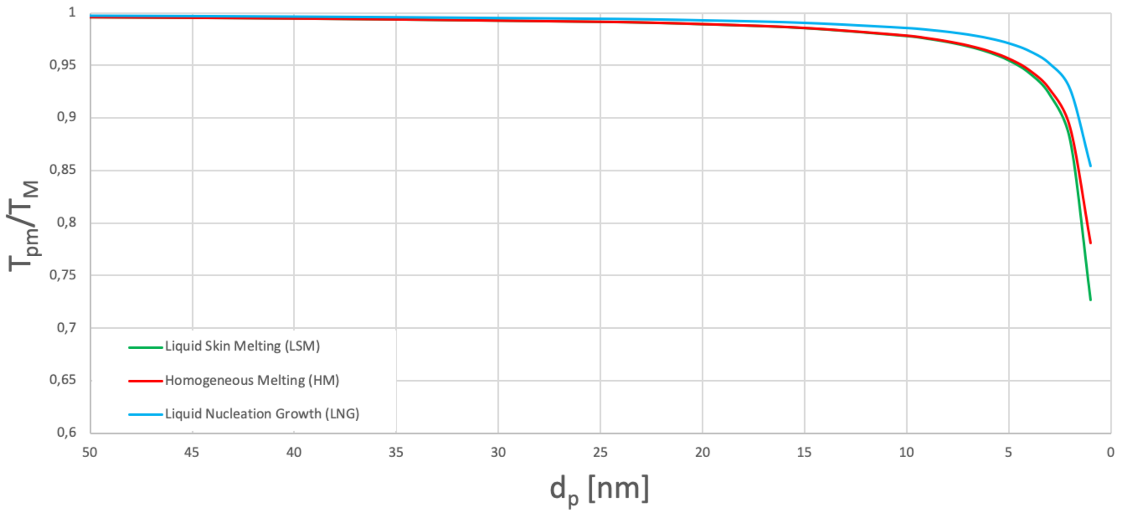

Figure 4.13: Diagram of the different melting hypotheses HM, LSM and LNG for various particle sizes.

is only possible through SEM analysis, which is not as accurate as a Microtrac particle size analyzer. What this means is that after the milling the respective melting points could be even lower and have to be taken into account.

Table 4.6: Calculated melting point temperature for V_8C_7, VC and TiC.

Material	**Particle Size**	**Melting Point Bulk Material**	**Melting Point Calculated**
VC	$100\ nm - 33\ \mu m$	2810 °C [168]	2473 - 2670 °C
VC	$50\ nm - 5\ \mu m$	2810 °C [168]	2473 - 2670 °C
V_8C_7	$100\ nm - 33\ \mu m$	2667 °C [168]	2347 - 2533 °C
V_8C_7	$50\ nm - 5\ \mu m$	2667 °C [168]	2347 - 2533 °C
TiC	$50\ nm - 2\ \mu m$	3160 °C [169]	2781 - 3002 °C

4.4 Theoretical Approach

To calculate and predict phases and solidification models, Thermocalc (Thermo-Calc Software AB, Sweden) was used. It is commonly used to construct and solve statements of equality of chemical elements between phases. Thermocalc relies on databases and thermodynamic data and uses uses mass-balance or direct constraints in compositional variables. This way, equilibrium phases can be predicted and Scheil solidification diagrams can be plotted. Furthermore, the solidification range of an alloy can be calculated and a segregation can be estimated, if applicable. In the Scheil-Gulliver solidification simulation, the following assumptions are made:

- The diffusion of all included elements in the liquid material are infinitely fast.
- The diffusion of all elements is zero in the solidified phase.
- The solid/liquid interface is in a thermodynamic equilibrium.

Thermocalc was used in this thesis work to get an understanding of the expected phase formations. First, the maraging steel composition (MS1) was analyzed and simulated, which is shown in Figure 4.14. It can be seen that there are several phases forming, especially below approximately

600 ° C. The predominant phase was the face-centered cubic Fe system, which consisted of Fe atoms and possible vacancies (Va) in the $L1_2$ crystal structure. The main reinforcing intermetallic phases Ni_3Ti and CoMoFe (μ - phase) were precipitating and forming at around 750 ° C. At about 450 ° C the monocarbide TiC was forming. One inaccuracy has to be mentioned though. In the liquid phase should all other elements be included, as the melt for sure does not just consist of Fe.

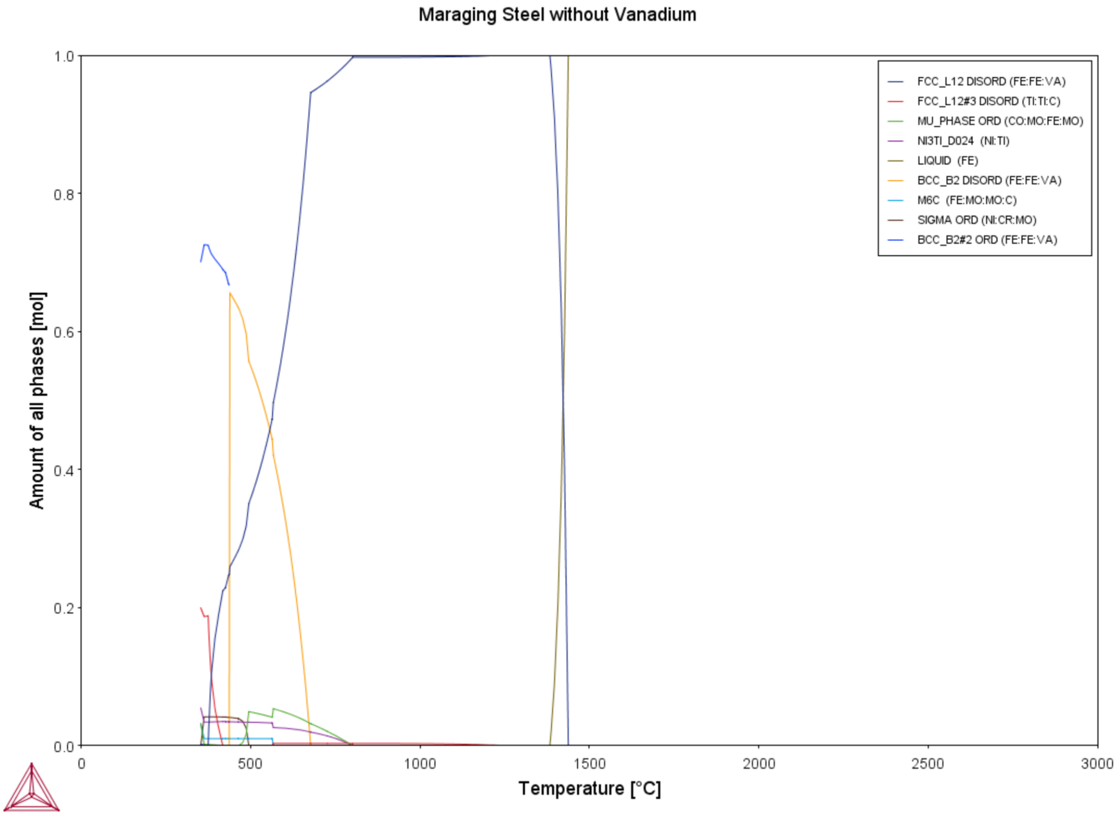

Figure 4.14: Equilibrium diagram of maraging steel MS1.

In Figure 4.15 the Scheil calculation results for the maraging steel system MS1 is given. In the diagram, the solid line represents the Scheil solidification simulation. It provides information at what temperature various phases solidify from the liquid phase. In the diagram of the maraging steel system, the solidification starts at around 1440 ° C with a mixture of a liquid FeNi phase and a face-centered cubic FeNi (Va possible) phase in a $L1_2$ crystal structure type.

It was then desired to understand the effects of the addition of vanadium on the equilibrium and the Scheil calculation. For this purpose, the calculations were repeated with an addition of 10 % V. However, it has to be mentioned that this was just done to understand the FeV system, rather than real phase predictions, as MA and SLM are non-equilibrium processing techniques. In Thermocalc, the calculations assume a perfect liquid phase of all elements and infinitely slow solidification. Obviously, this is not the case in real applications. In selective laser melting, the process is known to have a rapid solidification. Furthermore, the vanadium carbides have a significantly higher melting temperature and depending on their size, not all of them might have been molten completely. In Figure 4.16 the equilibrium diagram of the maraging steel composition MS1 and Vanadium is given. It can be seen that the vanadium significantly increases the martensite starting temperature. Martensite is formed at approximately 450 ° C in a standard maraging steel alloy. Due to the addition of vanadium, martensite is already starting to form at approximately 750 ° C.

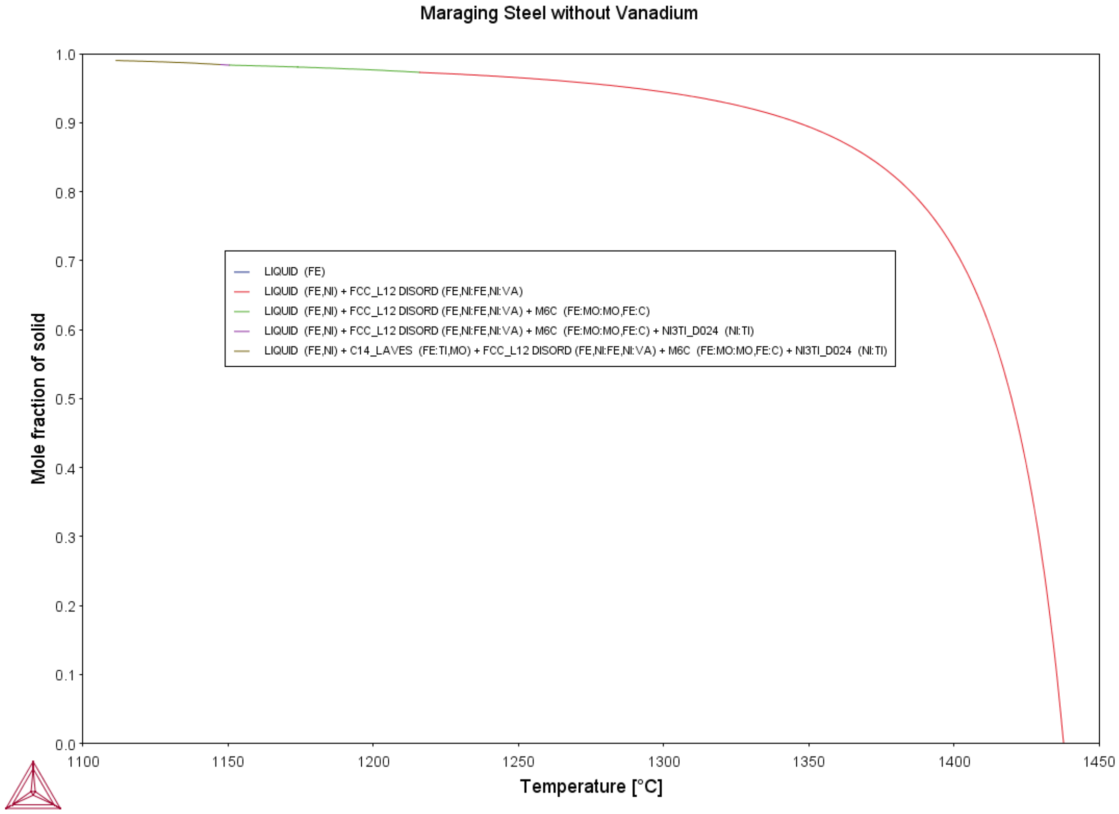

Figure 4.15: Scheil calculation diagram of maraging steel MS1.

Some carbides are formed at above 1200 ° C consisting of Ti, V, and C (TI,V:TI,V:C). Thermocalc describes sublattices in the lattice structure with possible elements that can place atoms in the sublattices' edges.

In the Scheil solidification diagram of the MS1 + V diagram, the austenitic phase is the first phase to form. But at about 1330 ° C, which is significantly sooner than without V, α-Fe is starting to form. Additionally, some V can be found in the lattice structure of the body-centered cubic crystal structure.

In Figure 4.18 the phase diagram of MS1 + V is given. It shows all phases, which would form, between 0 - 70 wt% of V. Obviously, very complex phases can form in this composition. An addition of more than 30 % of vanadium would cause severe phase changes and transitions, hence the vanadium level should be kept lower. It is worth mentioning that the melting point decreases, if vanadium is added to the composition. This fact is important for the experimental considerations and expectations.

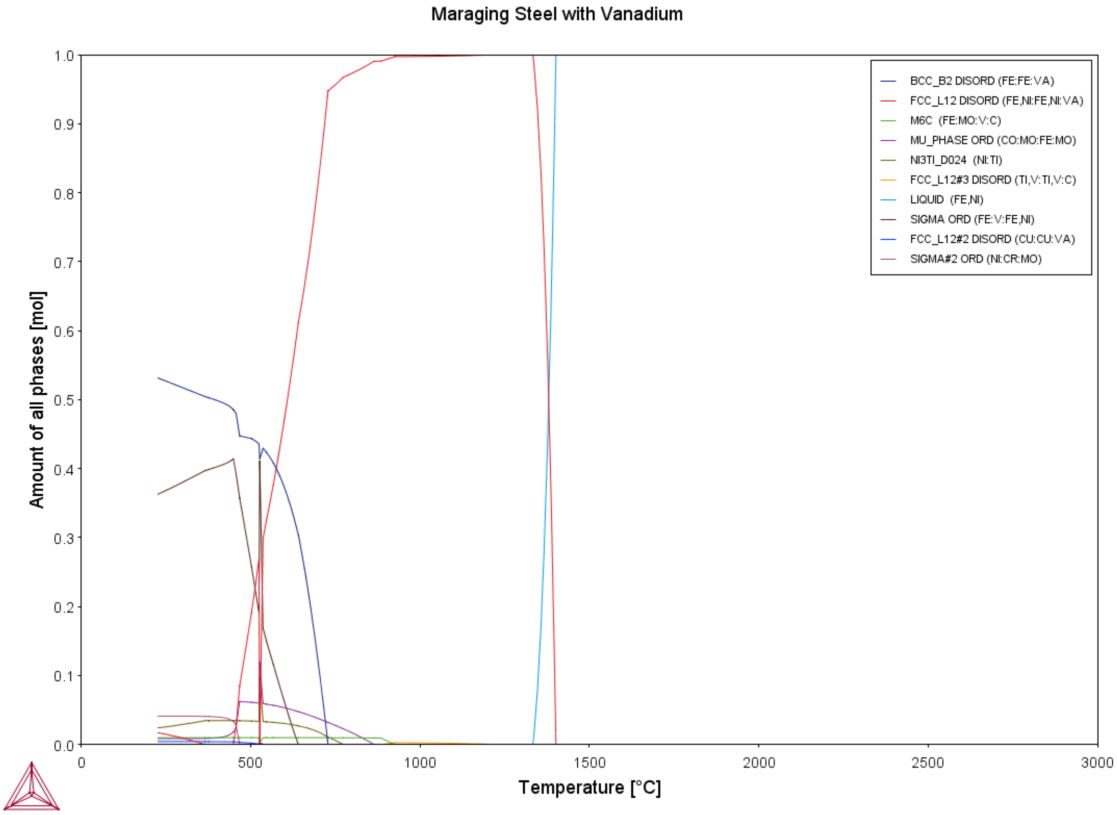

Figure 4.16: Equilibrium diagram of maraging steel MS1 with additional vanadium.

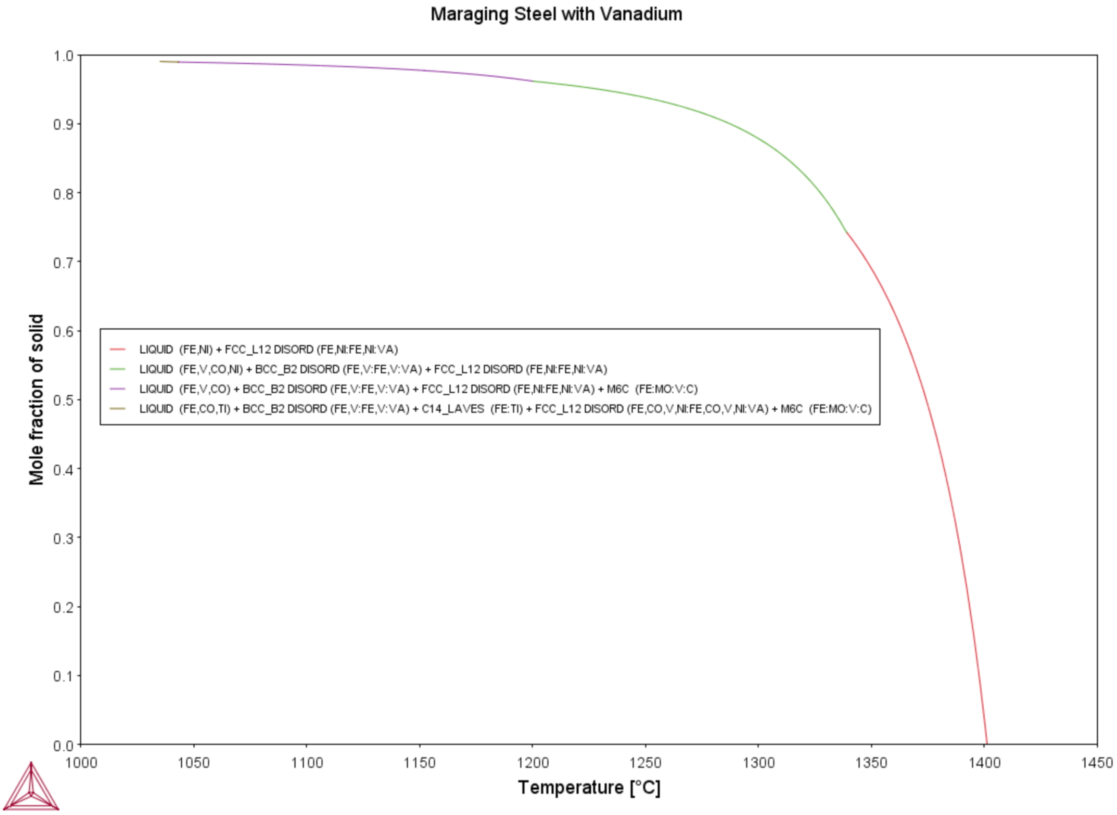

Figure 4.17: Scheil diagram of maraging steel MS1 with additional vanadium.

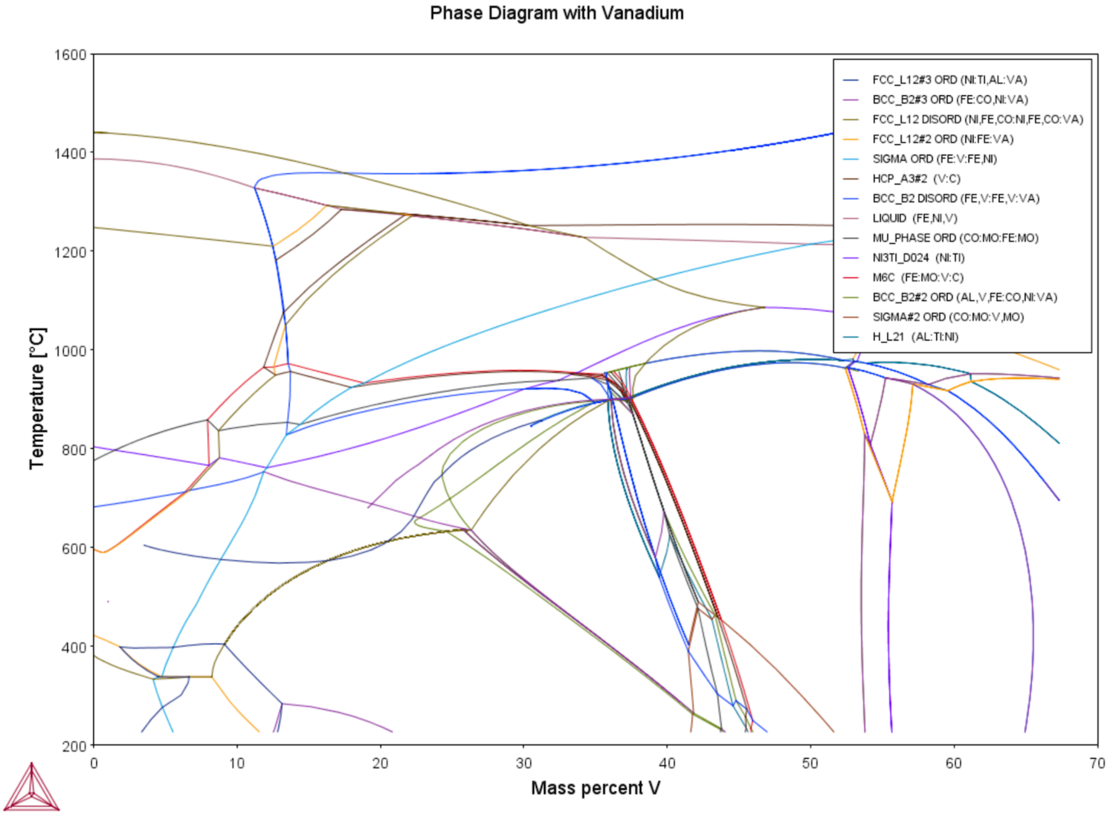

Figure 4.18: Phase diagram of maraging steel MS1 with 0 - 70 wt% of vanadium.

5

Equipment

> The science of today is the technology of tomorrow.
>
> Eduard Teller

5.1 Powder Preparation

5.1.1 Turbula Shaker Mixer

In this work, the focus was set on the fabrication of metal matrix composites. As some of these advanced materials are not or very hard produceable through conventional casting or atomization processes, an alternative way had to be found. In the first phase, regardless of what kind of post-processes are planned, it is advisable to start with a homogenous mixture of the desired alloy. For this purpose, a Turbula shaker mixer (Willy A. Bachofen AG, Switzerland) was used. It is described in detail in Section 2.2.2 and a schematic picture is given in 2.4b. It can hold various sizes of containers and has a fixed amplitude of movement.

Researchers often use mixing technologies to produce ex-situ metal matrix composites with a homogenous particle distribution for various applications [17, 79, 139, 170–174]. In some cases it is sufficient to just mix powders rather than mechanically alloy them. For this purpose, a shaker mixer is a cost effective tool to achieve the desired homogenous mixtures.

5.1.2 Planetary Ball Mill

After mixing powders in a shaker mixer, in this work a Fritsch Pulverisette 4 (Fritsch GmbH, Germany) high energy ball mill was used for mechanical alloying. As mentioned before, if the composite material is small enough (i.e. sub-micron sized), the powder processing step of mechanical alloying can be skipped and mechanical mixing can be sufficient, as small particles tend to stick to the bigger matrix material particles. However, if the composite particles are too big or a refinement during the milling process is desired, a high energy ball mill is the right tool of choice. Furthermore, through mechanical alloying an even better homogeneity can be achieved, as particles tend to form coalescences. In some cases, even an in-situ chemical reaction can be started [134].

The general function of planetary ball mills is described in Chapter 2 and a picture of a Fritsch Pulverisette 4 can be found in Figure 2.4a. The Pulverisette 4 only features place for one vial and can be adjusted in terms of rounds per minute. Furthermore, it is possible to set breaks to allow a cool-off of the jar and the milled powder.

The scientific world has been acknowledging this powder processing technique for many years [23, 75, 105, 109, 133–135, 175–188] as mechanical alloying is a cost effective way to process material far from equilibrium and has a higher potential than rapid solidification has [17, 96, 97].

5.2 SLM Equipment

As described in Chapter 1, for the process of selective laser melting various equipments are necessary. To produce samples out of metal powder, the correct bulk powder has to be used. In the SLM printer, the powder is then melted layer by layer and unused powder can be sieved in a post-process to be recycled and used for the next print job. While handling fine metal powders, it is important to take precautions as some of the metals used are very reactive with oxygen (i.e. titanium).

5.2.1 MCP Realizer SLM 250

The German company MCP-HEK Tooling GmbH developed their first SLM machine back in 2002. The company was one of the pioneers in the SLM technology and mainly focused on the production of custom made tools. The MCP Realizer SLM 250 used in this PhD thesis work has a build chamber of 250 x 250 x 220 mm and is equipped with a single ytterbium 100 W fibre laser. The laser spot diameter is 0.12 mm. It is possible to flood the building chamber constantly with argon to prevent unwanted oxidation during the process. The layer height is adjustable and was set accordingly. The machine is also equipped with a heating system to heat up the building chamber, which can increase densification and reduce stress in the part.

The MCP Realizer 250 SLM, shown in Figure 5.1b, used in this work was modified to be able to work with low amounts of powder. For this purpose a separate cylindrical build platform was built into the original build chamber. Furthermore, a glovebox with special gloves was attached to the building chamber, in case the operator had to work inside the chamber. The advantage of such a system is, that there is no need to open the chamber while it is flooded with argon and to maintain a constantly low level of oxygen. Re-flooding the chamber again is time consuming, which is why especially in research applications, in which often difficulties and complications occur during a process, a glovebox is a great advantage. A schematic overview of the Realizer machine is given in Figure 5.1a, which is basically very similar to other machines.

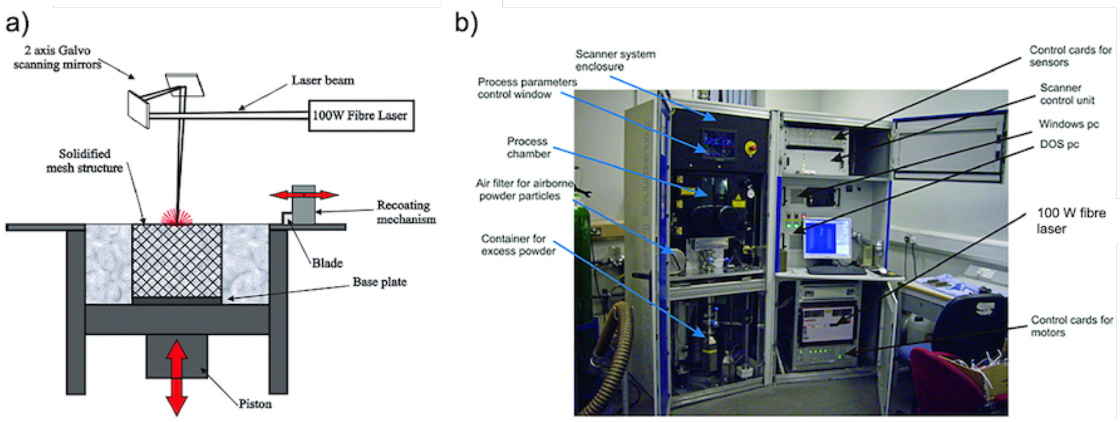

Figure 5.1: a) Schematic of the MCP Realizer SLM process showing the laser path and b) a picture of an MCP Realizer SLM 250 machine. [33]

5.2.2 Farsoon FS121M

Chinese manufacturer Farsoon Technologies is a quite unknown brand in Europe and America, but they are striving to gain a foothold in the western market. One of their smaller machines is the so called FS121M, which was also used in this work and can be seen in Figure 5.2a. It features a single 200 W fibre laser controlled by a high-precision three-axis digital galvo system. The minimum laser spot size is 40 microns and can be set to a maximum of up to 100 microns. The layer height can be set between 20 and 80 μm. The FS121M is meant for small parts in research applications and for scientific powder development works. Because of this, the building chamber is smaller than most other SLM machines and it has a size of 120 x 120 x 100 mm. It has to be mentioned though, that the given height does not include the height of the building platform. This factor is very important and has to be taken into account while planning the print job. Especially while printing the common ASTM E8 ultimate tensile strength specimens in the Z - direction, the height of the building platform is a critical variable. Another important note must be given in terms of the building size. The scanner optic is able to control the laser further than the actual maximum platform size, which means, the laser can damage the machine, if the parts are not placed within certain borders in the controlling software.

The software is, compared to other bigger manufacturers of SLM machines, surprisingly effective, intuitive and powerful. The controlling software runs on a Windows computer and even has a part editor for simple manipulations. The parts can be visualized in three dimensional views and an example is given in Figure 5.2b. During the printing process, parts can be removed from the job, or their parameters can be edited accordingly. The software supports lots of different parameters free to edit, which is a plus.

Overall the machine offers some good features for the comparably low purchase price. However, some design related flaws should be improved in future generations. The container for excess powder for example, is too small for one print job and there is no sensor causing an alarm if the container is full. If the excess powder container is full, the machine will be hard to clean afterwards. Furthermore, the layout of the three chambers, the fresh powder container, the building platform and the excess powder container are designed to be behind one another, which makes working and cleaning of the printer relatively hard. Another negative design decision, is the lack of enough powder and fume suction canals, which causes a lot of dust in the machine and in the end worse part densities.

5.3 Software

5.3.1 Slicing Software

To design simple cubes for first parameter tests, but also for the design of support structure, the designated 3D printing software Magics (Materialise, Belgium) was used. It furthermore allows to place and orientate CAD files in a specific area, which is equal to the maximum available space of the used 3D printing machine. This way, the print job can be perfectly prepared and distances to other parts can be kept in mind. Through the specialized software, the design of very particular support structure can be designed easily. Magics allows to export the STL files into machine readable files like CLI, SLI, SLC files, or Concept Laser specific files like CLS. Additionally, Magics can repair files in terms of walls, which are too thin for the technology used, non-watertight designs, and other common errors. It is, by time of writing this thesis, one of the most common softwares used in the additive manufacturing industry.

5.3.2 Design of Experiments

Performing experiments of all kinds always requires resources. On one hand, experiments should be conducted as accurately as possible, on the other hand, resources have to be kept in mind. With

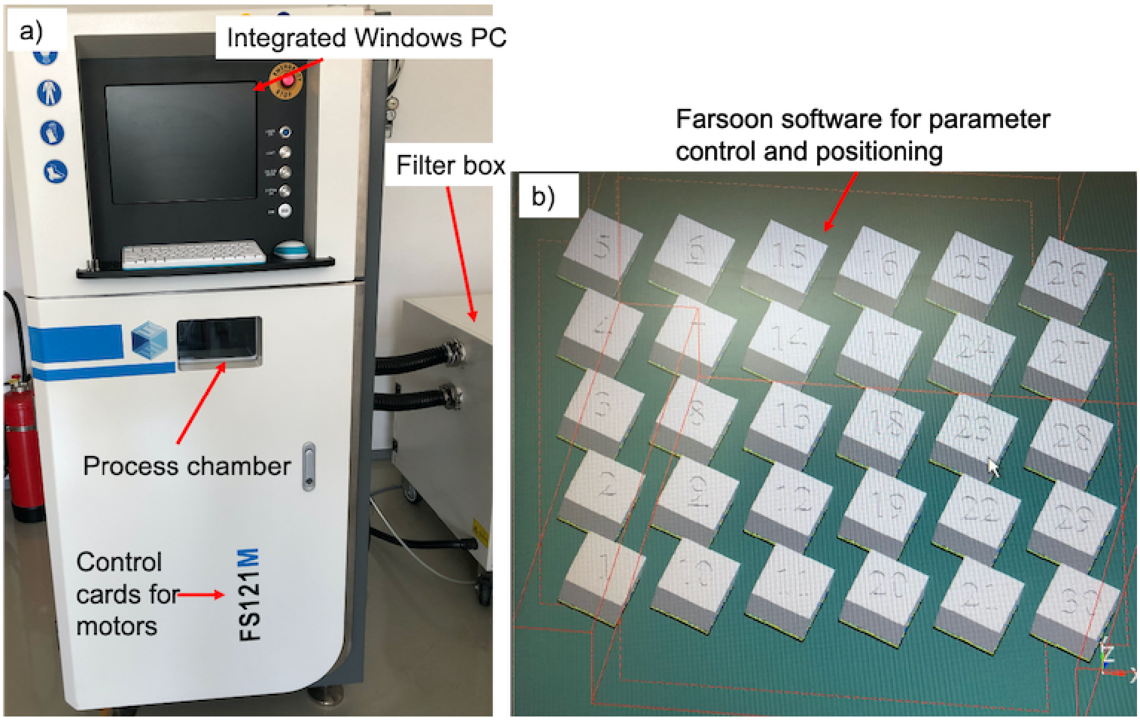

Figure 5.2: Picture of a) the Farsoon FS121M SLM printer and b) the positioning and parameter software.

a well planned Design of Experiments (DoE), the total number of experiments can be decreased. In a DoE, the relationships between influencing factors (= unconditional variables) and target variables (= conditional variables) are investigated and determined as precisely as possible with as few individual experiments as possible.

The Federov method assumes that there is an initial optimal design with n number of runs [189]. One of the rows in the initial design has to be exchanged with one of the rows from the candidate runs. The initial design is called X_{old} and the design after the row exchange is called X_{new}. The determining factor of the new information is:

$$|X'_{new}X_{new}| = |X'_{old}X_{old}| \times (1 + \Delta(x_i, x_j)) \tag{5.1}$$

in which x_i is the row of the current optimal design. The x_i needs to be exchanged with x_j, which is a candidate run from the candidate set. The amount of change in the determining factor of the information matrix is expressed by $\Delta(x_i, x_j)$. It is calculated using the formula:

$$\Delta(x_i, x_j) = d(x_j) - [d(x_i d(x_j) - d(x_i, x_j)^2] - d(x_i) \tag{5.2}$$

where:

- $d(x_i, x_j) = x'_i(X'_{old}X_{old})^{-1}x_j$ is the covariance for x_i and x_j and
- $d(x_i)$ and $d(x_j)$ are the variance of x_i and x_j. They are calculated with the current optimal design X_{old} [189].

The Federov algorithm aims to calculate the Δ-value for all possible exchange pairs from the current design and the candidate runs [189]. Afterwards, the pair with the highest value is chosen and the calculation is continued. Each iteration calculates $n \times N$ delta values, in which n is the number of runs in the current design matrix and N is the number of runs in the candidate run matrix. Again, the highest value is chosen for an exchange. The algorithm is finished, when the change of the determining factor is less than a user defined small value [189].

To perform these calculations, R Studio was used in this thesis work. The laser power, the scanning speed and the hatch distance were set as the variable parameters. The layer height was defined as a fixed parameter. The initial parameter set was developed around the standard EOS parameter set for maraging steel MS1, but adjusted in terms of laser power due to the limitations of the SLM equipment. The parameters were:

- laser power: 190 W,
- scanning speed: 640 mm/s,
- hatch distance: 110 μm.

For the Design of Experiments calculation, five levels and three variables were defined:

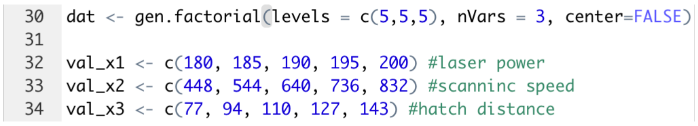

```
dat <- gen.factorial(levels = c(5,5,5), nVars = 3, center=FALSE)

val_x1 <- c(180, 185, 190, 195, 200) #laser power
val_x2 <- c(448, 544, 640, 736, 832) #scanninc speed
val_x3 <- c(77, 94, 110, 127, 143) #hatch distance
```

Then, a new matrix was programmed and the equation for the energy density was defined:

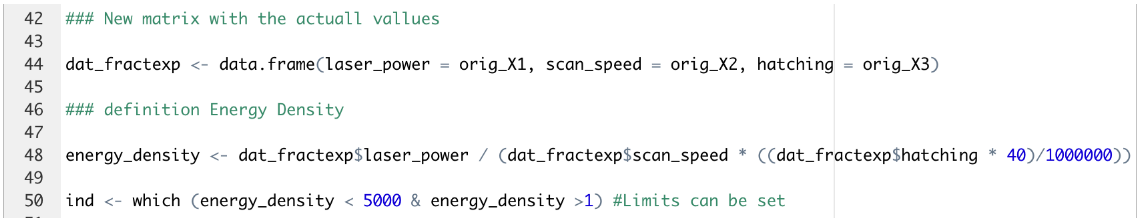

```
### New matrix with the actuall vallues

dat_fractexp <- data.frame(laser_power = orig_X1, scan_speed = orig_X2, hatching = orig_X3)

### definition Energy Density

energy_density <- dat_fractexp$laser_power / (dat_fractexp$scan_speed * ((dat_fractexp$hatching * 40)/1000000))

ind <- which (energy_density < 5000 & energy_density >1) #Limits can be set
```

To use the Federov method, the original parameter had to be identified for R Studio:

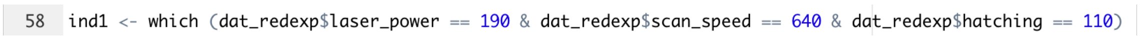

```
ind1 <- which (dat_redexp$laser_power == 190 & dat_redexp$scan_speed == 640 & dat_redexp$hatching == 110)
```

Finally, the Design of Experiments calculations using the Federov operator could be performed. The number of trials was limited to 20, as this was the maximum number of specimens fitting to the process chamber:

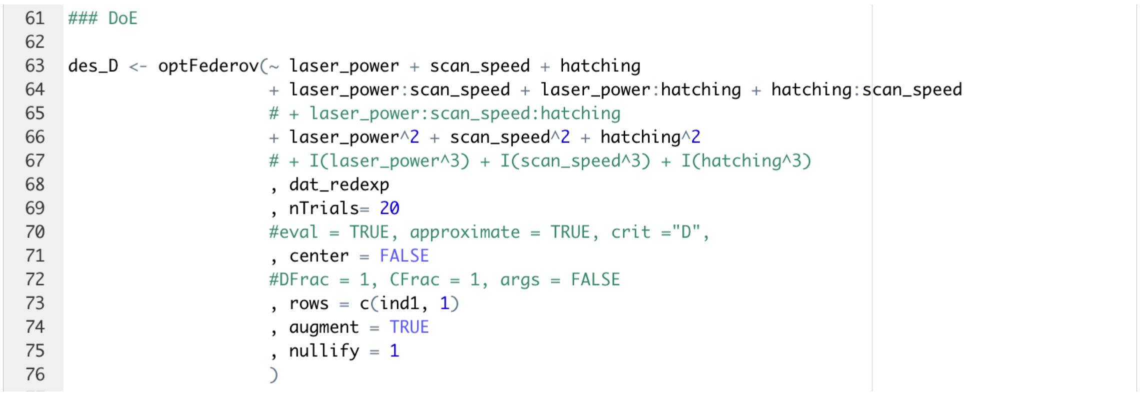

```
### DoE

des_D <- optFederov(~ laser_power + scan_speed + hatching
                    + laser_power:scan_speed + laser_power:hatching + hatching:scan_speed
                    # + laser_power:scan_speed:hatching
                    + laser_power^2 + scan_speed^2 + hatching^2
                    # + I(laser_power^3) + I(scan_speed^3) + I(hatching^3)
                    , dat_redexp
                    , nTrials= 20
                    #eval = TRUE, approximate = TRUE, crit ="D",
                    , center = FALSE
                    #DFrac = 1, CFrac = 1, args = FALSE
                    , rows = c(ind1, 1)
                    , augment = TRUE
                    , nullify = 1
                    )
```

5.4 Heat Treatment

The resulting microstructure and grain growth of the selective laser melting process is transversal isotropic, which leads to lower material strengths and properties in Z - direction. Furthermore, the laser remelts the layers underneath about two times, which increases the probability of grain growth through the layers and therefore might increase the brittleness of the material according to the study of Kruth et al. [47].

One of the most important post-processes after selective laser melting is the heat treatment of the printed parts. As SLM is an anisotropic process, it is often required to perform heat treatments. SLM causes internal stresses in the parts, which will cause deformations, if there is no stress relieving post-process performed, after printing. This process has to be done before the support structures of the building plate are removed obviously. Different heat treatment cycles for different materials exist. For casted maraging steels, a heat treatment is particularly important. After several hours in a furnace, intermetallic precipitations form within the soft martensite matrix material causing increased material properties. Due to the repeated re-melting and the high cooling rates, the annealing cycle is not as important as with monolithic material, but can still improve the material properties of the SLMed part. In this study, some of the samples were heat treated according to EOS recommended annealing cycle. For this purpose, a Linn High Term (Germany) VMK-135 furnace was used. It can reach maximum working temperatures of 1200 ° and has a chamber size of 250 x 180 x 300 mm. The radiation is realized from three sides to ensure consistent temperatures throughout the whole chamber. To prevent direct radiation to the part, the walls are fibre insulated. The furnace is controlled through two independently working temperature controllers to ensure redundancy and they are capable of following preprogrammed heat treatment cycles. Of course the whole process can be done in an inert gas atmosphere to prevent oxidation.

5.5 Analysis

5.5.1 Microscopy

Inspection Microscopy

A microscope is an instrument that can magnify objects, which would be too small to investigate through the eye. Most modern microscopes feature light sources, to get even higher magnification rates. The light microscope used in this thesis work was a Leica Aristomet (Leica Microsystems GmbH, Germany). The microscope is equipped with a trinocular head which allows the user to use a camera while simultaneously using both eyepieces. This system is ideal for frequent snapshots or even video recording. As the name of a light microscope suggests, the Aristomet is also equipped with a 12V/100W halogen illumination source to better analyse specimens. The microscope also allows to adjust the colour of the light source through filters to better understand the topology of the specimen. Sometimes defects and unmolten particle can occur very similar. The usage of filters helps clarifying, if a spotted anomaly is actually a defect or a particle.

The microscope, respectively its camera system, is connected to PC with the Leica Application Suite, which allows not just to take pictures, but also to calculate the part density through image analyzation algorithms.

Stereo Microscopy

Stereo microscopes are a special type of microscopes. The difference to a binocular or trinocular microscope is the way the light travels through the microscope. In standard microscopes, even with setups for both eyepieces, the light is split up to show both eyes an image. In stereo microscopes however, there are two separate optical paths with two objectives. Resulting from this, there is a slightly different viewing angle to the eyes, providing a three-dimensional visualization. This type

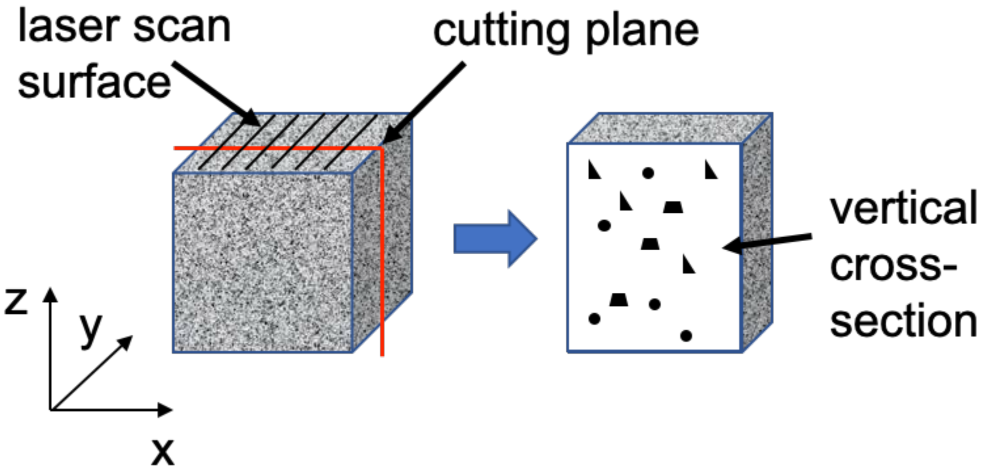

Figure 5.3: Overview of the samples and how they were cut for analysis.

of microscope cannot reach such a high magnification as others can, but it can provide information about the topology of a specimen, even if it is very complex. In this study, an Olympus SZX10 (Olympus Corporation, Japan) with a ColorView imaging sensor was used for specimen analysis. The zoom ratio of the SZX10 is 10, but it offers different magnifications. The microscope works with a fluorescence illuminator for higher brightness and better optical images. Furthermore, the stereo microscope is equipped with a ColorView II camera (Soft Imaging System GmbH, Germany), which was especially designed for material science applications. The camera has a dynamic range of 3 x 12 bit in the colour mode and can vary the exposure time from 100 μs to 160 s. The maximum possible resolution is 2080 x 1544 in colour mode. The camera is connected to a PC running an image processing software to export taken photos.

Sample Preparation

Specimen preparation for further analysis in most cases begins with an embedding process. In the first phase, it has to be decided which direction should be investigated. This is particularly important for SLMed specimens as the process is anisotropic. In most cases the Z- direction is the most interesting, which is why an X - Z or a Y - Z plane is chosen. A schematic is given in Figure 5.3. While cutting the solid specimen for embedding, it is important to not heat up the material, as this might cause an unwanted heat treatment, or could cause an unwanted phase transformation. This was done with a Struers (Struers Inc., USA) Secotom cutting machine, with automatic cooling and cutting programs, eliminating the risk of specimens, that become too hot.

Afterwards, the specimen has a reasonable size and the solid block - or in some cases the powder - is placed in a cylinder, which is then filled carefully with the embedding powder. The machine of choice for this study was the Struers CitoPress-15 equipped with a single cylinder electro-hydraulic mounting press. The process was done with warm-processed mounting powder, which is heated up and melted to secure a solid embedding. After liquefaction, the system is cooled down with water and solidified. After the mounting process, the samples can be grinded and polished.

Again, a Struers device was chosen for this study. To be precise, a Struers Tegramin automatic polishing for reproducibility was selected. It offers an electronically controlled dosing of the polishing and water supplement. However, the fine polishing often has to be done manually and a lot of experience is necessary to achieve the best possible results.

Density Measurement

One of the main goals in the development process of new materials for selective laser melting is to achieve a very high relative part density. Typically, densities above 99 % are recognized as sufficiently high. However, this is not always possible, respectively it is hard to achieve. Two main techniques were used in this PhD thesis work to measure the relative density of solid parts. The first technique, which is probably the most common and most accurate, is the Archimedes' principle. As commonly known, the Archimedes' principle suggests, that there are several forces acting on a solid, if it is immersed in a fluid. The force of gravity acts against the upward buoyancy force F_b. This buoyancy force equals to the weight of the fluid that the solid body displaces. As a measurement device, a hydrostatical scale is used. In the first step, the specimens weight m_a is measured in standard air environment. Afterwards, the specimen is submerged in water, while it must not sink to the bottom, but rather hang on the scale to measure its weight m_w. Furthermore, it is important that there are no air bubbles sticking to the specimens as they would influence the measurement. Especially with SLMed parts and their sometimes rough surface, this can be challenging. The difference of the two measurements equals to the force F_b. The density ρ_w of the water at room temperature is approximately 0.9977 g/cm^3. Equation 5.3 can now be used to calculate the density of the specimen ρ_s.

$$\rho_s = \frac{\rho_s * m_a}{(m_a - m_w)} \tag{5.3}$$

To evaluate the relative density of the specimen and to find out how much porosity and defects it has, the bulk density of the standard solid material has to be known, which can be found in the literature. As the density of the specimen ρ_s and the density of the pure defect-free block material ρ_b are known, Equation 5.4 can be solved.

$$\frac{100 * \rho_s}{\rho_b} = Relative\ density\ [\%] \tag{5.4}$$

The relative density now indicates the defects of the printed part and gives information of the amount of blowholes and pores. As mentioned before, a relative density above 99 % is considered as an excellent value in material development sciences.

The second method to evaluate the relative density of an SLMed part, is through analysation of the microstructure. After cutting, mounting-in, grinding and polishing of a specimen, images with a microscope can be taken. In this study three images per specimen were taken with a Leica Aristomet light microscope (Leica Microsystems GmbH, Germany) and a Leica Application Suite (Leica Microsystems GmbH, Germany) software was used for the image processing and analysis. The software uses algorithms to estimate what colours refer to a pore and what refer to the solid material. This can of course be adjusted. One problem of this technique is the fact, that some particles tend to have a more greyish colour than the rest of the material. This can lead to a lower relative density result as the software misinterprets the image. On the other hand this way of analysis is much faster and can be done while analysing other aspects of the specimen.

5.5.2 Microhardness

The method of microhardness testing is especially meant for small samples or specimens in which only a small region is to be measured for its hardness. The advantage of microhardness testing is the possibility to get information of the material hardness even if the material is prone to cracking or has a fine microstructure. In some cases even multi-phase or non-homogenous materials can be analyzed. This is especially important for particle reinforced metal matrix composites or high entropy alloys with multiple phase formations. For metal hardness tests three main techniques exist, which involve a diamond or a carbide indenter:

- Brinell hardness with a steel or tungsten carbide ball indenter

- Vickers hardness using a diamond indenter formed as a pyramid
- Rockwell hardness either with a steel sphere or a diamond sphere for harder materials

All three of the hardness tests measure the resistance against deformation caused by an indenter, which is loaded with constant force. The applied force is adjustable and therefore known to the operator. After the indenting process, the resulting surface of the indention is measured under the microscope and is used to calculate the respecting hardness according to the used technique.

In this thesis work a Frank (Karl Frank GmbH, Germany) hardness tester was used. The technique used for hardness testing was following *Vickers hardness* standards. The device is equipped with a microscope camera system to measure the diagonals of the rectangular shaped indent. The camera is connected to a computer software program, which allows automatic calculations of the hardness and sample management. The applied force for the Vickers microhardness tests was 9.8 N.

5.5.3 Tribological Analysis

One of the reasons to reinforce materials with carbides and to design metal matrix composites is to increase the mechanical properties of the material. In this study, it was desired to increase the hardness and the wear resistance of maraging steel. To analyze the behaviour of an abrasive movement, tribological tests were performed. For this, a tribometer (Micro Scratch Tester, Anton Paar, Austria) was used. An indenter was applied with 5 N of force and moved back and forth for 1000 times on a track with a length of 5 mm. The indenter was a stainless steel ball with a diameter of 6 mm. After the tests, the track was analyzed to understand the depth and width. These values were used to calculate the coefficient of friction. Through various (i.e. at least five) measurements in a profilometer (Dektak 150, Veeco, USA) a mean value was calculated and multiplied with the track length (i.e. 5 mm), to calculate the volume of the wear track. With the information of the ablated material in the MMC and the volume of the ablated calotte of the ball, the total lost volume could be calculated. In Equation 5.5 the formula for the calotte volume is given, in which V is the volume, h the height of the calotte, and d is the ball wear scar diameter.

$$V = \left(\frac{\pi h}{6}\right)\left(\frac{3d^2}{4} + h^2\right) \tag{5.5}$$

To calculate the height, equation 5.6 is needed, in which r is the radius of the ball.

$$h = r - \sqrt{r^2 - \frac{d^2}{4}} \tag{5.6}$$

The ball wear rate, which is given in mm^3/Nm, is then calculated by dividing the calotte volume with the product of the load (i.e. 5 N) and the sliding distance (i.e. 8 m). The same calculation is performed with the volume of the track wear to calculate the track wear rate, also given in mm^3/Nm.

The higher the wear rate of the track, the more volume was removed and therefore, the weaker the material against the indenter ball was. Thus, the higher the wear rate of the ball, the better the wear resistance of the material against the indenter ball. If the ball wear rate is relatively high and the track wear rate is low, the material has a good resistance against wear and a high hardness. The coefficient of friction provides information about the sliding properties of a material. If the COF is comparably low, it can be assumed that there was some kind of an effect happening which caused the indenter to better glide over the surface. To understand the effects during tribological tests, the penetration depth is an important factor. It provides information about the depth the indenter was able to scratch into the material. The deeper this depth, the weaker the material. It is called relative penetration depth as it measured from the initial surface before the test was started and the maximum depth the indenter was able to reach after scratching the surface for the last time.

5.5.4 X-Ray Diffraction

Ordered structures are usually formed in crystal structures and these symmetric patterns are repeated along all three dimensions. The smallest formation of atoms with such a repeating pattern is called a *unit cell.* A unit cell always reflects the structure and the form of the whole crystal, no matter how large it appears to be. If the lattice points are only at the corners of the unit cell, it is a primitive lattice and there are seven different of them, namely triclinic, monoclinic, orthorhombic, tetragonal, trigonal, hexagonal and cubic. However, to better describe the crystal structure it can be sometimes advisable to use one of the four centering methods for the crystal systems, which are an addition to the seven primitive unit cells. Theoretically, there should exist 28 lattice types, but as some of them are redundant, respectively some of them are not possible due to symmetry reasons, there are only 14. All these unit cells are also known as Bravais lattices. One important property of a unit cell is the possibility of repetitive translation along the principal axes, which also applies for centered cells [190]. The nodes of the Bravais lattices are defined by the the vectors of the translation.

To analyze the lattice parameters of a crystal, the technique of X-ray diffraction (XRD) is used. A sample is placed in an X-ray diffractometer, which uses, as the name suggests, X-rays to illuminate the sample. The emitting X-ray tube and the detector are rotating in a synchronized motion. The signal coming from the sample is then recorded and graphed. Peaks of the graph are related to the atomic structure of the specimen.

The wavelength λ of X-rays is very similar to the distance d between atoms in a crystal. Typically a λ(Cu K_α) X-ray energy is used in instruments with a wavelength of 0.154 nm. As soon as an X-ray encounters an atom, it's energy is absorbed by the electrons of the atom. This energy however, is not sufficient to release the electron, it is emitting the energy again in the form of a new X-ray, which has the same energy as the original X-ray. This process is called elastic scattering. As described before, crystals consist of ordered structures with a certain distance of each atom. When the atomic plains are exposed to an X-ray beam, X-rays are scattered by the equally spaced atoms. At specific angles, strong amplification of the X-rays occur, which is called constructive interference or diffraction effect. Other angles lead to destructive interference causing a destruction of the signal and therefore no signal in the detector. The angle between the incident and the scatter beam at the atom is called 2Θ. As the incoming X-rays will make different paths before they reach the detector, they will also travel further. If this difference in distance is equal to an integer of λ, constructive interference will occur. The relationship between the diffraction angle Θ and the spacing between the atoms d can be determined by applying a sine function.

$$sin\Theta = \frac{\frac{\lambda}{2}}{d} \tag{5.7}$$

Rearranging this equation yields in an equation (5.8 commonly known as *Braggs law*, named after father-son team Sir William Henry Bragg and William Lawrence Bragg.

$$n\lambda = 2 * d * sin\Theta \tag{5.8}$$

In conventional XRD experiments, the given property is the fixed wavelength and the d-spacing of the crystal structure is the unknown, which has to be analyzed in the specimen. The diffraction angle is the resulting property that can be observed with the detector. In Figure 5.4 a schematic of a XRD experiment with a crystal structure is shown. If the X-rays illuminate deeper planes and hits atoms in such a plane, both the distance between the atoms and of course λ multiplies by an integer.

To determine the size of crystals, Scherrer's formula can be used, which is provided in Equation 5.9. The equation is expressed through:

- τ, which stands for the mean size of the ordered domains
- K, the Scherrer form factor with a value of approximately 1
- λ the x-ray wavelength
- $\Delta(2\theta)$ the full width at the half maximum intensity (FWHM)
- θ the Bragg angle.

$$\tau = \frac{K * \lambda}{\Delta(2\theta) * cos(\theta)} \tag{5.9}$$

Bragg's law is often used to describe the diffraction principle and it is expected, that the X-rays are simply reflected to the detector with the same angle and intensity. However, this is physically incorrect. In Figure 5.4 it is assumed that all atoms are positioned above each other, which is not correct in most crystals. Atomic planes are not mirror-like and atoms do not simply reflect X-rays. Nevertheless, Bragg's condition is necessary for constructive diffraction, but it is not a sufficient condition [191]. In fact, atoms react with X-rays through scattering and energy is re-radiated through a wave, which will form a spherical-shaped wave around each atom that is hit by an X-ray. Interferences will occur from all interacting atoms. This explains, why there are constructive and deconstructive interferences which will then cause patterns on the XRD graph.

As mentioned before, there is always an X-ray emitting tube and a detector used, which are moving in synchronized motions, to analyze specimens in an X-ray diffractometer. In this thesis work, a PANalytical PW 3040/6 X'Pert Pro (United Kingdom) device was used. It was operating at 40 kV and 35 mA with Cu Kα radiation ($\lambda = 0.15406$ nm). In all experiments two-theta was recorded in the range of 30° and 90° with a step size of 0.05 and a counting time of 200 seconds per step.

5.5.5 Ultimate Tensile Strength

In the ultimate tensile strength test, the maximum stress a material can withstand, while it is stretched and pulled, shall be investigated. A specimen is applied with constant tension in a tensometer. Depending on the material it will undergo plastic deformation and necking before fracture. Other materials, like very brittle ones, tend to break very sharply. The ultimate tensile strength is measured as force per unit area (i.e. Pascal and Newton per square meter) as it is defined as a stress acting on the sample and is the maximum stress a sample can handle before fracture. The yield strength is corresponding to the point at which a material will overcome the elastic limit and will start plastic deformation. Beneath the yield point, the samples do not show any kind of deformation. Above this point, the specimen will produce permanent deformation and elongation. It is described as Hooke's law which basically says that the extension is proportional to the force. In some materials a phenomenon called Lüder's bands occur, which is an oscillation of strain and stress [192]. This occurs especially in materials with interstitial defects. Interstitial atoms are reinforcing the material as they act against dislocation movements in the matrix. As strain increases, the forces are becoming too high and the atoms are moving until another cluster of interstitial atoms (Cottrell atmosphere) hinder motions. This process repeats until the material has no Cottrell atmospheres left. Afterwards, the stress has to be increased again due to the cold work hardening of the material [193, 194].

The shape of the specimen and the process are standardized to make results comparable internationally and with various materials. Before force is applied, the length and the width of the specimen is measured. After the specimen fractured, these values are measured again. The

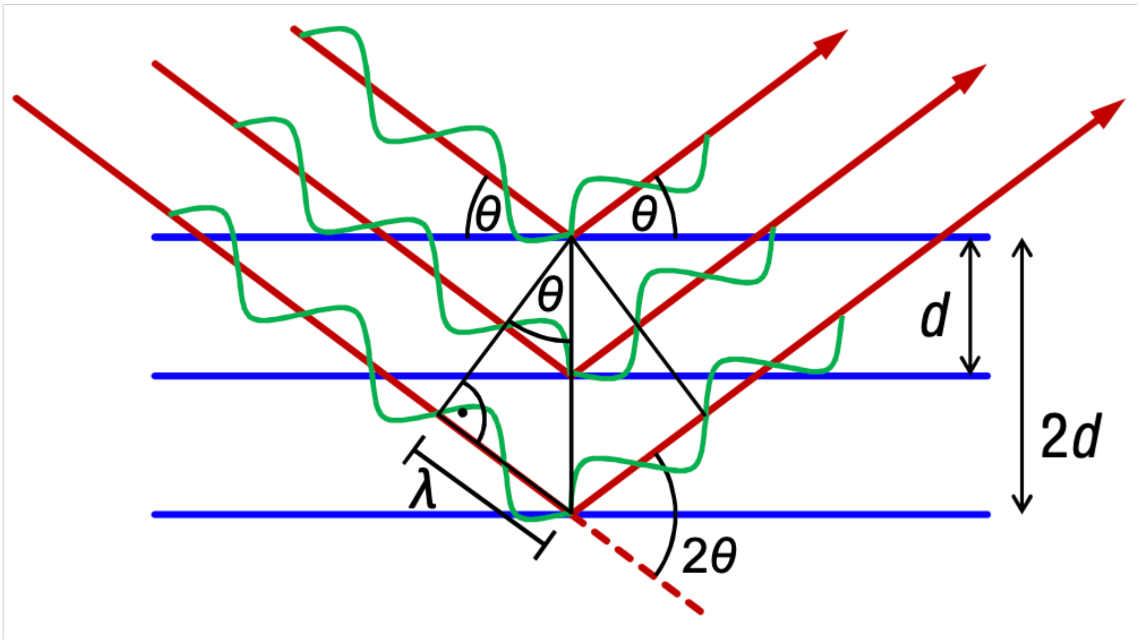

Figure 5.4: The principle of Bragg's law with the X-rays illuminating atoms and the followed elastic scattering [34].

elongation at break is given in percent, as it describes the ratio between the initial length and the length after break. It represents the capability of a material to resist strain without cracking. If the specimen deformed before fracture, it will show some necking. This necking leads to smaller widths which describe the ductility of the specimen. Another important material information, that can be discovered with an ultimate tensile strength test, is the Young's modulus. It describes the stiffness of a material and is the relationship of stress and strain. It is defined in Equation 5.10 in which E is the Young's modulus, σ is the stress given in force per unit surface and strain ε which is the change in length [195].

$$E = \frac{\sigma}{\varepsilon} \tag{5.10}$$

For the scientific world, the internationally acknowledged standard is the ASTM (American Society for Testing and Materials, USA) E 8 norm, which also has a section for powder based fabricated samples.

In this study, a Zwick / Roell Zmart.Pro (ZwickRoell AG, Germany) tensometer was used for ultimate tensile strength tests. The machine was equipped with contacting extensometers to directly measure the length throughout the whole test until fracture. The control of the machine and the data acquisition software (Xpert II Test, ZwickRoell AG, Germany) was running on a connected computer nearby. The software managed and recorded the sensor inputs and calculated the achieved results accordingly after the test.

5.5.6 Hot Ultimate Tensile Strength

Just as described in Section 5.5.5 material properties are best investigated through an ultimate tensile strength test. However, in some cases it is also interesting to understand the material behaviour under higher temperatures. Especially for materials which will be used mostly in environments with high temperatures. For this reason, the hot ultimate tensile strength test was introduced. The procedure for tension tests at elevated temperatures is described in ASTM E21 and E151.

The hot ultimate tensile strength tests for this study have been performed on a Gleeble 3800 (Dynamic Systems Inc., USA). The system had a maximum tension force of 20 tons and was able to heat specimens with 10,000 °C/second at the specimens surface. The maximum theoretical temperature was at 3,000 ° C and it was possible to hold the temperature on the set level within a steady-state equilibrium of +/− 1 ° C. The tests in this thesis work were performed at 450 ° C.

5.5.7 Charpy Impact Toughness

The Charpy impact test, which is also known as the Charpy V-notch test, is a standardized test method to measure the amount of energy that is absorbed by a material during fracture. The test is easy and cheap to conduct with a pendulum that swings and fractures the sample. The shape of the notch and the size of the samples are standardized by ASTM A370 and ISO 148. Even though there are subsize specimens, most commonly the dimensions are 10 mm x 10 mm x 55 mm. Qualitative results can be used to understand the ductility of a material. Flat plane breaks indicate a brittle fracture and a deformed break indicates ductile material properties.

5.5.8 Scanning Electron Microscopy

A scanning electron microscope (SEM) is a very important tool for metallurgical scientists, as it allows to investigate the morphology and the grain formation of samples. First, the samples have to be prepared for the microscope. For SLMed specimens this can be done as described in Section 5.5.1. Depending on the sample and what exactly shall be investigated, it can be advisable to etch the samples after polishing. If powders have to be analyzed, they must adhere to a sticking surface on a special specimen mount. It is very important to understand that the specimens must not have any loose particles as they could damage the detector of the SEM.

In a SEM, a focused electron beam, emitted from a tungsten cathode, is scanning the specimen surface. The electron beam is bundled and accelerated through anode-magnets. Because of the high energy of the beam, some electrons of the specimen will be released. These electrons are called secondary electrons. An electrically positive charged scattered electron (SE) detector absorbs the negatively charged electrons and literally attracts them. If there are lots of secondary electrons detected in a raster element, it will appear as a white point. The less electrons can be detected, the darker the picture will appear. If the electron beam enters the specimens surface perpendicularly, there are less secondary electrons released than in an angle.

Another type of image creation is through a backscattered electron detector. This type of detector focusses on high-energy electrons from the electron beam which are reflected from the specimen. BSE detectors are used to analyze different chemical compositions, whereas SE detectors are used for topographical analyzes.

All specimens have to have an electrical conductivity to be analyzed in a SEM. If they are nonconductive, the electron beam will charge them and cause scanning faults or other artifacts. To increase a specimens electrical conductivity, physical vapour deposition or sputtering is a common process. The specimen will be coated with a very conductive material, for example with gold. Atoms of the gold are battered with ions and will form plasma. This happens in an argon atmosphere, which acts as the sputter gas, and a magnetron vacuum tube utilizes a strong electric and magnetic field to limit the plasma flow. Therefore, the gold plasma will collide with and coat the specimen with a very thin layer.

The samples manufactured with SLM in this thesis work were all cross-sectioned, polished and etched in a solution of 30 ml 32 % HCl, 15 ml 65 % HNO_3 and 30 ml 48 % HF, whereas the pure MS1 specimens were etched in a solution of 10 ml 65 % HNO_3 and 100 ml 96 % ethanol, also known as nital. Some samples for detailed microstructure analysis were etched in Adler's reagent. This etchant was mixed with 9 gr of copper ammonium chloride, 150 ml hydrochloric acid, 45 gr ferric hydrated chloride and 75 ml of distilled water. Afterwards the specimens were observed by a Tescan Vega 3 (Czech Republic) scanning electron microscope. Sputtering for SEM analysis was done with a Dressler Cesar 136 (Advanced Energy Industries, Inc., USA) sputtering system and the chamber was pumped down to $1.7 * 10^{-5}$ mbar.

5.5.9 Electron Dispersive X-Ray Spectroscopy

In a scanning electron microscope primary accelerated electrons batter secondary electrons out of a random atom shell of the specimen. Because of this, the atom has a vacancy of one electron. If an electron of one of the inner shells is missing, an electron out of the next higher shell will fill the hole. During this movement, energy in form of an X-ray will be released. This X-ray can be measured by an energy-dispersive spectrometer (EDX). The atomic structure and the characteristics of the X-ray allow to analyze which element the emitting source was [196].

The SEM used for this work was also equipped with a silicon drift detector (Ultim Max 40, Oxford Instruments, United Kingdom) for energy dispersive X-ray spectroscopy.

5.5.10 Particle Size Analysis

In powder technology processes, it is very important to know the different particle sizes in the used bulk material. A powder will behave different, if the particle sizes differ a lot and if the size distribution is very broad. For example. very fine particles are more likely to form agglomerates. Furthermore, the packing density is influenced by different powder particle sizes and has to be considered when calculating the necessary amount of powder for a volume. A common technology to understand the particle size distribution is laser diffraction.

For the particle size distribution analysis in this work, a Microtrac SDC in combination with a Microtrac S3500 (Retsch GmbH, Germany) was used. The device uses three precisely placed red laser diodes to accurately characterize particles. It can measure from 0.02 to 2800 μm.

6

Investigation of Mechanically Mixed MS1/VC by SLM: Influence of Initial Particle Size

> From error to error one discovers the entire truth.
>
> Sigmund Freud

In this chapter, an introduction about maraging steels and their precipitation hardening is given. As a processing technology for the maraging steel powder, selective laser melting was chosen. The goal of this chapter was, to prove the possibility of producing metal matrix composites based on ex-situ formed MS1 and vanadium carbide. It was decided to use a powder mixture of 90 % (wt%) MS1 and 10 % (wt%) VC. The initial particle size of the MS1 powder was between 15 μm and 40 μm. For the VC powder a particle size distribution of 1-33 μm was chosen in the first attempt to manufacture a metal matrix composite. For comparison reasons, pure MS1 was processed and analyzed first. Afterwards, the MS1/VC mixture was processed in the SLM machine. For SLM processing several energy densities were chosen to find the optimal parameters. For this, a preliminary design of experiments was performed. While analyzing the microstructure and the micro-hardness, it was very obvious that a finer particle size distribution of VC could improve the results, which is why another batch of specimens was printed. Through a refinement of VC particles, the results were significantly improved and the lack of fusion pores were reduced. However, the defects were indeed reduced, but not eliminated, which is why an alternative scanning strategy was tested. After each production of specimens, the results were analyzed accordingly. If was furthermore investigated, that under certain circumstances it is possible to fully melt the VC particles, even though VC has a considerably higher melting temperature than MS1.

6.1 Introduction

Maraging steels are a type of steel which were developed for high-performance applications in demanding industries. Even at temperatures of up to 500 °C maraging steel has a good machinability [197]. They consist of alpha-Fe and Ni with very low amounts of C. Their outstanding material properties, like the high strength and toughness, are derived from strengthening precipitations [198]. The gamma-Fe melt, which also contains the other elements and most importantly Ti and Ni, is cooled down at a moderate rate and relatively soft α-Fe martensite is formed. The martensitic phase almost contains no carbon, but is a supersaturated solution of Ni in α-ferrite [199]. Afterwards, the material is heat treated with an aging process. This causes the formation of Ni_3Ti or Ni_3Mo intermetallic compounds, which are the reason for the superior material properties [27]. Due to the good weldability and a high ductility, maraging steels became available for selective laser melting, an additive manufacturing method. The melt pool formed by the laser in an SLM machine experiences rapid solidification with a very high cool-down (i.e. up to 10^8 K/s) rate [200]. Because of this, the material has some unique metallurgical features and the microstructure differs from monolithic materials. On the other hand, the laser remelts every solidified layer two to three times, causing cracks in some materials. Therefore, it is very important in SLM applications that the processed materials have a high resistance against quenching cracks as SLM involves high heating and cooling rates. Due to the low carbon content of maraging steels, the tendency for quench cracks is significantly lower compared to high carbon steels.

The technology of selective laser melting has proven its capabilities and has been applied in numerous industries and areas [16,47]. A research field which attracts many laboratories, but also commercial companies, is the field of powder production. It is of great interest for the industry due to the high cost of commercial powders and limited variety of materials. Usually powder production for SLM applications is done by plasma, gas or water atomization processes [201–204], in which pre-alloyed wires or solid blocks are melted and atomized through the immediate cool-down by gas or liquids. Typically, the powder used for SLM printers has a particle size distribution of 15 to 63 μm and must have a spherical morphology to increase flowability and packing density [204].

In the studies of Hermann and Kempen [27,205] the microstructure and the mechanical properties of maraging steel grade 300 (18Ni-300) was investigated. They reported a high densification and comparable mechanical properties to its wrought counterpart. Dalmau et al. investigated martensitic stainless steel for its wear, corrosion and tribocorrosion properties [206,207]. It was found that maraging steels have a limited wear resistance, which restricts their use in some environments. Especially forging dies and injection molding dies, which are used in harsh environments, will undergo constant wear. Even though these steels have a different composition and a better corrosion resistance, mostly because of their high Cr content, their other properties are very similar to MS1. One reasonable way to improve the wear behaviour of maraging steels is the addition of reinforcing composite particles. According to the literature, the technology of SLM has reportedly been used to fabricate high performance metal matrix composites. While designing MMCs the goal is to combine the high toughness of the matrix material with the high hardness of the composite material [204]. Furthermore, they can be processed with similar technologies as for monolithic materials [208]. An overview of some scientific papers for ex-situ formed metal matrix composites and alloys are given in Table 6.1, to name just a few.

Table 6.1: Literature overview of ex-situ formed MMCs and alloys fabricated with SLM.

Reference	Matrix Material	Composite Material	Mixing Time	Porosity
Aversa et al. [170]	AlSi10Mg	1 wt% nano TiB_2	48 hours	1 %
Aversa et al. [170]	AlSi10Mg	10 wt% micro TiB_2	48 hours	2.2 %
Tan et al. [171]	Al-2.54Li-1.49Cu-0.91Mg-0.13%Zr	20 wt% sub-micro SiC	5 hours	...
Tan et al. [171]	Al-2.54Li-1.49Cu-0.91Mg-0.13%Zr	10 wt% micro SiC	5 hours	...
Yan et al. [139]	maraging steel 300	15 wt% micro WC	200 minutes	0.83 %
Kang et al. [172]	maraging steel 18Ni-300	15 wt% micro WC	1 hour	0.4 %
Strouf [209]	maraging steel 1.2709	5 wt% micro CuCrZr	1 hour	0.06 %
Strouf [209]	maraging steel 1.2709	10 wt% micro CuCrZr	1 hour	0.06 %
Strouf [209]	maraging steel 1.2709	20 wt% micro CuCrZr	1 hour	0.02 %
Strouf [209]	maraging steel 1.2709	30 wt% micro CuCrZr	1 hour	0.15 %
Iveković et al. [210]	tungsten	1 wt% tantalum	24 hours	5.6 %
Iveković et al. [210]	tungsten	5 wt% tantalum	24 hours	4.9 %
Iveković et al. [210]	tungsten	10 wt% tantalum	24 hours	2.5 %
AlMangour et al. [185]	316L	2.5 wt% micro TiB_2	1 hour	...
AlMangour et al. [185]	316L	15 wt% micro TiB_2	1 hour	8.5 %
Song et al. [211]	Fe	2.2 wt% nano SiC	2 hours	0.13 %

In the literature, mixing in a tumbling mixer, like in a Turbula shaker mixer, is very present. The matrix material and the composite material are mixed homogeneously together and then used in an SLM machine. This powder processing route is called ex-situ MMC formation, as the two components are not alloyed nor do they form coalescences in most cases. However, if properly done, the solidified material will have better mechanical properties than the matrix material without reinforcing particles. This approach was also chosen for this study.

The aim of this study was to investigate the possibility of reinforcing maraging steel with vanadium carbide. Through conventional mixing, powder combinations with two different VC particle sizes were fabricated. Both mixtures had a ratio of 10 wt% of VC and 90 wt% of MS1. The MS1/VC powder was then processed in a SLM machine and analyzed to find the optimal laser parameters and to investigate the density and microhardness. Furthermore, the behaviour of the VC particles were inspected after SLM processing. For comparison reasons, pure MS1 was fabricated too and examined.

6.2 Experimental Procedures

6.2.1 Design of Experiments

To find the best parameters for the SLM process, a design of experiments was performed in R Studio. The main parameters *laser power*, *scan speed* and *hatch distance* were taken into account. Other parameters were set to fixed values. Reasonable limits were set for the energy density η. The DoE consisted of five levels and three variables:

- laser power: val_x1 <- $c(180, 185, 190, 195, 200)$
- scanning speed: val_x2 <- $c(448, 544, 640, 736, 832)$
- hatch distance: val_x3 <- $c(77, 94, 110, 127, 143)$

The values were chosen according to the study of Tan et al. [212], in which the optimum energy density was found at 67 J/mm^3 for EOS MS1 fabricated on an EOS M290 SLM machine. It was expected that the η-values for pure MS1 had to be in the same range of energy density, whereas the η-values for the MS1/VC mixture probably were slightly higher due to the higher melting point of VC (2810 °C). As the Farsoon FS121M, which was used in this work, had a less powerful laser, the values had to be adjusted accordingly. The values were chosen within a range of 70 - 130 % and the maximum number of specimens was set to 20. For the R script calculations, the limits for η were set to 35 J/mm^3 and 180 J/mm^3. In Table 6.2 the output of the R script can be seen. The specimens (spec.) were numbered in ascending order, but also the DoE numbers are given.

Table 6.2 contains values for the hatching distance, which were calculated through the R script. Based on Equation 1.2 the resulting energy density could be calculated based on the laser power, the hatching distance, the scanning speed and the layer thickness. However, the so called *Build Manager* software of the Farsoon printer did only allow values with a step size of five, some parameters had to be adjusted accordingly. This is the reason, why there are further values in the table. The parameters were used for SLM processing the pure MS1 and the MS1/VC mixture.

6.2.2 Powder Preparation

In the first phase a homogeneous mixture of the maraging steel and VC powder had to be achieved. For that, commercially available spherical gas atomized maraging steel powder (MS1, EOS GmbH, Germany) with a size distribution between 15 μm and 40 μm was mixed with irregular shaped VC powder (Treibacher Industrie AG, Austria) with a size distribution of 1 - 33 μm (furthermore called VC-33). Another batch of powder mixture was created with the same MS1 matrix material and VC powder (Treibacher Industrie AG, Austria) with a smaller size distribution of $< 2.5\mu$m (furthermore called VC-2.5), but with the same chemical properties as the VC-33 had. The chemical composition of the VC powder consisted of mostly V_8C_7, with very small amounts of V_2C, V_6C_5 and stoichiometric VC possible. Both powder mixtures with 90 wt% of MS1 and 10 wt% of

Table 6.2: Parameters from the design of experiments R script.

Spec. No.	**DoE Nr.**	**Laser Power [W]**	**Scan Speed [mm/s]**	**Hatching DoE [μm]**	**Hatching Real [μm]**	**Energy Density DoE [J/mm^3]**	**Energy Density Real [J/mm^3]**
1	1	180	448	77	80	130.45	125.56
2	2	185	448	77	80	134.08	129.05
3	5	200	448	77	80	144.95	139.51
4	6	180	544	77	80	107.43	103.41
5	10	200	544	77	80	119.37	114.89
6	20	200	736	77	80	88.23	84.92
7	21	180	832	77	80	70.25	67.61
8	22	185	832	77	80	72.20	69.49
9	25	200	832	77	80	78.05	75.13
10	63	190	640	110	110	67.48	67.48
11	76	180	448	127	130	79.10	77.27
12	80	200	448	127	130	87.88	85.86
13	96	180	832	127	130	42.59	41.61
14	100	200	832	127	130	47.32	46.23
15	101	180	448	143	140	70.25	71.75
16	105	200	448	143	140	78.05	79.72
17	106	180	544	143	140	57.85	59.09
18	110	200	544	143	140	64.28	65.66
19	121	180	832	143	140	37.83	38.64
20	125	200	832	143	140	42.03	42.93

VC were mechanically mixed in a Turbula tumbler (Willy A. Bachofen AG, Switzerland) shaker mixer - each batch for 15 min. In preliminary studies it was exhibited that demixing of powders can occur, if the mixing times are too long. The morphologies of this mixture and the VC-33 bulk material are shown in Figure 6.1. The picture shows some sub-micron particles, which are sticking to the bigger MS1 particle, whereas >1 μm are laying next to each other. The chemical composition of the MS1 powder, which acts as the metal matrix in this study, is shown in Table 4.1 and is described in detail in Section 4.1.2. The bulk material of the VC-2.5 is shown in Figure 4.8a. In this figure, one can see that even though - according to the manufacturers specification - there should be no particle bigger than 2.5 microns, some particle, as a matter of fact, are. Nevertheless, the tests were still continued, but this anomaly has to be considered in the analysis. Overall, the VC-2.5 powder had a significantly lower mean particle size and maximum particle diameter.
The pure MS1 powder was used as delivered without any pre-processing or treatment.

6.2.3 SLM Process

For SLM processing, a Farsoon FS121M (Farsoon Technologies, China) was used to create cubic specimens (10 mm x 10 mm x 10 mm). The device was equipped with a 200 W fibre laser which featured a laser spot diameter of 55 μm. The layer height was set to 40 microns. Before the actual SLM process was started, the building chamber (120 mm x 120 mm x 100 mm) was flooded with argon to keep the oxygen level below 0.4 %. This way possible oxidation and a stable welding process could be provided. The coating of the building platform was increased in the beginning of the process to achieve even coated layers. After approximately 10 layers, the standard coating parameter was chosen. The scanning strategy for the solid parts included an alternating hatch pattern. The pattern was rotated 90 ° every other layer.

6.2.4 Microstructural Observation and Density

The cubic formed specimens were cut-off the build plate and then their weight was measured. Archimedes' principle was used to measure the density of the samples using a dedicated scale. Afterwards the cubic specimens were mounted in resin (Struers CitoPress-15, Struers Inc., USA), cross-sectioned and polished (Struers Tegramin, Struers Inc., USA). To get as much information

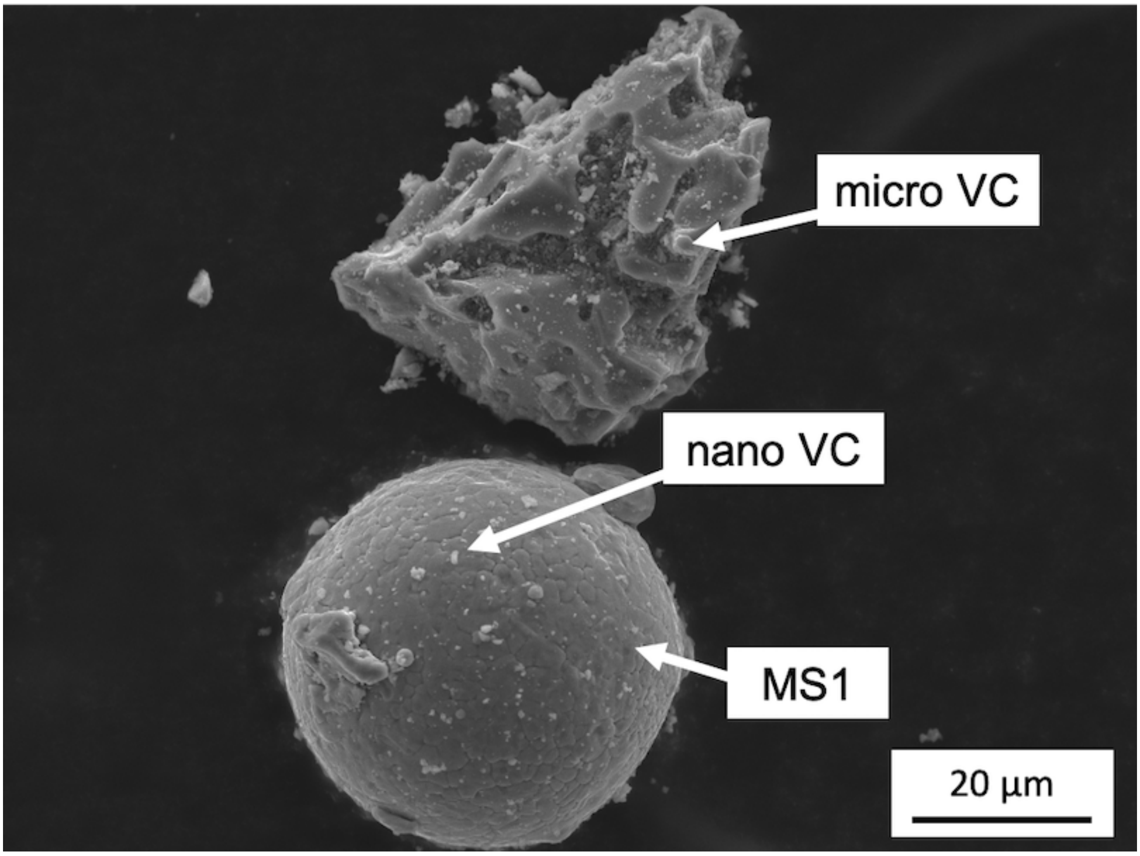

Figure 6.1: SEM image of the initial mixed spherical MS1 and the irregular shaped VC-33 bulk powder.

about each layer of the samples, the X-Z plane was cut for further analysis. The next step was the etching of the samples. For the MS1/VC specimens a solution of 30 ml 32 % HCl, 15 ml 65 % HNO_3 and 30 ml 48 % HF was used and for the pure MS1 specimens nital (10 ml 65 % HNO_3 and 100 ml 96 % ethanol) was used. After the etching, the laser tracks were visible and could be observed under the microscope. For the microstructural analysis an optical microscope (Leica Aristomet, Leica Microsystems, Germany) and appropriate software (Leica Application Suite, Leica Microsystems, Germany) was used.

6.2.5 Microhardness

A micro-hardness testing device (Karl Frank GmbH, Germany) was used to observe the Vickers hardness of the samples. For all specimens the device was loaded with 9.8 N (HV1). At least three measurements were done at each specimen.

6.3 Results and Discussion

6.3.1 Microstructural Characterization and Density of MS1

Before the actual MMCs were tested, some pure MS1 was processed in the Farsoon SLM machine. Unfortunately, some of the parameters caused troubles during SLM processing. The maraging steel samples had a tendency to break-off of the build platform and some emergency stops were necessary to prevent damage to the carbon fibre coater. If possible, the deformed samples were just deleted in the software and the build job was continued. However, some of the samples were a severe danger to the coater and therefore, the samples had to be removed manually. In Table 6.3 the built specimens and their related SLM parameters with the resulting energy densities (Energy D.) are given. Furthermore, the measured and mean relative densities (Rel. D.) are added to the table. Because of the 55 μm spot diameter, there was no direct overlap of each scan track. However, the laser spot diameter does not equal to the melt pool diameter. The melt pool will always be bigger than the laser spot which means that it is not necessary to overlap the tracks. It is important though, to get an overlap of the melt pools of each track to achieve a high relative density in the manufactured part.

Table 6.3: Overview of the SLM parameters and the density measurements of MS1.

Spec. No.	**Laser Power [W]**	**Scan Speed [mm/s]**	**Hatching Real [μm]**	**Energy D. Real [J/mm^3]**	**Rel D. 1 [%]**	**Rel. D. 2 [%]**	**Rel. D. 3 [%]**	**Rel. D. Mean [%]**
1	180	448	80	125.56	90.03	86.86	86.07	87.65
2	185	448	80	129.05	94.43	93.57	94.33	94.11
3	200	448	80	139.51	96.59	97.20	96.68	96.82
4	180	544	80	103.40	97.84	97.65	98.23	97.91
5	200	544	80	114.89	98.10	97.95	97.92	97.99
6	200	736	80	84.92	88.12	90.25	89.42	89.26
7	180	832	80	67.61	91.65	91.30	90.48	91.14
8	185	832	80	69.49	98.08	98.24	98.26	98.19
9	200	832	80	75.12	97.8	97.61	97.55	97.65
10	190	640	110	67.47	95.33	95.27	94.40	95.00

Table 6.3 indicates that the highest density was achieved at 69.49 J/mm^3 for pure maraging steel powder. The relative density and the microstructure strongly depends on the laser parameters and the goal in SLM manufacturing is always to produce near fully dense parts. To compare and to better understand the effects of the various parameters, the energy densities and the related relative densities were plotted in Figure 6.2. Representative micrographs were chosen, to show the densification characteristics. Sample nr. 1 stands out though, due to the high standard deviation,

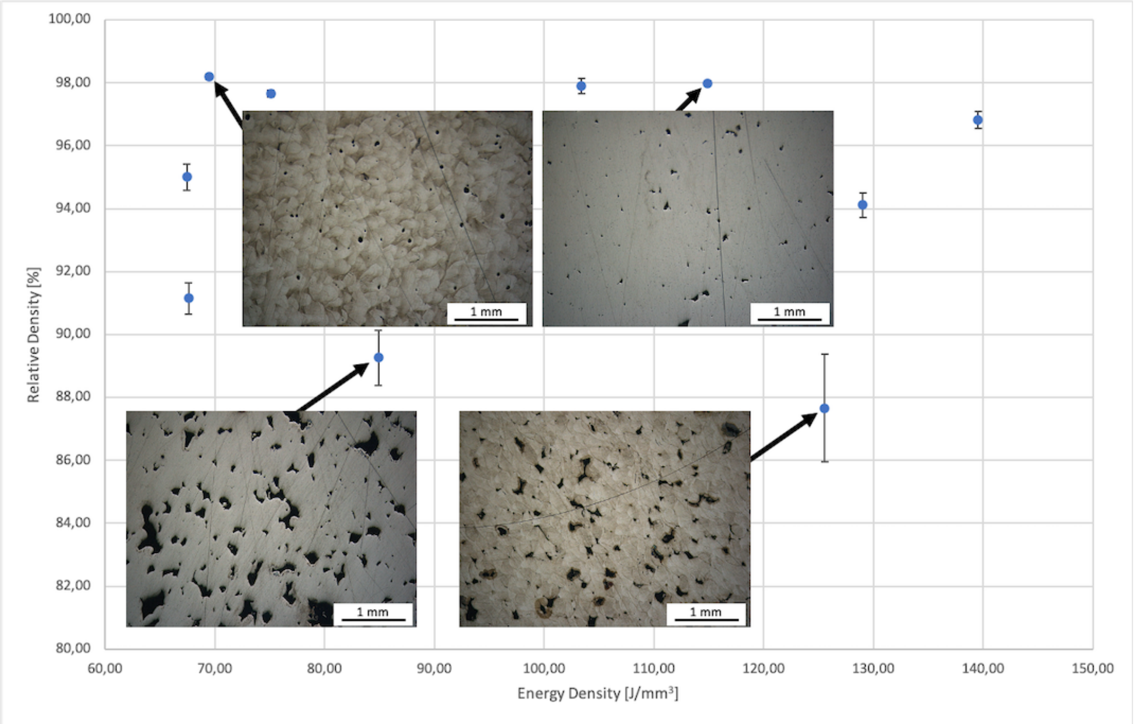

Figure 6.2: Graph of the achieved MS1 densities with the Farsoon SLM machine and micrographs of selected samples.

respectively due to the different measured densities.

Figure 6.3a shows the microstructure and laser tracks of sample nr. 8 etched with nital and 6.3b shows nr. 5 unetched. Both samples have a relative high density, but nevertheless, their microstructure is very diverse. Sample 5 was fabricated with a higher laser powder and a lower scanning speed resulting in a higher energy density overall, whereas sample 8 was produced with lower energy density in the system. Obviously, two different pores can be found in the samples. In sample 8 there are mostly spherical pores, which indicates that gas inclusions, that were unable to escape the melt pool due to a high solidification rate, caused this type of pore. Gas can be trapped in the bulk material, if the powder itself contains a lot of process-related (i.e. from gas atomization) gas inside [213]. Zhang et al. [214] furthermore describe the possibility of spherical porosities with metal powders with a low packing density (i.e. under 50 percent). Another possibility is that the laser energy input was too high for some alloy constituents and that they evaporated. These gas bubbles are then trapped in the solidified material and cause spherical pores [215]. In contrast to this, specimen nr. 5 shows irregular shaped pores, which also indicate too much energy. However, in this case it is very likely, that not just gas bubbles were formed. If the melt pool exhibits severe energy input, the melt pool becomes very unstable and in certain cases the matrix material can evaporate or have an increased tendency to form spatters. The melt pool will then solidify, but due to the lack of sufficient material, poor bonding defects will occur. Figure 6.3b furthermore shows some artefacts of the polishing and the post cleaning process with ethanol.

To give an overview of all produced MS1 specimens and their cross-sections in X-Z plane, Figure 6.4 is given. The samples are ordered in an ascending order according to their energy density.

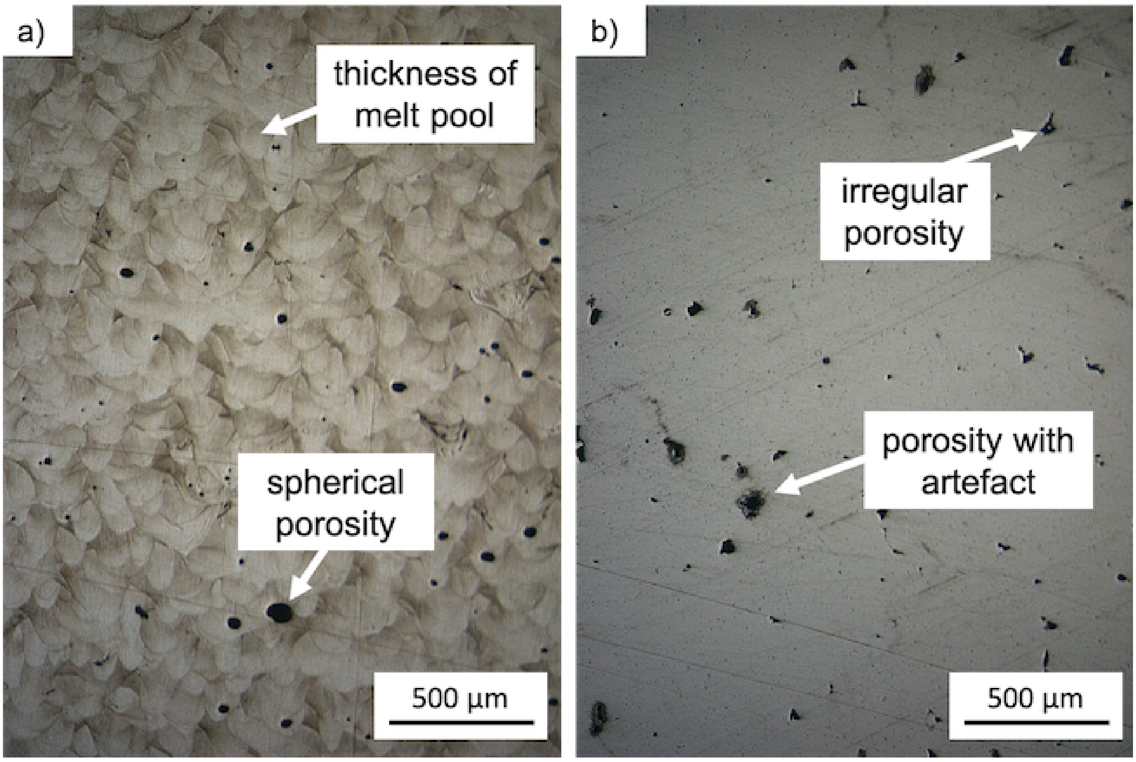

Figure 6.3: Microstructure of a) specimen nr. 8 after etching in nital and b) specimen nr. 5 unetched using OM.

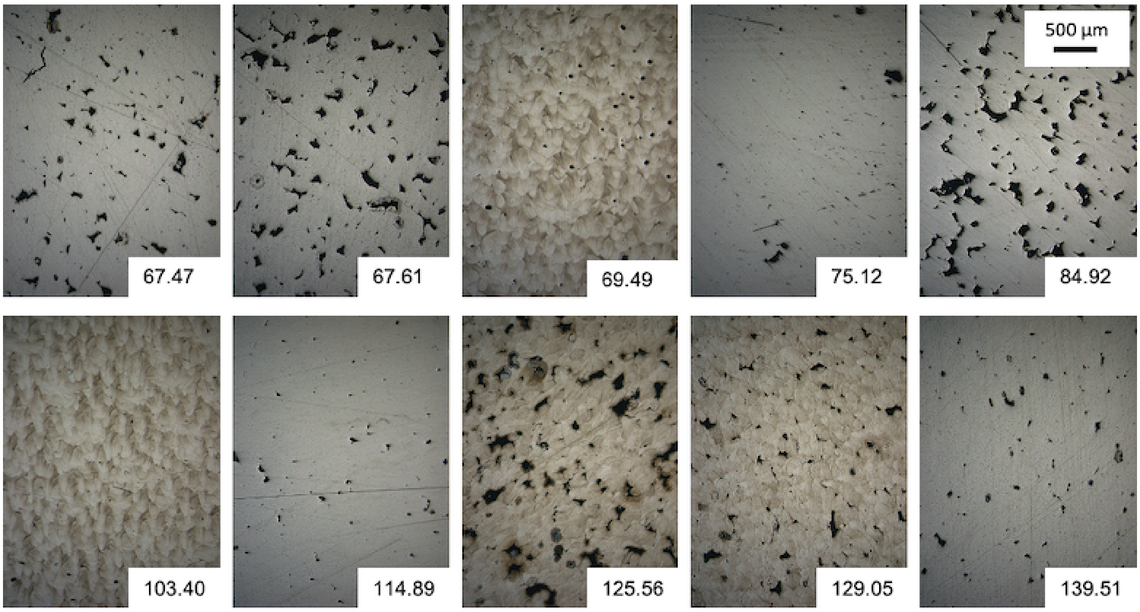

Figure 6.4: Microstructure of all MS1 SLM processed specimens using OM.

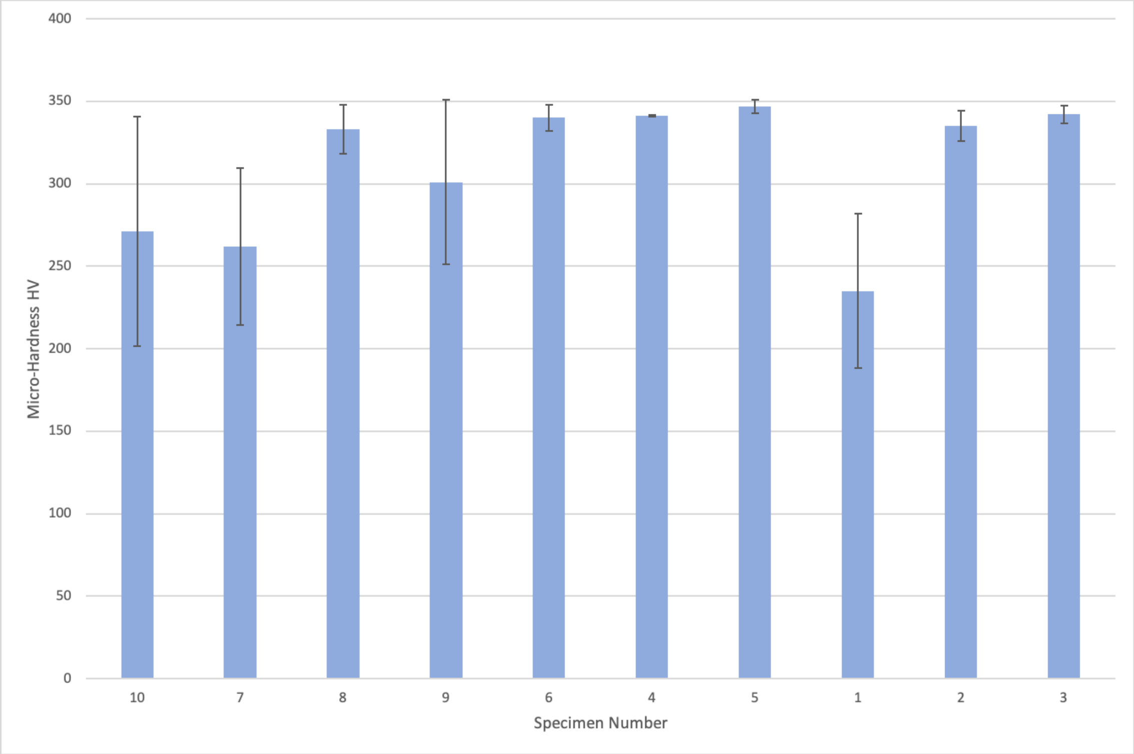

Figure 6.5: Micro-hardness values of the MS1 specimens.

6.3.2 Microhardness of MS1

After the microstructural analysis, Vickers micro-hardness was tested. The results can be found in Figure 6.5 in which the results are arranged according to the related energy density in an increasing order.

The highest mean hardness was measured with sample nr. 5, but the highest value overall was measured with specimen nr. 8, which also had the highest density. According to the powder manufacturer EOS, hardness values of parts in an as-built state, should be between 330 and 360 HV. Sample nr. 8 had a peak value of 354 HV and the mean value of specimen nr. 5 was 347 HV. These numbers are matching the manufacturers specifications. In Table 6.4 all of the other results are given for the sake of completeness and in Table 6.5 the according statistical information is provided.

Table 6.4: Overview of the SLM parameters and the micro-hardness measurements of MS1.

Spec. No.	**Laser Power [W]**	**Scan Speed [mm/s]**	**Hatching Real [μm]**	**Energy D. Real [J/mm^3]**	**Hardness 1 [HV]**	**Hardness 2 [HV]**	**Hardness 3 [HV]**	**Hardness Mean [HV]**
1	180	448	80	125.56	239	176	290	235
2	185	448	80	129.05	323	345	337	335
3	200	448	80	139.51	341	336	349	342
4	180	544	80	103.40	341	341	342	341
5	200	544	80	114.89	350	341	349	347
6	200	736	80	84.92	329	344	347	340
7	180	832	80	67.61	329	231	225	262
8	185	832	80	69.49	322	324	354	333
9	200	832	80	75.12	232	347	325	301
10	190	640	110	67.47	342	177	295	271

Table 6.5: Statistical information for micro-hardness measurements of the MS1 samples.

Specimen Nr.	Range R	Variance σ^2	Standard Deviation σ
10	165	4817.67	69.41
7	104	2273	47.68
8	32	214.33	14.64
9	115	2484.33	49.84
6	18	62	7.87
4	1	0.33	0.57
5	9	16.33	4.04
1	114	2174	46.63
2	22	82.67	9.09
3	13	28.67	5.35

6.3.3 Microstructural Characterization and Density of MS1/VC-33

The micrographs of the MS1/VC-33 powder mixture revealed that VC particles were not molten in most cases. Throughout the whole specimen there are many VC particles visible, which were not molten. Their homogeneous distribution is remarkable though. In Figure 6.6 an example is given. There are some micro-cracks visible, some blowholes, and multiple unmolten VC particles. Especially the spherical pores are worth mentioning. They are called lack-of-fusion pores and appear because of interferences during SLM processing [216]. However, if the VC is not molten during the SLM process the particles can still increase some mechanical properties. In preliminary studies it was found, that especially the wear resistance will be increased. The VC particles have a very high hardness and therefore, will resist against abrasion. On the other hand, there is a higher tendency for micro-cracks in the matrix material starting from the hard VC particle. Stress caused by strain can furthermore crack the VC particle itself, which is then a potential source for material failure [140, 141]. Generally speaking, material properties will increase overall and be more stable, if particles are molten completely and precipitate homogeneously distributed in the solidified material. The achieved relative densities and the mean density of the MS1/VC-33 SLMed material can be found in Table 6.6.

The highest relative density was achieved with specimen nr. 18 which had a similar energy density (i.e. 65.65 J/mm^3) as the best sample of the pure MS1 had (i.e. 69.49 J/mm^3). However, the laser power was higher and the scan speed was comparably lower causing a stabilization of the melt pool. The introduction of the composite particles probably interfered the melt pool slightly, but with an overall slower process, this was compensated. Obviously, the VC composite material brought into the matrix did have a big effect on the melt pool and the melting temperature, as most VC particles did not melt at all and more energy was necessary for a more dense microstructure. A plot of the energy densities and the respective relative densities is given in Figure 6.7 which also includes some representative micrographs.

In Figure 6.8 a complete overview is given of all SLM processed samples. It can be seen that especially at higher energy densities the material was more likely to be built without porosity. This clearly indicates the influence of the VC particles, as the η-values had to be significantly higher than for the MS1 samples.

6.3.4 Microhardness of MS1/VC-33

Figure 6.9 shows the achieved microhardness values of the MS1/VC-33 specimens and the respective standard deviations sorted to the energy density from low to high. The highest mean hardness value, but also the highest mean value overall was achieved with specimen nr. 5 which was 463 HV

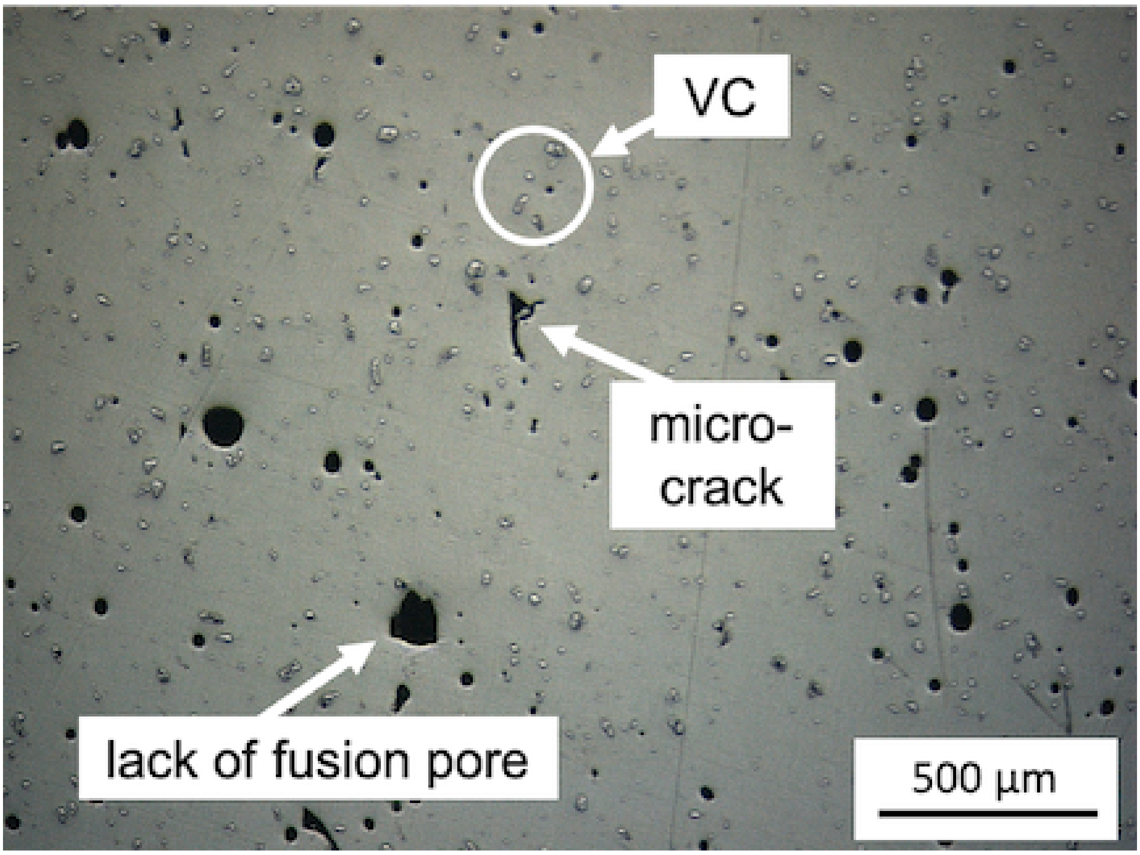

Figure 6.6: Micrograph of SLM processed MS1/VC-33 with micro-cracks, porosity and unmolten VC particles.

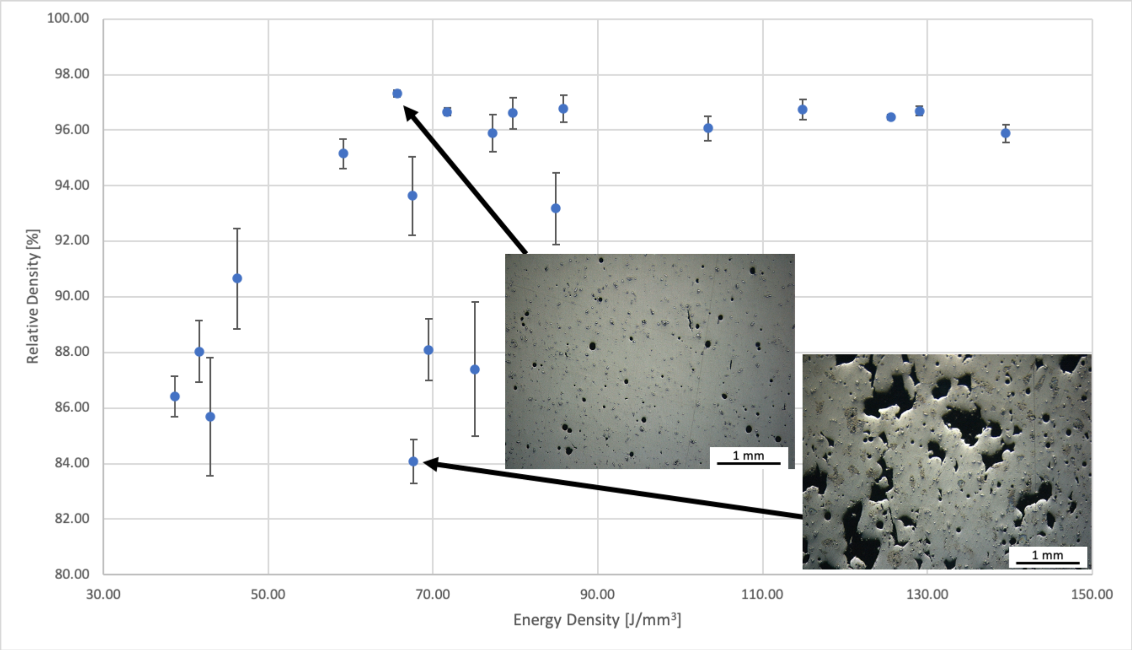

Figure 6.7: Graph of the achieved MS1/VC-33 densities with the Farsoon SLM machine and micrographs of selected samples.

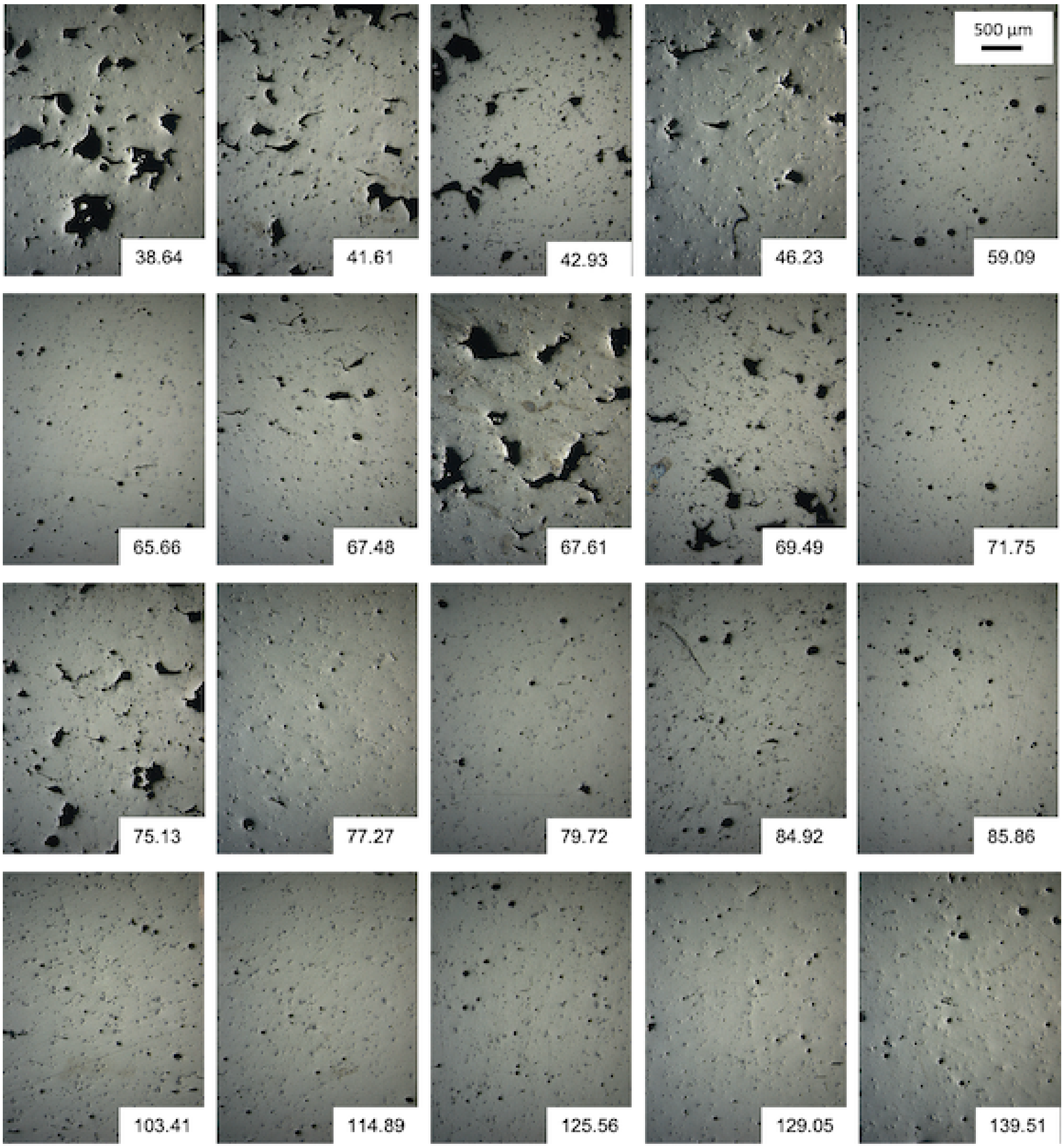

Figure 6.8: Microstructure of all MS1/VC-33 specimens which were SLM processed.

Table 6.6: Overview of the SLM parameters and the density measurements of MS1/VC-33.

Spec. No.	**Laser Power [W]**	**Scan Speed [mm/s]**	**Hatching Real [μm]**	**Energy D. Real [J/mm^3]**	**Rel D. 1 [%]**	**Rel. D. 2 [%]**	**Rel. D. 3 [%]**	**Rel. D. Mean [%]**
1	180	448	80	125.56	96.50	96.54	96.34	96.46
2	185	448	80	129.05	96.93	96.57	96.58	96.69
3	200	448	80	139.51	95.64	95.66	96.32	95.87
4	180	544	80	103.4	96.65	95.90	95.63	96.06
5	200	544	80	114.89	96.21	97.06	96.95	96.74
6	200	736	80	84.92	94.56	91.47	93.51	93.18
7	180	832	80	67.61	84.14	83.09	85.00	84.08
8	185	832	80	69.49	88.69	86.53	89.08	88.10
9	200	832	80	75.12	87.04	84.63	90.51	87.39
10	190	640	110	67.47	95.28	91.84	93.76	93.63
11	180	448	130	77.27	96.65	96.00	95.03	95.89
12	200	448	130	85.85	96.93	96.09	97.28	96.77
13	180	832	130	41.61	86.47	88.94	88.68	88.03
14	200	832	130	46.23	92.54	88.21	91.22	90.66
15	180	448	140	71.75	96.73	96.48	96.77	96.66
16	200	448	140	79.72	97.05	95.81	96.98	96.61
17	180	544	140	59.09	94.43	95.69	95.33	95.15
18	200	544	140	65.65	97.28	97.20	97.48	97.32
19	180	832	140	38.63	85.83	85.98	87.43	86.41
20	200	832	140	42.93	82.89	86.11	88.07	85.69

and a peak value of 486 HV. Compared to the pure MS1 fabricated samples, this is an increase of 132 HV or 37.29 % for the peak values and an increase of 116 HV or 33.43 % for the mean hardness values. This proves that even though most VC particles did not melt at all, the micro-hardness was improved significantly. The VC particles act against dislocation movements and therefore increase the hardness of the material. Furthermore, the particles themselves have a very high hardness. Table 6.7 shows all of the samples and their according results.

Table 6.7: Overview of the SLM parameters and the micro-hardness measurements of MS1/VC-33.

Spec. No.	**Laser Power [W]**	**Scan Speed [mm/s]**	**Hatching Real [μm]**	**Energy D. Real [J/mm^3]**	**Hardness 1 [HV]**	**Hardness 2 [HV]**	**Hardness 3 [HV]**	**Hardness Mean [HV]**
1	180	448	80	125.56	392	321	430	381
2	185	448	80	129.05	436	422	428	429
3	200	448	80	139.51	439	448	435	441
4	180	544	80	103.4	408	462	427	432
5	200	544	80	114.89	437	486	466	463
6	200	736	80	84.92	394	387	437	406
7	180	832	80	67.61	436	437	433	435
8	185	832	80	69.49	407	358	459	408
9	200	832	80	75.12	419	438	448	435
10	190	640	110	67.47	364	428	363	385
11	180	448	130	77.27	427	404	467	433
12	200	448	130	85.85	411	429	442	427
13	180	832	130	41.61	361	364	433	386
14	200	832	130	46.23	447	373	439	420
15	180	448	140	71.75	454	442	418	438
16	200	448	140	79.72	386	335	452	391
17	180	544	140	59.09	391	417	406	405
18	200	544	140	65.65	427	480	403	437
19	180	832	140	38.63	426	426	454	435
20	200	832	140	42.93	394	356	398	383

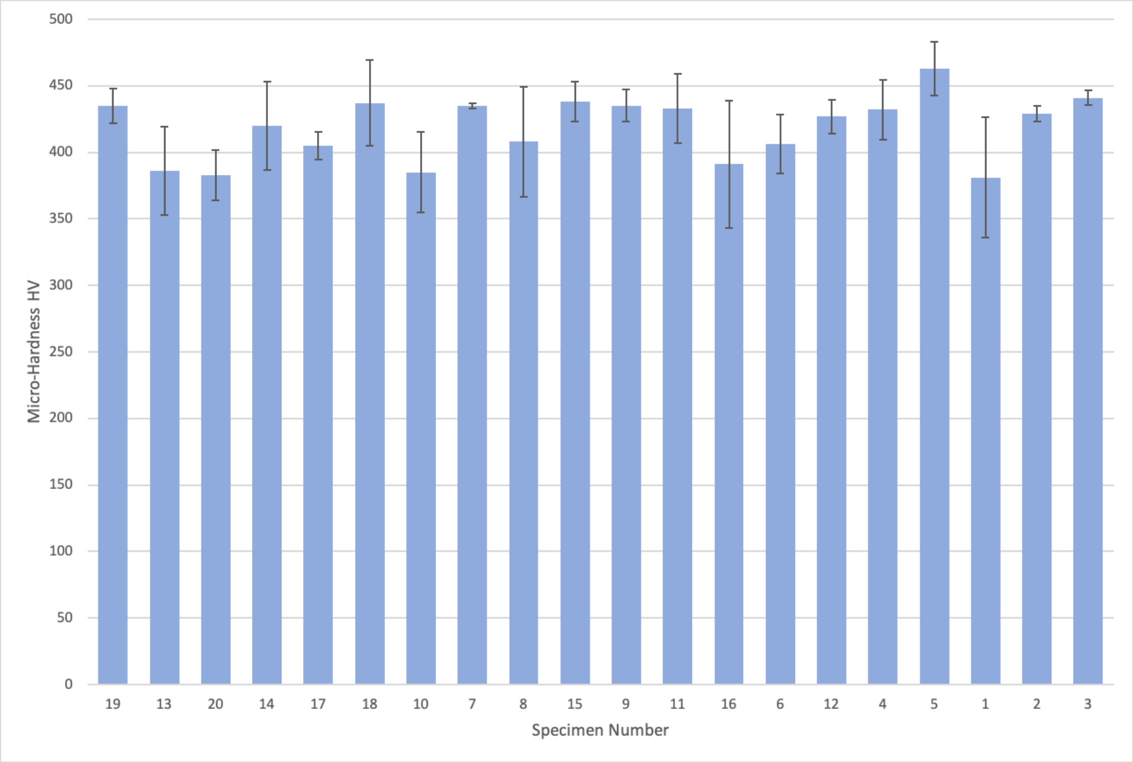

Figure 6.9: Micro-hardness values of the MS1/VC-33 specimens.

6.3.5 Microstructural Characterization and Density of MS1/VC-2.5

To further improve the hardness results and to achieve a more homogeneous distribution of the composite material, finer VC particles were mixed to the MS1 matrix material. It was expected to fully melt a higher amount of VC particles due to the comparably smaller size distribution. The new batch had a maximum size of 2.5 microns. It was also believed that a more homogeneous distribution would cause better part densities and less porosity. If the melt pool is not interfered by large VC particles, a more stable melt pool should form in theory. Furthermore, micro-cracks can be reduced or avoided, if the introduced composite material particles are smaller. However, it was observed that finer particles also hinder the powder coating after each layer during the SLM process. Due to agglomerating fine VC powder particles, the coating of the powder layers was interrupted, causing an uneven powder layer. It was possible to partially compensate this with a higher powder feed rate. The measured relative densities and the mean density of the MS1/VC-2.5 SLM processed composite can be found in Table 6.8.

The results reveal that the overall density of all specimens was increased with the introduction of smaller sized VC particles and the expected outcome of the tests was confirmed. Specimen nr. 8 had the lowest porosity respectively the highest relative density with 98.02 % at 69.49 J/mm^3. Compared to the composite material with 33 μm average sized particles, the laser power and the hatch distance was lower, but the scanning speed was higher. Some micrographs and a plot of the energy densities over the relative energy densities are given in Figure 6.10. The figure also includes the standard deviation of the measurements. Furthermore, some details about the microstructure are given in Figure 6.15a. The figure shows micro-cracks in the sample and lots of unmolten VC particles, even though it was expected to fully melt some of them, due to the smaller initial particle size. Obviously, this was not really the case. Their distribution in the specimens was remarkable though and even better than with the VC-33 material. If one compares Figure 6.15a and Figure 6.6 it can be seen that there is a difference in the average particle size of the vanadium carbide.

Table 6.8: Overview of the SLM parameters and the density measurements of MS1/VC-2.5.

Spec. No.	**Laser Power** [W]	**Scan Speed** [mm/s]	**Hatching Real** [μm]	**Energy D. Real** [J/mm^3]	**Rel D. 1** [%]	**Rel. D. 2** [%]	**Rel. D. 3** [%]	**Rel. D. Mean** [%]
1	180	448	80	125.56	97.23	98.10	97.76	97.70
2	185	448	80	129.05	97.68	97.85	97.32	97.62
3	200	448	80	139.51	97.76	97.31	97.20	97.42
4	180	544	80	103.40	96.48	96.79	97.05	96.77
5	200	544	80	114.89	96.71	96.56	97.43	96.90
6	200	736	80	84.92	94.23	97.37	95.69	95.76
7	180	832	80	67.61	97.02	97.30	97.10	97.14
8	185	832	80	69.49	98.02	98.03	98.00	98.02
9	200	832	80	75.12	97.46	98.21	97.35	97.67
10	190	640	110	67.47	97.77	97.28	98.03	97.69
11	180	448	130	77.27	97.89	97.64	98.14	97.89
12	200	448	130	85.85	97.69	96.15	97.43	97.09
13	180	832	130	41.61	97.66	97.82	97.97	97.82
14	200	832	130	46.23	96.38	96.93	97.37	96.89
15	180	448	140	71.75	95.08	95.90	95.96	95.65
16	200	448	140	79.72	98.00	97.99	97.35	97.78
17	180	544	140	59.09	97.58	98.16	97.42	97.72
18	200	544	140	65.65	98.11	97.64	98.04	97.93
19	180	832	140	38.63	96.14	97.34	97.86	97.11
20	200	832	140	42.93	97.38	98.05	97.75	97.73

Figure 6.11 shows all of the manufactured specimens. Overall it can be said that the MS1/VC-2.5 mixture had a better behaviour while SLM processing. The densities were higher and the pores were smaller than with the MS1/VC-33 mixture. However, there was no clear trend of a higher or lower relative density related to the energy density. This would make a further parameter optimization tough as there would be no starting point, which parameters should be adjusted.

6.3.6 Microhardness of MS1/VC-2.5

The microhardness values of the MS1/VC-2.5 specimens were even higher than the specimens printed with the MS1/VC-33 powder mixture. Obviously, the vanadium carbide particles reinforced the composite material. The MS1 and the VC-2.5 powders were mixed based on weight contents. Because of this, there were more particles in the mixture as the initial particle size was finer. This means that, due to more particles in the SLM processed composite material, there were more particles hindering dislocation movements, causing higher microhardness values. In Table 6.9 can all of the achieved values be found. Especially specimen nr. 11 had a remarkable and outstanding Vickers hardness. The mean value was 544 HV and the peak value was as high as 597 HV. Another influencing factor for a better hardness is the porosity in a sample. As the samples had a higher density compared to the MS1/VC-33 specimens, it was highly expected to achieve higher microhardness results. However, the specimen with the highest density (i.e. nr. 8) did not show the highest microhardness results interestingly, which indicates that the porosity can be an influencing factor, but the distribution of the reinforcing particles is even more important. Furthermore, specimen nr. 11 had a higher energy density, which might have lead to more dissolved and precipitated primary VC particles in the solidified material, causing an even higher and more homogeneous particle distribution and therefore, a higher hardness.

To visually compare the results, Figure 6.12 is provided, which also includes the standard deviation of the measurements. The results are arranged in order of the energy density from low to high.

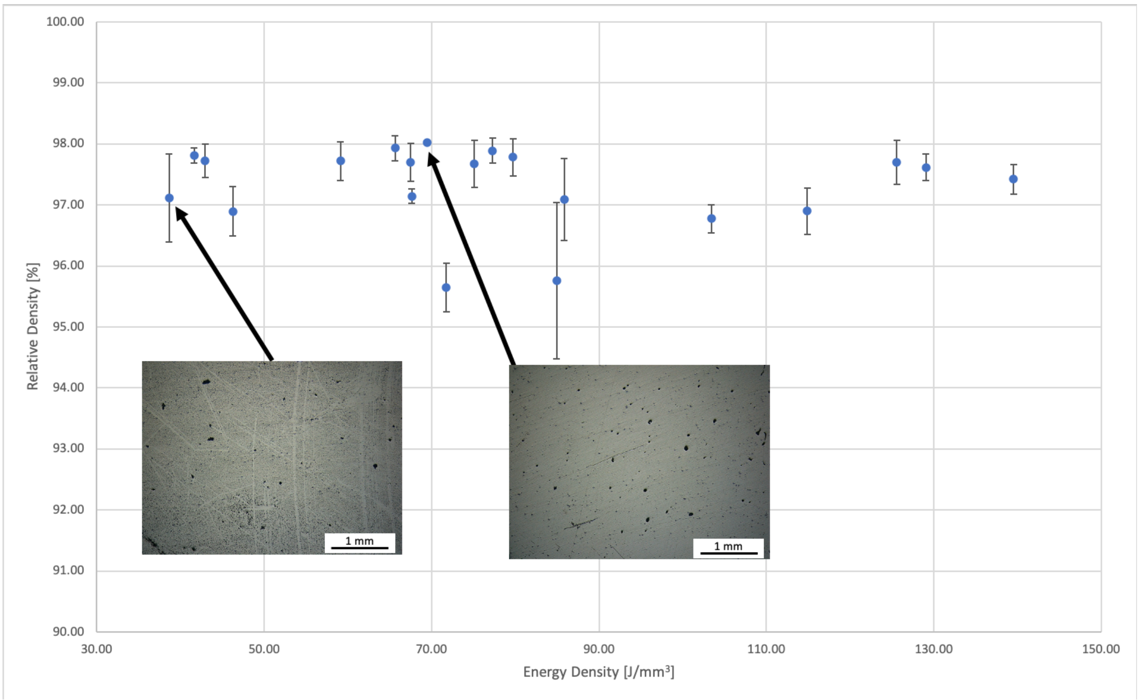

Figure 6.10: Graph of the achieved MS1/VC-2 densities with the Farsoon SLM machine and micrographs of selected samples.

Table 6.9: Overview of the SLM parameters and the micro-hardness measurements of MS1/VC-2.5.

Spec. No.	**Laser Power [W]**	**Scan Speed [mm/s]**	**Hatching Real [μm]**	**Energy D. Real [J/mm^3]**	**Hardness 1 [HV]**	**Hardness 2 [HV]**	**Hardness 3 [HV]**	**Hardness Mean [HV]**
1	180	448	80	125.56	424	428	443	432
2	185	448	80	129.05	422	463	450	445
3	200	448	80	139.51	426	428	410	421
4	180	544	80	103.4	424	427	434	428
5	200	544	80	114.89	462	420	414	432
6	200	736	80	84.92	430	441	424	432
7	180	832	80	67.61	388	418	423	410
8	185	832	80	69.49	463	497	447	469
9	200	832	80	75.12	403	413	409	408
10	190	640	110	67.47	475	467	477	473
11	180	448	130	77.27	490	545	597	544
12	200	448	130	85.85	424	460	499	461
13	180	832	130	41.61	450	464	476	463
14	200	832	130	46.23	483	490	494	489
15	180	448	140	71.75	477	479	495	484
16	200	448	140	79.72	438	415	452	435
17	180	544	140	59.09	409	415	477	434
18	200	544	140	65.65	445	464	439	449
19	180	832	140	38.63	462	459	464	462
20	200	832	140	42.93	435	415	416	422

6.3.7 Analysis of Density

After obtaining all results of the density evaluations, R Studio was used to analyze the relative density of the specimens. Using the same model as for the Design of Experiments calculations, a prediction for the highest possible relative density was be done. The laser power was set to a constant value of 190 watts for the model. Figure 6.13 shows the coloured diagram of the predictions. The theoretical maximum is represented by a red dot in the image. In Figure 6.13b, which shows

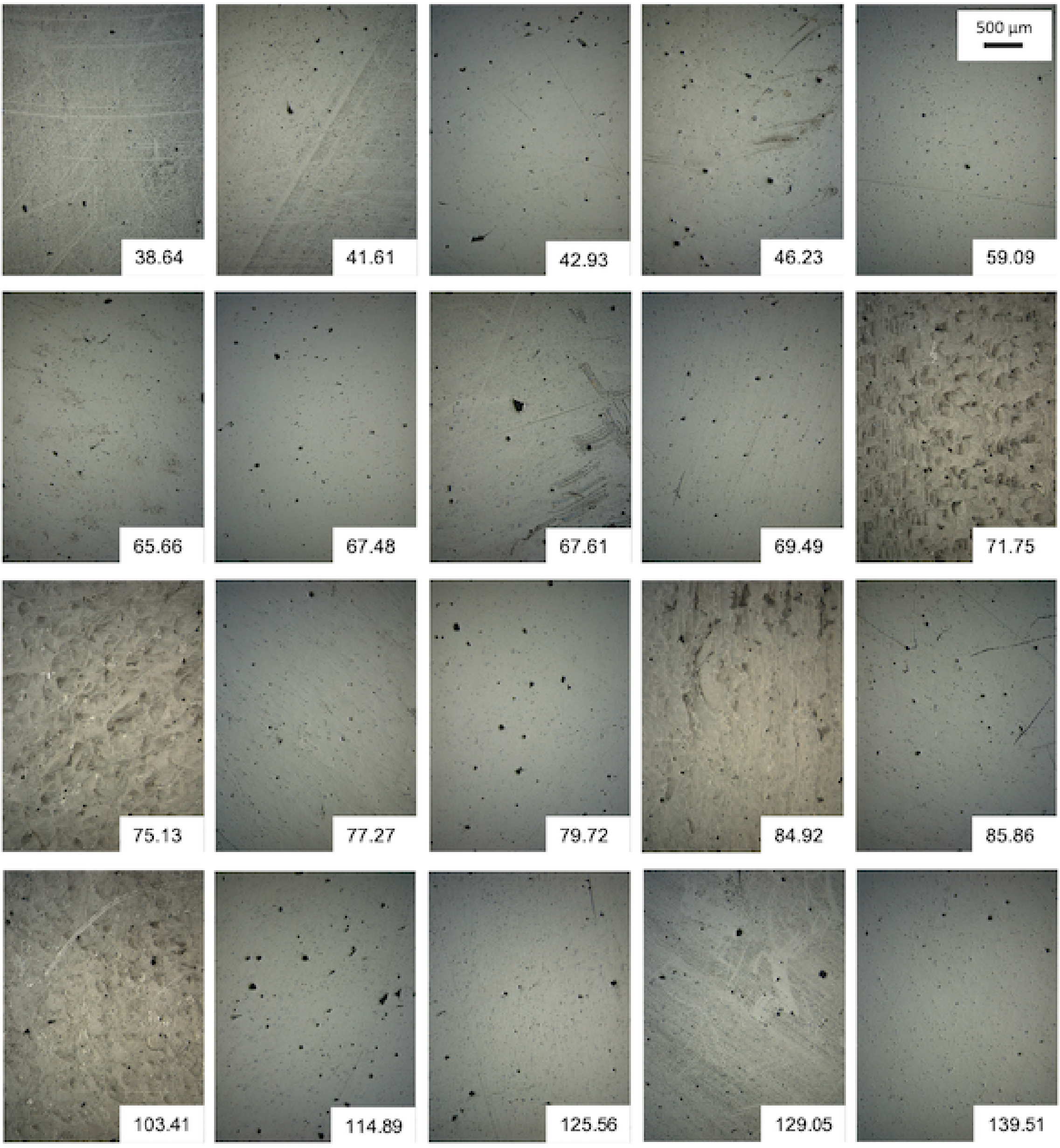

Figure 6.11: Microstructures of all manufactured samples with MS1 and 10 wt% VC-2.5.

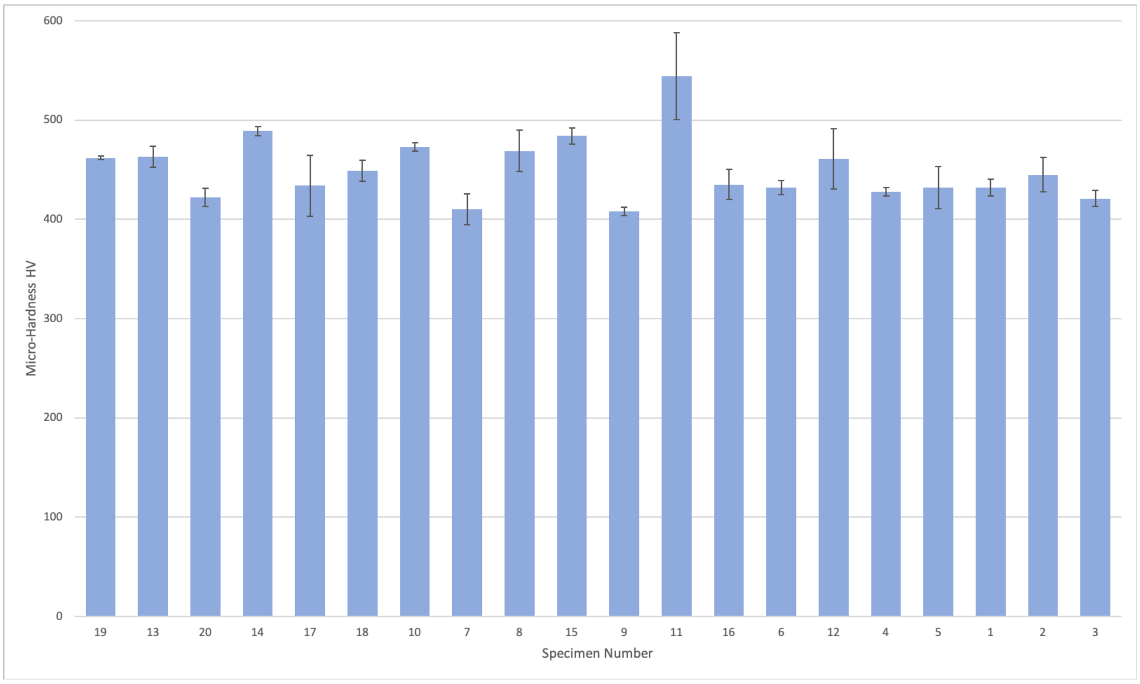

Figure 6.12: Micro-hardness values of the MS1/VC-2.5 specimens.

the results for MS1VC$_{10}$ with a particle size distribution of 1-33 microns, the theoretical maximum at a laser power of 190 watts is at approximately 510 mm/s scan speed and 127 μm hatching. However, Figure 6.13a shows a very strange prediction for the MS1VC$_{10}$ 2.5 micron mixture. In the middle of the image, a worse relative density is predicted. This can be explained due to the comparably high values of relative density of all specimens. As the results are very close, the R Studio script cannot calculate appropriate prediction models and the values are fluctuating in a very minor way.

6.3.8 Improvement of Results

In the fabricated specimens, the microhardness was improved and the porosity was decreased by decreasing the mean particle size of VC. However, there were some blowholes and imperfections which had to be addressed in further parameter studies. Liu et al. [216] describe the appearance

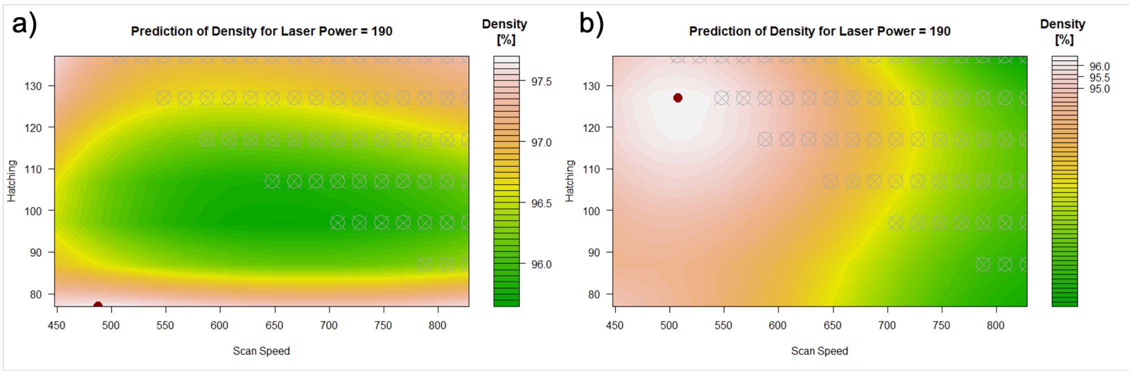

Figure 6.13: Prediction of the optimal relative density for MS1VC$_{10}$ with a) 2.5 μm particles and b) 33 μm particles.

of lack-of-fusion porosity in SLM processed parts similar to the ones in the MS1/VC samples. In their study they proposed to use alternative exposures. One of them is to double exposure every layer before the next layer is coated with powder. This way, some of the material is remelted and a higher density can be achieved. The size of pores can be diminished and the percentage of porosity can be decreased. Similar results were found for Cu-Al-Ni-Mn [217], Al-Mg-Zr [218] and 5CrNi4Mo [219]. Demir et al. investigated the achievable part densities of 18Ni300 maraging steel using single exposure, double exposure, soft remelting and polishing scanning strategies [220]. It was found that remelting can significantly improve the part density and reduce defects. However, the remelting capabilities of the laser are limited due to the material transformation from a powder to a solid material. A solid block has a different thermal conductivity and reflectivity than bulk powder material has. Therefore, the second exposure will not remelt the material as deep as the first exposure does.

To further improve the material density, another batch of samples was produced with the same SLM parameters as already used and shown in Table 6.2. Except, in this case the specimens were exposed with the laser twice. Hatch distance, scan speed and laser power were kept the same and there was no rotation of the laser tracks in between the two exposures. The first exposure run aimed to deposit the powder material evenly onto the layer and the second exposure was aimed to reduce the porosity in the layer. The results of the density can be found in Table 6.10. Unfortunately, not all of the specimens were built respectively some had to be aborted and removed from the build platform. Due to the increased energy brought into the specimens, there was also more stress brought into them. This caused deformations and the cubes started to bend and crack off of the build platform. In Figure 6.14 a comparison of the achieved relative density of the samples manufactured with single and double exposure is given. The figure also shows the non-manufactured specimens on the bottom of the diagram. One can see that the double exposure scanning strategy lead to a higher relative density in most cases. However, the results were not improved significantly, as it was expected in the beginning of the test series. According to the density measurements there were just minor improvements, if there were any at all, compared to the single exposure scanning strategy. On the other hand, analyzing the microstructure of the samples with an optical microscope revealed that indeed the porosity was decreased. Especially the amount of lack-of-fusion errors was decreased significantly. In Figure 6.15 a comparison of the two different scanning strategies and the achieved microstructure is given. In Figure 6.15a the MS1/VC-2.5 powder with single exposure can be seen and in Figure 6.15b the same powder with the same applied energy density and SLM parameters, except the double exposure, is given. It is clearly visible that the lack of fusion defects were reduced and the overall results were improved. It was also expected, to dissolve and fully melt more of the fine VC particles. While comparing the samples with the highest relative density (i.e. no. 8), there were no notable changes of unmelted VC particles. However, while comparing the specimens with the highest energy density (i.e. no. 3) the amount of unmelted VC was remarkably lower in the specimen exposed twice and can be seen in 6.15. This proved that it is possible to fully melt VC with SLM, even though the material has such a comparably higher melting point. As the VC cannot disappear, it must have formed primary VC particles in the solidified material. For the sake of completeness, Figure 6.16 shows all micrographs obtained with the double exposure scanning strategy.

To understand the effects of double exposure on the material properties, the micro-hardness was measured. It was expected that especially specimen nr. 3 must have had an improvement of the micro-hardness, due to the high amount of primary VC particles. In Table 6.11 the SLM parameters for the double exposed samples and the micro-hardness measurements are given. A comparison of the Vickers micro-hardness values of the MS1/VC-2.5 single exposed and double exposed materials can be found in Figure 6.17. The figure also includes the respective standard deviations. Against expectations, the micro-hardness in specimens nr. 3 and nr. 8 were not improved. Instead, the Vickers hardness was decreased. Some of the specimens however, did show higher micro-hardness values, but there was no clear trend investigated. Maraging steels commonly are solution annealed to homogenize the microstructure before the ageing treatment to maximize hardness. Because of

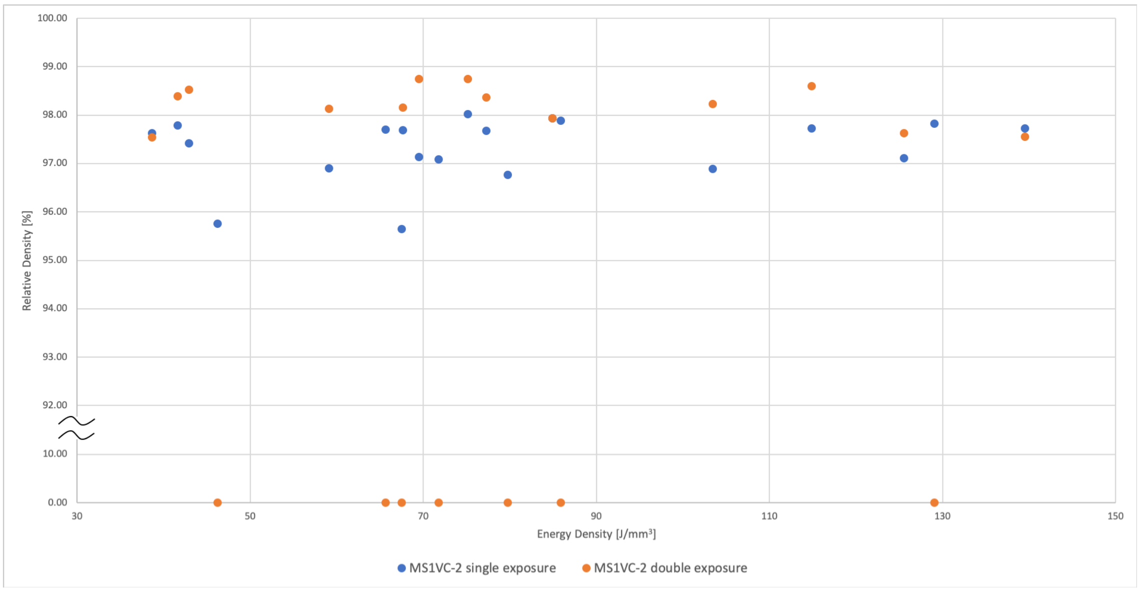

Figure 6.14: Comparison of the density of the MS1/VC-2.5 specimens processed with single and double exposure.

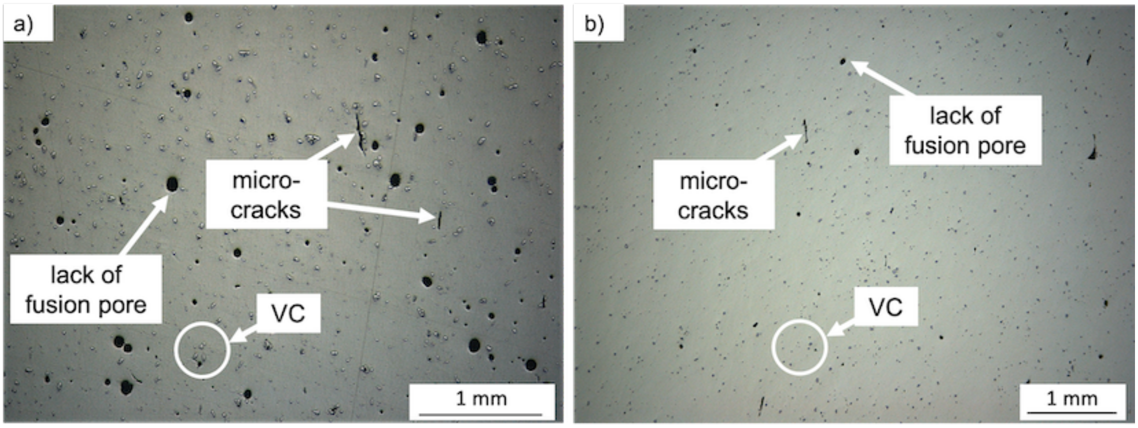

Figure 6.15: Micrograph of SLM processed MS1/VC-2.5 (No. 3) with micro-cracks, porosity and unmolten VC particles after a) single and b) double exposure.

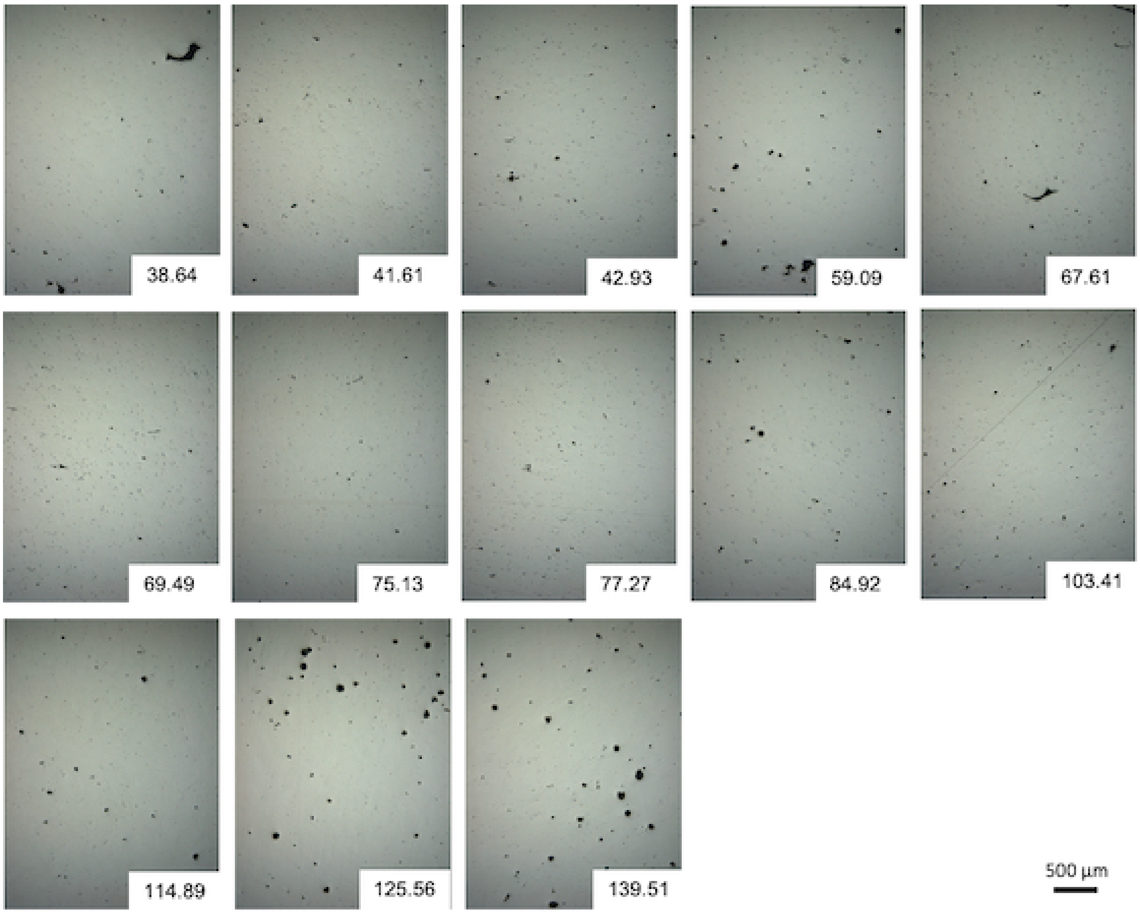

Figure 6.16: Micrographs of all SLM processed MS1/VC-2.5 specimens obtained with the double exposure technique.

Table 6.10: Overview of the SLM parameters and the density measurements of double exposed MS1/VC-2.5.

Spec. No.	**Laser Power** [W]	**Scan Speed** [mm/s]	**Hatching Real** [μm]	**Energy D. Real** [J/mm^3]	**Rel D. 1** [%]	**Rel. D. 2** [%]	**Rel. D. 3** [%]	**Rel. D. Mean** [%]
1	180	448	80	125.56	97.76	97.68	97.44	97.63
3	200	448	80	139.51	97.44	97.46	97.76	97.55
4	180	544	80	103.40	98.10	98.42	98.17	98.23
5	200	544	80	114.89	98.68	98.67	98.46	98.6
6	200	736	80	84.92	97.48	97.90	98.43	97.93
7	180	832	80	67.61	98.54	98.07	97.84	98.15
8	185	832	80	69.49	98.73	98.68	98.80	98.74
9	200	832	80	75.12	98.64	98.68	98.91	98.74
11	180	448	130	77.27	98.47	97.94	98.69	98.37
13	180	832	130	41.61	98.71	98.80	97.65	98.39
17	180	544	140	59.09	98.26	98.00	98.11	98.13
19	180	832	140	38.63	96.88	97.86	97.87	97.54
20	200	832	140	42.93	98.53	98.82	98.21	98.52

the double exposure, some unwanted coarsening might have happened. Demir et al. [220] found a correlation between preheating, SLM processing and coarsening. As the second exposure results in higher part temperatures, a coarser microstructure is very likely to form. Furthermore, the thermal history of the material is influenced and therefore, the grain growth, martensitic phase formation, the formation of plate or lath martensite and precipitation hardening effect is affected.

Table 6.11: Overview of the SLM parameters and the micro-hardness measurements of the double exposed MS1/VC-2.5.

Spec. No.	**Laser Power** [W]	**Scan Speed** [mm/s]	**Hatching Real** [μm]	**Energy D. Real** [J/mm^3]	**Hardness 1** [HV]	**Hardness 2** [HV]	**Hardness 3** [HV]	**Hardness Mean** [HV]
1	180	448	80	125.56	424	452	459	445
3	200	448	80	139.51	277	445	361	361
4	180	544	80	103.40	490	474	432	465
5	200	544	80	114.89	482	455	411	449
6	200	736	80	84.92	475	391	447	438
7	180	832	80	67.61	464	382	441	429
8	185	832	80	69.49	457	469	418	448
9	200	832	80	75.12	411	418	477	435
11	180	448	130	77.27	424	438	447	436
13	180	832	130	41.61	425	442	428	432
17	180	544	140	59.09	468	470	469	469
19	180	832	140	38.63	502	479	434	472
20	200	832	140	42.93	448	448	514	470

6.4 Conclusions

In this chapter, a powder mixing technique was used to ex-situ form a metal matrix composite. SLM processing the maraging steel and vanadium carbide mixture revealed that the large VC particles caused instabilities in the melt pool and therefore, causing porosity in the printed material. Through particle refinement of the composite material, higher porosity levels were achieved. According to the LNG theory, the surface melting temperature decreases, with a decrease in particle size. First, bonding between particles occurs and then the liquid phase of the whole particle will be reached. However, the distribution of the fine and the coarse VC fluctuates due to the particle size. The coarse VC particles will not be as homogeneously distributed in the powder mixture and therefore, the laser melted front of a melt pool tends to be interrupted and becomes discontinuous. This then results in irregular shaped pores and uneven laser tracks. The matrix material will also

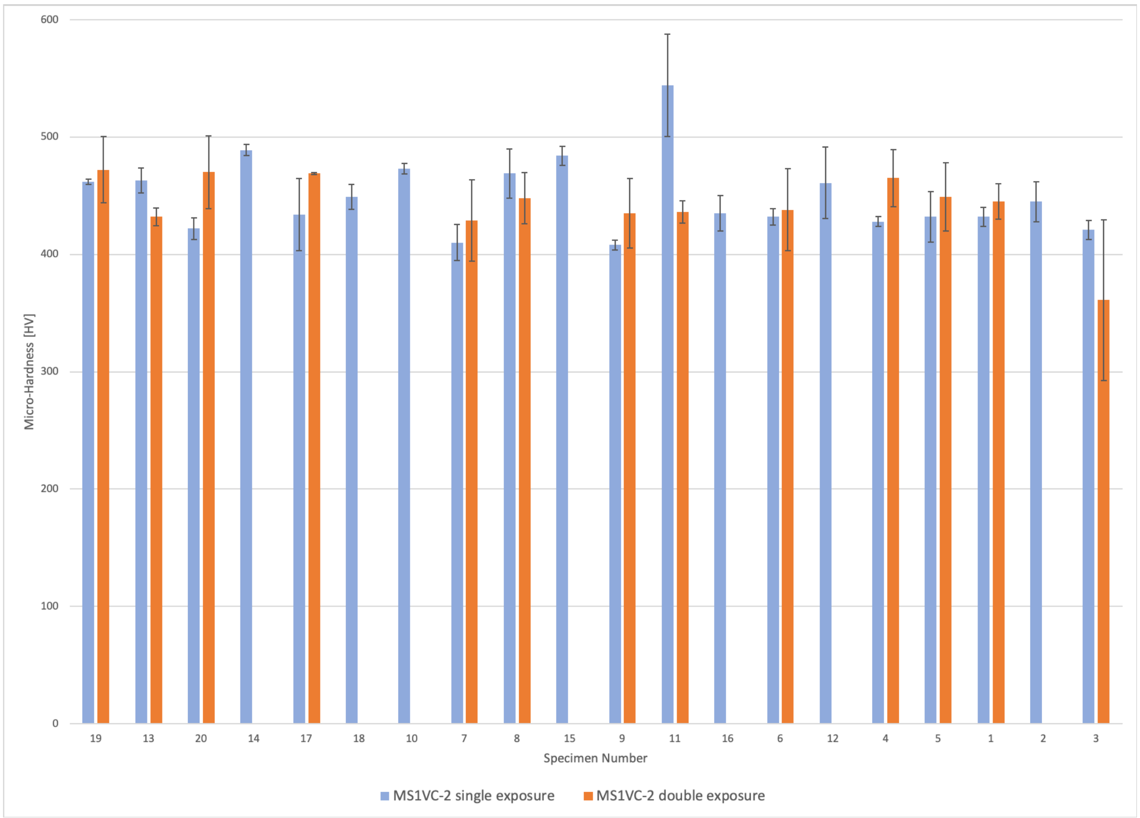

Figure 6.17: Comparison of the micro-hardness values of MS1/VC-2.5 with single and double exposure scanning strategy.

have a lower wettability with coarse VC particles, as the interfacial bonding is significantly lower, compared to a finer reinforcing component with a comparably much higher surface area. On the other hand, while using finer VC-2.5 powder, the powder coating process after each layer was not as smooth and unproblematic as with the VC-33 material unfortunately. Due to the particle refinement, there were a lot of very small particles in the mixture causing agglomerations. Small VC particle stuck on the bigger MS1 particles and hindered the even coating, as non spherical powder agglomerates were formed. This was especially problematic for specimens placed at the end of the building platform and therefore, were coated with less powder material. The feedstock rate had to be increased accordingly.

As the powder refinement showed an increased relative density, but the desired density of 99 % was still not reached, an alternative scanning strategy was applied to the MS1/VC-2.5 material. Through double exposure of each layer, an overall higher relative density was achieved. However, through the increased amount of energy and heat, there was also higher stress in the specimens, causing cracks in some of them. Furthermore, the double exposure scanning strategy leads to longer building times. The porosity was decreased though, but the technique of double exposure should be applied on demand. A monitoring system could automatically decide after each layer, if a second scan of the layer is necessary or not. The technology could be based on an image processing technique. This would reduce lead times and improve the part quality. Furthermore, the double exposure can affect the phase formation and martensitic growth significantly. This might cause unwanted material properties.

The main results of this study are as follows.

- While designing MMCs with diverse melting temperatures, the particle size of the component with the higher melting temperature should be chosen smaller than the component with the lower melting temperature, according to the LNG theory.
- A Turbula shaker mixer is an efficient and cost effective tool to homogeneously mix powders. The VC particles were evenly distributed throughout the whole mixture.
- A decrease of the composite material in particle size resulted in a higher relative density after SLM processing. However, the smaller particle size also affected the coating process of each layer during selective laser melting.
- It was proven, that it is possible to fully melt the VC particles in a combination of MS1, if the VC powder is very small and the energy density during SLM processing is very high. If the VC is molten completely, it will form fine reinforcing primary VC, which is homogeneously distributed in the solidified material.
- Through the particle reinforcement with vanadium carbide, the maraging steel showed improved micro-hardness values. Especially the finer VC-2.5 increased the results significantly. The highest result was measured at 597 HV1 using 77.27 J/mm^3.
- An alternative scanning strategy increased the relative density slightly. Double exposing each layer lead to a maximum mean density of 98.74 %. According to microstructural analysis using optical microscopy, it was found that the defect were reduced significantly though. The technique of double exposure is an effective tool to optimize the part quality and reduce lack of fusion defects, but it will also increase the overall SLM processing time.

7

Fabrication of Mixed MS1/VC by SLM with Different Weight Contents

7.1 Introduction

As mentioned in Chapter 6, the particle size of the VC powder played a significant role to produce parts with a high relative density. Furthermore, the results of the microhardness measurements were improved. It was decided to use 10 wt% of VC in Chapter 6, to prove an enhancement of the material properties, but using such a high amount of reinforcing carbides during SLM processing can cause problems for the melt-pool. To better understand the metal matrix composite system of MS1/VC, it was decided to investigate the microstructure, ultimate tensile strength, hot ultimate tensile strength and micro-hardness with various amounts of VC. The densification behaviour was controlled by the starting VC content. It was expected to find an optimum for the material strength on one hand and relative part density on the other hand.

During this study, the maraging steel and the vanadium carbide powders were homogeneously mixed and then processed in an SLM machine. It was aimed, to produce several specimens for all the planned tests. The mixtures of the powders were chosen as:

- 97.5 wt% maraging steel MS1 and 2.5 wt% vanadium carbide VC-2.5, in the further course referred to as $MS1_{97.5}/VC_{2.5}$
- 95 wt% maraging steel MS1 and 5 wt% vanadium carbide VC-2.5, in the further course referred to as $MS1_{95}/VC_{5}$
- 92.5 wt% maraging steel MS1 and 7.5 wt% vanadium carbide VC-2.5, in the further course referred to as $MS1_{92.5}/VC_{7.5}$
- 90 wt% maraging steel MS1 and 10 wt% vanadium carbide VC-2.5, in the further course referred to as $MS1_{90}/VC_{10}$

7.2 Experimental Procedures

7.2.1 Powder Preparation

In this study, maraging steel (MS1, EOS GmbH, Germany) was used as the matrix material and the reinforcing component was vanadium carbide (Treibacher Industrie AG, Austria). The MS1 powder had a particle size distribution between 15 microns and 40 microns. To improve the relative part density, fine VC powder with a particle size under 2.5 microns was chosen. It has to be mentioned that there were VC particles found in the bulk powder, which had a size of about 10 microns, even though the manufacturers data sheet stated a maximum of 2.5 μm. The chemical composition of the MS1 powder can be found in Table 4.1. The VC powder was a mixture of mostly V_8C_7, as this composition is the most stable form VC can crystallize in [29], with some amounts of V_2C, V_6C_5 and stoichiometric VC. The two different powders were mixed accordingly (i.e. $MS1_{97.5}/VC_{2.5}$, $MS1_{95}/VC_5$, $MS1_{92.5}/VC_{7.5}$ and $MS1_{90}/VC_{10}$) in a Turbula shaker mixer (Willy A. Bachofen AG, Switzerland). Each batch was mixed for 15 min and the powder morphology of the initial VC powder can be found in Figure 4.8a and b.

7.2.2 SLM Process and Post-processing

To SLM process the different powders, a Farsoon FS121M (Farsoon Technologies, China) was used. The 200 W fibre laser with a spot diameter of 55 μm was used to melt the powders under an argon atmosphere. All produced samples were printed on a steel substrate, which was mounted and levelled on the building platform. An automatic powder spreading system applied the various MS1/VC composite materials uniformly on the substrate with a layer thickness of 40 μm. The SLM process was controlled by the Farsoon Build Manager software. For the SLM process, the same parameters as in the design of experiments in Chapter 6 were used and can be found in Table 6.2. An alternating hatch pattern, which rotated 90 ° after each layer, was chosen.

In the first step, the optimal parameters had to be found for each composite mixture, which is why cubic specimens with dimensions of 10 mm x 10 mm x 10 mm were fabricated via SLM. Afterwards, ultimate tensile strength specimens according ASTM E8 for powder metallurgical applications, hot ultimate tensile strength specimens and charpy impact specimens were produced. Some of these samples were heat treated at 490 ° C for 6 hours and cooled down at room temperature in standard air environment.

7.2.3 Microstructural Observation and Density

The cubic samples were cut and mounted in resin (Struers CitoPress-15, Struers Inc., USA). Afterwards, the samples were polished (Struers Tegramin, Struers Inc., USA) to analyze the microstructure and the density. For the analysis, an optical microscope (Leica Aristomet, Leica Microsystems GmbH, Germany) was used. The computer controlled microscope was capable of calculating the relative density of the cross-sectioned surface areas using image analysis algorithms in the dedicated software (Leica Application Suite, Leica Microsystems, Germany).

7.2.4 Microhardness

For the microhardness tests, the cubic specimens were used. A microhardness tester (Karl Frank GmbH, Germany), calibrated for Vickers hardness, was used and appertaining software calculated the respective values using the diagonals of the indent. The microhardness tests were performed according to HV1 standards with a load of 9.8 N.

7.2.5 Ultimate Tensile Strength

Samples according to the ASTM E8 standard with an overall length of 75 mm and a diameter at the center of the reduced parallel section of 4.75 mm. The samples were used as-built and not polished or post-processed in a lathe. However, some samples were heat-treated. All samples were tested in a Zwick / Roell Zmart.Pro (ZwickRoell AG, Germany) tensometer, which was equipped with extensometers for length measurements during the testing cycle. The surface of the fracture planes of some of the samples were furthermore analyzed with an Olympus SZX10 (Olympus Corporation, Japan) stereo microscope.

7.2.6 Hot Ultimate Tensile Strength

For further material analysis under harsh environments, special designed tensile strength specimens were produced via SLM. The samples were specifically made for the tensometer used. In this case, a Gleeble 3800 (Dynamic Systems Inc., USA) tensometer was used and the testing temperature was set to 450 ° C.

7.2.7 Charpy Impact Toughness

The Charpy impact test was performed with samples manufactured according to the ASTM A370 / ISO 148. The specimens had a standard V-notch and a dimension of 10 mm x 10 mm x 55 mm.

7.3 Results and Discussion

7.3.1 Microstructural Characterization and Density

In Table 7.1 all SLM manufactured samples are given with their respective mean relative densities and SLM parameters. The table includes all values for $MS1_{97.5}/VC_{2.5}$, $MS1_{95}/VC_{5}$, $MS1_{92.5}/VC_{7.5}$ and $MS1_{90}/VC_{10}$, whereas the $MS1_{90}/VC_{10}$ results were already presented in Section 6.3.5.

Table 7.1: SLM parameters and mean measured relative densities of MS1 with 2.5, 5, 7.5 and 10 % of VC.

Spec. Nr.	**Laser Power** [W]	**Scan Speed** [mm/s]	**Hatch** [μm]	**Energy D.** [J/mm^3]	**Rel D. VC$_{2.5}$** [%]	**Rel. D. VC$_{5}$** [%]	**Rel. D. VC$_{7.5}$** [%]	**Rel. D. VC$_{10}$** [%]
1	180	448	80	125.56	99.16	98.75	98.16	97.11
2	185	448	80	129.05	99.66	98.82	98.70	97.82
3	200	448	80	139.51	99.99	98.86	98.64	97.73
4	180	544	80	103.40	99.67	98.35	97.88	96.89
5	200	544	80	114.89	99.72	98.43	97.95	97.72
6	200	736	80	84.92	99.54	92.09	92.39	97.93
7	180	832	80	67.61	99.98	79.30	91.66	97.69
8	185	832	80	69.49	99.64	84.02	93.71	97.14
9	200	832	80	75.12	99.93	88.17	93.55	98.02
10	190	640	110	67.47	99.67	97.81	98.03	95.65
11	180	448	130	77.27	99.90	98.75	98.04	97.67
12	200	448	130	85.85	99.97	98.32	98.85	97.89
13	180	832	130	41.61	99.51	82.57	93.93	97.78
14	200	832	130	46.23	98.96	90.95	97.94	95.76
15	180	448	140	71.75	99.93	98.40	98.11	97.09
16	200	448	140	79.72	99.59	98.73	98.63	96.77
17	180	544	140	59.09	99.97	97.74	98.09	96.90
18	200	544	140	65.65	99.67	98.90	98.78	97.70
19	180	832	140	38.63	98.89	94.38	98.11	97.62
20	200	832	140	42.93	99.94	70.43	88.59	97.42

Obviously, the amount of VC had a huge impact on the part density. As the amount of VC was increased, a lower relative density was achieved after SLM processing. The micrographs of the polished surfaces of the SLM processed micro- / nanocomposites revealed the tendency for more defects, if there was a higher amount of vanadium carbide in the material. At a comparably low amount of reinforcing VC content, the polished surfaces were almost free of defects. Only a few minor micro porosities were found. While comparing the sample with the lowest energy density (i.e. specimen nr. 19) and the sample with the highest energy density (i.e. specimen nr. 3), it was found that the small VC particles were more likely to be molten and that particle-particle metallurgical bonding occurred, as there were less unmolten particles found in samples nr. 3. This result also suggests that the laser beam provided a sufficiently high energy density to possess a stable molten pool. Defects with less than 100 μm are probably associated with similar casting defects, like shrinkage or inclusions of gas within the melt pool. Gas can furthermore be trapped during the mechanical mixing process in which some particles are consolidated [12].

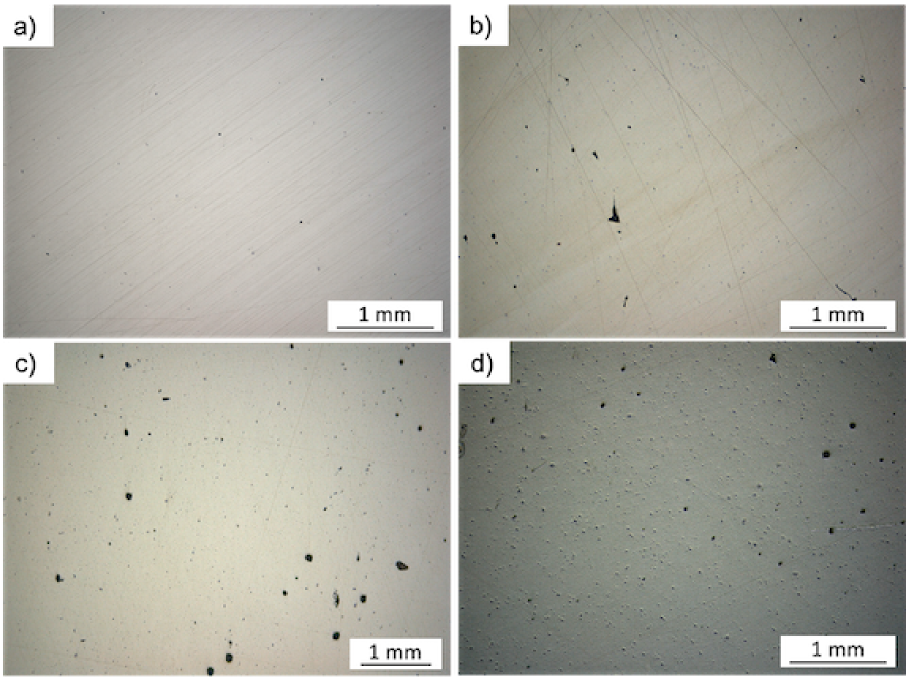

Figure 7.1: Micrographs of the SLM processed metal matrix composite material with a) 2.5 %, b) 5 %, c) 7.5 % and d) 10 % of VC.

However, as the amount of the reinforcing composite material was increased, more porosities were observed in the SLM processed material. In Figure 7.1 micrographs of the $MS1_{97.5}/VC_{2.5}$, $MS1_{95}/VC_5$, $MS1_{92.5}/VC_{7.5}$ and $MS1_{90}/VC_{10}$ SLM processed composite materials are shown. It is clearly visible that the relative density decreased. The formation of these defects can be attributed to rapid solidification of the molten material without a complete filling of all the gaps in the melt pool [221, 222]. Due to the contrasting melting temperatures and the dissimilar thermal heat conductivities of VC and MS1, non-linear solidification with regions of different melting and solidification behaviours can occur. This leads to instable melt pools and results in part defects. As the reinforcing component is increased, the surface tension and Marangoni flow gradient increase. As a result, the melt pool becomes more and more unstable and droplets can form, which splash from the liquid melt pool front, due to the decrease in the surface energy. When the direction of the liquid flow changes from outward to inward, the liquid molten material flows from the periphery to the melt pool center [12, 70]. As the liquid flows radically to the center and therefore, close to the laser beam, the liquified material is forced to spheroidize. The tendency for the formation of pores is increased, because of this flow inversion. Thereby, the melt pool has a high instability and chances for an occurrence of the balling effect is more likely. During this situation, the surface tension and the viscosity of the melt pool are relatively large causing disordered heterogeneous heat and mass transfers.

A comparison of the same energy densities and the resulting relative densities showed that the porosity was lower for the MS1/VC composite materials with lower amounts of reinforcing VC. This indicates the higher risk for interruptions during SLM processing, while introducing more vanadium carbide particles into the melt pool. It was also discovered that composites with a higher content of VC had a higher tendency for spatters, which resulted from an increased balling effect occurrence.

In Figure 7.2 all SLM manufactured samples of the $MS1_{97.5}/VC_{2.5}$ are shown. Figure 7.3 shows the $MS1_{95}/VC_5$ samples, Figure 7.4 gives an overview of the $MS1_{92.5}/VC_{7.5}$ samples and the samples obtained with the $MS1_{90}/VC_{10}$ composite material can be found in Figure 7.5.

7.3.2 Analysis of Density

To predict the best values for further specimen production, R Studio was used. Based on a model using the Federov operator and the obtained relative densities, a theoretical maximum was calculated. For all calculation models, the energy density was calculated and the obtained results set in correlation. The prediction was done for 190 W laser power and can be found in Figure 7.6. In Figure 7.6a the prediction for 2.5 % of VC is found. According to the model, a wide range of parameters are suitable for the material and even the green zone indicates a very high relative density. Interestingly, the highest density (i.e. shown as white zone) is at approximately 750 mm/s scan speed and 130 microns hatch distance. However, the red dot which should indicate the highest value point is barely visible and almost out of the diagram. This indicates that not just one parameter set would lead to the highest relative density. Figure 7.6b shows the diagram for 5 % of reinforcing content and has a trend towards slower scanning speeds and a high hatch distance. The theoretical maximum was found to be at 510 mm/s scan speed and 127 microns hatch distance. In Figure 7.6c the diagram for the prediction of the mixture with 7.5 percent of VC can be found and in 7.6d the prediction for 10 % VC content is shown. Both mixtures have a theoretical density maximum similar to the 5 % mixture.

7.3.3 Microhardness

In Figure 7.7 an overview is given for all SLM processed samples and their according microhardness values. The graph is sorted by energy density in ascending order. One could assume that there is no clear trend or a correlation between the different results. However, if the results are compared to the achieved relative density of the samples, the results can be better understood. For this, Figure 7.8 is given. Obviously, the $MS1_{97.5}/VC_{2.5}$ samples had a higher microhardness due to their comparably high relative density, resulting in a better resistance against the indenting pyramid of the Vickers hardness tester. The samples with 5 % of VC were weaker than the samples with only 2.5 % of vanadium carbide. This can be explained due to a higher porosity in the material, as can be seen in Figure 7.8. However, when even more reinforcing particles were added to the composite material, the hardness values increased again. It is assumed that, even though the relative density was lower in the $MS1_{92.5}/VC_{7.5}$ samples compared to the $MS1_{97.5}/VC_{2.5}$ specimens, there were sufficient VC particles in the solid part, to act against the indenter and to hinder dislocation movements in the crystalline structure. This effect is even higher, if 10 % of reinforcing VC is added to the MMC.

The highest achieved hardness in the $MS1_{97.5}/VC_{2.5}$ samples was found in specimen nr. 2, which had 423 HV, but the highest mean values was found to be in specimen nr. 18 with 405 HV. In the $MS1_{95}/VC_{5}$ specimens, which had an overall very weak density, the peak value and the highest mean values was found in specimen nr. 10. The values were 319 HV for the peak value and 300 HV for the mean value. $MS1_{92.5}/VC_{7.5}$ had the maximum peak value at 377 HV and the highest mean value at 355. Both values were measured in specimen nr. 19. Specimen nr. 11 was the best performing in the $MS1_{90}/VC_{10}$ with values of 597 maximum and 544 HV mean value. The statistical data for the micro-hardness measurements is provided in Table 7.2. In the table R is the range, V is the variance and SD is the standard deviation.

7.3.4 Charpy Impact Strength

In Figure 7.9 the results of the Charpy impact strength tests are shown. Unfortunately, the absorbed energy was relatively low and there was barely necking observed. It can be concluded that the material was very brittle, which is mostly due to binding errors.

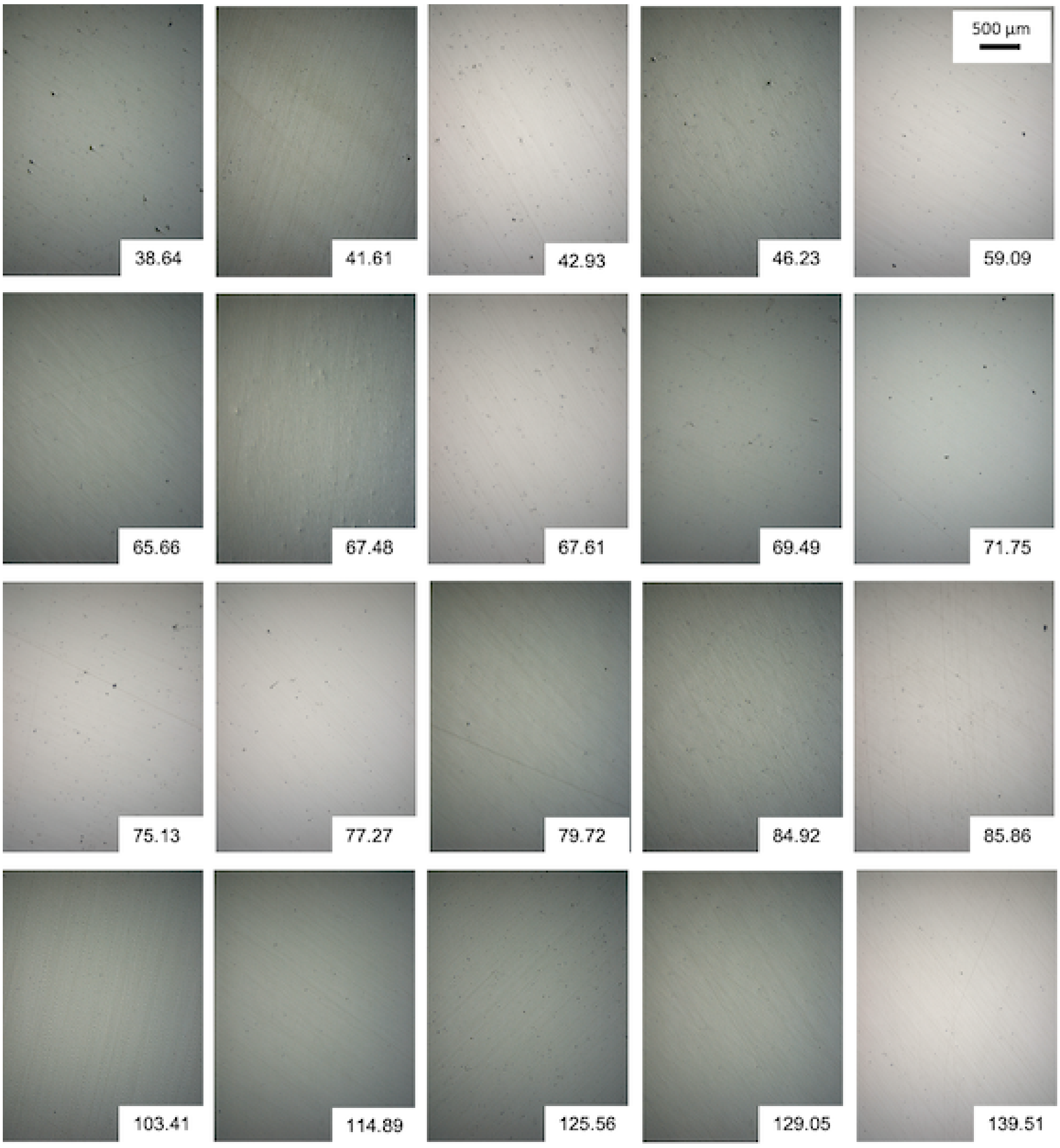

Figure 7.2: Micrographs of all SLM processed MS1VC samples with 2.5 % of VC.

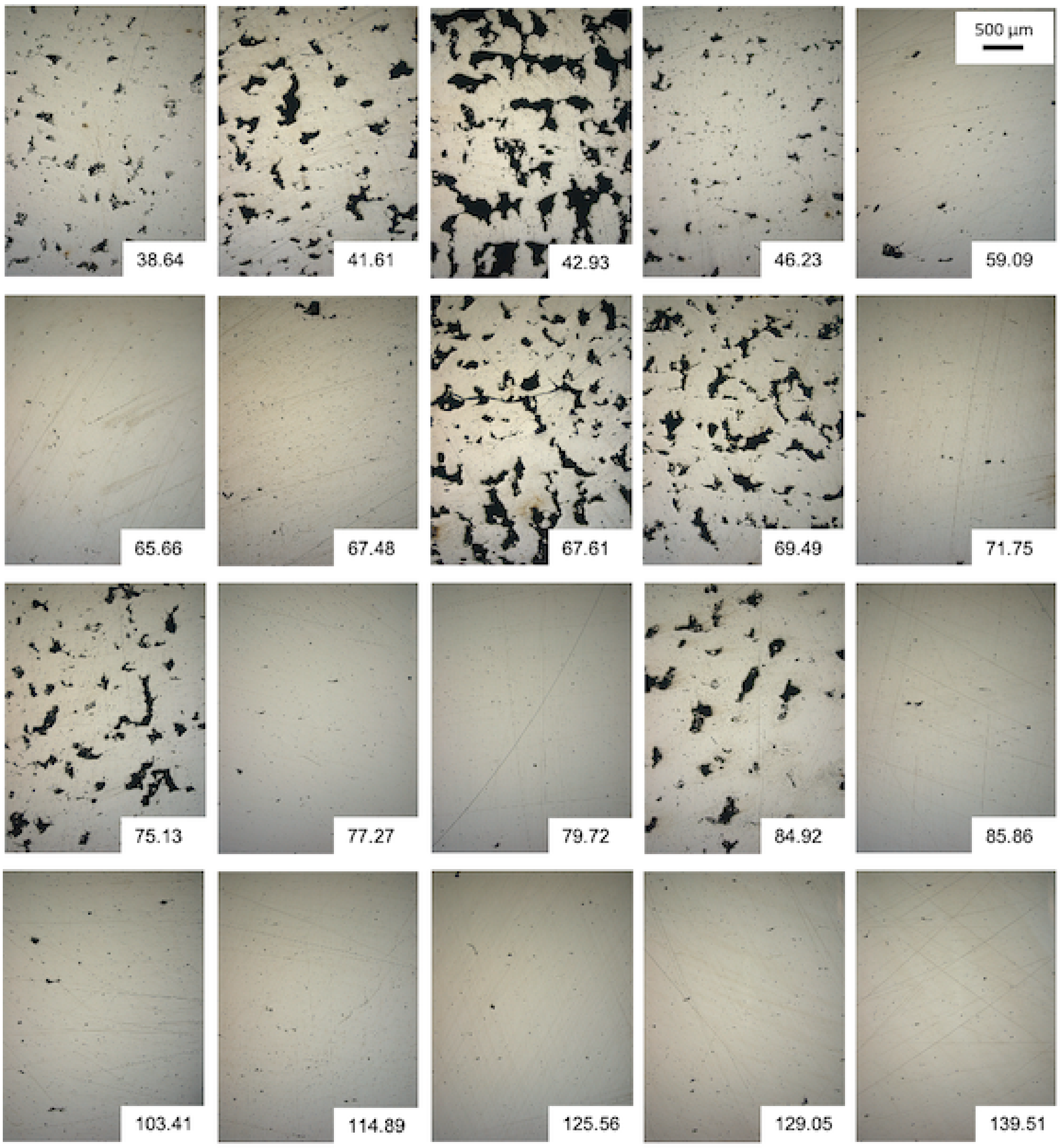

Figure 7.3: Micrographs of all SLM processed MS1VC samples with 5 % of VC.

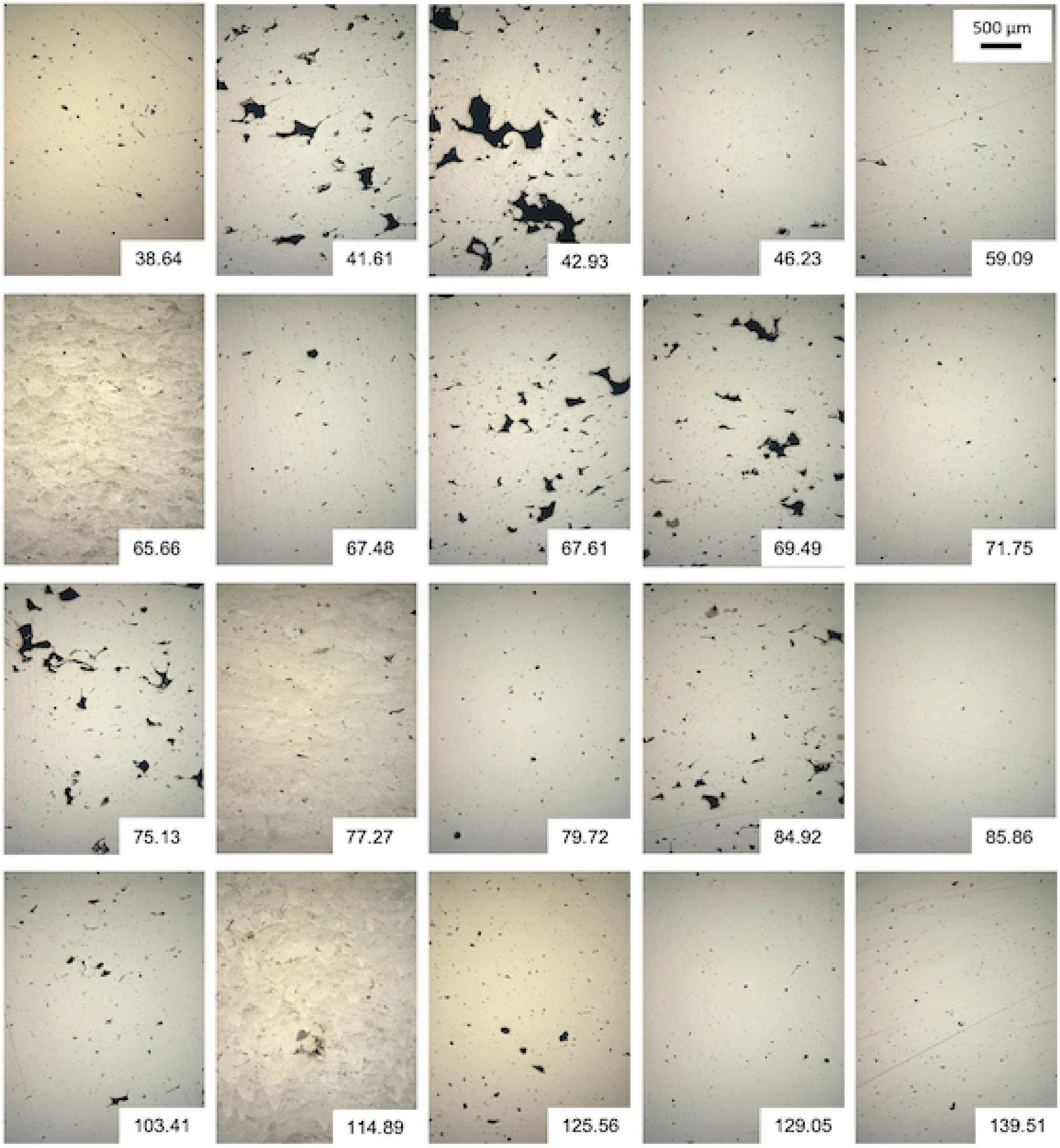

Figure 7.4: Micrographs of all SLM processed MS1VC samples with 7.5 % of VC.

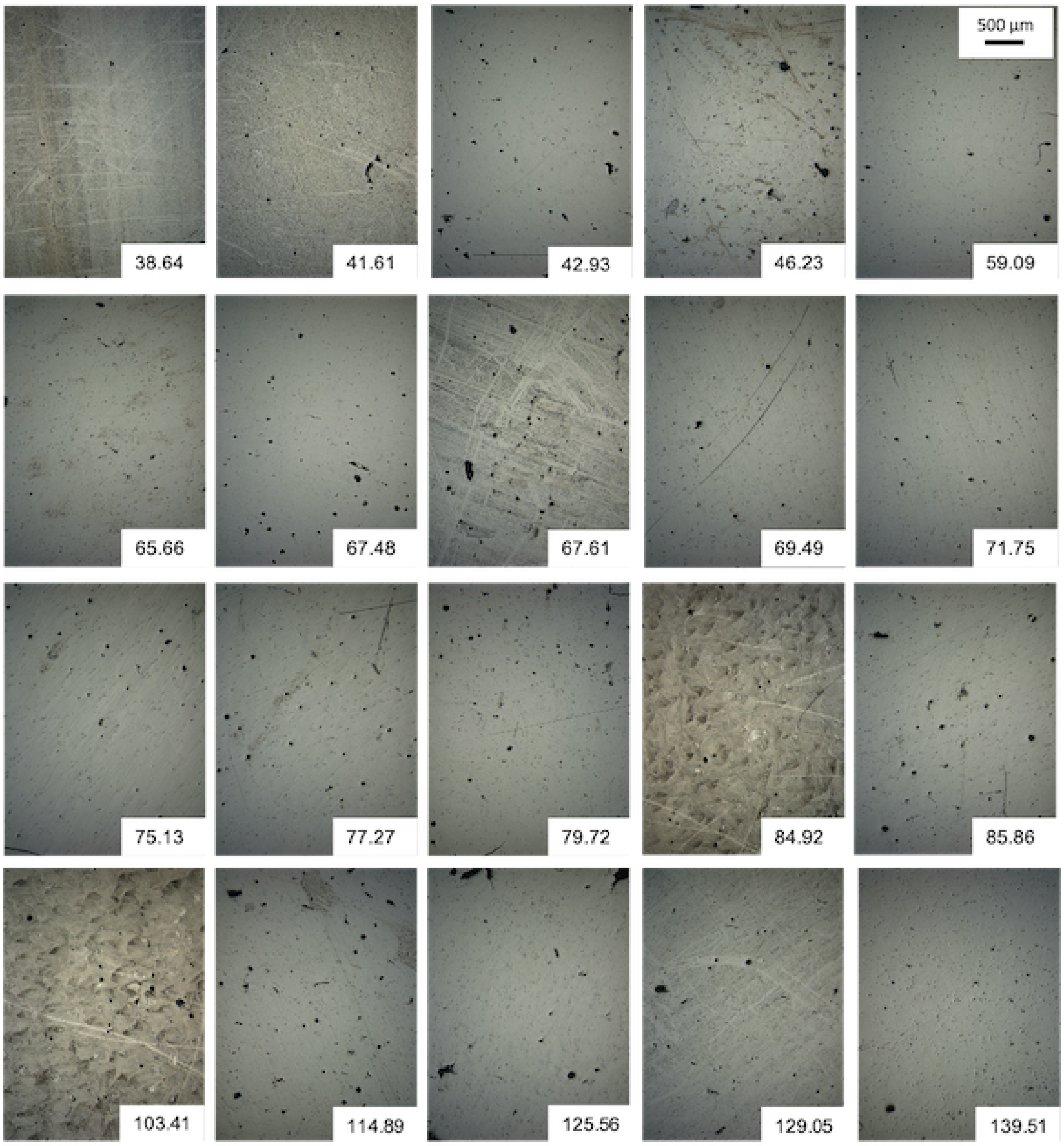

Figure 7.5: Micrographs of all SLM processed MS1VC samples with 10 % of VC.

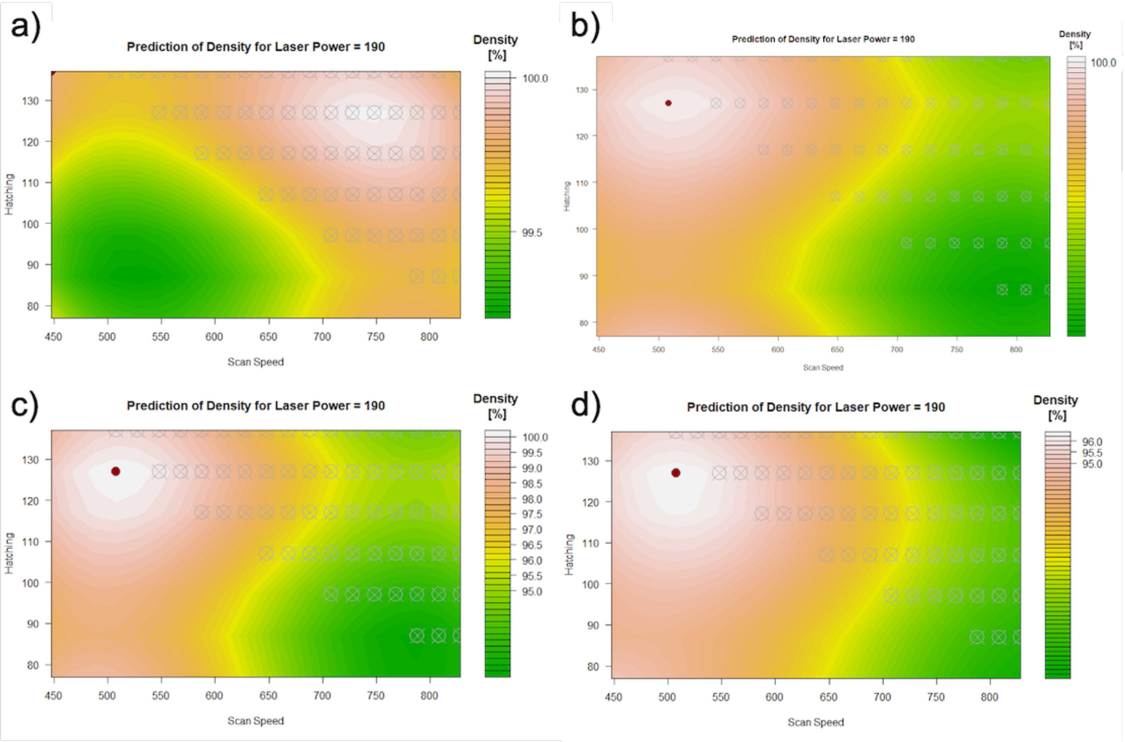

Figure 7.6: Prediction of the optimal relative density for MS1VC with 33 μm particles with a) 2.5 %, b) 5 %, c) 7.5 % and d) 10 % of reinforcing particles.

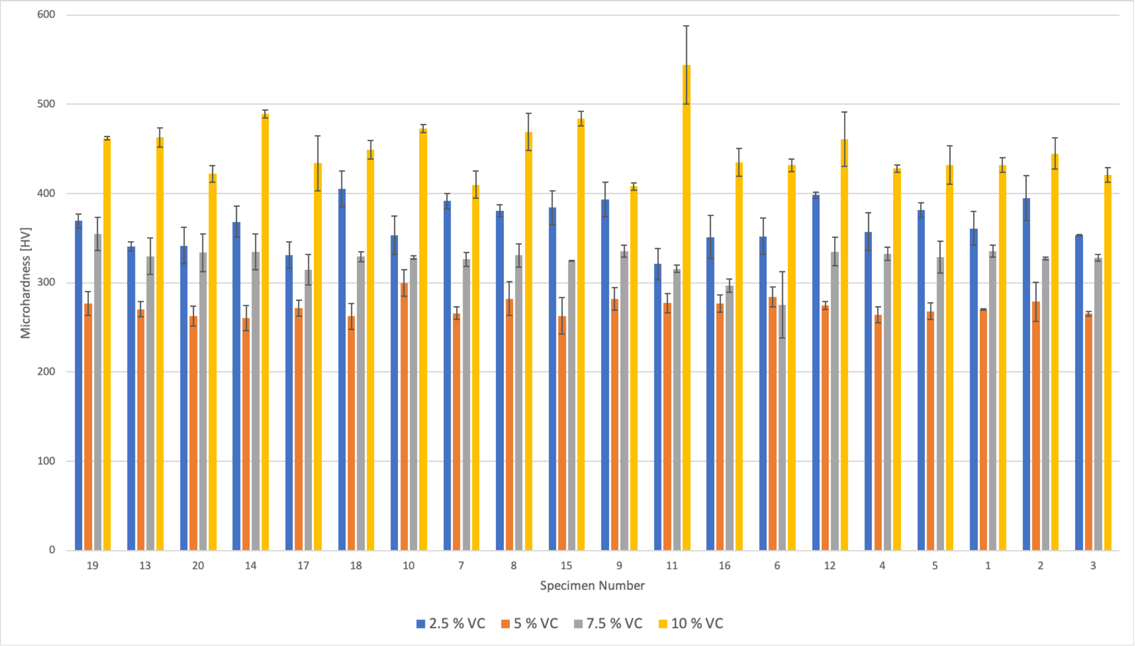

Figure 7.7: Vickers microhardness values of the SLM processed metal matrix composite material with 2.5 %, 5 %, 7.5 % and 10 % of VC.

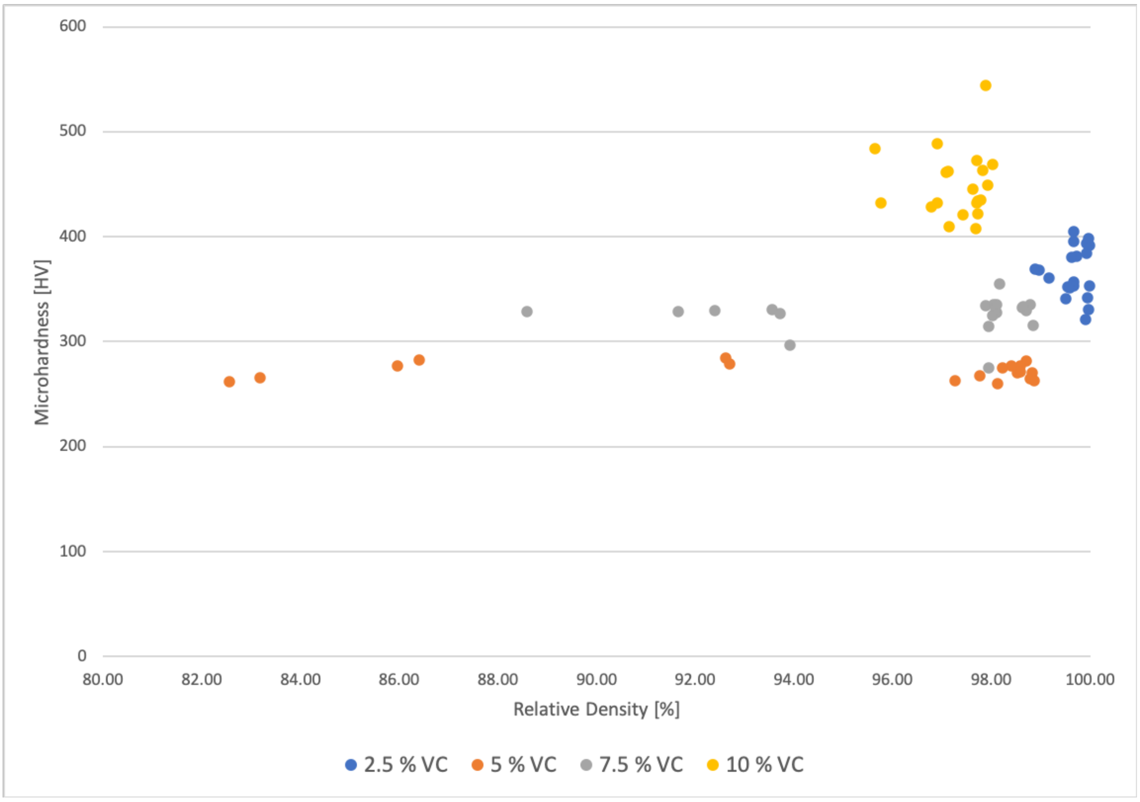

Figure 7.8: Vickers microhardness values and relative density of the 2.5 %, 5 %, 7.5 % and 10 % VC samples.

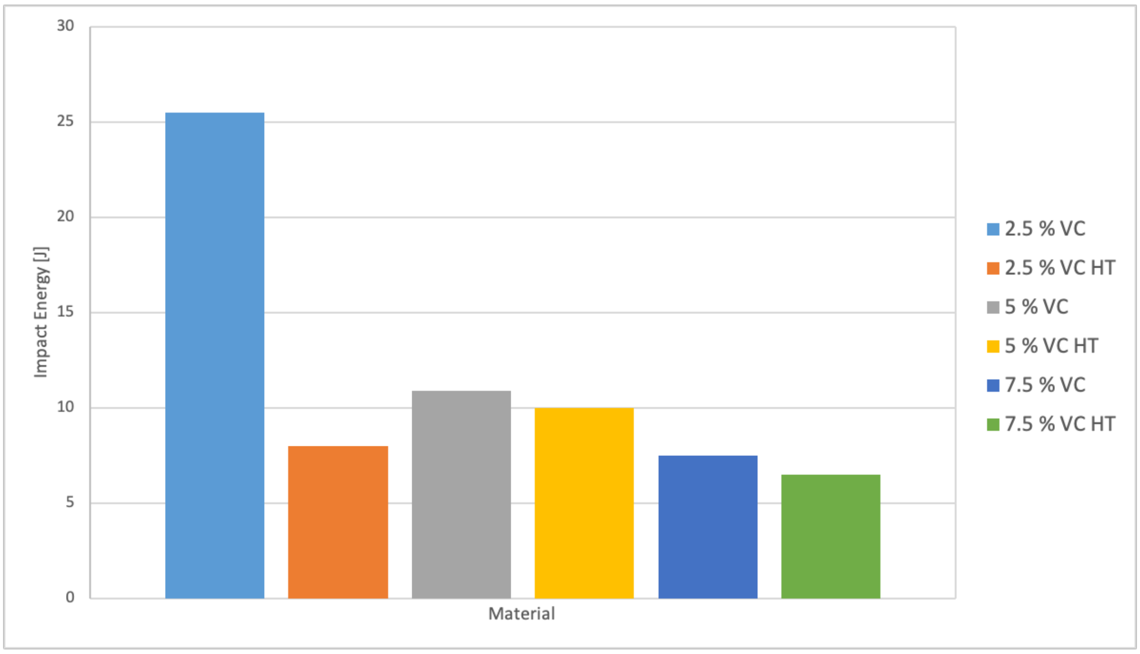

Figure 7.9: Charpy impact strength values of the 2.5 %, 5 % and 7.5 % VC samples with and without heat treatment (HT).

Table 7.2: Statistical information for micro-hardness measurements of the MS1 samples with 2.5 %, 5 %, 7.5 % and 10 % VC.

Spec. Nr.	**R 2.5 %**	**V** σ^2 **2.5 %**	**SD** σ **2.5 %**	**R 5 %**	**V** σ^2 **5 %**	**SD** σ **5 %**	**R 7.5 %**	**V** σ^2 **7.5 %**	**SD** σ **7.5 %**	**R 10 %**	**V** σ^2 **10 %**	**SD** σ **10 %**
19	17	57.56	7.59	32	184.89	13.6	46	353.56	18.8	5	4.33	2.08
13	13	30.89	5.56	21	74.89	8.65	47	421.56	20.53	26	113	10.63
20	46	409.56	20.24	27	121.56	11.03	50	443.56	21.06	20	84.67	9.2
14	40	304.22	17.44	34	193.56	13.91	47	402.89	20.07	11	20.67	4.55
17	35	228.67	15.12	21	76.22	8.73	42	299.56	17.31	68	945	30.74
18	43	401.56	20.04	32	208.22	14.43	13	29.56	5.44	25	113.67	10.66
10	50	473.56	21.76	36	218	14.76	4	2.89	1.7	10	18.67	4.32
7	19	76.22	8.73	17	48.67	6.98	19	62.89	7.93	35	239	15.46
8	17	48.22	6.94	42	358.22	18.93	32	176.22	13.27	50	434.67	20.85
15	45	353.56	18.8	49	404.67	20.12	1	0.22	0.47	18	65	8.06
9	47	374.89	19.36	28	162.67	12.75	15	44.22	6.65	10	17	4.12
11	42	296	17.2	23	117.56	10.84	9	16.22	4.03	107	1908.67	43.69
16	53	590.89	24.31	22	91.56	9.57	17	52.67	7.26	37	232.67	15.25
6	45	422	20.54	27	128.22	11.32	86	1382.89	37.19	17	49.67	7.05
12	7	10.89	3.3	10	17.56	4.19	39	258	16.06	75	938	30.63
4	52	461.56	21.48	21	80.22	8.96	16	53.56	7.32	10	17.67	4.2
5	17	64.22	8.01	20	84.67	9.2	44	322.89	17.97	48	456	21.35
1	43	368.67	19.2	2	0.67	0.82	15	44.22	6.65	19	67	8.19
2	61	632.67	25.15	52	464.89	21.56	4	2.89	1.7	41	292.67	17.11
3	1	0.22	0.47	6	6.22	2.49	8	14.22	3.77	18	65	8.06

7.3.5 Ultimate Tensile Strength

Figure 7.10 shows a diagram of all manufactured ultimate tensile strength specimens after testing. It was expected to achieve slightly lower results than standard MS1 can achieve, as the hard composite particles can act as a starting point for cracks. However, the results were surprising. Standard MS1 in an as-built condition has an ultimate tensile strength of approximately 1100 MPa +/- 100 MPa, if the sample was built in Z direction. The MS1$_{97.5}$/VC$_{2.5}$ composite material without heat treatment was right in the range of the manufacturers given values for MS1 without reinforcing particles. The manufactured specimens with 2.5 % of VC in this study had an astonishing ultimate tensile strength of 1311 MPa in the untreated state and 1861 MPa in the heat treated state. The elongation at fracture on the other hand decreased from 5.2 % of the untreated specimen to only 0.93 % of the heat treated one. These results were promising and it was expected to achieve similar, but slightly lower results for the samples with higher amounts of vanadium carbide. Unfortunately, the higher the amount of VC, the worse the ultimate tensile strength was. MS1$_{95}$/VC$_{5}$ achieved 733 MPa without heat treatment and with a 6 hour heat treatment the maximum stress was measured at 807 MPa. The elongation at break was measured at 2.83 % and 1.63 % respectively. The results of the MS1$_{92.5}$/VC$_{7.5}$ samples were devastating. The material was extremely brittle and it was impossible to measure any kind of elongation. The ultimate tensile strength was measured at 138 MPa in an untreated state and at 171 MPa for the heat treated sample. There were no samples built with 10 % of VC, because the print jobs always stopped after a couple of cm. It was possible to manufacture cubes for density tests, but the higher the specimens became, the more likely errors occurred in the MS1$_{90}$/VC$_{10}$ samples. The more VC content was used, the rougher the surface of the specimens was.

7.3.6 Hot Ultimate Tensile Strength

As maraging steel is especially interesting for high temperature applications, the ultimate tensile strength at an environment of 450 ° C was measured. However, just as the results under room temperature were not as good as desired, also the results in a hot temperature environment were not very positive. In Figure 7.11 the graph of the hot ultimate tensile strength tests are given. It includes all samples with 2.5 % VC, 5 % VC and 7.5 % VC, each as-built or furnace annealed (FA). It can be seen that the VC content influenced the stress resistance again and the heat treatment had a negative influence on the ultimate tensile strength. As mentioned, standard MS1 has a

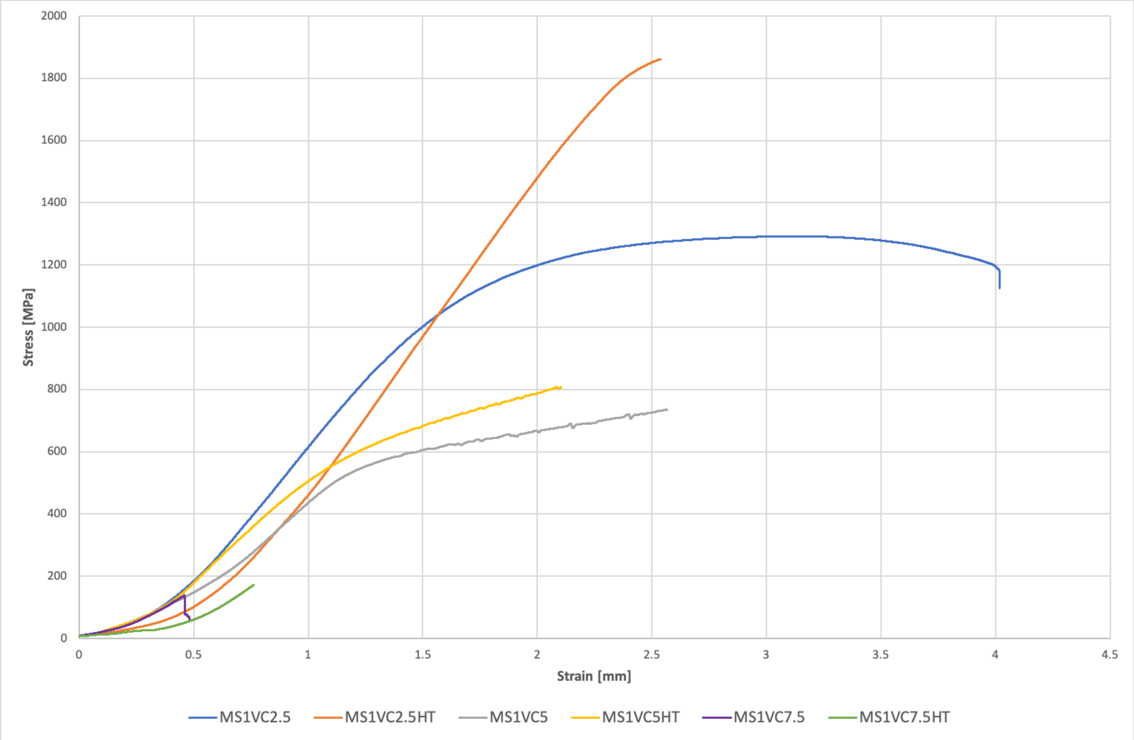

Figure 7.10: Ultimate tensile strength graphs of the as-built and heat treated samples with 2.5 %, 5 % and 7.5 % VC.

tensile strength of about 1100 MPa +/- 100 MPa. The particle reinforced $MS1_{97.5}/VC_{2.5}$ had a tensile strength of 1029 MPa in an environment of 450 ° C, which is a very good value. Because of the introduction of composite particles into the matrix, which can act as a starting point for cracks, it was expected to get a slightly lower tensile strength. The heat treated sample however, failed after 598.9 N/mm^2 of stress. The results of all samples are:

- $MS1_{97.5}/VC_{2.5}$ as-built: $R_{m_{450^\circ C}} = 1029$ MPa
- $MS1_{97.5}/VC_{2.5}$ heat treated: $R_{m_{450^\circ C}} = 598.9$ MPa
- $MS1_{95}/VC_{5}$ as-built: $R_{m_{450^\circ C}} = 816.09$ MPa
- $MS1_{95}/VC_{5}$ heat treated: $R_{m_{450^\circ C}} = 781.21$ MPa
- $MS1_{92.5}/VC_{7.5}$ as-built: $R_{m_{450^\circ C}} = 311.75$ MPa
- $MS1_{92.5}/VC_{7.5}$ heat treated: $R_{m_{450^\circ C}} = 321.76$ MPa

The powder manufacturer EOS claims that an age hardening at 490 ° C for 6 hours should improve the tensile strength to 2050 +/- 100 MPa with standard MS1 powder and therefore, should be higher than in an as-built state. However, the samples in this study failed at lower stress levels than their as-built counterparts. It was also discovered that the VC content decreased the tensile strength.

7.3.7 Analysis of Fracture Plane

To better understand the cause of the low stress resistance of the printed specimens, a light microscope and a scanning electron microscope was used to analyze the plane of fracture. In Figure 7.12

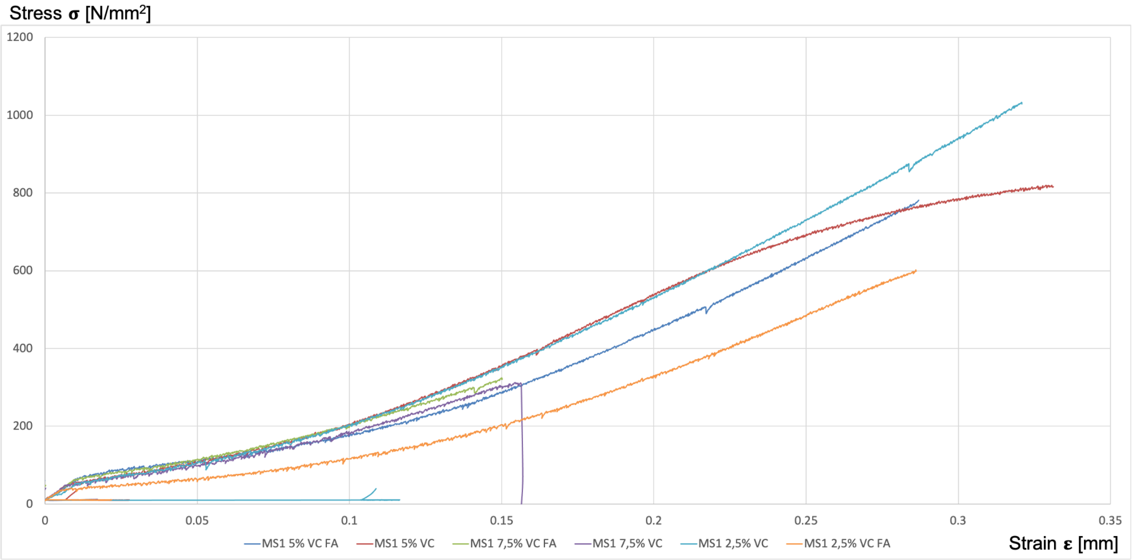

Figure 7.11: Hot ultimate tensile strength graphs of the as-built and heat treated samples with 2.5 %, 5 % and 7.5 % VC under 450 ° C environment.

the fracture planes of two heat treated specimens with 7.12a 2.5 % and 7.12b 5 % of reinforcing VC are shown. The $MS1_{97.5}/VC_{2.5}$ specimen had a higher elongation at fracture and showed some necking, but the $MS1_{95}/VC_5$ specimen did not show any elongation and the fracture can be classified as a brittle fracture. Obviously, something must have interfered the welding process. The light microscope revealed some spatters which indicated an unstable melt pool causing a balling effect. However, the spatters were not the only reason for the early fracture. To better understand the cause of the failure, Figure 7.13 is provided. It shows the heat treated $MS1_{95}/VC_5$ sample under a scanning electron microscope. Figure 7.13a gives an overview of the fracture starting point and 7.13b shows the same area with a higher magnification, revealing some small spatter particles in the lack of fusion area. Figure 7.13c shows a perfectly spherical spatter particle, which was included into the solid manufactured part. As these spatters are relatively small, they can not be the main reason for the fracture. As a matter of fact, spatters can be a starting point for cracks, but if one compares the size of a spatter particle and the lack of fusion area, it is obvious that the cause of this failure was not a spatter particle. The spatter particle had a size of 5 μm and the lack of fusion area had a diameter of approximately 500 microns. This relatively large area, in which there was some kind of binding error, was the starting point for the material failure. This phenomenon occurred in several samples and as only one layer with such a lack of fusion error is enough to significantly influence and decrease the material properties, it was very likely to happen somewhere in each specimen, as the SLM process caused a high amount of spatters, fumes and uneven layer weldings. Compared to other materials, there was a high formation of metal condensate. The reason for such a large lack of fusion area might be a chain reaction of circumstances. It was observed that the composite material had a tendency to grow faster in some areas in Z direction. Especially the area which was coated first with powder was sometimes growing slightly faster than other areas of each specimen. After some layers this might have lead to insufficient powder coating right behind the hump of solid material. These humps were sometimes broken off of the coater. If this excess material was pushed and coated to a surface, where a part was built, the laser was not able to expose this particle sufficiently, respectively to melt this area due to the big particle and its high melting point. Another reason for insufficient binding is a layer height, which is too high. Right behind the fast growing humps, there were craters as it was impossible to coat powder to these areas. After the hump was broken off, the coater was finally able to coat these spots with bulk powder again. However, the layer height in these craters were way too high

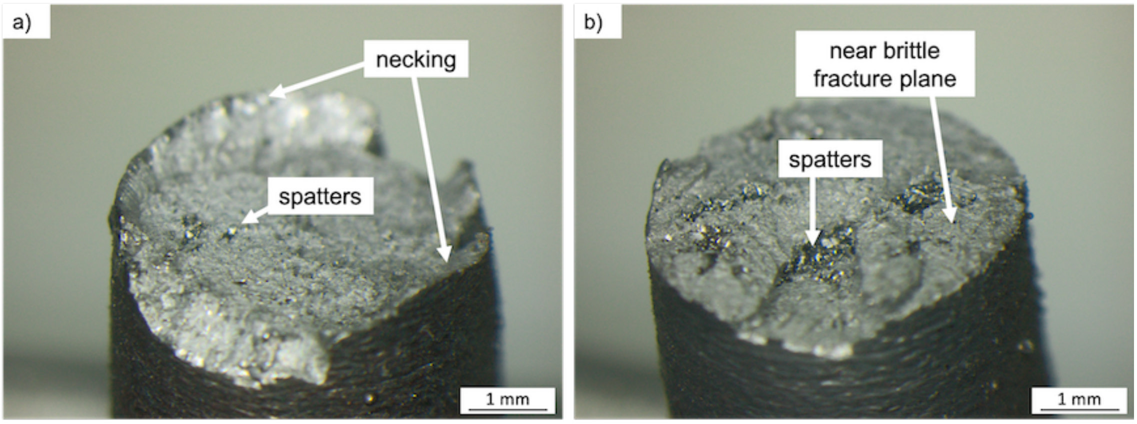

Figure 7.12: Heat treated ultimate tensile strength specimens with a) 2.5 % and b) 5 % VC under a light microscope showing a necking (2.5 % VC) and a brittle fracture (5 % VC) phenomenon.

for a perfect welding process, causing imperfect layer binding to the previous layer. In Figure 7.13d an agglomeration of VC can be seen. Due to the irregular shape of the VC particles, the powder had a high tendency to form agglomerations. Some of them were growing relatively large and it was impossible to prevent this behaviour. It can just be approximated of how large the agglomeration was in this figure, but it can be certainly said that they significantly influenced not just the melt pool, due to the considerably higher melting temperature, but also the end results in material properties. These agglomerations were not melted at all and were just bound into the final part.

To fully understand these agglomerations and their elemental composition, EDX was used. The point of analysis was set directly onto the found VC particles. According to the EDX analysis, which can also be found in Figure 7.14, the particles consisted of:

- 10.81 % carbon
- 90.76 % vanadium
- 4.89 % ferrit
- 0.83 % nickel

Obviously, the Fe and Ni contents were artefacts of the surrounding material, but the carbon vanadium composition clearly indicated V_8C_7.

7.3.8 Problems of Sieving

Mechanical mixing of different powders is common technique in the scientific world to fabricate metal matrix composites for SLM applications. Usually, the development of new materials requires intense work including several selective laser melting iterations and repetitions. In each SLM process, spatters occur, solid material humps can break off and a lot of metal condensate forms. To eliminate most of these contaminations, it is advisable to sieve the used powder after each printing process. The mesh of the sieve has to be adjusted according to the used size distribution of the powder. In this study, a 75 micron sieve was the recommended size for the sieving process. It was used in an automated and vibrating Retsch AS 200 sieving tower shaker (Retsch GmbH, Germany). However, it was found that the fine powders were blocking the mesh of the sieve and is was almost impossible to sieve the powders. One solution would be, to mix a new powder batch for each SLM job, which would be a waste of material. Instead, a slightly bigger sieve had to be used. As a result, the sieve had less tendency to get blocked by fine powder agglomerations, but it also resulted in a higher remaining amount of contaminations in the sieved material, causing

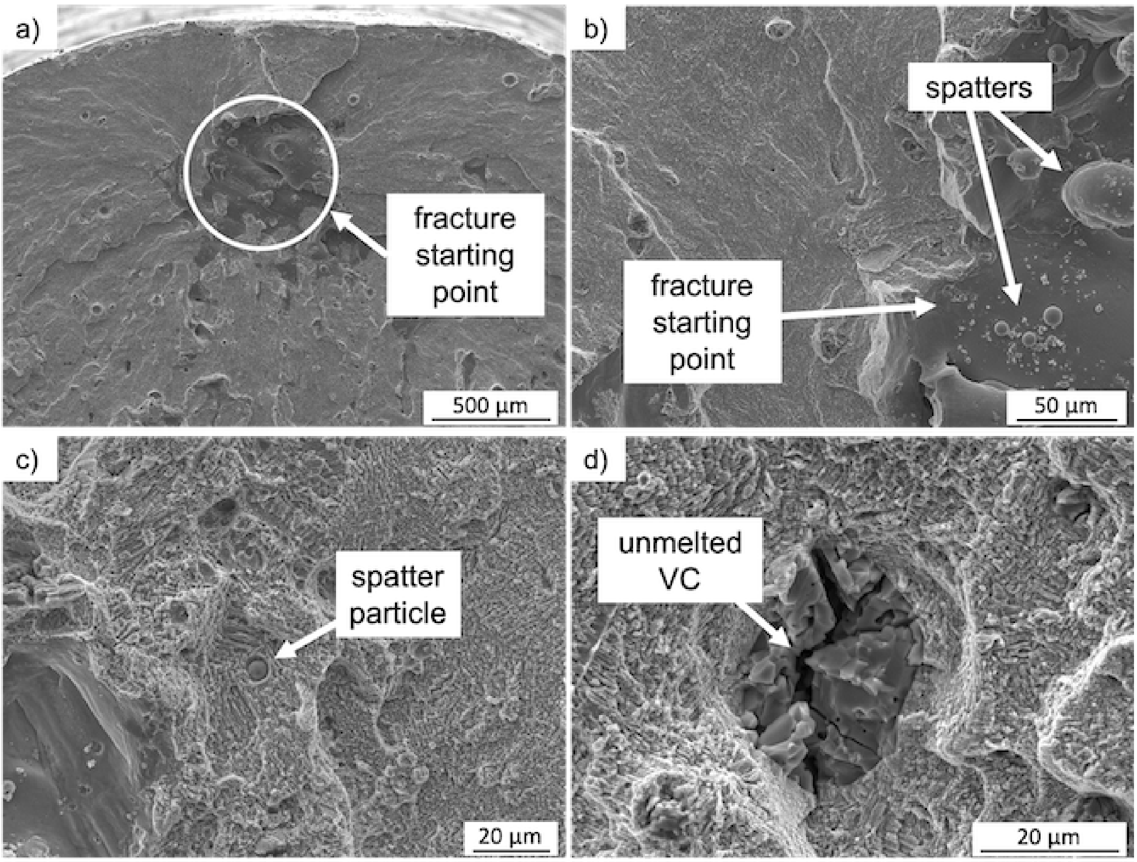

Figure 7.13: Heat treated SLM processed $MS1_{95}/VC_5$ specimen under a SEM showing a) and b) the fracture starting point, c) a spatter particle and d) unmelted VC.

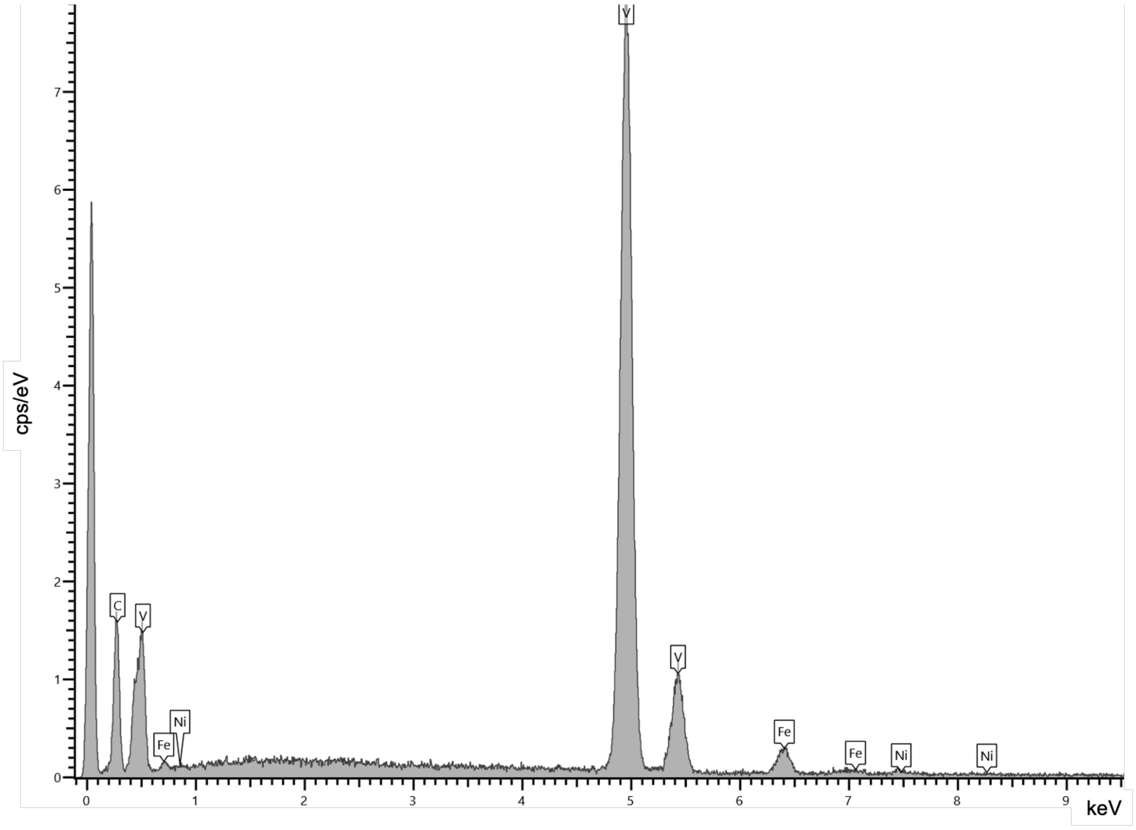

Figure 7.14: EDX spectrum of vanadium carbide found in the fracture plane of the ultimate tensile strength specimen with 5 % of VC.

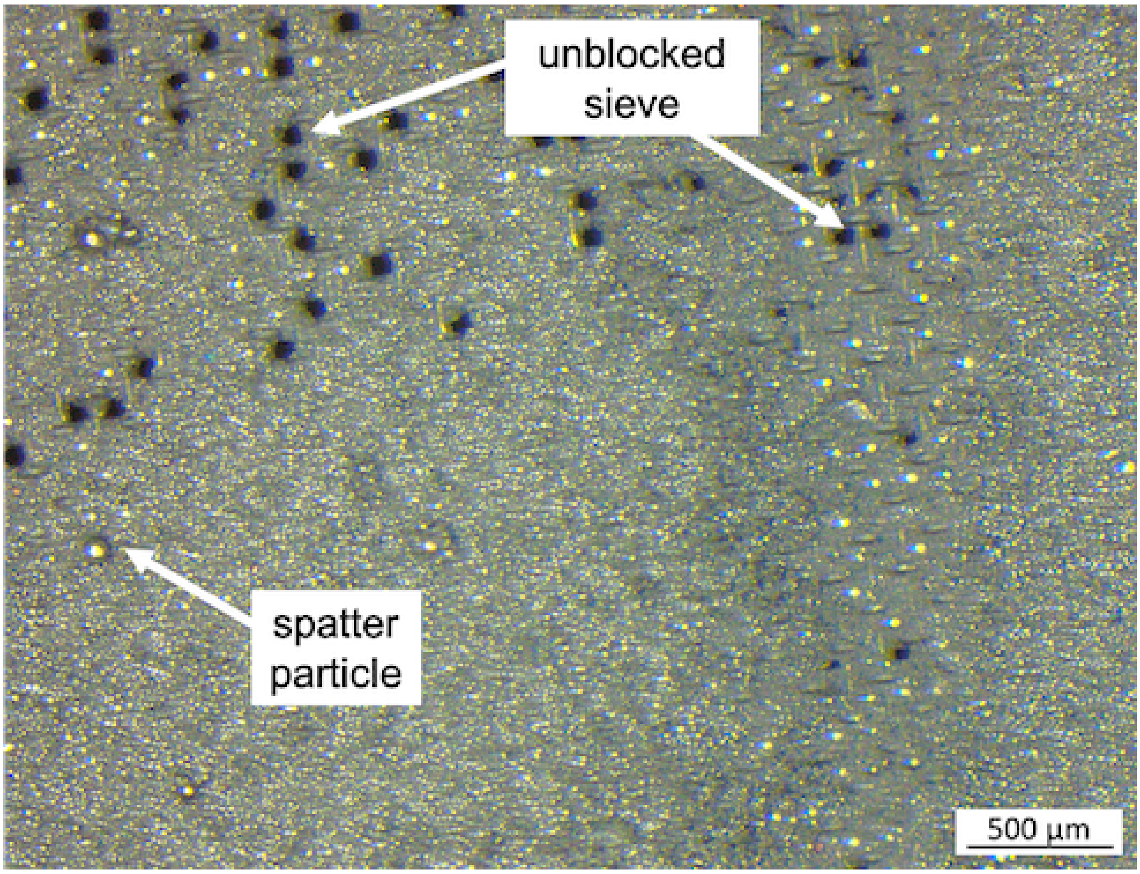

Figure 7.15: Heat treated SLM processed $MS1_{95}/VC_5$ specimen under a SEM showing a) and b) the fracture starting point, c) a spatter particle and d) unmelted VC.

a higher risk of potential errors in the following SLM process. Another significant problem of a blocked sieve is the demixing of the two powder fractions, resulting in an unknown amount of each elemental fraction and furthermore, a heterogeneous powder mixture. In other words, after such a sieving process one can not be sure, which percentage of composite material is left in the bulk powder. In Figure 7.15 the blocked sieve is shown with some spatter particles which would have been sieved out of the powder, but the mesh size was too small resulting in a blocked sieve.

7.4 Conclusions

To understand the influence of different amounts of reinforcing vanadium carbide contents, various mixtures (i.e. 2.5 % of VC, 5 % of VC, 7.5 % of VC and 10 % of VC) were prepared. To find the optimal SLM parameters for each mixture, a design of experiments based on the Federov operator was performed in R-Studio. Cubic samples were SLM processed accordingly and analyzed. Especially samples with low amounts of VC had promising density values. The results of the porosity and the microstructure were used to determine, which parameter set is the most promising to print further specimens. Ultimate tensile strength tests were performed under ambient temperature and under 450 ° C. Unfortunately, all samples with more than 2.5 % VC were devastating. The elongation at break and the ultimate tensile strength were comparably low. Analysis with a light microscope and SEM revealed binding errors. Large lack of fusion zones appeared in the samples, without any logical or comprehensible distribution in the specimens. The reason can be found either in huge agglomerations of VC, large spatter particles or uneven powder coating. However, the microhardness values were very promising and proved the increased achievable hardness in an MS1/VC metal matrix composite, if the porosity can be kept on a low level. The mean values were:

- $MS1_{97.5}/VC_{2.5}$: 405 HV
- $MS1_{95}/VC_{5}$: 300 HV
- $MS1_{92.5}/VC_{7.5}$: 355 HV
- $MS1_{90}/VC_{10}$: 544 HV

The sieving of the SLM processed powder revealed a problem that many researchers obviously ignore. Especially for industrial applications, in which a powder must be used several times, or in every field, which requires repetitions, it is inevitable to re-use powders without any changes in chemical composition. If one uses mixed metal matrix composites with a very small size distribution (mostly for the reinforcing content), the smaller component will likely form agglomerates and will block the sieve. Therefore, the contents of each material will change and it is impossible to determine how much of each component is left in the mixture. To solve this problem, a bigger mesh sieve can be used, which will result in a higher amount of contaminations in the powder. Another approach that arouse great interest in the scientific field is mechanical alloying, which can help creating coalescences of the different components and embed the smaller carbide particles into the bigger spherical maraging steel particles.

8

Selective Laser Melting of Mechanically Alloyed MS1/VC: Influence of Milling Times

> Bring forward what is true, write it so that it is clear, defend it to your last breath.
>
> Ludwig Boltzmann

8.1 Introduction

As observed in preliminary studies, carbides, especially ones with large particle diameters, can significantly affect the melt pool during SLM processing. Furthermore, small irregular shaped particles will cause problems during sieving. To decrease the challenging influence of hard carbide particles, they can be cracked into smaller ones before using them in combination with another metal, like maraging steel. A cost effective way to crack hard particles and to in-situ form coalescences of the metal matrix material and the composite particles, is mechanical alloying. This non-equilibrium powder processing technique is done in high energy ball mills in which different powders can be mixed and, if enough energy is used in the system, alloyed. The great advantage of this technology is not just its cost effectiveness, but also to cold-weld and fracture the particles repeatedly. Therefore, the particles are kept relatively cold and it is possible, to alloy materials without melting them. Some materials would not be combinable under near-ambient temperatures with other technologies like with rapid solidification, due to the far-from-equilibrium condition in a high energy ball mill. Another plus for ball mills, is the fact that they are capable of small batch productions, which is perfectly suitable for metallurgical research applications.

In this chapter, the focus was set to understand the effects of the milling times in a high energy ball mill on maraging steel MS1 and irregular shaped vanadium carbide. It was desired to achieve mechanically alloyed particles respectively coalescences of MS1/VC particles to increase the stability of the melt pool during SLM processing. For SLM applications, it is important to keep a near-spherical shape of the powder, which is why the optimal milling parameters had to be found. The milling time, the ball-to-powder ratio and the energy put into the milling system significantly influences the powder morphology and the homogeneous distribution of the different components in the metal matrix composite. It was furthermore desired, to investigate the behaviour of bigger VC particles after different milling times, to see, if a refinement took place. Afterwards, specimens had to be produced for material property investigations. To find the optimal parameters, a preliminary design of experiments analysis, based on previous results from preliminary studies, was performed. After SLM processing respective tests were performed to analyze the maximum part density, porosities, the microstructure and the microhardness. Due to the presence of vanadium carbide and the fact, that SLM can produce very fine microstructures, astonishing material properties were expected, due to the Hall-Petch grain boundary effects [204]. To give an overview of other researchers work and the state of the art of mechanical alloying in combination with selective laser melting a few scientific articles and their according materials are presented in Table 8.1, in which B/P stands for the ball-to-powder weight ratio.

Table 8.1: Literature overview of ball milled in-situ formed MMCs and alloys fabricated with SLM.

Reference	**Matrix Material**	**Composite Material**	**Time**	**B/P Ratio**	**Disc Speed**	**Density**
Rong et al. [223]	Inconel 718	25 wt.% micro WC	4 h	4:1	200 rpm	97.8 %
Khmyrov et al. [224]	Co	25 wt.% nano WC	2 h	...	200 rpm	> 90 %
Khmyrov et al. [224]	Co	50 wt.% nano WC	2 h	...	200 rpm	> 90 %
AlMangour et al. [185]	316L	2.5 vol.% micro TiB_2	2 - 8 h	5:1	200 rpm	91.5 %
AlMangour et al. [185]	316L	15 vol.% micro TiB_2	2 - 8 h	5:1	200 rpm	91.5 %
Wang et al. [225]	AlSi10Mg	15 wt.% micro TiC	2 - 15 h	10:1	250 rpm	...
AlMangour et al. [226]	316L	15 wt.% nano TiC	8 h	...	...	92.48 %
Han et al. [175]	Al	15 wt.% nano Al_2O_3	4 - 20 h	5:1	350 rpm	...
Lorusso et al. [227]	AlSi10Mg	1 wt.% micro TiB_2	48 h	...	...	99 %
Lorusso et al. [227]	AlSi10Mg	10 wt.% nano TiB_2	48 h	...	...	97.8 %
Gu et al. [228]	Ti	15 wt.% nano TiC	4 h	5:1	200 rpm	> 97 %

The available literature proves the capabilities and mechanical alloying in ball mills. Several approaches have been chosen by different researchers. Most scientific investigations included sub-micro or micro sized composite materials. It was desired to form coalescences of the two different components to homogenise the powders for SLM processing. Other works focused on nano sized composite powders to cover the metal matrix material. In both cases, some of the material properties were increased. However, researchers also reported the challenging influence of the increased melting temperature and therefore, a higher tendency for unstable melt pools. Developing parameters for MMCs is definitely more complex than for other materials. The goal in this study was to increase material properties of MS1 through reinforcing VC particles.

8.2 Material and Methods

8.2.1 Powder Preparation

First of all, a homogeneous mixture of the maraging steel metal and the vanadium carbide composite material had to be achieved. Commercially available spherical gas atomized MS1 (EOS GmbH, Germany) and irregular shaped VC powder (Treibacher Industrie AG, Austria) was mechanically mixed for 15 minutes in a Turbula tumbler (Willy A. Bachofen AG, Switzerland). The MS1 powder had a size distribution of 15 μm - 40 μm and the VC powder had a size distribution of < 33 μm. The values are given according to the manufacturers data. The chemical composition of the maraging steel powder is given in Table 4.1. The VC powder consisted mostly of V_8C_7, with very small amounts of V_2C, V_6C_5 and stoichiometric VC. The powder mixture was based on 90 wt% of MS1 and 10 wt% of VC. The morphology of the MS1 and the VC powder after mixing is given in Figure 6.1. As one can see, some sub-micron particles are already sticking to the bigger MS1 powder particle, but VC particles > 1 μm are still separated.

After the mixing process, the powder was mechanically alloyed in a high energy ball mill (Fritsch Pulverisette 4, Germany). The planetary ball mill was equipped with a tungsten carbide vial with a volume of 500 ml. After pouring the powder mixture into the jar, 10 mm WC balls were added and the ball-to-powder ratio was 5:1. If a higher ball-to-powder weight ratio is used, more energy is in the system and the powder particles need less time to get mechanically alloyed, as there are

Table 8.2: Parameters for the Fritsch Pulverisette 4 high energy ball mill.

milling time per cycle	60 min
break	15 min
speed of main disc	200 rpm
speed of planetary disc	400 rpm
weight of balls	369 g
weight of powder	74 g

Table 8.3: Milling times and cool-off breaks.

total milling time	2 h	4 h	8 h	12 h	16 h	24 h
total process time	2 h 15 min	4 h 45 min	9 h 45 min	14 h 45 min	19 h 45 min	30 h

a lot more collisions in the jar [17]. Collisions can occur as ball-powder-ball or ball-powder-wall collisions.

For the high energy ball mill, the parameters were set to values, which were found to be reasonable in preliminary investigations. On one hand it was desired, to crack the hard VC particles and to create coalescences of MS1 and VC. On the other hand, the soft and spherical maraging steel particles should not deform too much, to become a problem for the SLM process. The parameters are shown in Table 8.2 and are considered as low energy mechanical alloying. To investigate the influence of the milling time, it was decided to mill the powder for 2 - 24 hours and to take samples after every 2, 4, 8, 12, 16 and 24 hours. As there is a lot of energy involved in mechanical alloying, the mill was set-up to let cool-off the jar and the powders for 15 minutes after each hour of milling. Table 8.3 provides the milling times in detail.

The vial was furthermore equipped with valves to flood it with argon to prevent oxidation during the mechanical alloying process. During the MA process, no additives were used. Therefore, the process was performed under dry conditions.

8.2.2 SLM Process

An SLM machine (MCP-realizer SLM 250, Germany) was used to produce cylindrical specimens with a diameter and a height of 8 mm. The SLM device was equipped with a single ytterbium fibre laser with a theoretical output of 100 W. The laser spot diameter was set to 0.12 mm. The building chamber originally had dimensions of 250 mm x 250 mm x 220 mm, but was retrofitted with a cylindrical (Ø 50 mm) building chamber to process very low amounts of powder. The coating after each layer was scanned with the laser had to be performed manually. For the laser scanning process, the chamber was flooded with argon to keep the oxygen level below 0.4 % to avoid oxidation of the metal powder. After each layer, the scanning strategy rotated 90 ° to create an alternating hatch pattern. The layer thickness was constant and set to 40 microns. The hatch distance, the scanning speed and the laser power were set accordingly to a preliminary design of experiments. For this, R-Studio (R Foundation for Statistical Computing, Austria) open source software was used. The number of experiments needed in a full empirical test matrix can be drastically reduced, if an appropriate DoE based on statistical functions and physical correlations is used. In this study, the Federov operator was used in R-Studio, to determine the needed experiments. The calculations were based on the changeable variables:

- scanning speed
- hatching distance
- laser power

Table 8.4: Parameters for the SLM process

Laser power [W]	Scanning speed [mm/s]	Hatching [μm]	Energy density [J/mm^3]
65	179	77	117,90
99	179	77	179,57
53	256	77	67,22
99	294	77	109,33
87	333	77	84,83
99	179	94	147,09
76	333	94	60,70
99	179	143	96,69

As a target figure for the script, the maximal density was set. 60 J/mm^3 was the lower limit for the energy density and 180 J/mm^3 was set as the upper limit. Due to the size limitation in the SLM machine and the small build chamber, 8 parameter sets were selected for the SLM process. The parameters can be found in Table 8.4. To better understand the outcome and to have samples for a comparison, pure MS1 was also fabricated according to the study of Tan et. al. [212].

8.2.3 Material Characterization

The cylindrical specimens which were manufactured by SLM were embedded and prepared for cross-sectioning. The MS1/VC samples were polished and etched in a 30 ml 32 % HCl, 15 ml 65 % HNO_3 and 30 ml 48 % HF solution. The samples manufactured of pure MS1 were etched in a solution of 10 ml 65 % HNO_3 and 100 ml 96 % ethanol, which is also known as nital. After preparation and etching, the specimens were first analyzed regarding their microstructure, laser tracks, porosity and relative density in an optical microscope (Leitz Aristomet, Leica Microsystems, Germany). The density was measured using a dedicated analytical imaging software attached to the microscope.

For further analysis with a higher magnification, a scanning electron microscope (SEM, Tescan Vega 3, Czech Republic) which was also equipped with a silicon drift detector (Ultim Max 40, Oxford Instruments, United Kingdom) for energy dispersive X-ray spectroscopy (EDX) was used. X-ray diffraction was used, to get information about the phase composition of the obtained powders after mechanical alloying and of the SLM fabricated specimens. The structural evolution during the different milling times was studied with an X-ray diffractometer (PANalytical PW 3040/6 X'Pert Pro, United Kingdom) with Cu Kα radiation (λ = 0.15406 nm) operating at 40 kV and 35 mA. Two-theta was recorded in the range of 30 ° and 90 ° with a step size of 0.05 and a counting time of 200 seconds per step.

The hardness was measured with a micro hardness testing device (Karl Frank GmbH, Germany) and loaded to 9.8 N. For the particle size distribution analysis a Microtrac SDC in combination with a Microtrac S3500 (Retsch GmbH, Germany) was used. The device uses three precisely placed red laser diodes to accurately characterize particles. For the tribological analysis, an Anton Paar (Anton Paar Group AG, Austria) CPX in combination with an Anton Paar MST micro scratch tester was used. 5 N of force were applied to the indenter and moved for 1000 times on a track with a 5 mm length. The analysis of the wear of the indenter stainless steel ball was done with optical microscopy and the track was analyzed with a Dektak 150 profilometer (Veeco, USA).

8.3 Results and Discussion

8.3.1 Particle Size Distribution of the MA Powders

To get a better understanding of the effects of mechanical milling on a mixture of brittle and ductile powders, several samples were taken. A Microtrac particle size distribution analyzer was used to investigate the powder particle size after 2, 4, 8, 12, 16 and 24 hours of milling [204].

The particle size distribution can be measured with different techniques and are based on the expected particle sizes. The most common methods are the particle counting method and the particle volume method. In the Microtrac device, lasers are used to measure the halo of a diffracted light of particles, which pass though the laser beam. This method is good for measuring particles sizes of 0.1 to approximately 3000 microns. The technology can be used for counting passes and volumetric analyzes. The particle size distribution curve $Q(x)$ gives the standardized sum of all irregular shaped particles with an equivalent spherical diameter less than or equal to x. The particle counting method and the particle volume method are defined as:

- Particle counting method: If the number of all measured particles N_i with a diameter x are smaller than or equal to the defined diameter x_i and N is the sum of all measured particles, then
$$Q_c(x_i) = \frac{N_i}{N}. \tag{8.1}$$
- Particle volume method: If the mass of all measured particles m_i with a diameter x are smaller than or equal to the defined diameter x_i and m is the total mass of all measured particles, then
$$Q_v(x_i) = \frac{m_i}{m}. \tag{8.2}$$

In Figures 8.1a through f the results of the particle size analysis are shown based on the volumetric measurement. The diagrams give a graphical overview, while the percentile results are given next to each diagram to show the respective numerous results. According to the analysis, the particle size increased with the milling time and agglomerations must have formed. After 16 h however, the particles potentially grew too large and therefore had a tendency to crack into smaller ones. As can be seen in the diagram of the 24 h milled powder, the average particle size distribution was decreased. One possibility to control the formation of agglomeration is to use a liquid additive during the ball milling process. Liquid additives prevent such agglomerations especially during long-time millings, but as the powder was produced for selective laser melting, it was essential to keep the powder dry and free of contaminations.

To validate the results of the Microtrac, a backscattered electron detector in a scanning electron microscope was used. The images are shown in Figure 8.1g and h. The SEM images revealed some quite large particles, but overall, the 24 h milled powder was finer than the 16 h milled powder.

Of course, if one measures the absolute number of particles, the amount of small particles will be significantly higher with the particle counting method. But it provides interesting insights of the composition of the smaller bulk powder. As the initial powder was mixed based on weight percentages and the VC powder consisted of very fine particles, the mechanically alloyed powder also contained a lot of small particles, as not all particles form coalescences. Figure 8.2 shows the diagrams and the percentile numbers of the powder samples after 2, 4, 8, 12, 16 and 24 hours of milling.

8.3.2 Phase Analysis of the Powders

Figure 8.3 shows the XRD patterns of the VC and MS1 powder mixture after various milling times. The XRD patterns confirm that visible peaks belonging only to the VC reinforcing phase and the

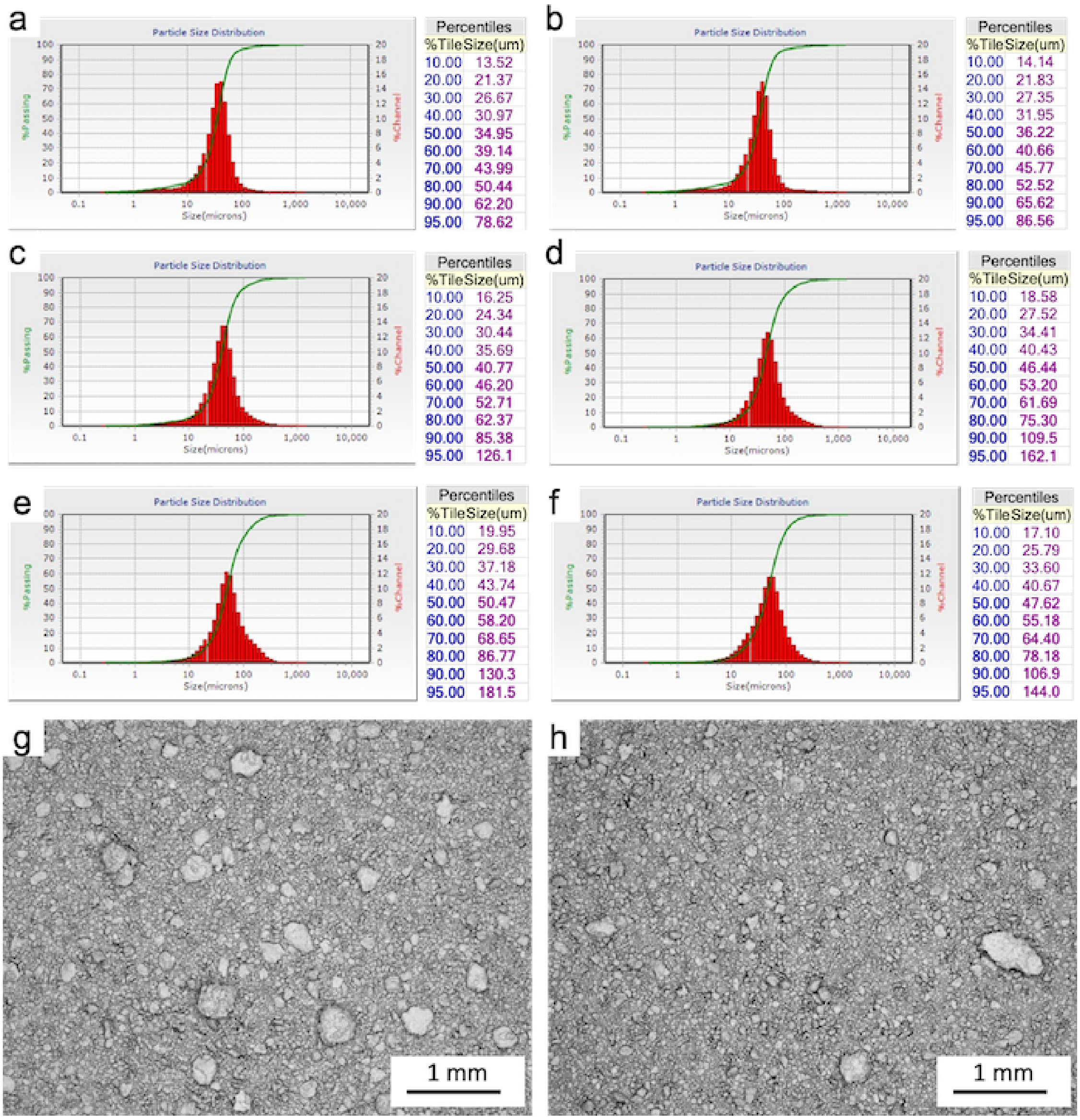

a

Percentiles	
%Tile	Size(um)
10.00	13.52
20.00	21.37
30.00	26.67
40.00	30.97
50.00	34.95
60.00	39.14
70.00	43.99
80.00	50.44
90.00	62.20
95.00	78.62

b

Percentiles	
%Tile	Size(um)
10.00	14.14
20.00	21.83
30.00	27.35
40.00	31.95
50.00	36.22
60.00	40.66
70.00	45.77
80.00	52.52
90.00	65.62
95.00	86.56

c

Percentiles	
%Tile	Size(um)
10.00	16.25
20.00	24.34
30.00	30.44
40.00	35.69
50.00	40.77
60.00	46.20
70.00	52.71
80.00	62.37
90.00	85.38
95.00	126.1

d

Percentiles	
%Tile	Size(um)
10.00	18.58
20.00	27.52
30.00	34.41
40.00	40.43
50.00	46.44
60.00	53.20
70.00	61.69
80.00	75.30
90.00	109.5
95.00	162.1

e

Percentiles	
%Tile	Size(um)
10.00	19.95
20.00	29.68
30.00	37.18
40.00	43.74
50.00	50.47
60.00	58.20
70.00	68.65
80.00	86.77
90.00	130.3
95.00	181.5

f

Percentiles	
%Tile	Size(um)
10.00	17.10
20.00	25.79
30.00	33.60
40.00	40.67
50.00	47.62
60.00	55.18
70.00	64.40
80.00	78.18
90.00	106.9
95.00	144.0

Figure 8.1: Volumetric particle size distribution of a) 2, b) 4, c) 8, d) 12, e) 16 and f) 24 hours of milling and SEM comparison of g) 16 and h) 24 h milled powder.

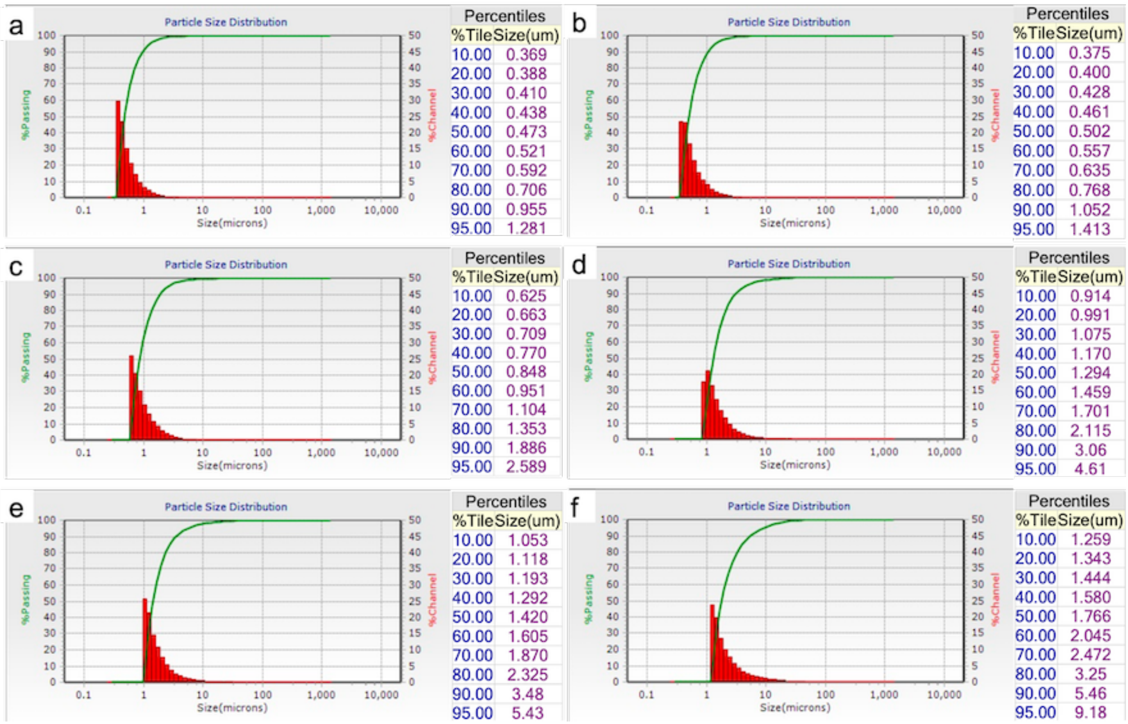

a

%Tile	Size(um)
10.00	0.369
20.00	0.388
30.00	0.410
40.00	0.438
50.00	0.473
60.00	0.521
70.00	0.592
80.00	0.706
90.00	0.955
95.00	1.281

b

%Tile	Size(um)
10.00	0.375
20.00	0.400
30.00	0.428
40.00	0.461
50.00	0.502
60.00	0.557
70.00	0.635
80.00	0.768
90.00	1.052
95.00	1.413

c

%Tile	Size(um)
10.00	0.625
20.00	0.663
30.00	0.709
40.00	0.770
50.00	0.848
60.00	0.951
70.00	1.104
80.00	1.353
90.00	1.886
95.00	2.589

d

%Tile	Size(um)
10.00	0.914
20.00	0.991
30.00	1.075
40.00	1.170
50.00	1.294
60.00	1.459
70.00	1.701
80.00	2.115
90.00	3.06
95.00	4.61

e

%Tile	Size(um)
10.00	1.053
20.00	1.118
30.00	1.193
40.00	1.292
50.00	1.420
60.00	1.605
70.00	1.870
80.00	2.325
90.00	3.48
95.00	5.43

f

%Tile	Size(um)
10.00	1.259
20.00	1.343
30.00	1.444
40.00	1.580
50.00	1.766
60.00	2.045
70.00	2.472
80.00	3.25
90.00	5.46
95.00	9.18

Figure 8.2: Particle size distribution using the counting method of a) 2, b) 4, c) 8, d) 12, e) 16 and f) 24 hours of milling.

MS1 matrix exist. It can be observed, that the intensity of VC peaks decreased, for increased milling times. The size of the crystallites had reduced significantly. The intensity of MS1 peaks, which are equal to α-Fe, did not change markedly, which means that the steel was undergoing plastic deformation rather than fragmentation [204].

8.3.3 Powder Morphology using SEM

Figure 8.4a - e shows the evolution of the powder after 2, 4, 8, 16 and 24 hours of milling and the influence on the powder morphology. It can be seen, that the particle shape and size is significantly influenced by the milling time. In the beginning the MS1 particles kept their spherical or near spherical shape and just barely formed agglomerations with the VC particles. The longer the milling time, the more particles merged together and started to form coalescences. Some of these particles grew faster and larger than others, which meant that post-processing sieving was necessary. The images furthermore show that even after long milling times, there is still a broad range of different particle sizes. This is due to the fact that some of the particles tend to get work-hardened and therefore have a limited ability to get plastically deformed during the milling process [17]. The mean VC particle size decreased as the initially big and brittle composite material tended to rather fracture than to undergo plastic deformation. The more ductile matrix material MS1 on the other hand, was more likely to deform and after some time get cold-welded respectively got mechanically alloyed with the smaller VC particles.

8.3.4 Powder Analysis by EDX

To investigate the effects of ball milling on the particles and their uniform distribution of the elements, an EDX map was taken for all of the milled powders. Figure 8.5 shows measured areas of the various milled powders and their main compositions, the matrix material (i.e. Fe) and the composite reinforcing particles (i.e. V). The complete chemistry of the alloy can be found in Table

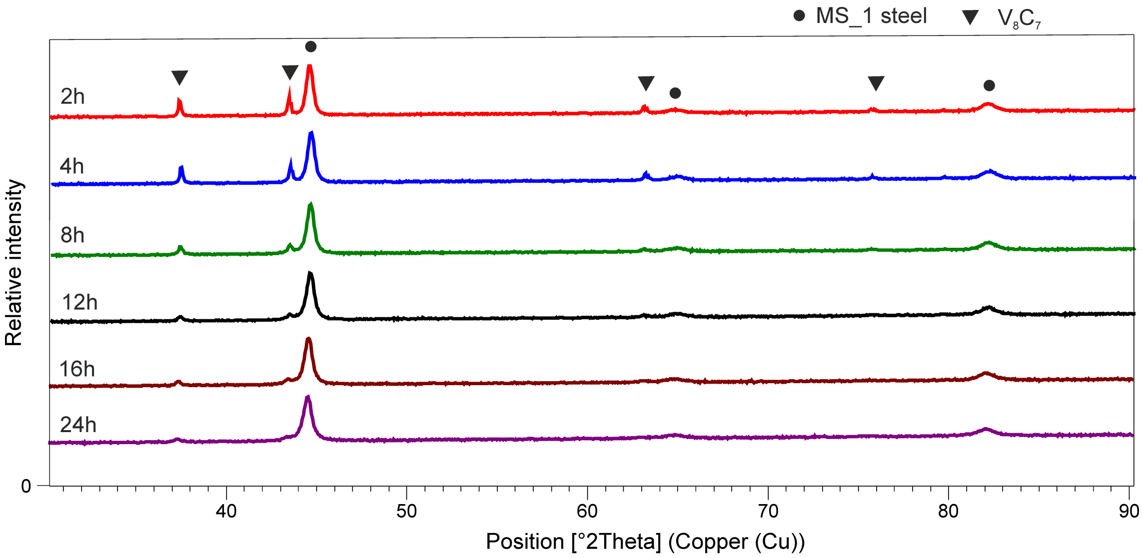

Figure 8.3: XRD patterns of MS1 with VC-33 powder after milling.

Table 8.5: Elements of the MA powders.

Element	wt% 2 h	wt% 4 h	wt% 8 h	wt% 16 h	wt% 24 h
Al	0.25	0.26	0.23	0.24	0.30
Ti	0.71	0.91	0.61	0.53	0.65
V	27.76	25.69	21.56	16.12	10.83
Cr	0.25	0.32	0.22	0.24	0.22
Fe	48.68	50.93	54.04	56.78	60.17
Co	6.42	6.88	7.35	7.88	8.32
Ni	12.01	11.73	12.35	14.04	15.13
Mo	2.98	3.22	3.23	3.75	4.37
W	0.93	0	0.42	0.42	0

8.5 and in the EDX map sum spectrum in Figure 8.6. SEM and EDX analysis also revealed, with longer milling times, less VC particles were found in the powder samples due to the decreasing median particle size of VC and their tendency of forming coalescences with the MS1 particles. This is very clearly visible in Figure 8.5f in which a 2 h milled particle can be seen, which was mounted and polished for SEM analysis. The VC particles attached to the still spherically shaped matrix material particles. Furthermore, powder analysis of the increased milling times evidently shows, that the vanadium particles were embedded deeply into the steel particles as the elementary percentage decreases indicatively, but also the EDX maps show less vanadium (i.e. red) particles. The relatively high amount of W in the EDX map can be explained due to wear of the tungsten carbide jar and balls of the high energy ball mill.

8.3.5 Phase Analysis of the SLM Specimens

XRD diffraction patterns of SLM composites obtained from powders with different milling time are shown in Figure 8.7. Phase composition of solid samples manufactured from powders after milling, reveal presence of γ-Fe and α-Fe which were created during SLM processing. In the XRD patterns of the samples that were milled for 2 h, 4 h, 8 h, 12 h and 16 h and SLM processed, there are peaks for γ-Fe visible. Pure maraging steel only forms α-Fe (bcc) with minor amounts

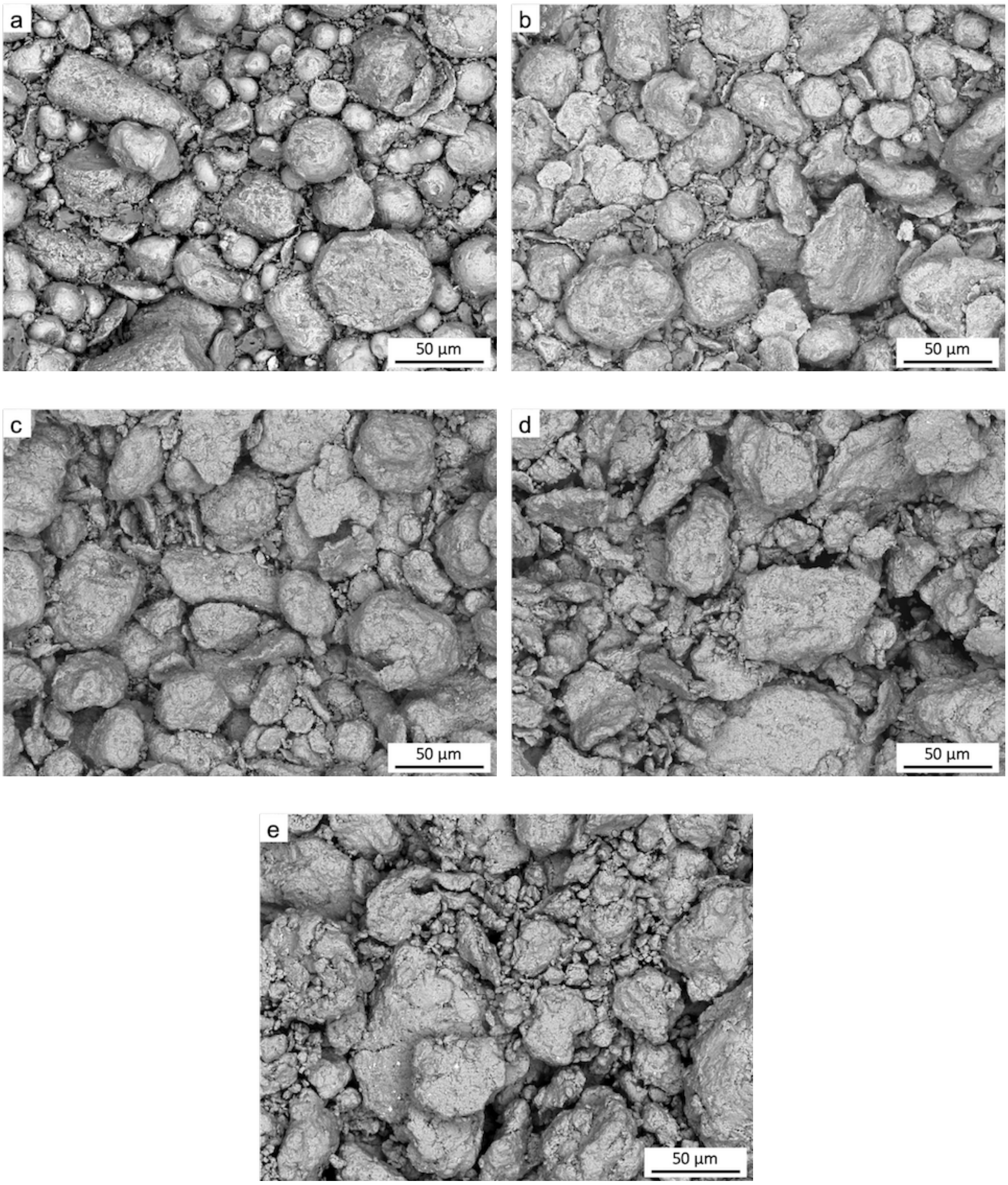

Figure 8.4: SEM of the MA powders after (a) 2, (b) 4, (c) 8, (d) 16, (e) 24 hours.

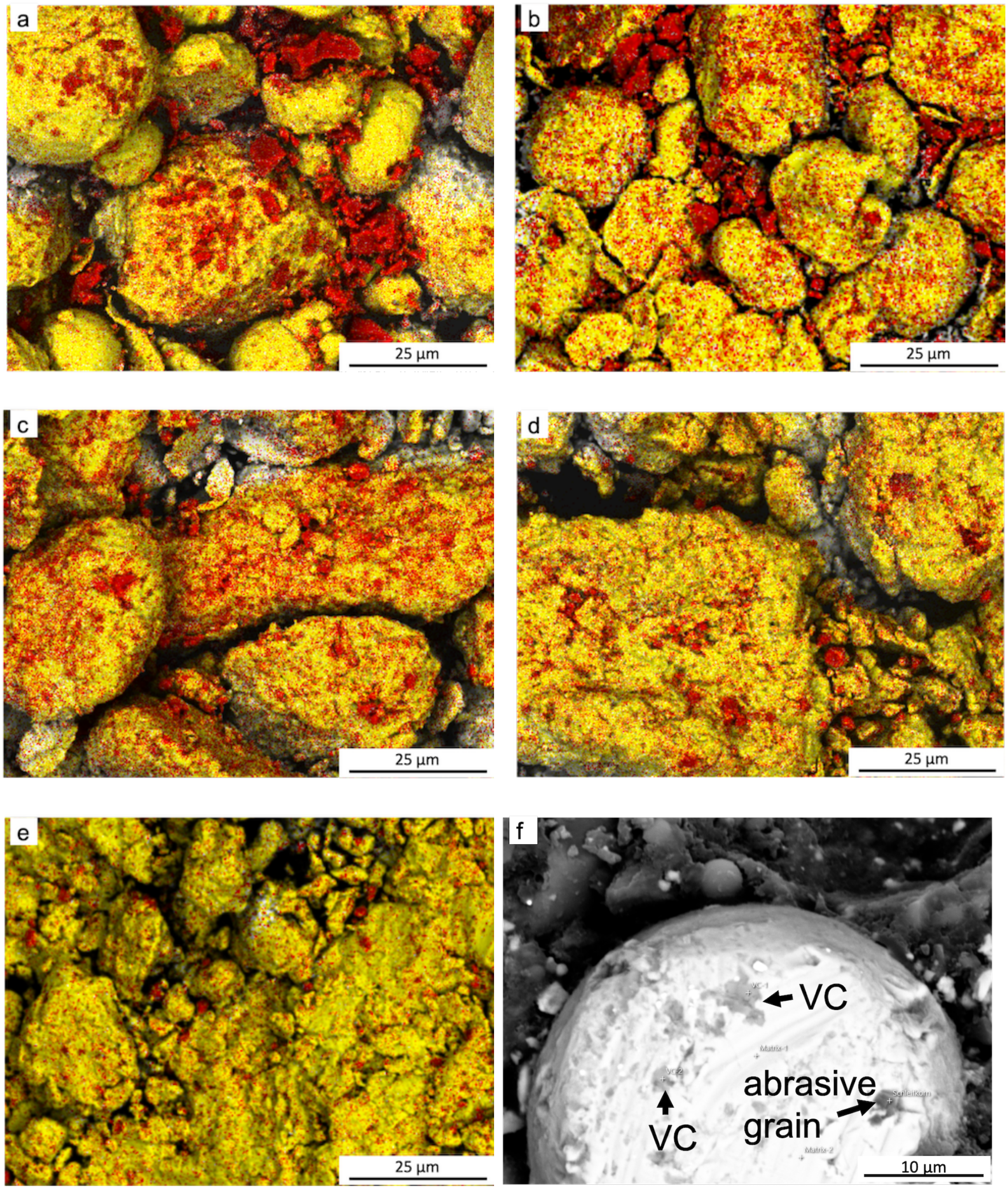

Figure 8.5: EDX maps of the MA powders after (a) 2, (b) 4, (c) 8, (d) 16, (e) 24 hours with Fe (i.e. yellow) and V (i.e. red) elements and (f) a SEM image of a 2 h milled and grinded particle.

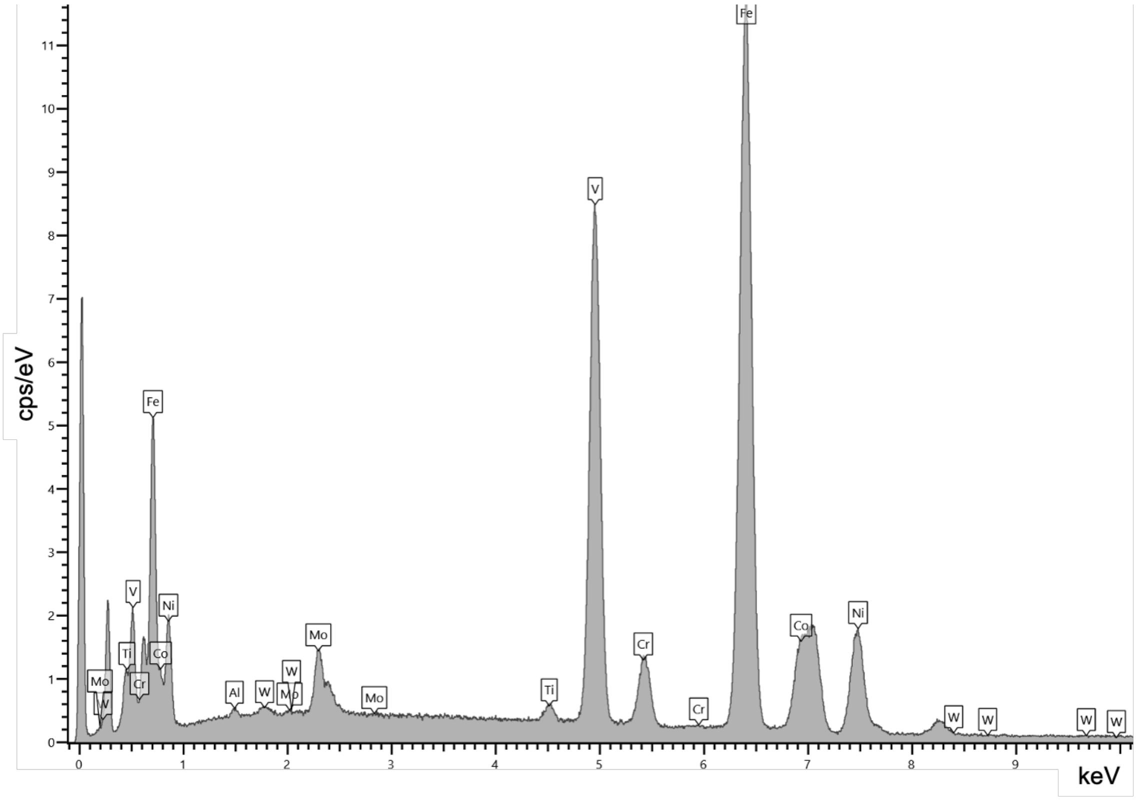

Figure 8.6: EDX map sum spectrum.

of retained austenite possible, but in the 2 h - 16 h samples the predominant phase was γ-Fe (fcc). This was also discovered by Yan et. al. [139] when maraging steel 300 was reinforced with WC. This might have happened due to a high cooling rate of some larger VC particles or a chemical composition change, when some of the VC particles were partially or fully melted. As VC has a higher thermal conductivity than maraging steel, it could affect the cooling rate of the melt pool and VC could hold back the phase transition of the high temperature γ-phase to the low temperature α-phase. However, this phenomenon did not occur with the 24 h samples. Instead, the material formed α-Fe. It is very likely, that the VC particles were too small to have an effect on the melt pool to cause the phase transition. The XRD chart revealed another phenomenon, which is about the vanadium carbide formation. The initially used non-stoichiometric V_8C_7 has formed to precipitated primary stoichiometric VC in the 24 h milled sample. Obviously, some of the carbon transferred to the VC. This further reduced the martensite starting temperature and therefore, alpha-Fe was the predominant phase again. Due to the decreasing particle size of the VC powder and the increasing embedding of these particles into the MS1 particles, the VC particles likely tended to fully melt and form precipitations.

8.3.6 Densification and Defects in the SLM-processed Specimens

For comparison reasons, the results of pure MS1 fabricated parts are presented first in Figure 8.8a. Tan et. al. [212] showed that the optimal energy density for SLM-processed parts out of maraging steel powders is at 67 J/mm^3. However, there are many factors influencing individual achievable results on different machines and the energy density is just an indicator. Therefore, various laser scanning speeds, hatch distances, and laser powers, which are resulting in a similar energy density level, have been used to get near fully dense parts. The pure MS1 powder was processed without any minor issues throughout all applied parameter variations and the highest

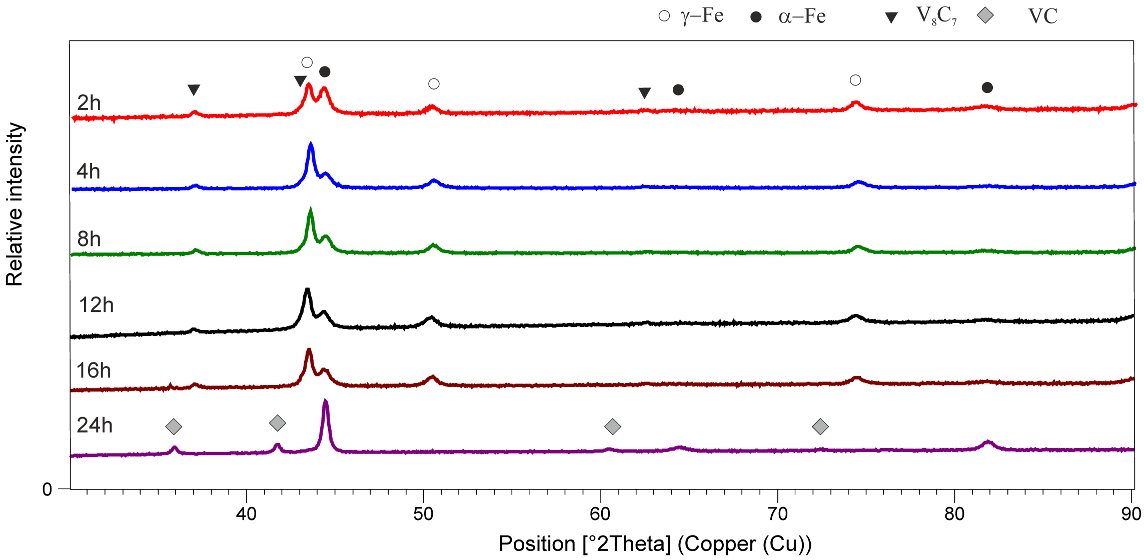

Figure 8.7: XRD pattern of milled and SLMed MS1 with reinforcing VC particles.

relative density, which was 98,2 %, was achieved with 69,49 J/mm^3. However, optical microscopy (OM) revealed small imperfections and pores, which are process related defects due to overheating of the laser resulting in evaporation of some constituents and subsequent fast cooling of the part causing quenching cracks [229]. During SLM low energy inputs or short dwelling times at the laser track boundaries, can lead to incomplete densification respectively incomplete melting of powder particles [177], which results in porosity. The MS1 specimen was etched with nital and laser scanning tracks became very apparent. They reveal that the laser power was too high, as the laser tracks had a depth of approximately 130 μm. Accordingly, the material was heated up and cooled down repeatedly. If the SLM parameters are adjusted accordingly, even higher densities can be achieved through further parameter optimization, but it was beyond the scope of this study.

In Figure 8.8b one of the SLM-processed MS1/VC samples is shown. The image reveals an elongated pore with a size of more than 50 microns across. These defects did occur - additionally to the before mentioned process-related defects - because of the introduction of VC particles and their significantly higher melting temperature. Processing two different materials with such diverse melting temperatures with a laser is challenging. Overall, the MS1/VC specimens had more defects than the specimens without the VC composite. Interestingly, the longer the milling time, the greater number of defects occurred after SLM, which was most likely due to the decreased spherical shape of the maraging steel particles. Samples also showed a tendency of spherical shaped defects to transform to elongated defects. Due to the finer and more homogeneous distribution of VC particles and their higher melting temperature, the melt pool was probably interfered and less stable than for pure MS1. OM also revealed, that with lower energy densities and therefore lower melting temperatures, the VC particles - dependent on their actual size - tended not to fully melt, even after long ball milling times, resulting in finer particle size distributions (i.e. about 1 - 2 μm). There is a higher chance to fully melt the VC particles in this composition, if their average size is decreased or a higher melting energy is brought into the system. During solidification the VC will form primary precipitations that are homogeneously distributed throughout the sample. It was found, that SLMed specimens with similar milling times but with a higher energy density (η) showed less visible unmelted VC particles in SEM and OM.

The smaller the VC particles and the higher the energy input, the higher the chances are to fully melt the particles and therefore form primary precipitated solidified VC. Printed specimens with

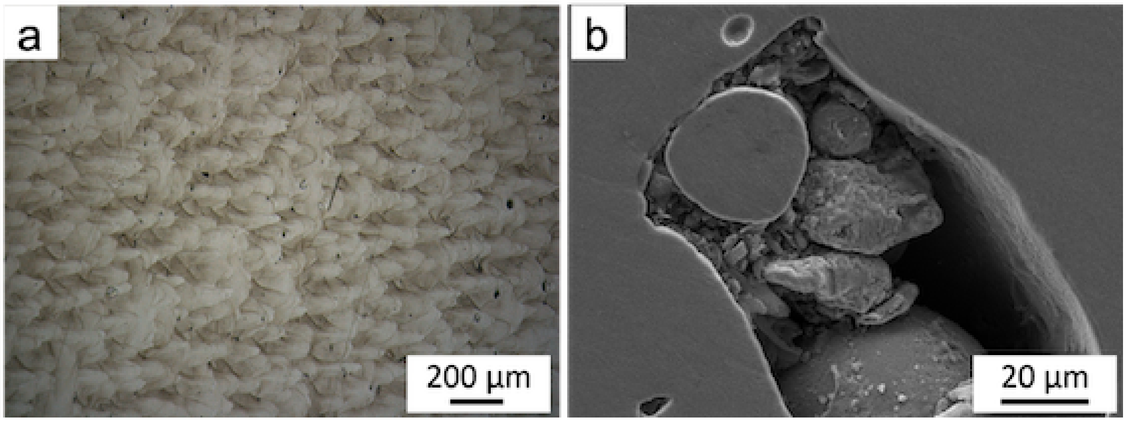

Figure 8.8: Images of (a) OM of SLMed MS1, (b) SEM of unmelted MS1/VC in an SLMed specimen.

Table 8.6: Achieved relative densities of all SLM processed specimens

Spec. Nr.	Energy density [J/mm^3]	Rel. D. 2 h [%]	Rel. D. 4 h [%]	Rel. D. 8 h [%]	Rel. D. 12 h [%]	Rel. D. 16 h [%]	Rel. D. 24 h [%]
2	117.90	92.45	83.75	91.70	87.70	91.83	81.90
3	179.57	97.12	95.8	92.40	93.24	83.83	93.28
5	67.22	72.36	67.43	69.83	72.57	68.42	72.56
6	109.33	95.90	90.44	88.55	83.84	84.53	79.02
8	84.83	82.47	83.24	72.70	77.38	73.86	77.77
10	147.09	95.12	91.69	85.78	71.84	89.20	79.43
11	60.70	69.05	67.81	65.42	63.64	68.04	67.37
18	96.69	81.69	82.91	84.15	79.70	78.43	75.82

the same ball milling times but with higher energy density used during SLM processing showed less visible VC particles. Moreover, the higher the energy density η the less unmolten VC particles were found. Especially smaller particles probably had a higher tendency to fully melt, because of the liquid nucleation growth theory. During solidification, these molten particles will form primary precipitated VC in the solid part and will increase the material strength of the produced parts.

Furthermore, the VC particle distribution after SLM processing was investigated. Using optical microscopy with a light filter, it was possible to determine the difference between pores and elevations of VC particles. Sometimes the difference was hard to see and one must be working very precisely. Figure 8.9 shows the SLM processed specimens after embedding, grinding and polishing. Interestingly, after approximately 12 hours of milling, the average particle size of the vanadium carbide decreased in the SLMed specimens. There were still some minor bigger VC visible, but overall, the mean particle size was smaller. After 16 h of milling and SLM processing there were no large VC particles found on the polished surface. Also, the overall amount of smaller VC particles seemed to be decreased. However, it has to be mentioned that the specimens with the highest energy density η were analyzed under the optical microscope. Therefore, the chance to fully dissolve the VC was higher than with any other samples, that is for sure. An overview of all achieved relative densities is given in Table 8.6. In Figure 8.10 a comparison of all energy densities and achieved relative densities can be seen.

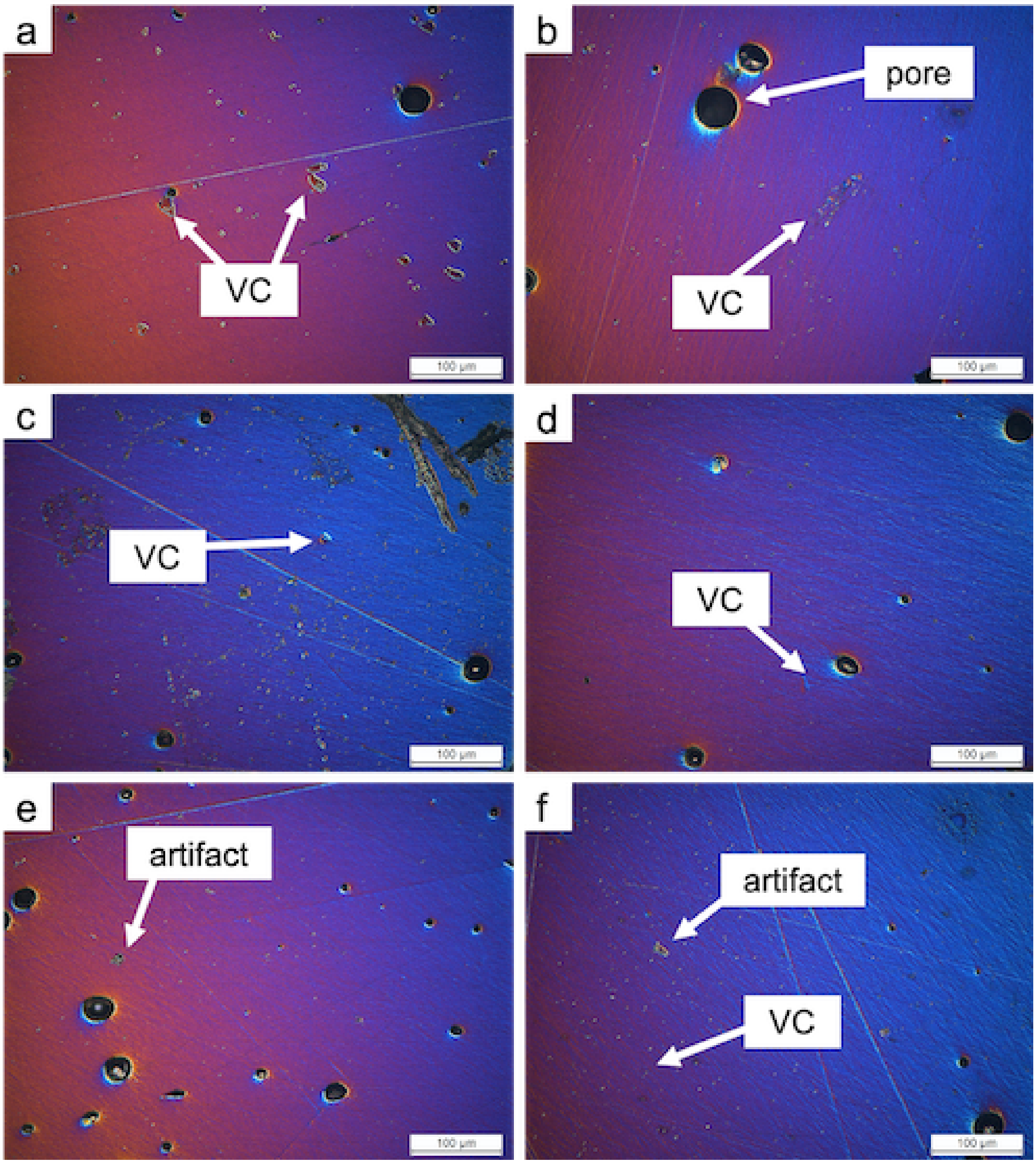

Figure 8.9: Optical microscopy images with light filter of SLMed and polished MS1/VC-33 after (a) 2, (b) 4, (c) 8, (d) 12, (e) 16 and (f) 24 h.

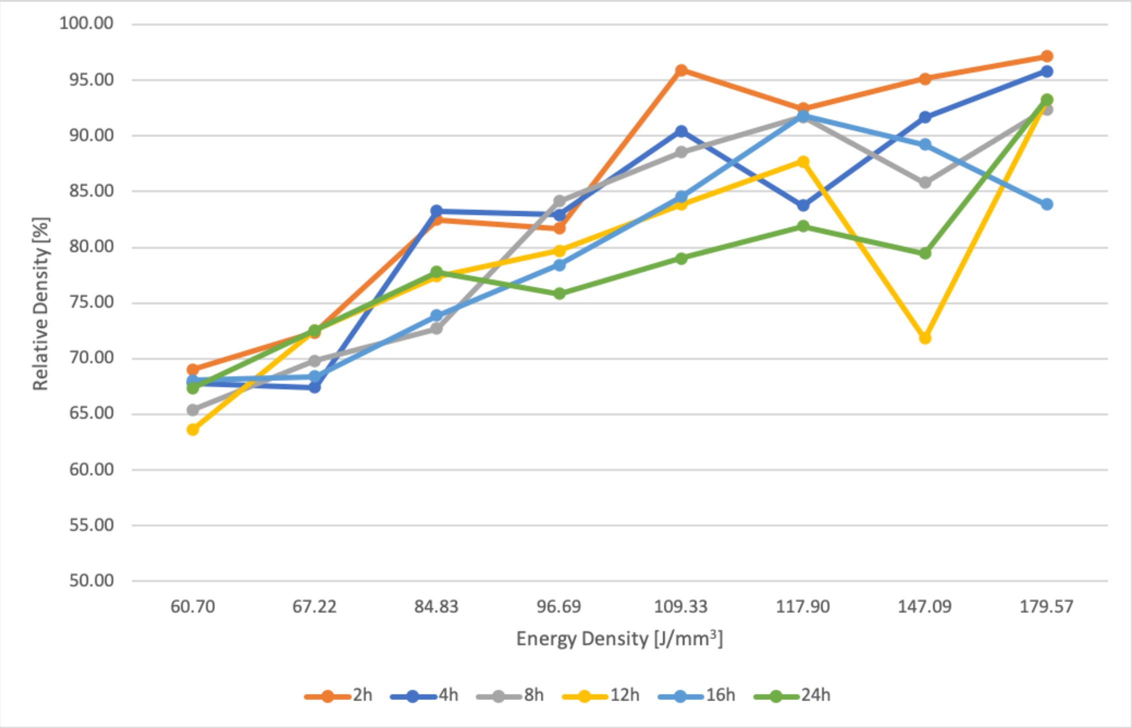

Figure 8.10: Relative densities of all samples after 2, 4, 8, 12, 16 and 24 hours of milling at different energy densities.

8.3.7 Analysis of Density

R Studio was used to create a prediction model for the highest relative density achievable with each mixture. The Federov operator was used to calculate an optimal set of parameters for the DoE and based on these calculations and the results of the density measurements, the optimal parameters for SLM processing were predicted. First, the energy density of the SLM process was calculated. The model was then based on the results of the measured specimen densities. The diagrams were made for 99 W laser power and are given in Figure 8.11. Basically, the models do not change drastically except the prediction for the 16 h mechanically alloyed powder. In all other models, the optimal scan speed was predicted to be at approximately 180 mm/s. This would increase the energy density and cause a more stable melt pool. Furthermore, the hatch distance was predicted to be at around 75 microns which would further increase the energy density and the laser tracks would be more overlapped. These predictions are correlating with the analysis using optical microscopy. The higher the energy density, the better the results were and the less porosity was found in the specimens. However, the model of prediction for the 16 h milled powder was very different and is shown in Figure 8.11e. According to the R Studio calculation, the optimal scan speed was at 240 mm/s and the hatch distance optimum was at 135 microns. This would significantly reduce the energy density and indeed, the maximum relative density was found to be at 117.90 J/mm^3. All other maxima were found to be at 179.57 J/mm^3.

8.3.8 Microstructure Analysis with SEM and EDX

Fig. 8.12 shows the mechanically alloyed and SLM-processed MS1/VC after 2 (8.12a), 4 (8.12b), 8 (8.12c), 16 (8.12d), 24 (8.12e) hours of milling with the aforementioned milling parameters. In the specimens with shorter milling times, there were still large unmelted VC particles visible. Specimens built with 179 J/mm^3 had the highest densities throughout all of the different milling times. Even higher results than 97.12 % of relative density might be possible, through further

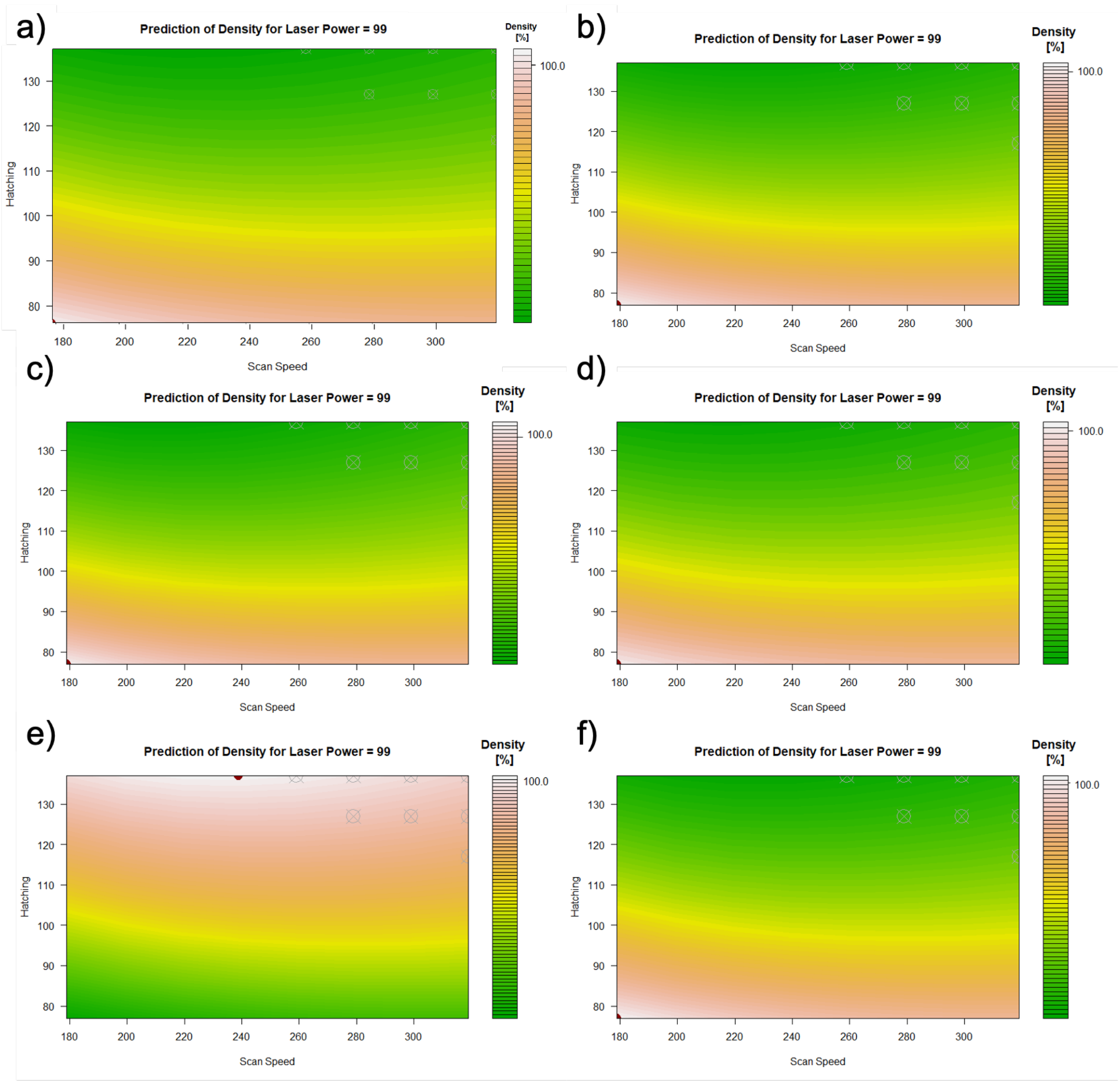

Figure 8.11: Prediction of the optimal relative density for MS1VC with 33 μm particles mechanically alloyed for a) 2 h, b) 4 h, c) 8 h, d) 12 h, e) 16 h and f) 24 h.

parameter studies. In this study it was found, that the highest energy density produced the highest relative density, so one can assume that higher η-values might be advisable. However, at high energy density levels welding mechanisms change from conduction mode welding to penetration keyhole mode welding, which can cause problems. The process temperature of a welding system can exceed the vaporization temperature if the energy, which is brought into a conduction weld, cannot dissipate fast enough. Materials start to evaporate and penetration keyhole welding occurs, whereas the vaporized material generates gas bubbles that form round pores during solidification [230]. This effect hinders near-full-dense part production. In Figure 8.12a the white arrow indicates some big unmelted VC particles, but also smaller already refined particles can be seen, whereas Figure 8.12b shows microporosity. In Figure 8.12f the red colour shows the vanadium and the yellow colour indicates the ferrite distribution. Furthermore, a black particle can be spotted, which might be a primary precipitated VC particle, but could also be a micro-keyhole. EDX analysis did not show any satisfactory results as the resolution of the sensor was not sufficient to analyze the black particles. According to the theory of liquid nucleation growth (LNG), particles will first melt a thin boundary layer after reaching a temperature, which is lower than the melting temperature of the solid material. The thickness of the melted boundary layer is increasing until the particle melting temperature is reached and the whole particle liquifies. Even when considering this theory, the sub-micron and nano sized VC has a significantly higher melting temperature. Nevertheless, it is highly possible that some VC particles were partially dissolved in the metal matrix composite and formed primary VC after solidification. There were almost no remaining VC particles visible in the SLM samples obtained from the 16 hours milled powders, which indicates a homogeneous and fine distribution throughout the whole specimen, either of ultra-fine or primary precipitated VC particles. Kang et al. [174] investigated the reinforcement of MS1 with tungsten carbide and describe the capability of the laser source to heat the molten to over 3000 ° C [210] and therefore, to fully or partially melt WC in the SLM process. The vanadium distribution was also validated through EDX analysis, which did not show any unmelted VC particles, but a fine distributed content of V throughout the whole specimen. Some unidentifiable grey particles in the 16 h and 24 h milled and SLMed solid part indicate that the VC has been melted completely and has formed primary precipitations after solidification.

8.3.9 Microhardness

The results of the microhardness tests of the MS1/VC composite are shown in Figure 8.13. The samples were fabricated with the same laser energy density and with the same SLM parameters. Typically, the as-built hardness of MS1 is between 330 and 360 HV. The highest achieved value was at 439 HV1, which indicates that the VC particles had a significant influence and increased the microhardness. The microhardness of the composite material is influenced by the phase composition, grain size and defects in the matrix [139], therefore, at least four microhardness tests were performed per specimen to reduce statistical errors. The increase in hardness is due to the generation of obstacles against grain motion, but also because of the presence of VC particles in the matrix and grain refinement. In some of the specimens, there was a relatively high standard deviation of the measured results. This can be explained with pores in the material, which are present under the surface and can not be seen with optical microscopy.

In Table 8.7 an overview of all mean hardness values and their statistical information is provided. Due to some pores underneath the surface, the range R and the variance V can be comparably high. This directly also affects the standard deviation SD.

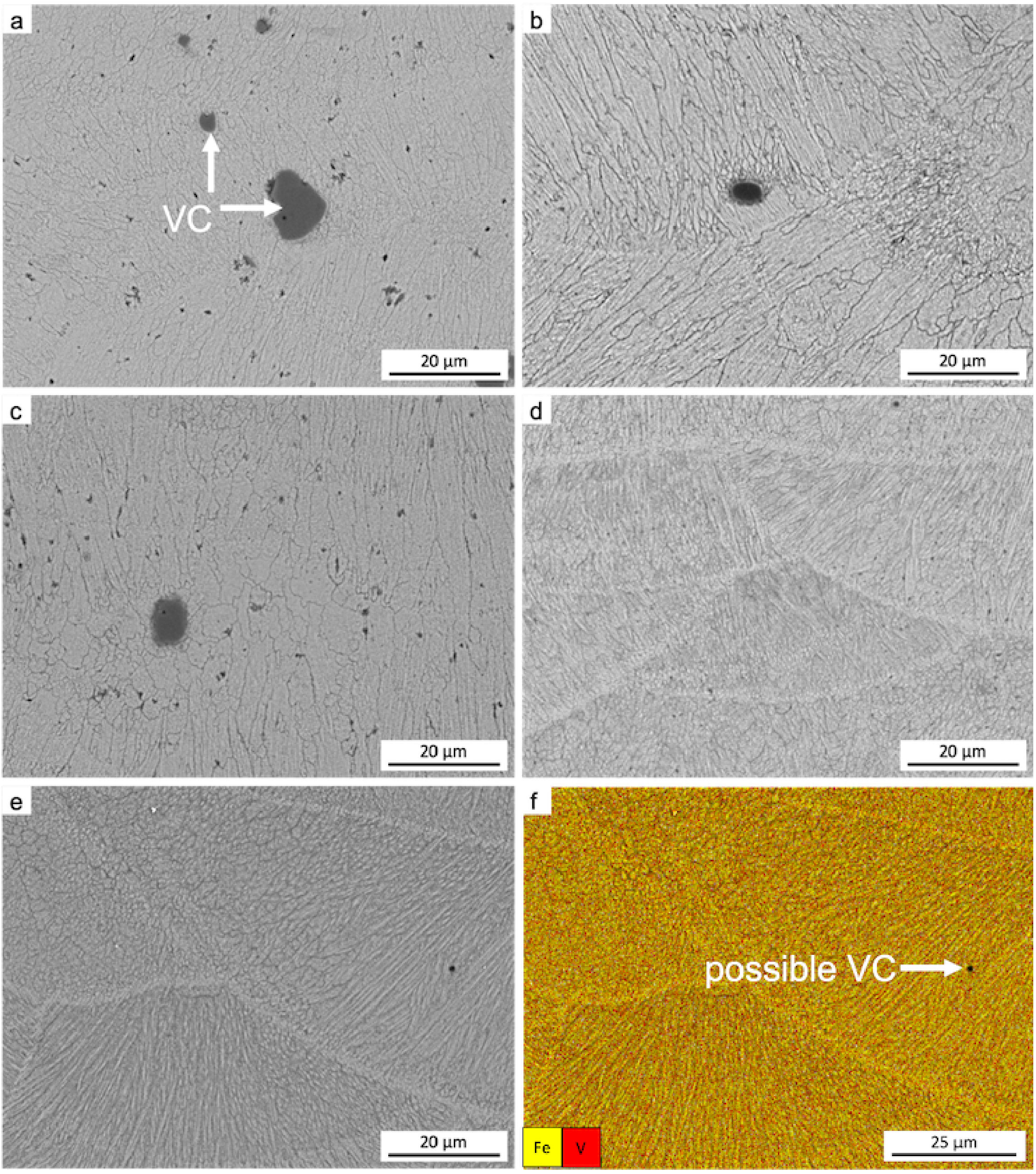

Figure 8.12: SEM images of: the SLM processed 179 J/mm^3 specimens after (a) 2, (b) 4, (c) 8, (d) 16, (e) 24 hours of milling and a (f) possible primary VC in the 24 h sample.

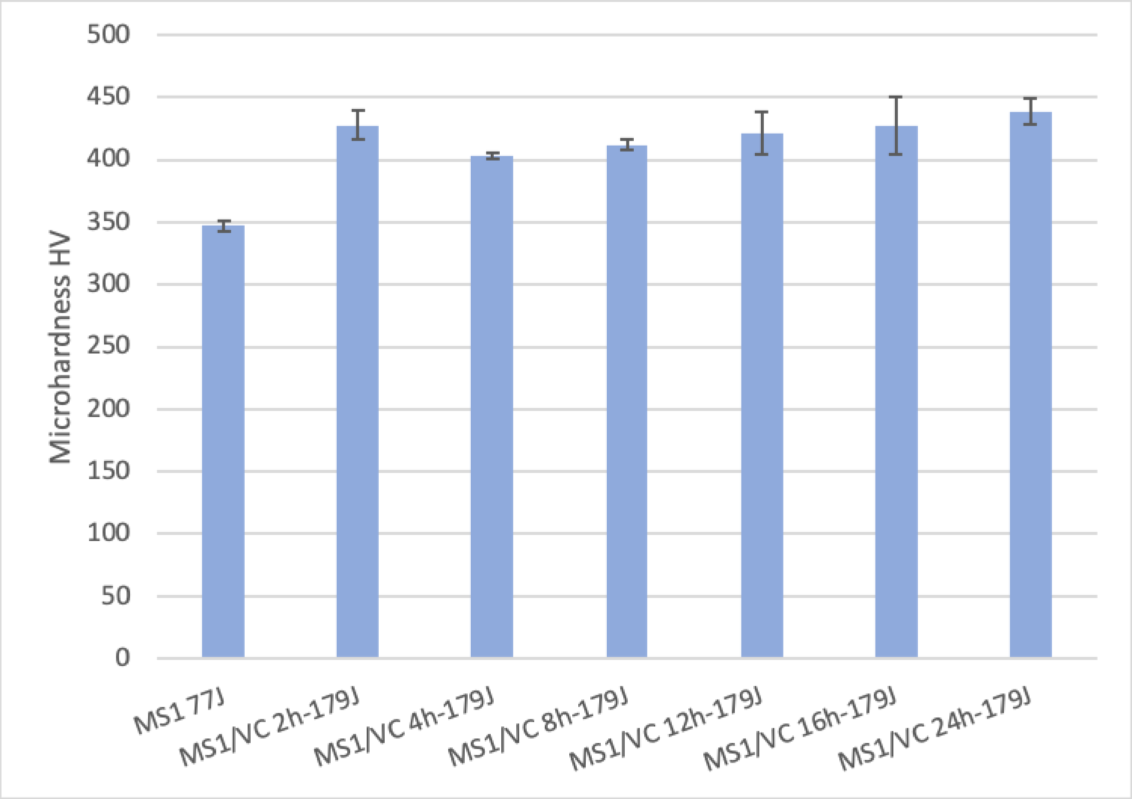

Figure 8.13: Microhardness measurement results with standard deviation.

Table 8.7: Statistical information for micro-hardness measurements of the MS1 samples after 2, 4, 8, 12, 16 and 24 hours of milling.

Spec. Nr.	**Mean 2 h**	**R 2 h**	**V** σ^2 **2 h**	**SD** σ **2 h**	**Mean 4 h**	**R 4 h**	**V** σ^2 **4 h**	**SD** σ **4 h**	**Mean 8 h**	**R 8 h**	**V** σ^2 **8 h**	**SD** σ **8 h**	**Mean 12 h**	**R 12 h**	**V** σ^2 **12 h**	**SD** σ **12 h**	**Mean 16 h**	**R 16 h**	**V** σ^2 **16 h**	**SD** σ **16 h**	**Mean 24 h**	**R 24 h**	**V** σ^2 **24 h**	**SD** σ **24 h**
2	407	18	65	8.06	340	48	395	19.87	406	85	1233.67	35.12	414	60	608	24.66	559	174	5049.67	71.06	387	97	1680.67	41
3	428	28	132.67	11.52	404	5	5.67	2.38	412	10	16.67	4.08	421	38	290.67	17.05	490	54	4440	66.63	439	23	108.33	10.41
5	341	88	1292.67	35.95	365	13	28.33	5.32	383	45	372.33	19.3	380	83	1292.67	35.95	432	118	12086.67	109.94	353	70	1016.67	31.89
6	401	27	141.67	11.9	425	20	67.67	8.23	378	42	331.67	18.21	376	15	39	6.24	460	76	6710.33	81.92	409	54	614	24.78
8	335	158	5444.33	73.79	376	42	305	17.46	356	55	557.67	23.62	360	37	237.67	15.42	438	48	8289.33	91.05	354	53	536.33	23.16
10	392	17	51	7.14	393	27	122	11.05	393	24	107	10.34	388	33	197.67	14.06	474	15	7434	86.22	418	63	722	26.87
11	322	101	1812.67	42.58	284	101	1720.33	41.48	342	15	50	7.07	320	94	1472.67	38.38	397	49	14036.33	118.48	349	12	29.67	5.45
18	398	32	214.33	14.64	369	64	688.33	26.24	397	19	67	8.19	381	21	76.33	8.74	463	53	9517.67	97.56	383	31	163	12.77

Table 8.8: Coefficient of friction, track wear rate and ball wear rate of MS1VC.

Material	COF (μ)	Track Wear Rate $[mm^3/Nm]$ x 10^{-5}	Ball Wear Rate $[mm^3/Nm]$ x 10^{-5}
MS1	0.74	1.51	1.44
MS1VC-2h	0.76	1.31	3.28
MS1VC-4h	0.73	1.71	4.51
MS1VC-8h	0.77	1.23	3.22
MS1VC-12h	0.74	1.31	6.25
MS1VC-16h	0.13	0.0863	1.45
MS1VC-24h	0.69	0.699	5.79

8.3.10 Tribological Performance

One of the main aims of reinforcing materials with carbides is to improve the wear resistance. Tribological analysis was performed with the manufactured composite samples and the results were compared to pure MS1 results. In Figure 8.14 a diagram is provided with the coefficient of friction (COF) results and in Figure 8.15 the relative penetration depth of the indenter. The relative penetration depth describes how deep the indenter was able to scratch into the surface based on the initial height. Obviously, the sample which was manufactured with 16 h mechanically alloyed powder had a significantly lower coefficient of friction. The sample was polished again and then the tribological test was repeated. The result remained pretty much the same. Accordingly, the wear rate was very low compared to the other results. In Table 8.8 the results of the coefficient of friction, the track wear rate and the ball wear rate after 1000 cycles is provided. The COF of the specimens with reinforcing VC did not change drastically compared to pure MS1, except in the 16 h milled sample. The wear rate however, decreased notably with a minimum value being $8.63x10^{-7}[mm^3/Nm]$ in the 16 h sample and $6.99x10^{-6}[mm^3/Nm]$ in the 24 h sample. The ball wear rate was found to be dependend of the track wear rate and a graphical comparison is given in Figure 8.16. While performing tribological tests, the densification plays a significant role. The tests were performed with the most dense samples, however, their densification level was relatively low in some cases. Nevertheless, the 16 h and 24 h specimens were able to increase the wear performance by 93.30 % and 53.80 % respectively.

Especially, the penetration depth was lower in the MS1/VC samples, which indicates that the indenter ball was not able to wear the track as much as the pure MS1 samples.

The worn surfaces were analyzed with optical microscopy and the tracks were covered with adherent material. VC particles acted against the indenter and were acting as adhesive points for the worn material. In Figure 8.17 the track of the 2 h milled sample is shown. The VC particle had a size of 20 microns and was covered with adherent worn material from the indenter and the worn track. This material was compressed and polished underneath the indenter and resulted in a gliding plane which somewhat falsified the COF results. Furthermore, the worn material must have become very hot as EDX analysis revealed a high amount of oxygen, which resulted in a layer of FeO. In Figure 8.18 a SEM image is given, showing the stuck worn material. Obviously, a VC particle was sticking out of the material causing the worn material to get stuck next to it. EDX analysis, provided in Table 8.9, shows the elemental punctual analysis. *Spektrum 38* refers to the pure worn material, which stuck on the surface and *Spektrum 39* refers to the VC particle underneath.

8.4 Conclusions

The analysis of the mechanically alloyed MS1/VC through SEM revealed the great capabilities of MA. It is a cost-effective and fast tool to form coalescences of separate powders. However, there is a unique process window suitable for each powder mixture and it is dependent on the initial size

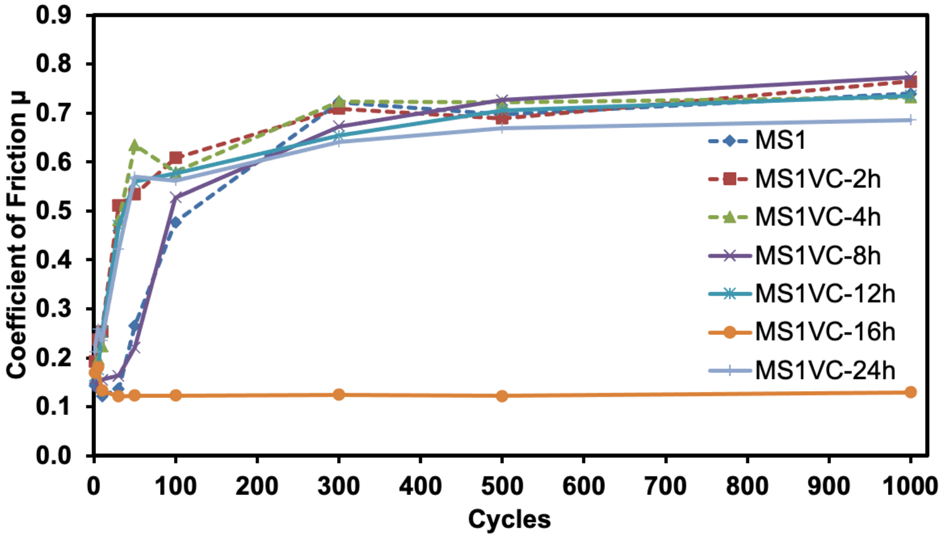

Figure 8.14: Graph of the coefficient of friction of the MS1VC samples with 33 microns of VC.

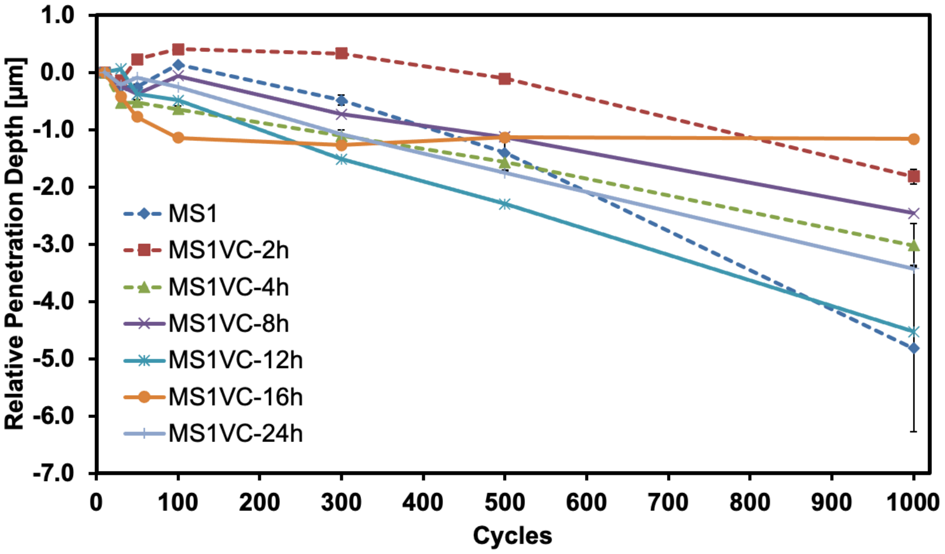

Figure 8.15: Graph of the relative penetration depth of the MS1VC samples with 33 microns of VC.

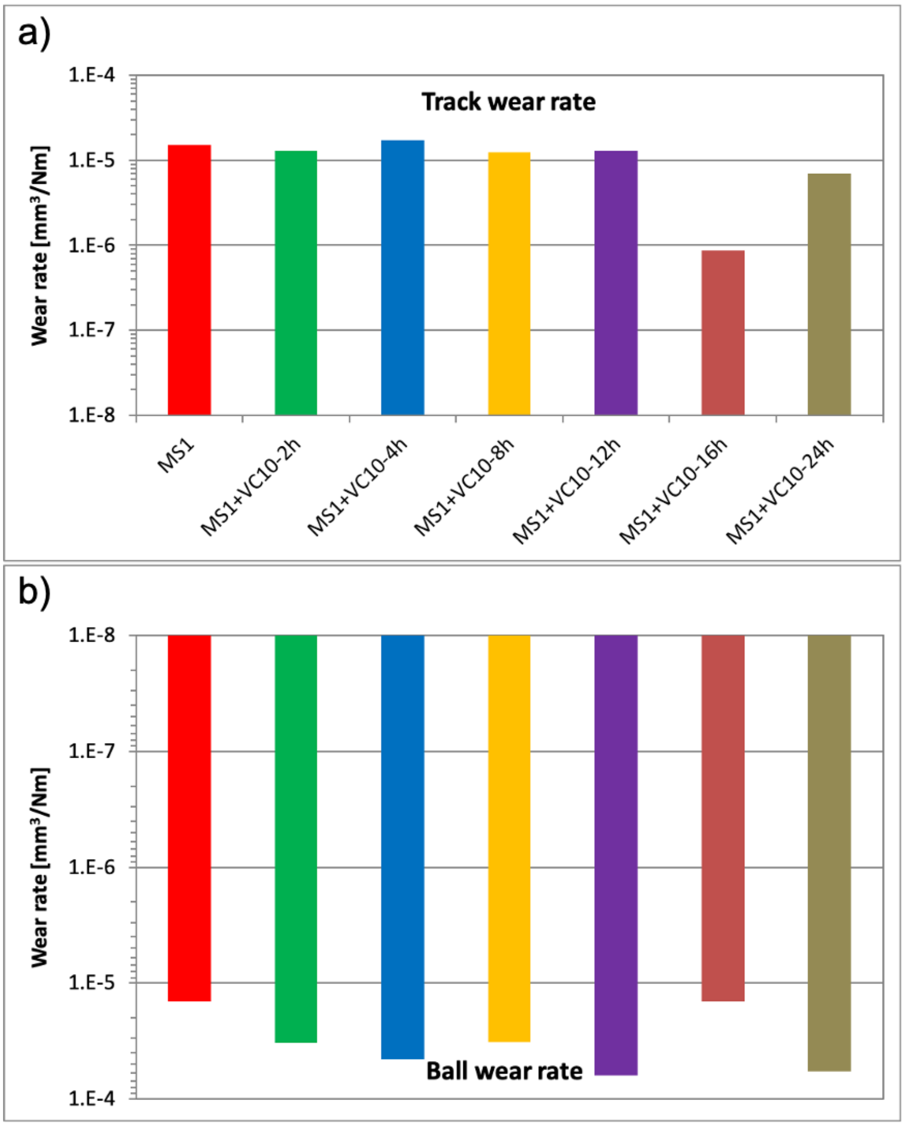

Figure 8.16: Graphs of a) the track wear rate and b) the ball wear rate of MS1VC.

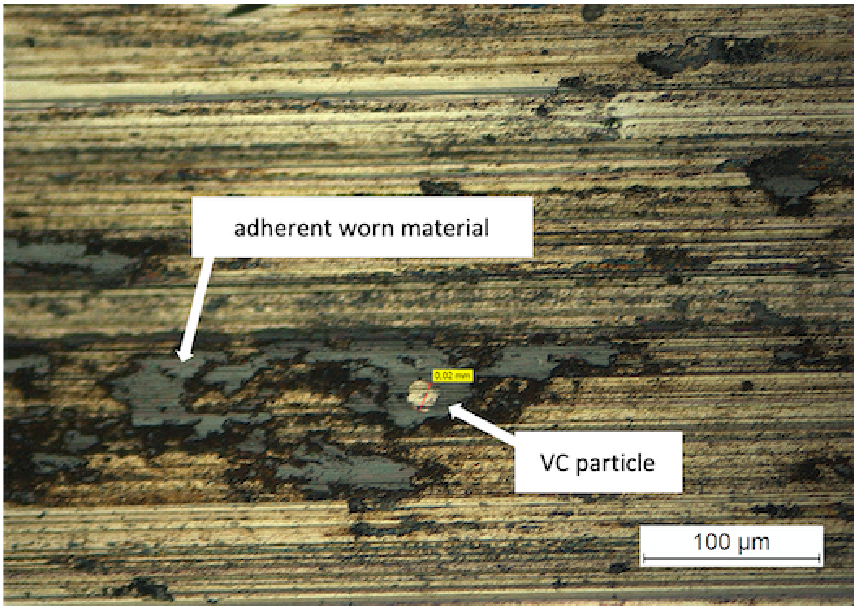

Figure 8.17: Optical microscopy of the track after tribological testing of the MS1VC 2 h milled sample.

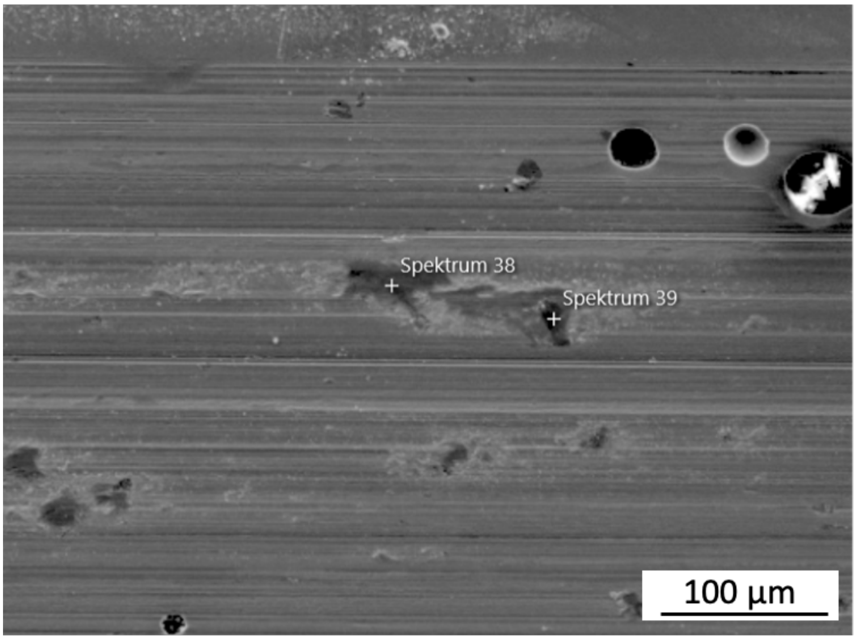

Figure 8.18: SEM image of the worn track after tribological testing.

Table 8.9: EDX analyses of the MS1VC sample that was milled for 2 h, SLM processed and tribologically tested.

Element	Mass Percent *Spektrum 38*	Mass Percent *Spektrum 39*
C	3.58	18.78
N	3.52	
O	33.17	
Al	0.25	
Si	0.15	
Ti	3.53	
V	1.83	79.71
Cr	0.60	
Fe	49.80	1.73
Ni	2.89	
Mo	0.68	
Sum:	100.00	100

distribution, material ductility and hardness, to mention the most important. Due to the big initial size distribution of 1-33 μm of the VC feedstock powder and its high strength, the VC experienced a significant decrease of the average particle size whereas the MS faced huge deformations leading to a non-spherical irregular shape the longer the milling took place. As the VC was fractured rather than deformed in the beginning of the MA process, particle refinement of VC as a pre-process is advisable. This way milling times could be kept lower and therefore keep the initial MS1 particles more spherical as a non-spherical shape leads to instability during SLM processing respectively instable melt pools and inhomogeneous layer coatings. However, after SLM processing the 16 h milled powder with various energy densities it was not possible to detect unmelted VC particles with a scanning electron microscope or energy dispersive X-ray spectroscopy. Instead, homogeneously distributed primary solidified VC particles were spotted in the SLM processed specimens. To prevent samples porosity further optimization studies should be performed. The resulting main conclusions are:

- The tendency to achieve fully melted VC particles during SLM processing is dependent on their size and the location in the powder. It was discovered that smaller sized particles of VC will more likely be melted if they are part of a bigger MS1 particle (i.e. in form of a coalescence).
- A high energy ball mill is a necessary and affordable tool to not just homogeneously distribute different powders, but also to achieve grain refinement and coalescences in one process. Furthermore, small amounts of powder can be processed.
- At 67 J/mm^3, which is the advisable energy input for pure MS1, the composite powders were poorly melted and the specimens showed lots of porosity and imperfections. At 179 J/mm^3 the results were remarkably better and a higher part density was achieved. Nevertheless, there were still some pores, which could be eliminated through further parameter development or initial VC refinement.
- After 8 hours of MA the amount of unmelted VC particles was very low and after 16 hours there were almost none visible, which indicates further refinement of VC. After 24 hours of milling there were no VC particles visible anymore and a phase formation from γ-Fe to α-Fe was observed. Furthermore, the non-stoichiometric V_8C_7 transformed to stoichiometric VC which indicates the formation of primary precipitated particles which solidified after being fully melted by the laser.

- The presence of VC in the metal matrix of the MS1 leads to superior hardness and even though the part density was not above the desired 99 % boundary, the in-situ formed MMC exceeded the maximum achievable hardness of the base material. While measuring microhardness at the 4 hour milled SLM processed specimen, the standard deviation was astonishingly low and the maximum measured hardness was at 439 HV1.
- The tribological performance can be increased with reinforcing VC particles. In specific, the 16 h and 24 h milled and SLM processed samples were able to decrease the wear rate by 93.30 % and 53.80 % respectively.
- The MS1/VC composite material was able to outperform the pure MS1 sample in the tribological tests. The indenter was not able to wear the MMC specimens as much as the pure MS1 samples and therefore, their penetration depth was lower.

9

SLM of Mechanically Alloyed MS1/VC: Optimization of Bulk Powder Morphology

> An expert is someone who knows some of the worst mistakes that can be made in his subject, and how to avoid them.
>
> Werner Karl Heisenberg

9.1 Introduction

It was discovered in preliminary studies that it is possible to reinforce martensitic steel with carbides, like vanadium carbide or tungsten carbide, and to improve some material properties. The process route of the bulk powder treatment is very critical to end up with high quality and dense selective laser melted parts. It was discovered that mechanical mixing of hard VC particles with soft maraging steel powders is not an optimal way to create metal matrix composites. Instead, mechanical alloying is a more advisable processing technique. However, if the milling parameters are not chosen wisely, the parts will very likely fail or will not meet the quality criteria. Too much energy in the ball milling system will plastically deform the MS1 particles before coalescences with the VC particles will be formed. In preliminary investigations, it was found that the initial particle size of the VC has to be relatively small, to decrease the milling time and therefore, to decrease the deformation process on the MS1 particles. However, if the initial particle size is too small (i.e. nano-sized), irregular shaped VC particles will agglomerate and therefore, the flowability of the powders will be decreased. It is advisable to use particles in the sub-micron to micron size range.

It was decided to deepen the investigations of the $MS1_{90}VC_{10}$ powder composition, which contains, as the name suggests, 90 wt.% of maraging steel and 10 wt.% vanadium carbide. In Chapter 8 a metal matrix composite was investigated with 10 wt.% of VC-33, which had a particle size between 1 - 33 microns. The first results were very promising, but the milling process deformed the maraging steel particles too much - especially after longer milling times. Therefore, the flowability decreased and the SLM process was not as stable as desired. The logical next step was to decrease the initial particle size of the bulk VC powder.

One of the most common techniques to identify the process window for a new type of alloy or powder system, is the approach of the volumetric energy density (VED or E_v). It is widely used in the scientific field and was also used in this study. The goal is to minimize porosity respectively to maximize the part density. It takes into account the combined effects of the main SLM process parameters. The scanning speed, the hatching distance, the layer thickness and the laser power. The parameters which produce the highest relative part density are the most desired ones. The literature [231] suggests Equation 1.2 found in Chapter 1. Equation 1.2 describes the volumetric energy density, expressed in J/mm^3, in which P is the power of the laser source, h stands for the hatch distance, v for the scan speed and t for the layer thickness. The maximum volumetric energy density is achieved with the maximum laser power, which was 100 W in this study. However, there are always unpredictable factors that influence the output of the laser, like a thin dust layer on the laser optics or a non-uniform continuous wave. Therefore, the maximum value for the DoE was set to 99 W or 99 % of the theoretical maximum. The values of the scanning speed, hatching distance and the layer thickness will decrease the volumetric energy density. To investigate the effect of various parameters on the hardness and density, eight parameter sets were chosen.

9.2 Experimental Procedures

In Chapter 8 a high energy ball mill with a tungsten carbide jar was used to investigate the MS1/VC powder system. The result were high deformations of the soft martensitic steel particles, which should be avoided respectively decreased. One way to influence the results was to decrease the milling times, but this also would have meant less coalescences of MS1 and VC particles. This is the reason why a VC powder with a smaller mean particle size was chosen for the mechanical alloying process. Because of the smaller initial VC particle size, there is less milling time needed to form the aforementioned coalescences, as the VC does not need to be cracked in advance. However, smaller particles are known to have a higher tendency for agglomerations due to the higher Van der Waals forces. Therefore, the particle size was chosen to be not in the nano-scaled size distribution. Another approach was to decrease the milling energy brought into the system during the mechanical alloying process. To understand the influence of different materials on the powder particles for the vial and the balls used during high energy ball milling, two materials (i.e. 440C steel and WC) were investigated. For the calculations of the effects, the calculations were based on the work of Schwarz and Koch [110]. Their theory assumes that particles are deformed by localized shear and the particle temperature increases through Equation 2.1. The respective calculations can be found in Chapter 2. According to the performed calculations, the irradiated temperature rises per impact are:

- $\Delta T_{VC_{440C}} = 32.19$ K
- $\Delta T_{VC_{WC}} = 70.52$ K

It can be said that the tungsten carbide balls significantly increase the temperature compared to 440C steel balls. The WC balls and jar increase the temperature by approximately 219 %. However, there is little known about the real influence of different materials used for mechanical alloying and there were no scientific research papers found in the literature. The optimal way to investigate the effects of ball milling would be an in-situ process monitoring and a direct measurement of the particles, which is, at the time of writing this report, impossible. Therefore, a 440C and a WC ball milling equipment was used with MS1/VC powders and analyzed afterwards, to understand the effects of the different calculated temperature rises.

After the ball milling process, the powders were analyzed and then SLMed to produce samples for further analyses.

9.2.1 Powder Preparation

A homogeneous mixture of the maraging steel and the vanadium carbide was prepared. For this, gas atomized commercially available MS1 (EOS GmbH, Germany) and irregular shaped VC powder (Treibach Industrie AG, Austria) was mixed for 15 minutes in a Turbula tumbler mixer (Willy A.

Table 9.1: Milling times of the MS1/VC mixture and cool-off breaks.

total milling time	1 h	2 h	4 h
total process time	1 h 15 min	2 h 30 min	5 h

Bachofen AG, Switzerland). The maraging steel powder had a size distribution of 15 - 40 μm and the chemical composition can be found in Table 4.1. The particle size of the VC powder was given from the manufacturer as < 2.5 microns and the chemical composition of the VC powder was:

- V_8C_7 (main content)
- V_2C
- V_6C_5
- stoichiometric VC

The MS1/VC mixture consisted of 90 wt.% MS1 and 10 wt.% VC. After the mechanical mixing, a planetary high energy ball mill (Fritsch Pulverisette 4, Germany) equipped with a 500 ml WC jar and WC balls was used for the first batch of powder production. The balls had a diameter of 10 mm and the ball-to-powder weight ratio was set to 5:1. The whole mechanical alloying process was performed under argon atmosphere to reduce the risk of unwanted oxidations. The milling parameters were the same as in preliminary studies and can be found in Table 8.2. The milling times were adjusted according to the smaller particle size and are shown in Table 9.1. After each hour, there were 15 minutes of a cool-down break set.

For the second batch, a vial and milling balls made out of 440C stainless steel were used. The milling parameters were not changed, but the milling time was adjusted. Due to time restrictions and to get powders with meaningful results, the total milling time was set to 5 hours including 15 min of break after each hour. In preliminary studies and analyses it was found that in most cases mechanical alloying should be performed somewhere between 2 to 6 hours. Setting the milling time to 4 hours seemed legit for this study and the parameters can be seen in Table 9.1. However, it has to be mentioned that the 440C vial did not have the possibility to use an argon inert atmosphere during ball milling.

After milling, samples were taken for further analysis. Then, the powders were sieved with a 75 micron sieve. As previous works showed that this process can be critical, if shaker towers are used, the sieving was done manually. A small spoon was used to vibrate and move the powder. The advantage of this was the fact, that small agglomerations, which would have been sieved out, were cracked up and therefore, went through the sieve.

9.2.2 SLM Process

For selective laser melting, an MCP-realizer (MCP-realizer SLM 250, Germany) was used to fabricate cylindrical samples. The specimens had a diameter of 8 mm and were built with a height of approximately 6 mm. The SLM printer was equipped with a ytterbium fibre laser with an output of 100 W. The laser spot diameter was measured at 0.12 mm. During SLM processing, the oxygen level was kept below 0.4 % to prevent oxidation. The scanning strategy included an alternating hatch pattern (i.e. 90 degree rotation). The layer thickness was fixed at 40 microns and the rest of the parameters were similar to the parameters used for $MS1_{90}VC_{10}$-33 mechanically alloyed powders. The SLM parameters are given in Chapter 8 in Table 8.4 and were based on a DoE performed with R-Studio (R Foundation for Statistical Computing, Austria) and the Federov operator.

9.2.3 Material Characterization

For cross-sectioning, the SLM processed samples were embedded and polished. To analyze the microstructure, the specimens were etched in an acid of 30 ml 32 % HCl, 15 ml 65 % HNO_3 and 30 ml 48 % HF. An optical microscope (Leitz Aristomet, Leica Microsystems, Germany) was used to analyze the porosity and the laser tracks of the samples. The microscope was furthermore equipped, with analytical dedicated software to calculate the relative density of each sample.

To analyze the mechanically alloyed powders and the SLM processed specimens more detailed, a scanning electron microscope (Tescan Vega 3, Czech Republic) was used. Images were taken with 20kV and either with a SE or BSE detector according to the requirements. The SEM was also equipped with a silicon drift detector (Ultim Max 40, Oxford Instruments, United Kingdom) to perform EDX analyses. With energy dispersive X-ray spectroscopy it is easier to find possible coalescences and agglomerations of the powders. Some samples were etched with nital or Adler's reagent to analyze the microstructure. For the phase analysis of the bulk powder and the printed specimens, X-ray diffraction was used. A PANalytical PW 3040/6 X'Pert Pro (United Kingdom) diffractometer with a Cu Kα radiation source measured the samples at 40 kV and 35 mA with a continuous scanning mode and a scanning rate of 5 °/min. 2-Θ was recorded between 30 degree and 90 degree.

Micro-hardness was measured using a dedicated micro-hardness testing device (Karl Frank GmbH, Germany) with a load of 9.8 N. At least four indentations were performed per sample. The particle size distribution was performed with a Microtrac SDC in combination with a Microtrac S3500 (both systems from Retsch GmbH, Germany). Tribological tests were performed using an Anton Paar (Anton Paar Group AG, Austria) CPX and an Anton Paar MST micro scratch tester. The spherical stainless steel indenter was loaded with 5 N. The duration of the test was 1000 cycles on a 5 mm track. The calotte of the worn stainless steel ball was measured using the micro scratch tester software in combination with an optical microscope. The track wear was measured and calculated with a profilometer (Dektak 150, Veeco, USA).

Charpy impact strength tests were done with V-notch specimens in a 10 mm x 10 mm x 55 mm dimension. They were manufactured according to the ASTM A370 / ISO 148 standards and tested accordingly. For the ultimate tensile strength tests, specimens according to the German DIN 50125 standard for UT strength tests were manufactured in the SLM machine. They had a diameter of 4 mm and a specimen length of 65 mm. These specimens were chosen to decrease the necessary amount of powder for SLM processing. As the specimen head was too small for the Zwick / Roell Zmart.Pro (ZwickRoell AG, Germany) tensometer, an adapter had to be designed and manufactured. The specimens were used in an unpolished as-built condition, but some specimens were heat treated at 490 ° C for comparison reasons.

9.3 Results and Discussion

9.3.1 Particle Size Distribution

First of all, the pure MS1 was analyzed. Both, the particle counting method and the particle volume method were used. In Figure 9.1 the results of the two methods are shown. The volumetric counting method indicates that there were slightly more particles found above 40 microns than the powder manufacturer suggested. However, if one compares the results with the numerical method, it is obvious that the amount of bigger particles must be relatively small.

The particle size distribution of the $MS1_{90}VC_{10}$-2.5 which was mechanically alloyed with WC equipment is shown in Figure 9.2. In Figures 9.2a), c) and e) the volumetric counting method was used and in Figure 9.2 b), d) and f) the numerical counting method was applied. Obviously, the amount of fine particles decreased with the milling time and more coalescences must have been formed. Interestingly, also bigger particles were decreased after 2 h of milling, but slightly

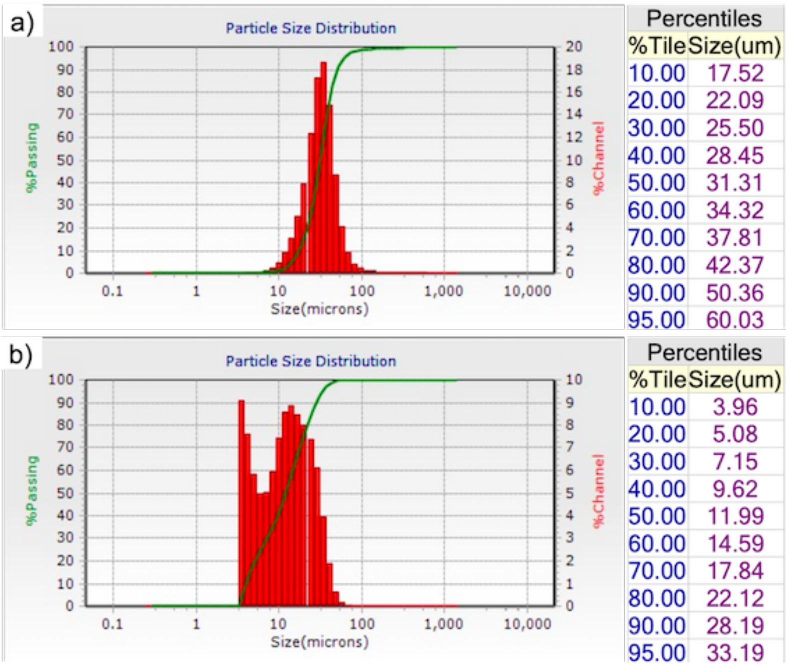

Percentiles	
%Tile	Size(um)
10.00	17.52
20.00	22.09
30.00	25.50
40.00	28.45
50.00	31.31
60.00	34.32
70.00	37.81
80.00	42.37
90.00	50.36
95.00	60.03

Percentiles	
%Tile	Size(um)
10.00	3.96
20.00	5.08
30.00	7.15
40.00	9.62
50.00	11.99
60.00	14.59
70.00	17.84
80.00	22.12
90.00	28.19
95.00	33.19

Figure 9.1: Particle size distribution using a) the volumetric method and b) the counting method of pure EOS MS1.

increased again after 4 h of milling.

Figure 9.3 shows the particle size distribution results for the mechanically alloyed powder using 440C stainless steel equipment. In Figure 9.3a and c the volumetric and in Figure 9.3b and d the numeric methods were applied. Figure 9.3a and b refer to an unsieved powder state, whereas Figure 9.3c and d show the results after sieving the powder with a 75 micron sieve. If one compares the unsieved results with the results of the unsieved WC equipment, it is very obvious that the 440C powders were substantially larger. This result is very surprising as the calculations of Equation 2.1 suggested a higher temperature and therefore, more energy in the WC system. It was expected that the higher energy would lead to more plastic deformation and as a result, a higher quantity of large particles. The obtained powders after 4 h of milling with the tungsten carbide ball milling equipment had a particle size distribution of $D_{10} = 9.49$ μm, $D_{50} = 28.50$ μm and $D_{90} = 61.24$ μm. The particles of the same powder composition and milling time, but mechanically alloyed with 440C stainless steel balls and jar, had a particle size distribution of $D_{10} = 21.82$ μm, $D_{50} = 46.83$ μm and $D_{90} = 127.7$ μm.

9.3.2 Powder Phase Formation using XRD

To identify any changes of phase formations after milling the powders in a high energy ball mill, an XRD apparatus was used. In Figure 9.4 the XRD chart, recorded with 2 theta is given. Unfortunately, only the 1 hour and the 2 hour results can be shown at the time of writing, as the results of the 4 h sample were not finished in time. However, no drastic changes are expected. It is just obvious that, the longer the mechanical alloying was applied, the less V_8C_7 peaks are visible due to a refinement of the VC particles.

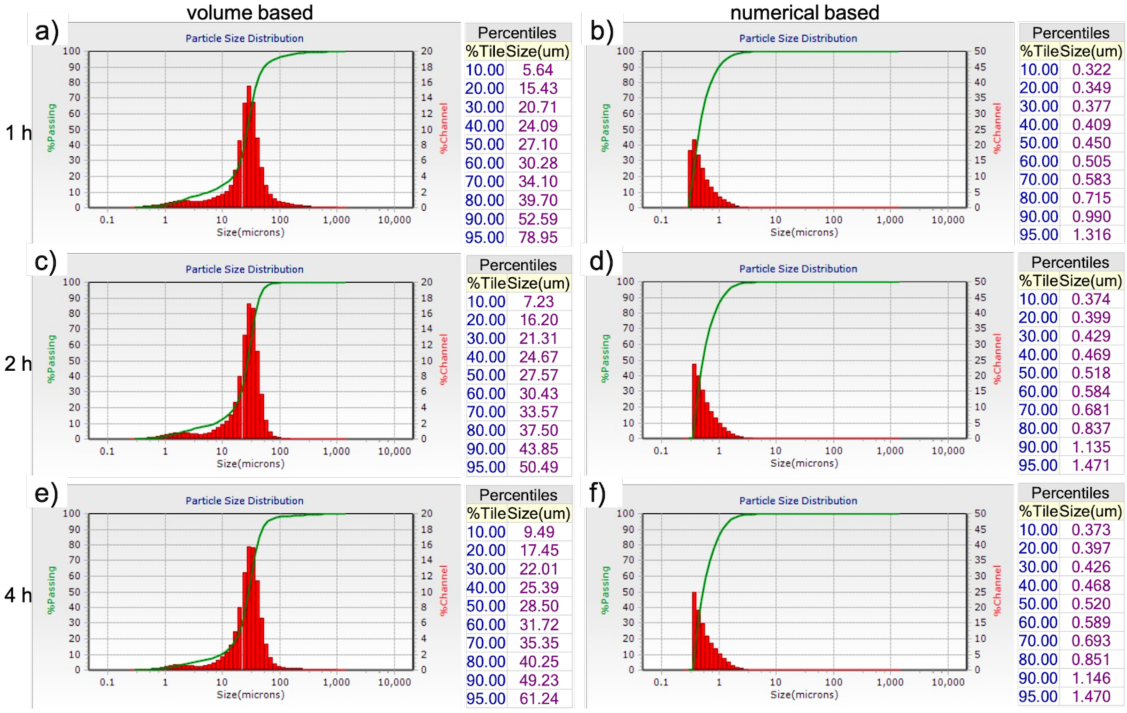

a) Percentiles

%Tile	Size(um)
10.00	5.64
20.00	15.43
30.00	20.71
40.00	24.09
50.00	27.10
60.00	30.28
70.00	34.10
80.00	39.70
90.00	52.59
95.00	78.95

b) Percentiles

%Tile	Size(um)
10.00	0.322
20.00	0.349
30.00	0.377
40.00	0.409
50.00	0.450
60.00	0.505
70.00	0.583
80.00	0.715
90.00	0.990
95.00	1.316

c) Percentiles

%Tile	Size(um)
10.00	7.23
20.00	16.20
30.00	21.31
40.00	24.67
50.00	27.57
60.00	30.43
70.00	33.57
80.00	37.50
90.00	43.85
95.00	50.49

d) Percentiles

%Tile	Size(um)
10.00	0.374
20.00	0.399
30.00	0.429
40.00	0.469
50.00	0.518
60.00	0.584
70.00	0.681
80.00	0.837
90.00	1.135
95.00	1.471

e) Percentiles

%Tile	Size(um)
10.00	9.49
20.00	17.45
30.00	22.01
40.00	25.39
50.00	28.50
60.00	31.72
70.00	35.35
80.00	40.25
90.00	49.23
95.00	61.24

f) Percentiles

%Tile	Size(um)
10.00	0.373
20.00	0.397
30.00	0.426
40.00	0.468
50.00	0.520
60.00	0.589
70.00	0.693
80.00	0.851
90.00	1.146
95.00	1.470

Figure 9.2: Volume based particle size distribution of mechanically alloyed MS1VC-2.5 with WC equipment after a) 1 h, c) 2 h and e) 4 h of milling and numerical based particle size distribution after b) 1 h, d) 2 h and f) 4 h.

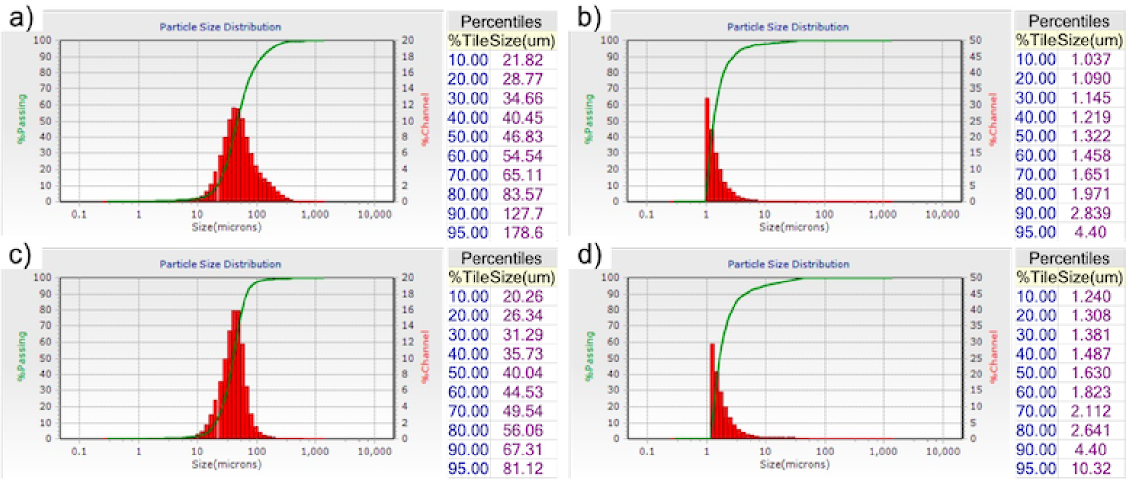

a) Percentiles

%Tile	Size(um)
10.00	21.82
20.00	28.77
30.00	34.66
40.00	40.45
50.00	46.83
60.00	54.54
70.00	65.11
80.00	83.57
90.00	127.7
95.00	178.6

b) Percentiles

%Tile	Size(um)
10.00	1.037
20.00	1.090
30.00	1.145
40.00	1.219
50.00	1.322
60.00	1.458
70.00	1.651
80.00	1.971
90.00	2.839
95.00	4.40

c) Percentiles

%Tile	Size(um)
10.00	20.26
20.00	26.34
30.00	31.29
40.00	35.73
50.00	40.04
60.00	44.53
70.00	49.54
80.00	56.06
90.00	67.31
95.00	81.12

d) Percentiles

%Tile	Size(um)
10.00	1.240
20.00	1.308
30.00	1.381
40.00	1.487
50.00	1.630
60.00	1.823
70.00	2.112
80.00	2.641
90.00	4.40
95.00	10.32

Figure 9.3: Particle size distribution of mechanically alloyed MS1VC-2.5 using 440C equipment after 4 h of milling diagrams showing the volumetric method with a) unsieved and c) sieved powder and the numeric method with b) unsieved and d) sieved powder.

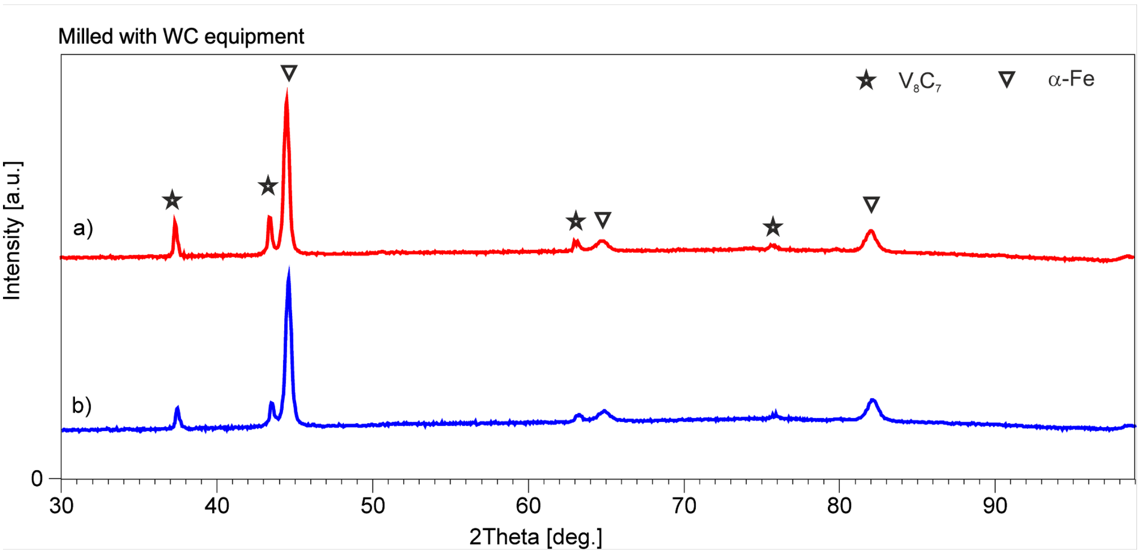

Figure 9.4: XRD graphs of the a) 1 h milled and b) 2 h milled MS1VC powders milled with WC equipment.

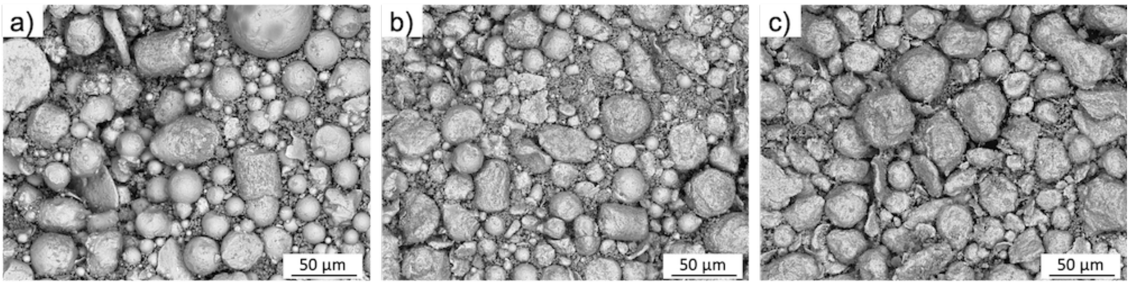

Figure 9.5: SEM images of the MS1/VC-2.5 powder ball milled with WC equipment after a) 1 h, b) 2 h and c) 4 h.

9.3.3 Powder Morphology using SEM

The particle morphology and the microstructural evolution of the mechanically alloyed powders with WC equipment as a function of the ball milling time is described in the SEM images in Figure 9.5. The images confirm the results of the particle size distribution diagrams. The powder decreased in size in the beginning, but after 4 h of milling the powder increased again. According to the morphology of the powders, there was some plastic deformation in the beginning due to the ductile nature of MS1 and after 2 h there was a lot of fracturing of particles. Figure 9.5a to c indicate that the applied mechanical alloying had an effect on the particle morphology, particle size and the particle size distribution. After 2 h of milling, the cold-welding mechanism became dominant and the particle size slightly increased. Furthermore, there were more and more coalescences found in the powder. The images also reveal a minor tendency for elongated cylindrical shaped particles and flat flake-like shaped particles.

The evolution of the mechanical alloying process is perfectly illustrated in Figure 9.6. In Figure 9.6a the ball milling caused stress concentrations on the outside of the powder particles and the MA process slowly intensified. However, these reinforcements of the composite material are very minor and just on the surface of the matrix material. In Figure 9.6b a powder particle is shown, that was already undergoing plastic deformation, fracturing and more intense cold-welding mech-

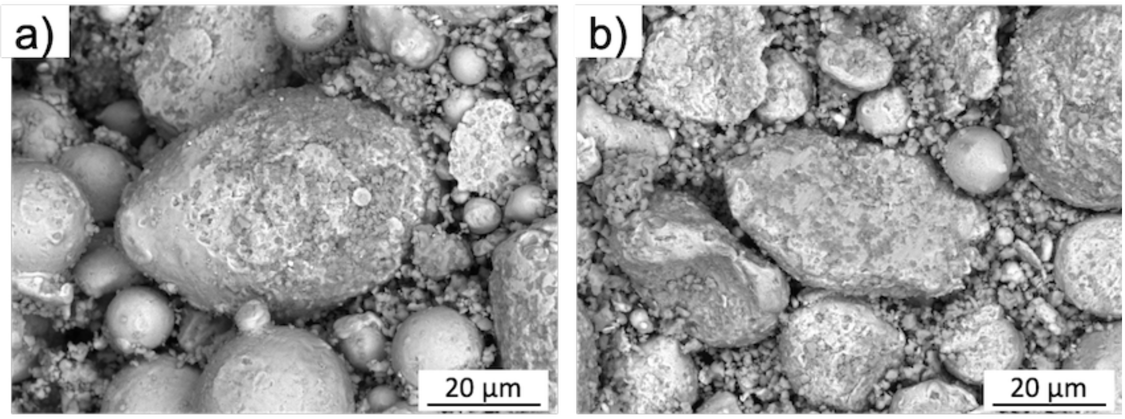

Figure 9.6: Detailed SEM images of powder MA with WC jar and balls after a) 1 h and b) 2 h.

anisms. The reinforcing carbides already are deeply embedded into the MS1 particle.

The other powder batch that consisted of MS1 and VC and was ball milled with the 440C milling equipment, was analyzed with an SEM too. The powder was sieved with a 75 micron sieve and two separate SEM analyses were made. In the beginning of this study, thoughts about how the powder morphology would look like and how the powders would differ from each other were made. It was expected, due to the calculation results of Equation 2.1, that the WC ball milling equipment would deform the powder particles more than the 440C equipment. A higher energy in each ball-to-ball or ball-to-wall impact causes a higher temperature rise and therefore, the MS1VC powder should plastically deform more in the WC ball milling equipment. However, the results were different than expected as one can see in Figure 9.7.

The image shows the significant differences of the size distributions, but also shows how perfectly embedded the VC particles were. There were almost no free VC particles in the powder mixture and therefore, the MS1 and the VC powders were obviously mechanically alloyed. However, the morphology of the powders was far from spherical. This caused severe problems during SLM processing. Further, it was against the expectations to see such a plastic deformation and fracturing in this powder batch. As mentioned, the theoretically calculated temperature rise per impact was lower and therefore, less deformation was expected.

To understand, if there were any other elements in the sample, due to wear of the 440C material, EDX analysis was performed. The results can be found in Table 9.2. Due to the mechanical alloying under standard atmosphere, some oxygen can be seen. The level of oxygen (i.e. ˜2.36 %) was higher than in the WC equipment. In fact, there was almost no oxygen found in the powder batch milled with WC equipment. However, it is unlikely that oxygen caused the bigger average particle size distribution and the more extreme plastic deformation.

Mechanical alloying always forms cold welded particles and builds flattened layered composites in form of a compact. The size of these formed compacts depends on the balance between cold welding and subsequent fracturing. Eventually, a steady state size can be reached [232]. In this study, all parameters were kept as similar as possible to compare the results of the different ball milling equipments. It was understood that the WC equipment causes a higher temperature rise per impact. The radiuses of the main disks, the rotational speeds, the diameters of the jars, and the ball-to-powder weight ratios were kept the same. The only differences were the atmospheres, the used materials for the balls and the jars and of course the amount of balls used due to the lower density of steel. As the oxygen was not significantly different and the different heat capacities were considered in the calculations, the only influencing difference was found in the amount of used balls. As the ball-to-powder weight ratio was kept the same, more balls had to be used with 440C.

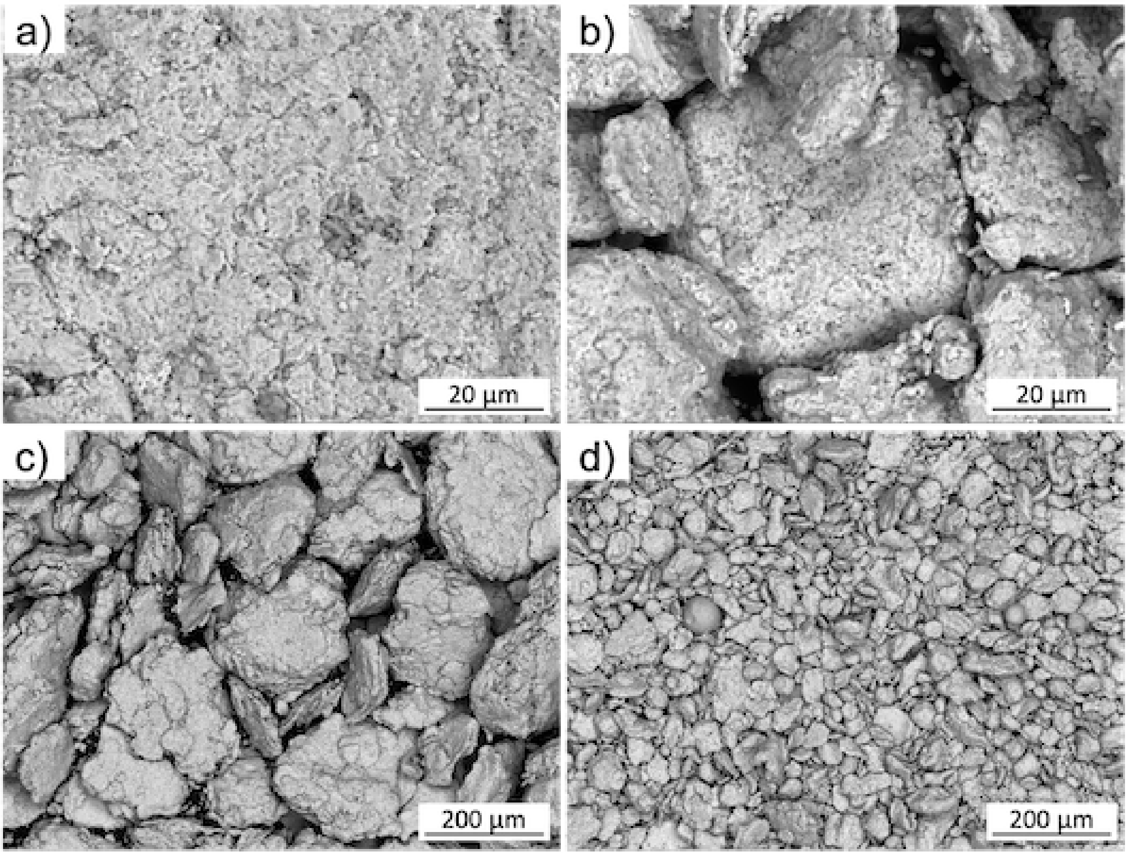

Figure 9.7: SEM images of the MS1/VC-2.5 powder ball milled for 4 h with 440C equipment with a particle size of a), c) > 75 μm and b), d) < 75 μm.

Table 9.2: EDX analyses of MS1VC powder that was milled for 4 h with 440C equipment.

Element	Mass Percent *Measurement 1*	Mass Percent *Measurement 2*
C	8.13	7.87
O	2.46	2.25
Ti	0.73	0.65
V	10.29	11.53
Fe	55.82	54.96
Co	7.73	7.54
Ni	12.20	12.53
Mo	2.65	2.67
Sum:	100.00	100

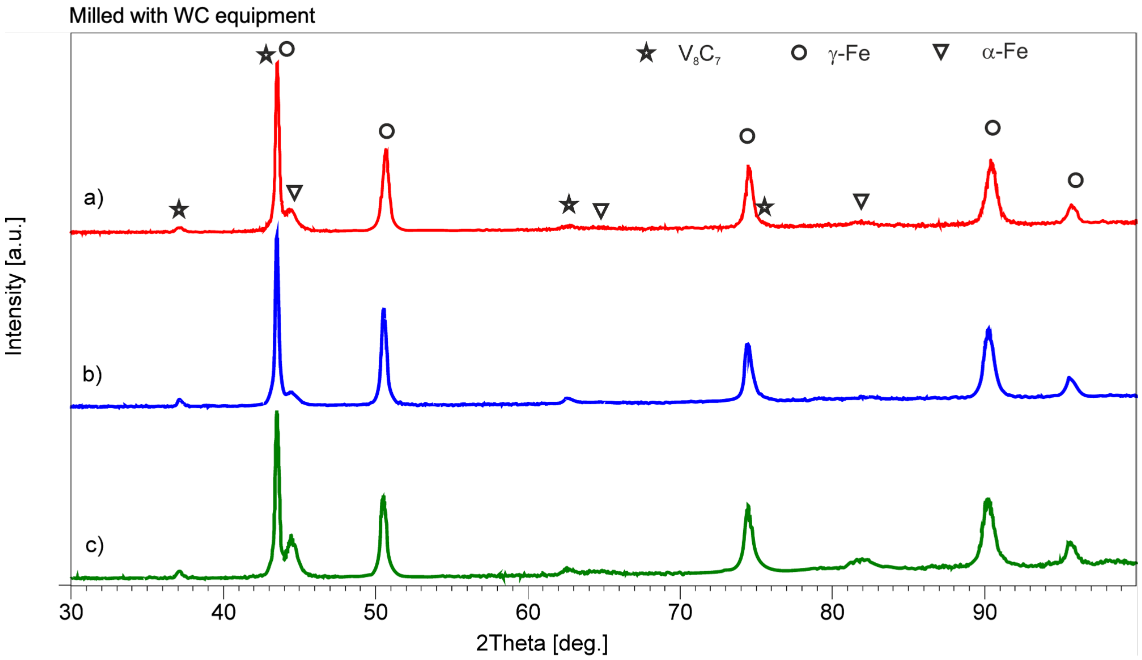

Figure 9.8: XRD graphs of the a) 1 h , b) 2 h and c) 4 h milled and SLMed MS1VC samples milled with WC equipment.

More balls in the vial also meant more impacts on the powder and this very likely caused such diverse powder morphologies.

9.3.4 Phase Analysis of the SLM Processed Samples

In the SLM processed and mechanically alloyed specimens it was found that austenite was formed during solidification. In Figure 9.8 the XRD results of the samples after 9.8a 1 hour, 9.8b 2 hours and 9.8c 4 hours of milling and SLM processing are shown. The gamma-phase is shown as a circle and the peaks for γ-Fe are very dominant. As a matter of fact, pure MS1 is a martensitic α-Fe (bcc), but similar results were found in Chapter 8. Obviously, the high cooling rate of the V_8C_7 influenced the martensite starting temperature and therefore, preventing a martensite formation. The non-stoichiometric V_8C_7 did not form to stoichiometric VC, as in Chapter 8, which indicates that there was no elemental transition between the constituents.

9.3.5 Densification and Defects in the SLM-processed Specimens

Specimens were SLM processed using the 440C ball milled powder and the powder that was manufactured with tungsten carbide equipment. Even though, it was possible to fabricate samples with the 440C powder, the results were far from acceptable. Several attempts were necessary to finally print test cubes for density measurements, but due to their high porosity, the samples were not analyzed any further. It was found that the far-from-spherical powder morphology significantly influenced the outcome of the SLM processed samples. Their densification results are shown in Figure 9.9 after etching. Figure 9.9a shows the sample without heat treatment and Figure 9.9b shows a sample after 6 hours of 490 ° C.

The embedded and polished WC equipment based samples were analyzed with an optical microscope. In Table 9.3 the specimens and their measured respective relative densities are given. The smaller average particle size, compared to the investigations with VC-33, significantly improved the achieved relative densities and the porosities. The overall highest density was measured

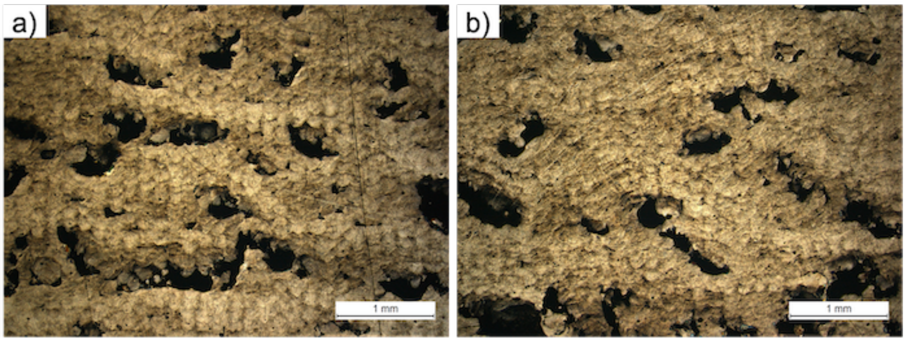

Figure 9.9: OM images of the MS1/VC-2.5 powder ball milled for 4 h with 440C equipment after SLM processing a) without and b) with heat treatment.

at specimen nr. 10 which had a laser power of 99 W, a scan speed of 177.78 mm/s and a hatch distance of 94 microns. Therefore, the energy density was 147.09 J/mm^3. In Figure 9.10 specimen no. 10 is shown after 9.10a 1 h, 9.10b 2 h and 9.10c 4 h of milling. After 1 h of milling, there were some lack of fusion pores, which might have been caused by uneven powder coatings. If the powder layer was too high in these areas, there was insufficient energy put into the powder and the welding process was not perfect, causing interlayer porosity [233]. Figure 9.10c shows some blowholes which are related to gas entrapments owing to vaporization. These defects are described by the Marangoni effect and were found mostly in the 4 h milled samples. As milling times increased, the reinforcing component was more and more mechanically alloyed with the matrix material. This lead to a higher influence in the melt pool as MS1 and VC have a contrasting melt temperature and dissimilar heat conductivities. The surface tension and the Marangoni flow increase and the melt pool becomes unstable. Droplets can form, if the direction of the material flow changes from outward to inward and therefore, to the laser beam. As a result, spatters will form through the balling effect. In these areas, there is insufficient material and gas can be trapped causing blowholes [12].

Another possibility for defects is insufficient energy density resulting from too little laser power or too high values for the hatching distance, layer thickness or scanning speed. In Figure 9.11 all SLM processed samples are shown, which were made out of 1 h mechanically alloyed powder. Obviously, lower energy levels (i.e. around 67.21 J/mm^3) are heating the melt insufficiently, to bind the various layers together. As a result, there was a lot of porosity in these specimens. Figure 9.12 shows the MS1/VC-2.5 samples manufactured with 2 h milled powder and in Figure 9.13 the samples based on 4 h mechanically alloyed powder. One can see that the high energy ball milling must have had an impact on the melt temperature and the heat conductivities. The more VC was embedded into the MS1 matrix material, the more energy density during SLM processing was necessary, to melt the material properly and to increase the relative density. Between 67.21 and 96.69 J/mm^3 there was a lot of porosity found in the 4 h milled specimens.

9.3.6 Analysis of Density

To understand the results of the relative density measurements, R Studio was used to predict the optimal parameter zone. The prediction model was performed for 99 W of laser power. In Figure 9.14 the predictions for 1 h, 2 h and 4 h of mechanically alloying are given. The calculations were very similar and the optimal parameters are suggested at approximately 75 microns of hatch distance and below 180 mm/s scan speed. These parameters indicate that an even higher melt temperature than in the produced samples is advisable.

Table 9.3: Achieved relative densities of all SLM processed specimens.

Spec. Nr.	Energy density [J/mm^3]	Rel. D. 1 h [%]	Rel. D. 2 h [%]	Rel. D. 4 h [%]
2	117.90	97.09	96.86	94.83
3	179.56	98.16	98.09	97.87
5	67.21	76.44	83.38	74.18
6	109.33	97.98	98.53	96.78
8	84.82	95.09	91.30	95.30
10	147.09	98.41	99.28	98.44
11	200.89	98.16	98.48	93.70
18	96.69	97.49	98.47	96.63

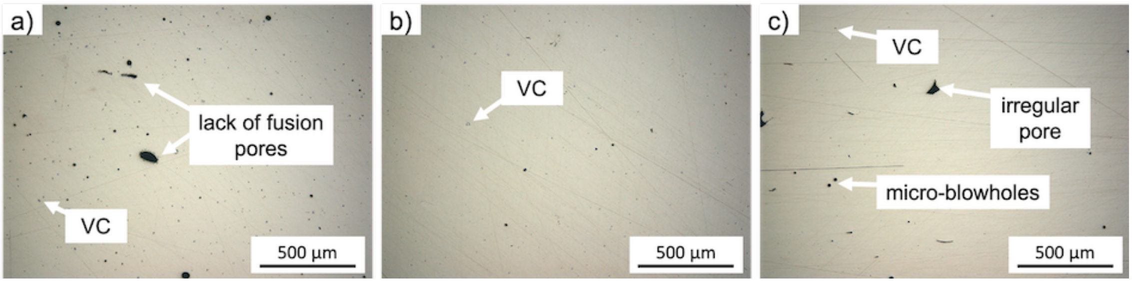

Figure 9.10: SEM images of a) 1 h, b) 2 h and c) 4 h milled (WC) and SLM processed samples with the same energy density.

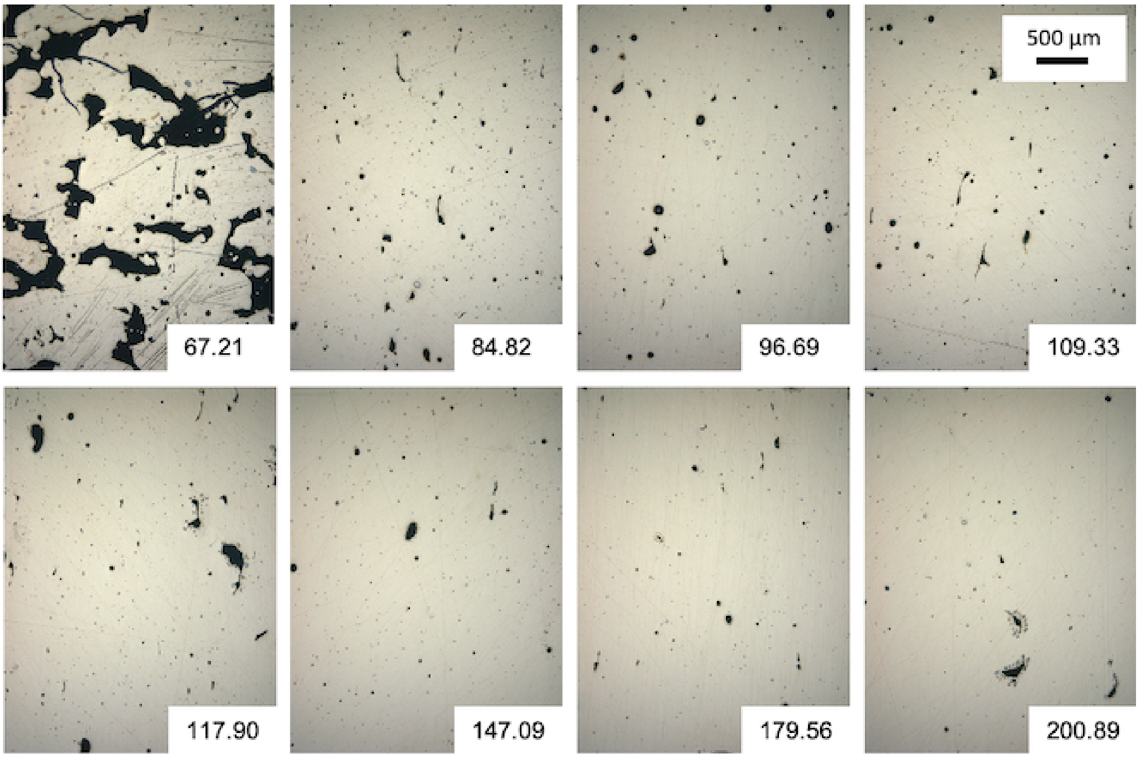

Figure 9.11: Optical microscopy of all SLM processed MS1/VC-2.5 samples mechanically alloyed (WC) for 1 h.

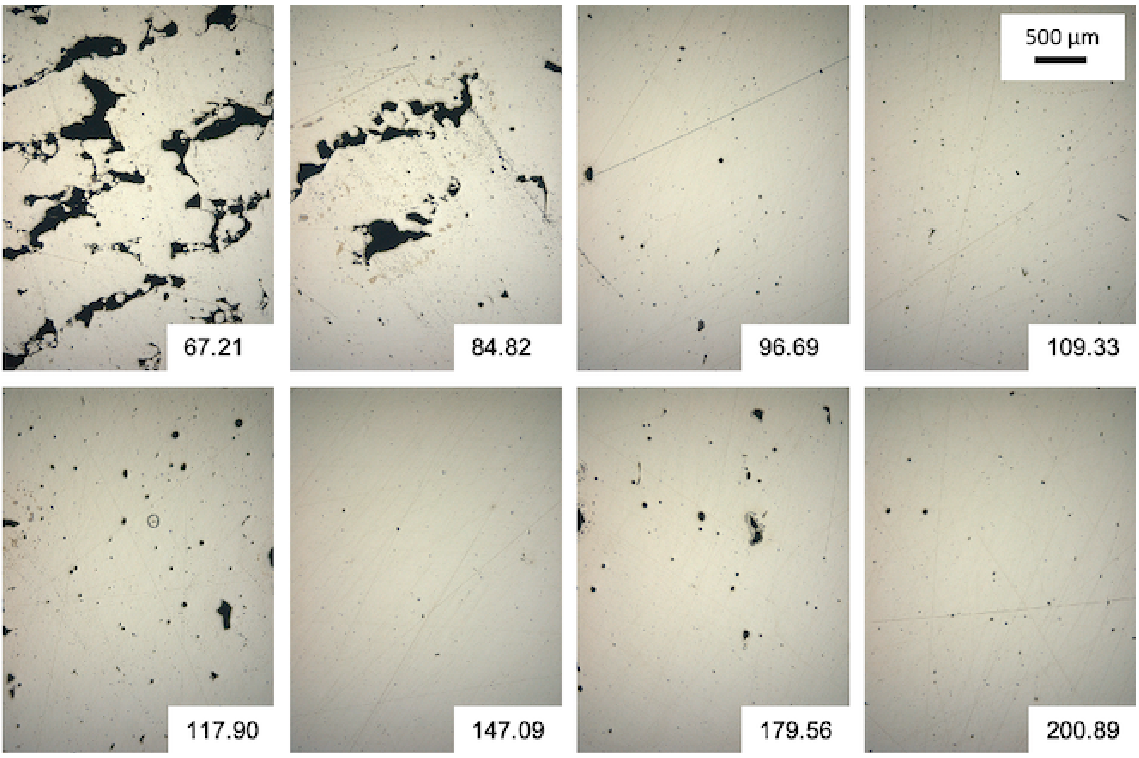

Figure 9.12: Optical microscopy of all SLM processed MS1/VC-2.5 samples mechanically alloyed (WC) for 2 h.

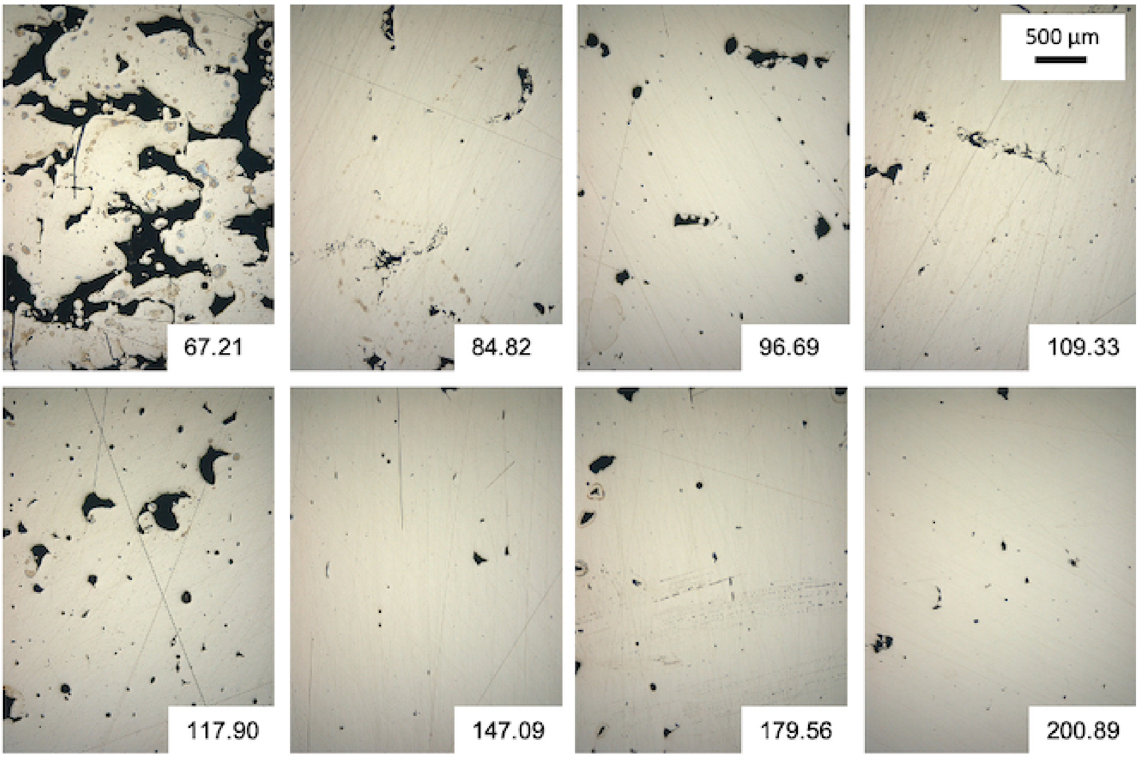

Figure 9.13: Optical microscopy of all SLM processed MS1/VC-2.5 samples mechanically alloyed (WC) for 4 h.

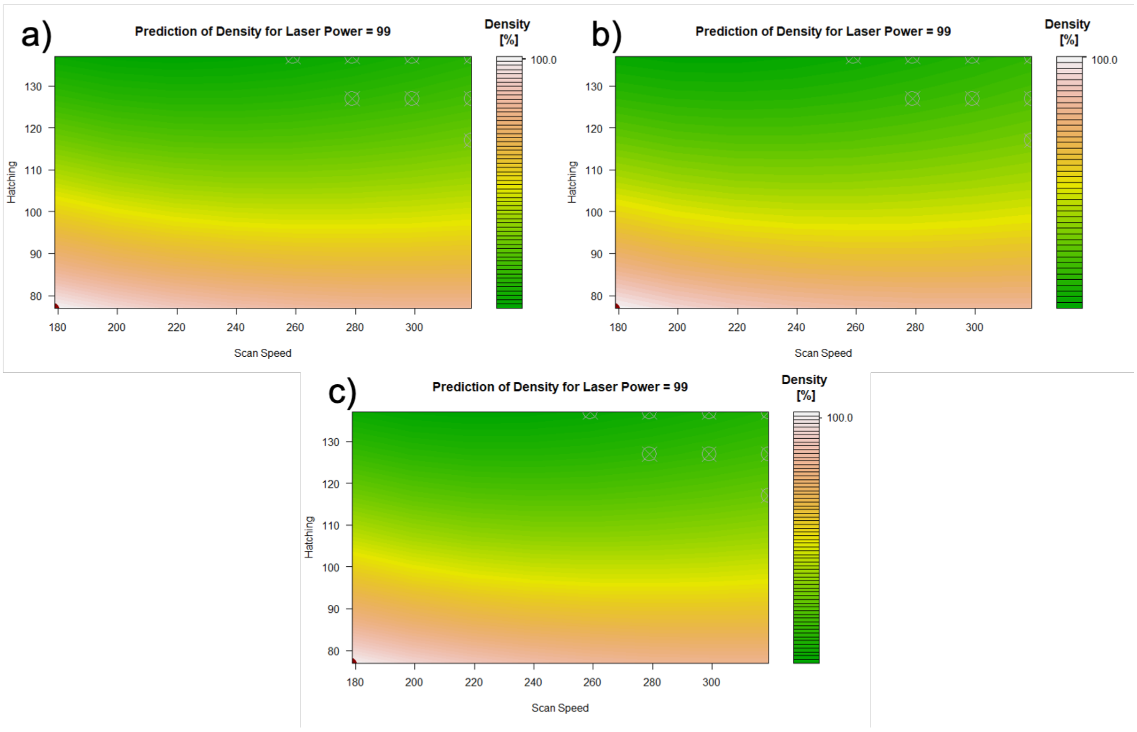

Figure 9.14: Prediction of the optimal relative density for MS1VC with 2 μm particles mechanically alloyed for a) 1 h, b) 2 h and c) 4 h.

9.3.7 Microstructure Analysis with SEM

In Figure 9.15 an SEM microstructural image is shown of the composite material after 9.15a 1 h of milling, 9.15b 2 h of milling and 9.15c 4 h of milling. In Figure 9.15a some undissolved VC is visible, which was not melted by the laser. A small round-shaped black particle can also be seen in the image, but it was impossible to analyze which kind of particle it was. One explanation could be that there was already some primary VC in the SLM processed sample. On the other hand the black particle could also be just a nano blowhole. Neither the EDX detector nor the SE detector delivered any helpful information due to the resolution of the detectors. The image also shows a primary formed grain with a size of several tens of microns. These grains can sometimes even grow across laser tracks and become relatively large. Due to the fast cooling happening during selective laser melting, these grains are normally significantly smaller compared to their casted counterparts. However, under certain circumstances, they continue to grow. Figure 9.15b again shows some primary grains, but more interestingly several black particles. In this case it was very likely that these particles were primary solidified vanadium carbide particles. After 2 h of milling, the VC was refined and embedded into the MS1 particles. Therefore, the laser was more likely melting the VC. The VC composite material is completely dissolveable above the liquidus line, but separates underneath and forms precipitated primary carbides during solidification.

Compared to the microstructure of pure MS1, the grain size was slightly decreased. However, this cannot be concluded solely to the introduction of VC. During SLM processing, there are many influencing parameters. Especially, the rapid solidification plays a significant role on grain refinement. Therefore, other factors could have lead to finer grains. Nevertheless, it is well known that reinforcing elements and particles can act as starting point for grain growth and nucleation [12]. The SEM revealed some nucleation sites starting from undissolved VC which assisted the nucleation process. As there were also columnar dendrites found in the SLM processed samples (i.e. 9.15d), the temperature gradient in the SLM process must have been positive (G > 0) and a lot

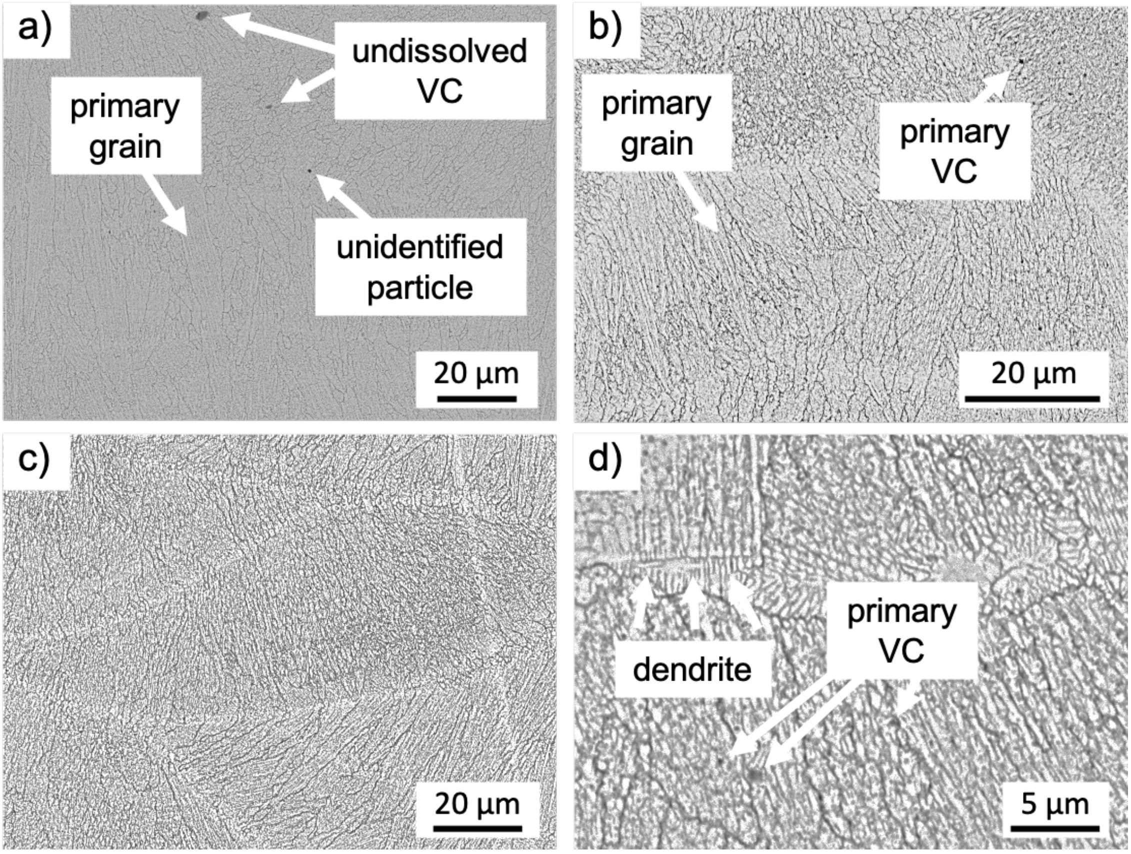

Figure 9.15: SEM images of MS1/VC-2.5 mechanically alloyed for a) 1 h, b) 2 h, c) 4 h and d) a detail image of dendrites forming (WC).

of energy was in the melt. If high energy levels are used, the thermal gradient is lower and slower undercooling occurs, which will result in a coarse dendritic microstructure [231, 234]. In selective laser melting, the overall cooling rate is significantly higher than with other techniques, and the undercooling rate can be controlled with the laser scan speed. Further, the microstructure typically contains grains formed by epitaxial growth. While solidification occurs, the grains grow according to the direction of the thermal gradient. As each previous layer is continuously remelted, the grains will be remolten and then adopt to the crystal structure and orientation as the ones below. This is called the *epitaxial growth mechanism.* The second grain growth mechanism is caused by dissonance of the melt pool front. Much finer grain structures grow toward the center of the melt and form columnar grains [12]. An overview of the various solidification forms is given in Figure 9.16. Further, Figure 9.15d did not just reveal very fine dendrite forming, but also a lot of evenly distributed primary VC in the microstructure. Such a fine distribution is exactly what is desired for strengthening mechanisms.

Interestingly, the specimen processed with the 440C ball milling equipment had a very different microstructure compared to the other batches. The microstructure was investigated using a scanning electron microscope and can be seen in Figure 9.17. The formed grains were significantly larger and the dendrites were forming much longer. This is caused by either a slower solidification speed or the laser remelted more layers and therefore, the track depth was higher. As the samples were manufactured with the same parameters, a different microstructure seemed to be very unlikely, but was still discovered. However, the formed microstructure of this powder batch was less favourable than the finer microstructure of other powder batches. Therefore, no further analyses

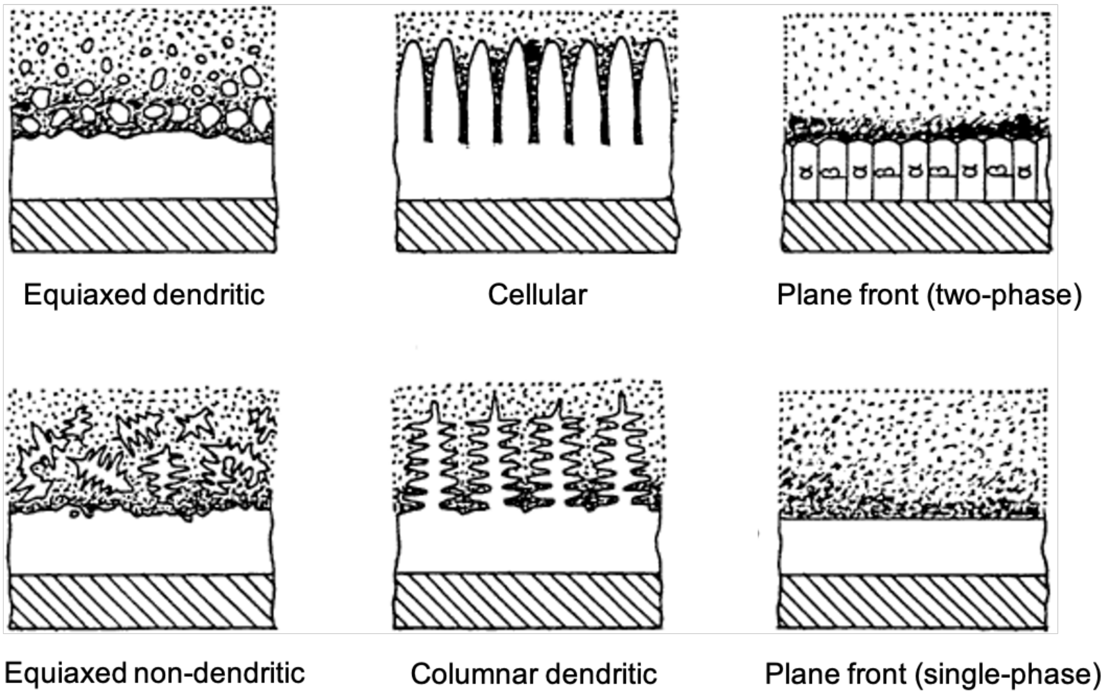

Figure 9.16: Solidification structures (based on [35]).

were performed with these samples.

9.3.8 Microhardness

In Figure 9.18 the microhardness measurements are given and in Table 9.4 the according statistical information is provided. *R* is the range of the measurements, *V* the variance, *SD* the standard deviation and the *Mean* the mean values. The samples in the figure are sorted in ascending order according to their energy density. Interestingly, the 4 h milled samples did not outperform the other specimens as expected. Instead, the SLM processed specimens, which were fabricated with powder that was mechanically alloyed for 2 h, was the most promising. The highest mean values of 455 HV were achieved equally with sample no. 6 and 10. However, sample 10 had a lower standard deviation and therefore, had a more homogeneous hardness distribution. But as a matter of fact, the energy density of 109.33 J/mm^3 of specimen no. 6 lead to higher results than with less energy density (i.e. 147.09 J/mm^3). Specimen no. 6 had a maximum value of astonishing 471 HV, which is, compared to the more coarse MS1/VC-33 of Chapter 8, even higher by 32 HV. Therefore, the particle refinement notably improved the microhardness of the MMC.

9.3.9 Tribological Performance

In Figure 9.19 the results of the coefficient of friction are shown and in Figure 9.20 the relative penetration depth of the indenter is given. The MS1 had a slightly higher COF with a mean value of $\mu = 0.382$. The MS1 sample had a comparably low COF in the beginning of the test (i.e. $\mu = 0.12$), but the values rose to $\mu = 0.74$ after 1000 cycles. The reinforced samples had higher COF values in the beginning of about $\mu = 0.20$, but just rose to about $\mu = 0.64$. In Table 9.5 the COF after 1000 cycles of all samples are given, plus, the track wear rate and ball wear rate values. It has to be mentioned that there was some residue of the abrasive tribological tests stuck on all samples. Material of the indenter and the specimen was coated on the wear track and compressed. This caused a polished gliding plane and therefore, some COFs were lower. According

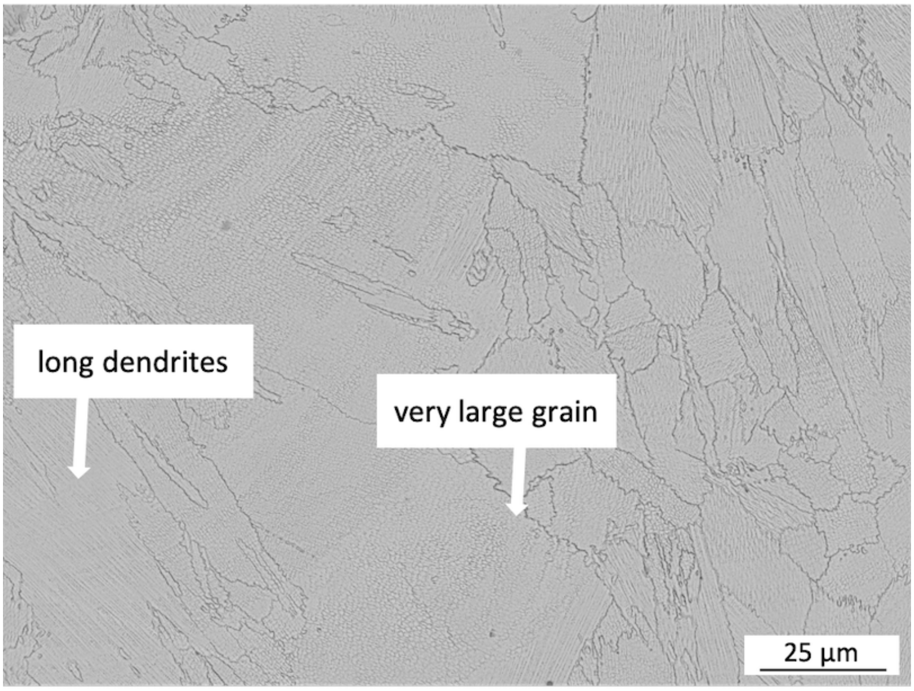

Figure 9.17: SEM image of the 440C ball milled and SLM processed MS1/VC.

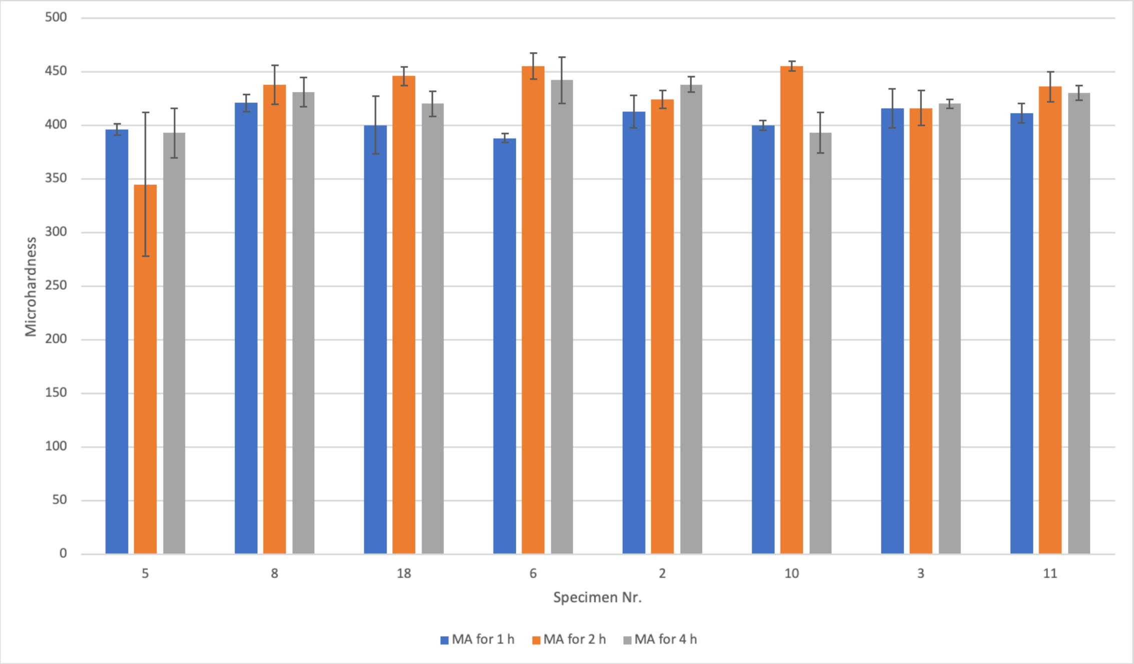

Figure 9.18: Diagram of the microhardness measurements of the mechanically alloyed MS1/VC-2.5 (WC equipment).

Table 9.4: Statistical information for micro-hardness measurements of the MS1 samples after 1, 2 and 4 hours of milling.

Spec. Nr.	**Mean 1 h**	**R 1 h**	**V σ^2 1 h**	**SD σ 1 h**	**Mean 2 h**	**R 2 h**	**V σ^2 2 h**	**SD σ 2 h**	**Mean 4 h**	**R 4 h**	**V σ^2 4 h**	**SD σ 4 h**
5	396	12	29,67	5,45	345	154	4530,67	67,31	393	52	531	23,04
8	421	18	62	7,87	438	44	333,67	18,27	431	32	193	13,89
18	400	66	727	26,96	446	21	75	8,66	420	29	143	11,96
6	388	10	17	4,12	455	29	143	11,96	442	53	472,67	21,74
2	413	33	228,33	15,11	424	20	68,67	8,29	438	16	50,67	7,12
10	400	11	20,67	4,55	455	11	21,67	4,66	393	42	366	19,13
3	416	44	337	18,36	416	37	263	16,22	420	10	16,67	4,08
11	411	22	84,33	9,18	436	32	202,67	14,24	430	15	47	6,86

Table 9.5: Coefficient of friction, track wear rate and ball wear rate of MS1VC.

Material	COF (μ)	Track Wear Rate [mm^3/Nm] x 10^{-5}	Ball Wear Rate [mm^3/Nm] x 10^{-5}
MS1	0.74	1.51	1.44
MS1VC-1h	0.64	2.30	1.62
MS1VC-2h	0.64	1.09	4.51
MS1VC-4h	0.69	1.14	1.70

to the measured results, the 1 h milled MS1VC had a higher track wear rate and ball wear rate, which indicates a very abrasive process. The 2 h and 4 h samples had a lower track wear rate, but the 2 h sample obviously had a higher resistance against the indenter as the ball wear rate was significantly higher. A graphical overview of the results of the track wear rate and the ball wear rate is provided in 9.21. It can be said that the wear resistance of the 2 h and the 4 h mechanically alloyed samples was improved by 28.18 % and 24.96 % respectively.

9.4 Charpy Impact Strength

To understand the ductility of the mechanically alloyed metal matrix composite material, specimens for Charpy impact strength tests were built and tested. Just as expected for such a hard material, the ductility was relatively low and no necking of the specimens was observed. The impact energies were measured between 8.9 and 10.2 J, which is definitely lower than standard unreinforced maraging steel would achieve, but better than the results that were achieved with the mixed powders - especially, if one considers the much higher reinforcing content.

9.5 Ultimate Tensile Strength

In Figure 9.22 the results of the ultimate tensile strength tests of the samples without heat treatment are provided and in Figure 9.22 the samples with heat treatment at 490 ° C for 6 hours are shown. It becomes very obvious that the heat treatment did not have such a significant influence as it had with the mixed powders. Overall, the results were quite good for such a hard material, but it has to be mentioned that all samples again broke at a similar plane. This fracture plane was at a spot at which the samples had a larger diameter than at the center of the specimen. This means that, again, a binding error was causing the fracture and the material itself could have had lead to tougher results and higher ultimate tensile strengths. This was caused by an SLM defect and could have been prevented, if the specimens would have been built in the X-Y direction. The fracture plane did not show any necking. Therefore, the material was not very ductile.

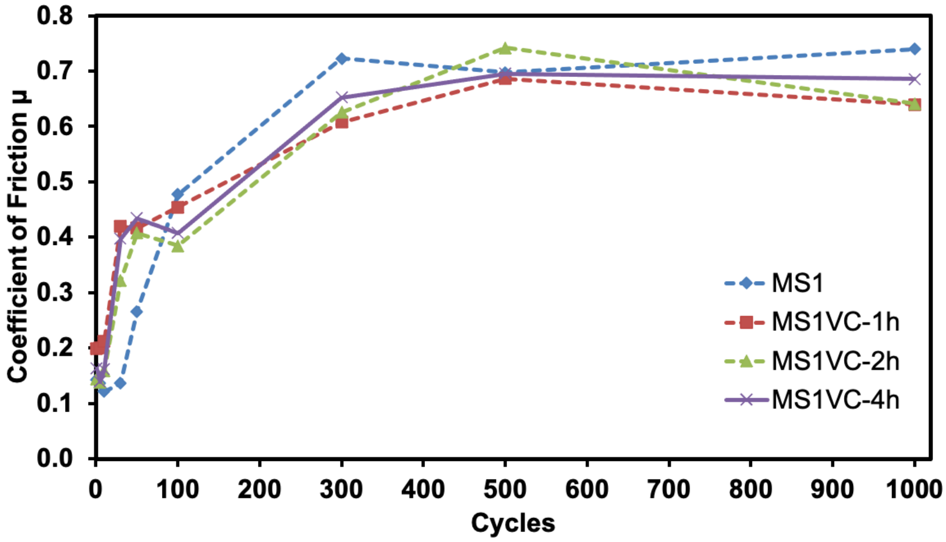

Figure 9.19: Graph of the coefficient of friction of the MS1VC samples with 2.5 microns of VC.

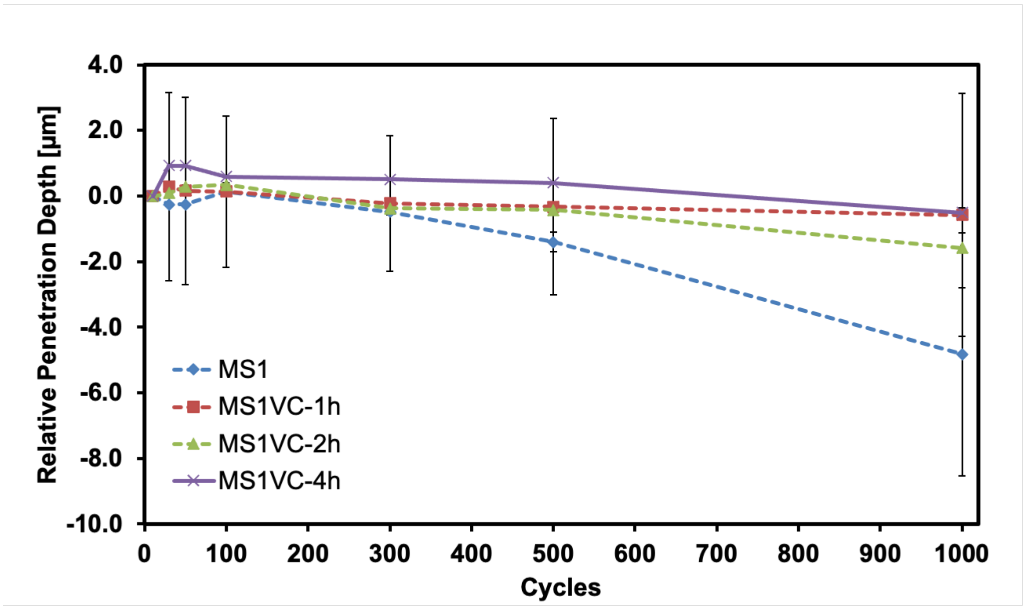

Figure 9.20: Graph of the relative penetration depth of the MS1VC samples with 2.5 microns of VC.

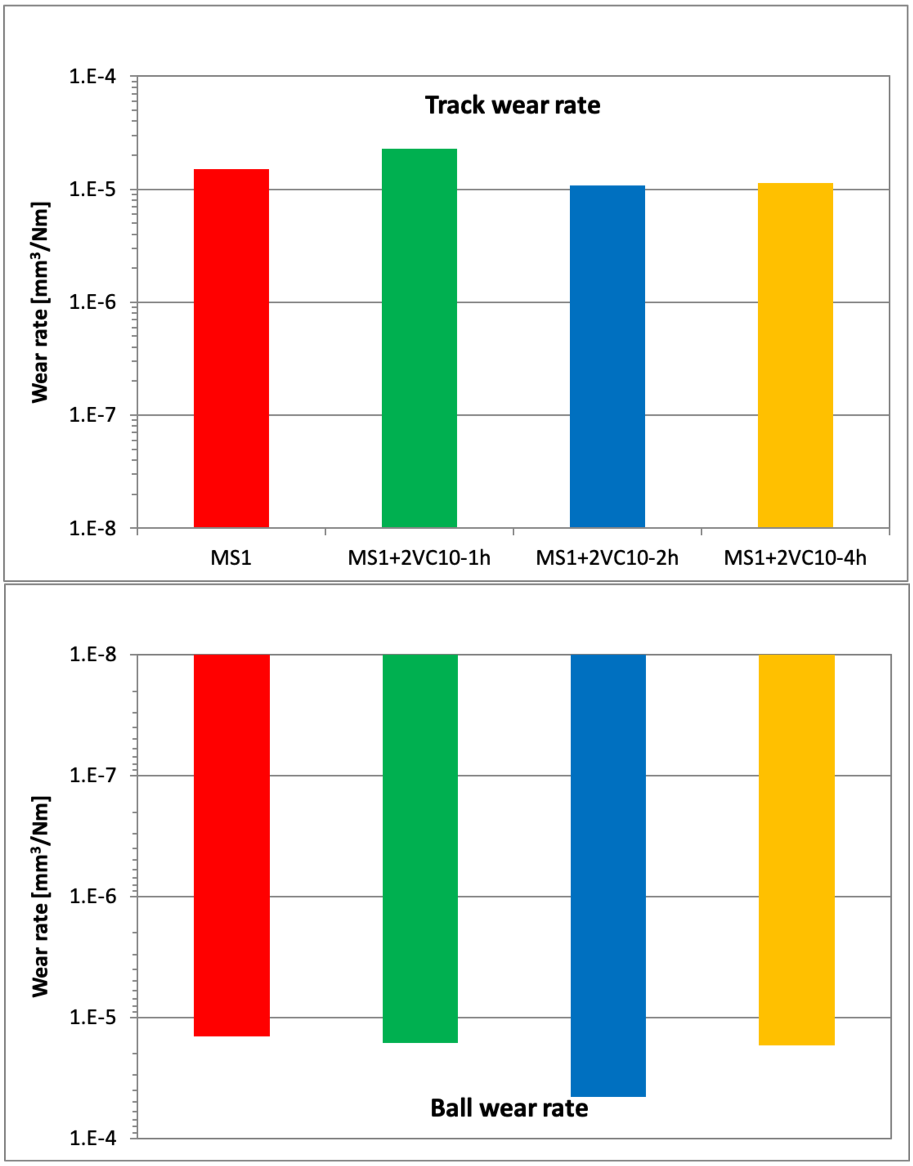

Figure 9.21: Graphs of a) the track wear rate and b) the ball wear rate of MS1VC-2.5.

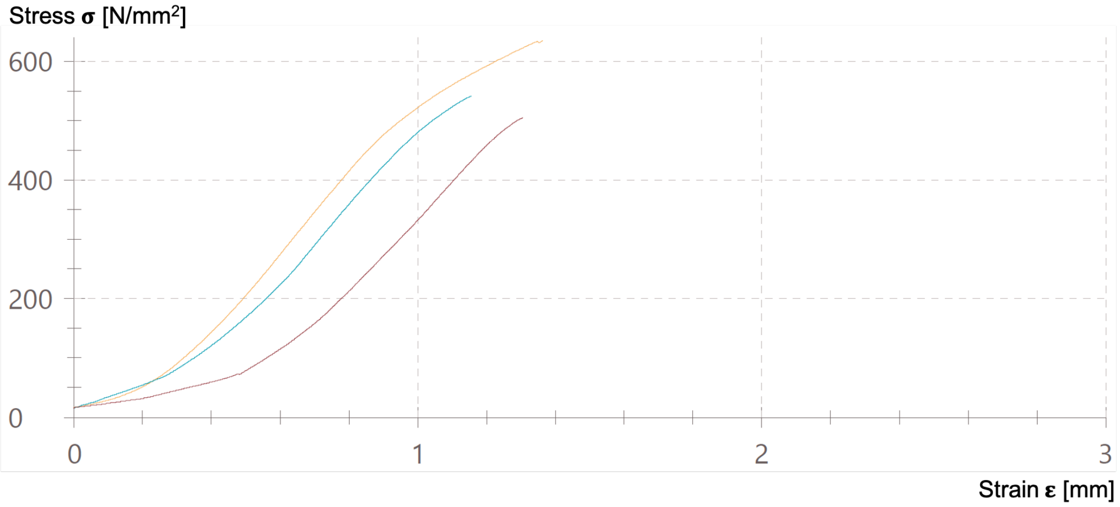

Figure 9.22: Ultimate tensile strength test graphs of the MS1VC samples without heat treatment, but same composition and milling time.

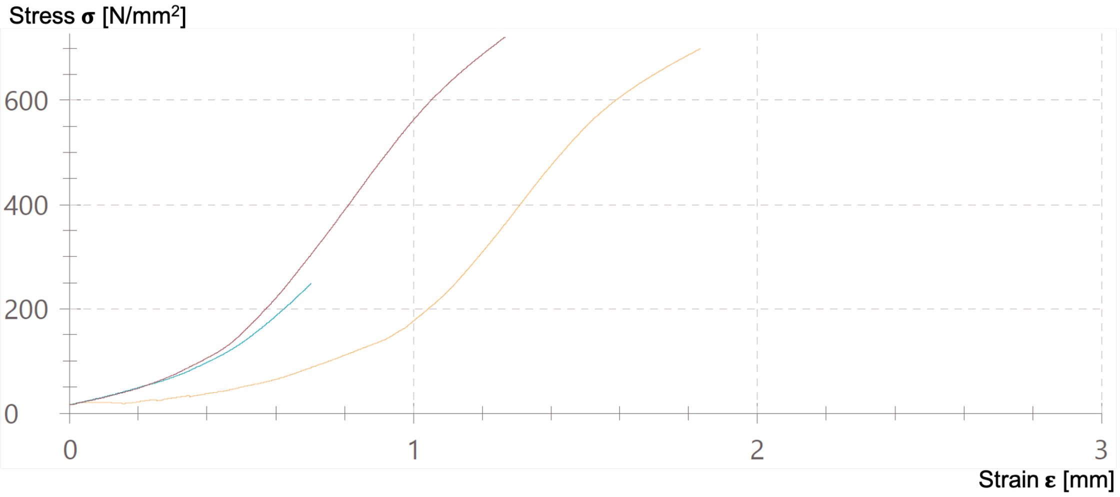

Figure 9.23: Ultimate tensile strength test graphs of the MS1VC samples with heat treatment, but same composition and milling time.

9.6 Conclusions

In this study, it was desired to further improve the capabilities of maraging steel MS1 in combination with vanadium carbide. Mechanical alloying equipment was used to create coalescences of MS1/VC. To understand the real impact of different MA equipment on the powder morphology, two different materials for the vial and the milling balls were used. According to some calculations, the WC equipment has a higher temperature rise per impact and therefore, more energy is put into the powder during milling. Through the reinforcement material, a metal matrix composite was created. As there was no similar study performed yet, comparing different high energy ball milling equipments, it was desired to first calculate the theoretical outcome and then investigate the real results. It was found that the theory did not match the reality. The only explanation was found in the amount of used balls. As the density of 440C is much lower compared to WC, more balls had to be used to keep the ball-to-powder weight ratio equal. As there were more balls in the jar, more ball-to-ball or ball-to-wall impacts must have happened and therefore, more plastic deformation was discovered. The theoretical temperature rise should be much higher with WC ball milling equipment. Therefore, the morphology of the 440C ball milled MS1VC powders should be more spherical. However, the results of the actual ball milled powders was vice versa and plastic deformation was more dominant in the 440C ball milled samples. But as there were more impacts in total, the temperature probably was higher with the 440C equipment. For future investigations, a deeper analysis, using various powders and milling parameters, is suggested.

Furthermore, the initial particle size of the VC composite material was reduced. Through this step, a more homogeneous distribution of VC in the metal matrix was achieved after SLM processing. The powders were ball milled with a WC jar and balls for mechanical alloying. A lot of vanadium carbide particles were embedded and the morphology was kept at a near spherical level. The maximum achieved relative densities were 98.41 % for the 1 h milled sample, 99.28 % for the 2 h milled specimen and the 4 h milled samples achieved a relative density of 97.87 %. The morphology of the ball milled powders influenced the porosity after SLM processing, due to the flowability decrease. However, it was desired to improve the density of the MS1/VC metal matrix composite material and to improve the mechanical properties. The micro-hardness of the MS1/VC-2.5 specimens was even higher than the hardness of the MS1/VC-33 SLM processed samples. The maximum hardness was measured at 471 HV, which was notably higher than the hardness of the more coarse MS1/VC-33. Further, the wear performance of the metal matrix composite was compared to pure MS1. According to the tribological tests, using a stainless steel indenter, the coefficient of friction was not significantly higher and the track wear rate was not improved notably. However, the penetration depth of the 2 h and the 4 h samples was lowered by 28.18 % and 24.96 %, respectively.

10

Microstructure and Mechanical Properties of MS1/TiC MMCs Fabricated by SLM

> Only a few know, how much one must
> know to know how little one knows.
>
> Werner Heisenberg

10.1 Introduction

In recent years, there was an increased demand for metal matrix composites owing to their high strength, stiffness and wear performance. If MMCs are designed properly, their material properties can outperform conventional alloys. Due to their high performance, MMCs are also referred to as advanced materials. However, standard processing routes for MMCs are not optimal and there are some major problems associated with them. Usually, metal matrix composites are processed with casting or powder metallurgical techniques [12]. During casting, there is always the demand for an expensive mold, which is also time consuming to produce. Furthermore, casting is critical for blowholes and due to high heat affected zones, the material can result in a coarse grain structure. Furthermore, if the powders are just mixed and then processed through casting or any other manufacturing route, the low particle-to-particle material bonding can be very critical [235]. In preliminary studies it was found that this processing route causes very low part quality and density. The formation of agglomerations is also very undesired, but typically occurs with powders, which have an irregular shape and are smaller than a few microns. If nano-scaled powders are used for MMCs it is very difficult to achieve a homogeneous distribution, due to the influence of Van der Waals forces, which will lead to non-uniform microstructures and agglomerates [236]. To crack-up these agglomerates and to form coalescences, mechanical alloying proved to be an excellent technique. A high energy ball mill is capable of destroying sub-micron and nano agglomerates and to embed the particles into the matrix material. It is very important to fully melt the reinforcing carbides to improve the wettability with the matrix material, which is why a fine composite bulk material is required and agglomerates have to be cracked-up in advance. High energy ball milling is a non-equilibrium technique that can process powders under relatively low temperatures. The planetary mills are easy to use and comparably cheap to other technologies. The powders used in these mills are repeatedly plastically deformed, cold welded and fractured. As a result, the grain size of the particles is refined and therefore, the mechanical properties are enhanced.

During SLM processing, a relatively small melt pool is induced by a laser beam. As the melt pool is surrounded by either powder or solid material, the cooling rate is very high and was measured between 1 - 40 K/μs [237]. The rapid solidification during selective laser melting are beneficial for a fine microstructure and therefore, improved material properties.

Thus far, selective laser melting was successfully used for MS1 maraging steel [26, 27, 137, 139, 143, 172, 174, 197, 199, 200, 204, 205, 212, 219, 220] and some researchers even investigated the possibilities of reinforcing this type of steel, as the applications are somewhat limited, due to the relatively wear resistance and mechanical strength. In preliminary studies it was found that VC can be used to successfully increase some material properties, if the powders are mechanically alloyed. As TiC has even higher hardness values and influences the melt different than VC does, a new batch of powder was prepared in a high energy ball mill using MS1 and 10 wt.% of TiC. Titanium carbide features a comparably low density of 4.93 g/cm^3, a good corrosion resistance and a high hardness of approximately 3200 HV. A thorough literature review showed that there were very few investigations of maraging steel and titanium carbide. Titanium carbide was investigated with steel matrices in some scientific investigations [238–241]. Akhtar et. al. investigated maraging stainless steel 465 which was reinforced with TiC [242]. In their study they focused on conventional powder metallurgy through pressing and sintering. AlMangour et al. used a high energy ball mill and SLM to reinforce H13 and 316L with TiC [12, 133–135, 180, 187, 226].

In this study, the powder batches were first mechanically mixed, mechanically alloyed, and then SLM processed and analyzed to understand the microstructure and the mechanical properties. Especially, the XRD analysis brought some interesting results of the SLM processed samples.

10.2 Material and Methods

10.2.1 Powder Preparation

To get a homogeneous mixture of the bulk maraging steel powder and the titanium carbide powder, the two components were poured into a Turbula shaker mixer (Willy A. Bachofen AG, Switzerland) and mechanically mixed. The MS1 maraging steel powder was obtained directly from the manufacturer (EOS GmbH, Germany) and had a spherical shape with a particle size distribution of 15 μm - 40 μm. The TiC was also obtained from the manufacturer (Treibacher Industrie AG, Austria), was irregular shaped and had a particle size distribution of < 2.0 μm. The values were provided from the manufacturers. The chemical composition of the EOS MS1 powder can be found in Table 4.1 whereas the chemical composition of the Treibacher TiC is given in Table 10.1. TiC generally has a large degree of freedom in carbon stoichiometry in the $\gamma - Ti_xC(\sim 1 < x <\sim 2)$ phase, which is why there was a high interest in the exploration of the equilibrium geometry, the distribution of the charge density, the structure of the energy band and the stacking fault energy in terms of the vacancy concentration [243]. There are deviations of the cubic NaCl phase of TiC reported with a homogeneity range of $TiC_{0.50}$ to $TiC_{0.97}$ [32]. The Treibacher titanium carbide had a structure of sub-stoichiometric $TiC_{0.79}$. The typical bulk powder morphology of the TiC can be found in Figure 4.9a, but Figure 4.9b shows a relatively large agglomerate of TiC particles.

Table 10.1: Chemical composition of TiC powder

Element	Al	C-free	C-tot	Ca	Fe	N	O	S	Si	W	Ti
wt%	0.01	0.50	19.0-19.9	0.01	0.03	0.20	0.60	0.01	0.01	1.00	rest

For the mechanical alloying, a planetary ball mill was used (Fritsch Pulverisette 4, Germany). The mixed MS1/TiC powder was milled with the goal, to embed the fine TiC particles into the bigger MS1 particles. Furthermore, it was desired to crack-up the agglomerations of the TiC

Table 10.2: Milling times and cool-off breaks for the TiC powder.

total milling time	2 h	4 h	8 h
total process time	2 h 15 min	4 h 45 min	9 h 45 min

powder, to get a homogeneous distribution in the MS1/TiC mixture. These agglomerates would not be melted during SLM processing, due to the significantly higher melting temperature, and would lead to inhomogeneities in the metal matrix composite. The ball-to-powder weight ratio was 5:1 and the milling balls and the vial were made out of tungsten carbide. The milling process was done under argon atmosphere to prevent unwanted oxidation. The parameters for the mechanical alloying process in the high energy ball mill can be found in Table 8.2 and were exactly the same as in previous studies for comparison reasons. However, the milling times were adjusted to the smaller average particle size of the TiC powder. The milling times with the cool down breaks can be found in Table 10.2.

10.2.2 SLM Process

For the selective laser melting process, a single ytterbium fibre laser machine was used (MCP-realizer SLM 250, Germany). The machine normally has a build size of 250 x 250 x 220 mm, but was retrofitted with a build-volume reduction system, to work with low amounts of powders. This cylindrical build-volume reduction was specifically designed for research applications and to study different mechanically alloyed powders. The maximum laser power was 100 W and the laser spot diameter was 0.12 mm wide. The laser system was computer controlled with a dedicated software for process control. The mounted and levelled base plate was made out of steel. Cylindrical samples were manufactured with a diameter of 8 mm and a height of approximately 7 mm. During the SLM process, the chamber was flooded with an inert gas (i.e. argon) and the oxygen level was kept under 0.4 %. The layer thickness was set to 40 microns and the variables scan speed, hatch distance and laser power were variated. The parameters were calculated using the Federov operator in R-Studio (R Foundation for Statistical Computing, Austria) open source software and were also used in previous studies. The parameters can be found in Chapter 8 in Table 8.4. The X - Y laser scanning strategy was alternated after each layer.

10.2.3 Microstructural Characterization

After SLM processing, the cylindrical samples were cut-off the base plate with a Struers Secotom (Struers Inc., USA). They were then embedded with a Struers CitoPress-15 and polished in Struers Tegramin automatic polishing machine. After polishing, the samples were etched in a solution of 30 ml 48 % HF, 15 ml 65 % HNO_3 and 30 ml 32 % HCl. To analyze the porosity of the specimens, they were first analyzed under an optical microscope (Leitz Aristomet, Leica Microsystems, Germany). The microscope was connected to a computer system equipped with a density measuring software.

High resolution images were taken with a scanning electron microscope (Tescan Vega 3, Czech Republic). In the SEM, the powders and the etched SLM processed samples were analyzed for their microstructure. The SEM was furthermore equipped with an energy dispersive X-ray spectroscopy silicon drift detector (Ultim Max 40, Oxford Instruments, United Kingdom) to characterize the elements.

The phase identification of the milled powders and the SLM processed samples was done with an X-ray diffractometer (PANalytical PW 3040/6 X'Pert Pro, United Kingdom) with Cu Kα radiation ($\lambda = 0.15406$ nm) operating at 40 kV and 35 mA. Two-θ was recorded in the range of 30 and 90 degree with a step size of 0.05 and a counting time of 200 seconds per step.

Microhardness was measured with a dedicated hardness testing device (Karl Frank GmbH, Germany) using a diamond pyramid indenter for Vickers hardness. The samples were loaded with 9.8 N and the indentation time was 10 s.

The particle size distribution was measured with a Microtrac SDC and a Microtrac S3500 (Retsch GmbH, Germany). For the tribological analysis a micro scratch tester setup was used (Anton Paar MST and CPX, Anton Paar Group AG, Austria). The indenter was applied with 5 N of force and moved on the samples' surface for 1000 cycles on a track length of 5 mm. The track was then analyzed with a Dektak 150 profilometer (Veeco, USA).

10.3 Results and Discussion

10.3.1 Particle Size Distribution of the MA Powders

In Figure 10.1 the particle size distribution of the mechanically alloyed $MS1_{90}TiC_{10}$ is given. In Figure 10.1a, c and e the volumetric particle size measurement method was used for the 2 h, 4 h and 8 h milled powder respectively. Obviously, the powder had a tendency to form bigger particles after longer milling hours. The particle size distribution after 2 h (i.e. $D_{10} = 2.07$ μm, $D_{50} = 32.19$ μm and $D_{90} = 54.59$ μm) of milling did not change significantly compared to the powder milled for 4 h (i.e. $D_{10} = 2.40$ μm, $D_{50} = 33.56$ μm and $D_{90} = 56.45$ μm), but the amount of small particles (< 3 μm) did indeed change. The small TiC particles were embedded into the MS1 particles and after 8 h of milling the process of cold welding was dominant. The particle size distribution after 8 h of milling was measured as $D_{10} = 14.10$ μm, $D_{50} = 37.77$ μm and $D_{90} = 70.43$ μm. As known from preliminary studies, after even longer milling hours the particles would have been fractured into smaller sizes again. The numeric method to count each powder particle was applied in 10.1b, d and f. One can see that the amount of small particles was significantly increased after 4 h of milling. This is very likely, due to the cracking of the large amount of agglomerations in the TiC powder. After cracking the agglomerates into fine particles again, the particles were embedded into the matrix material and the amount of small particles decreased again.

10.3.2 Phase Analysis of the Powders

After each milling cycle, some powder was taken to analyze the phase formation after 2, 4 and 8 hours of mechanical alloying. The black circles in Figure 10.2 represent the alpha-Fe martensitic phase, which is defined as MS1 steel. As one can see, the high energy ball milling in the planetary ball mill did not affect this phase. However, the sub-stoichiometric $TiC_{0.79}$ phase showed weaker diffraction peaks after longer milling hours. This is due to the grain refinement and the cracking of the agglomerates.

10.3.3 Powder Morphology using SEM

To understand the effects of the high energy ball on the morphology of the powders, a scanning electron microscope was used. It was important to keep the spherical shape of the MS1 matrix material as near-spherical as possible. In the same manner, it was desired to embed the TiC particles into the MS1 powder and to form coalescences. In Figure 10.4 the MS1/TiC powder after a) 2 h, b) 4 h and c) 8 h is given. It is clearly visible how not just the morphology, but also the particle size distribution was affected. After 2 h or milling, the powder still had a very spherical shape and only a few particles underwent severe plastic deformations. However, even after 2 h there were some MS1 particles embedded with reinforcing TiC composites. Figure 10.3 shows a detailed SEM image of the 2 h mechanically alloyed powder. The particle is very spherical and there are several TiC particles embedded into the surface. Because of this, the laser, during selective laser melting, would very likely completely melt the TiC and after solidification the formed primary TiC would be homogeneously distributed in the maraging steel matrix.

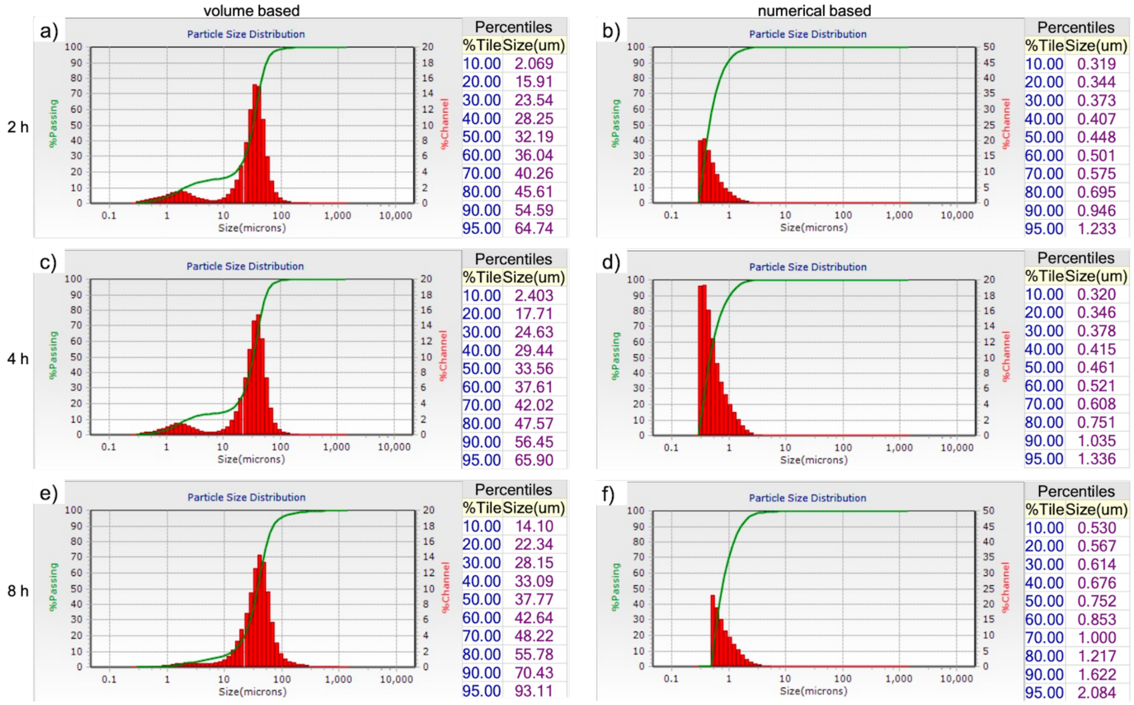

a)

%Tile	Size(um)
10.00	2.069
20.00	15.91
30.00	23.54
40.00	28.25
50.00	32.19
60.00	36.04
70.00	40.26
80.00	45.61
90.00	54.59
95.00	64.74

b)

%Tile	Size(um)
10.00	0.319
20.00	0.344
30.00	0.373
40.00	0.407
50.00	0.448
60.00	0.501
70.00	0.575
80.00	0.695
90.00	0.946
95.00	1.233

c)

%Tile	Size(um)
10.00	2.403
20.00	17.71
30.00	24.63
40.00	29.44
50.00	33.56
60.00	37.61
70.00	42.02
80.00	47.57
90.00	56.45
95.00	65.90

d)

%Tile	Size(um)
10.00	0.320
20.00	0.346
30.00	0.378
40.00	0.415
50.00	0.461
60.00	0.521
70.00	0.608
80.00	0.751
90.00	1.035
95.00	1.336

e)

%Tile	Size(um)
10.00	14.10
20.00	22.34
30.00	28.15
40.00	33.09
50.00	37.77
60.00	42.64
70.00	48.22
80.00	55.78
90.00	70.43
95.00	93.11

f)

%Tile	Size(um)
10.00	0.530
20.00	0.567
30.00	0.614
40.00	0.676
50.00	0.752
60.00	0.853
70.00	1.000
80.00	1.217
90.00	1.622
95.00	2.084

Figure 10.1: Volumetric particle size distribution of a) 2, c) 4, e) 8 h milled powder and numeric particle size distribution after b) 2, d) 4 and f) 8 hours of milling.

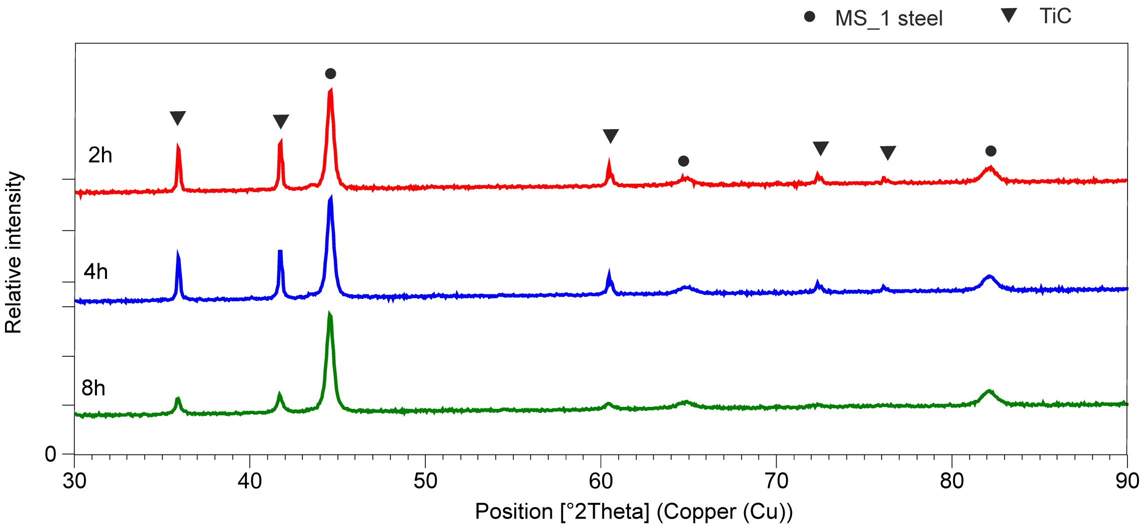

Figure 10.2: XRD graphs of the powder samples after a) 2, b) 4 and c) 8 hours of milling.

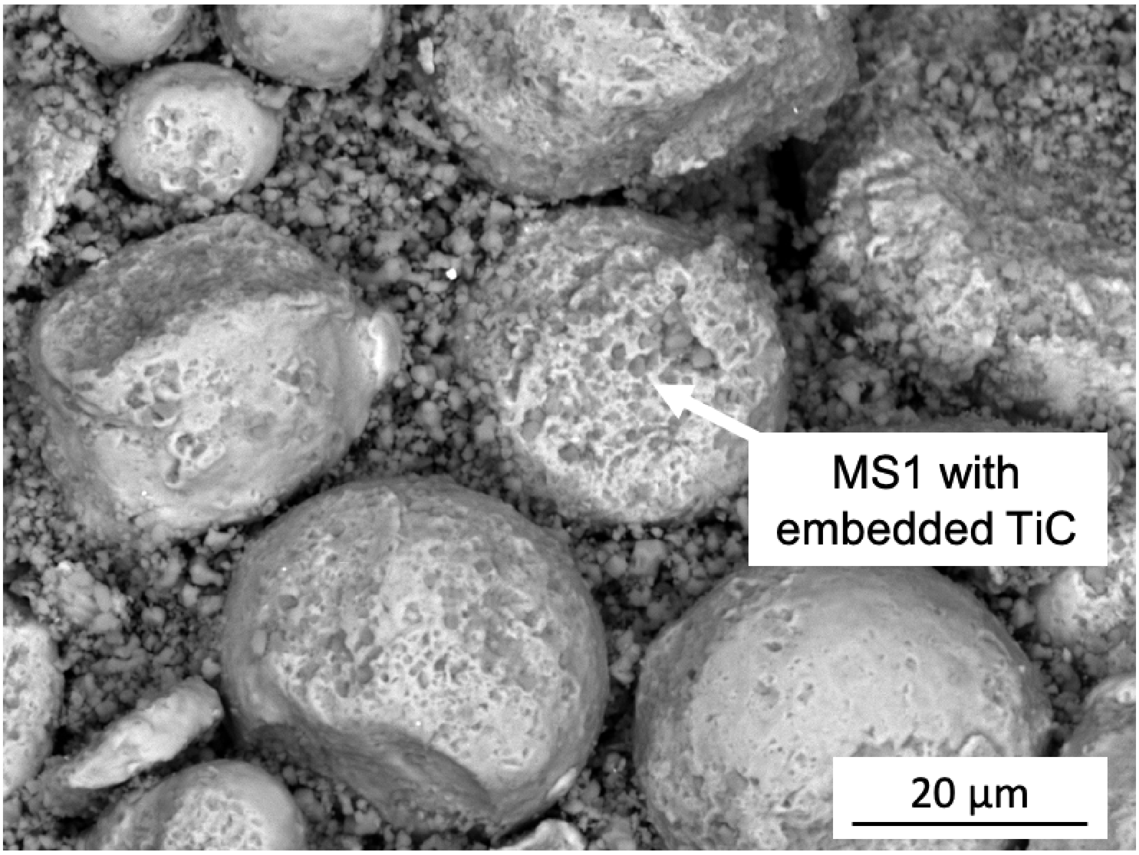

Figure 10.3: Detailed SEM graph of the MS1/TiC powder after 2 hours of milling.

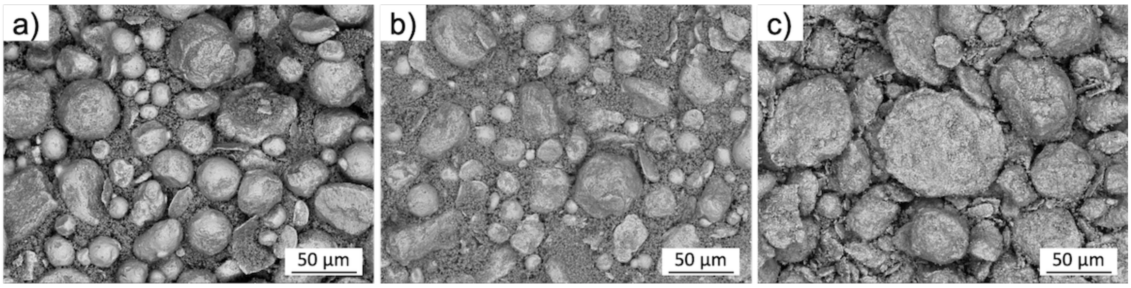

Figure 10.4: SEM graphs of the MS1/TiC powder after a) 2, b) 4 and c) 8 hours of milling.

Table 10.3: Elements of the MA MS1TiC powders.

Element	wt% 2 h	wt% 4 h	wt% 8 h
Al	0.23	0.21	0.21
Si	0.11	0	0.09
Ti	31.61	41.23	31.82
V	0.44	0.39	0.23
Cr	0	0	0.18
Fe	47.11	40.35	46.47
Co	6.51	5.49	6.34
Ni	11.18	9.84	11.74
Mo	2.80	2.49	2.91

10.3.4 Powder analysis by EDX

EDX analysis of the mechanically alloyed powders showed the evolution of the powders after 2, 4 and 8 hours. To understand the elements after the high energy ball milling, several EDX maps were made. In Figure 10.5 a graph of such a spectrum is given. As expected, there are high peaks of Ti, C, Ni and Fe, but also some other elements are visible. Some are from the alloy, but others might be artefacts of the etching solution, which appear differently in the EDX analysis and cause irregularities. In Table 10.3 all elements after each milling cycle are given. The relatively large difference in Ti and Fe contents can be explained, because of the size of the field of view. If there are more fine TiC particles in the image, there will be a higher Ti peak, than if there are more MS1 particles in the image visible. As the particle size varied quite extreme between the MS1 and the TiC powder and the mixture was based on weight rather than on volume, there are significantly more TiC particles in the bulk powder mixture. It has to be mentioned that the samples preparation also plays a big role in the SEM and EDX analysis. The powders were applied to a sticking pad. To avoid damages in the SEM detector, there must not be any loose particles left on the pad. As one can imagine, the surface will more likely be covered with small particles rather than with larger particles. Therefore, it appears as if the mixture would contain more than 10 wt.% of TiC.

In Figure 10.6 the evolution of the powders is shown. Even though the longer the milling was performed, the more TiC particles were embedded into the MS1 matrix material, some particles were perfectly embedded after just 2 h of milling. After 4 h of milling there were obviously more TiC particles embedded, but also plastic deformation occurred more extremely. In Figure 10.6c a particle is given, which was perfectly cracked up into a hemispherical-shaped particle. In this image, the cold-welding and plastic deformation mechanisms are demonstrated perfectly. The whole particle must have been cold-welded and fractured repeatedly. Therefore, the TiC and the MS1 powders formed a coalescence.

10.3.5 Analysis of Density

After obtaining all relative density results, R Studio was used to create diagrams which show the optimal parameters for SLM processing. In Figure 10.7 these diagrams are provided. The diagrams indicate that a higher energy density would be advisable to achieve the best results in terms of part density. An optimum of about 75 microns hatch distance and 180 mm/s scan speed is predicted to be the optimum for a laser power of 99 W. These parameters are suggested for 2 h, 4 h and 8 h of milling.

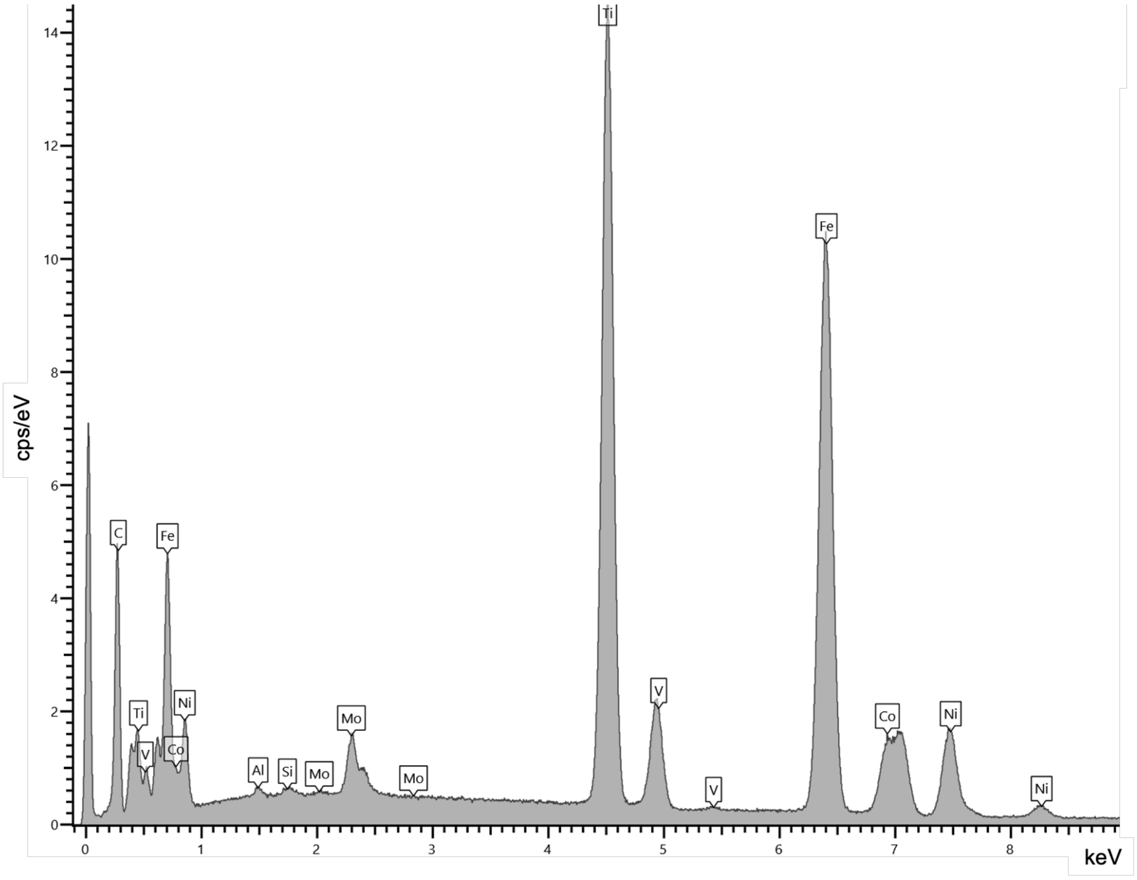

Figure 10.5: Graph of the elements observed by EDX in the 2h milled sample.

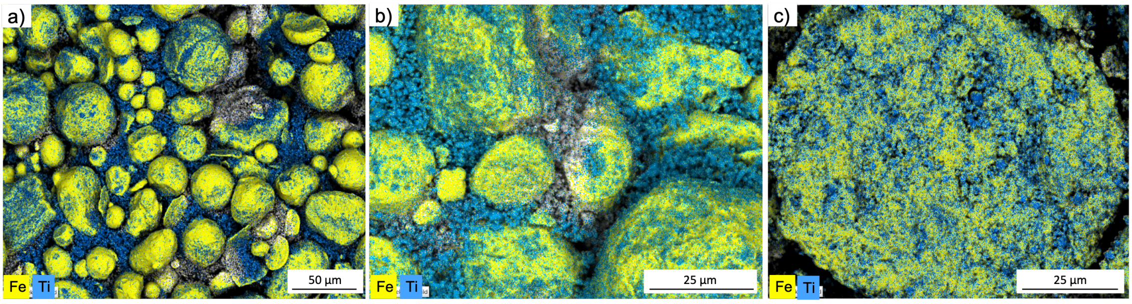

Figure 10.6: EDX images of the milled powder after a) 2 h, b) 4 h and c) 8 h.

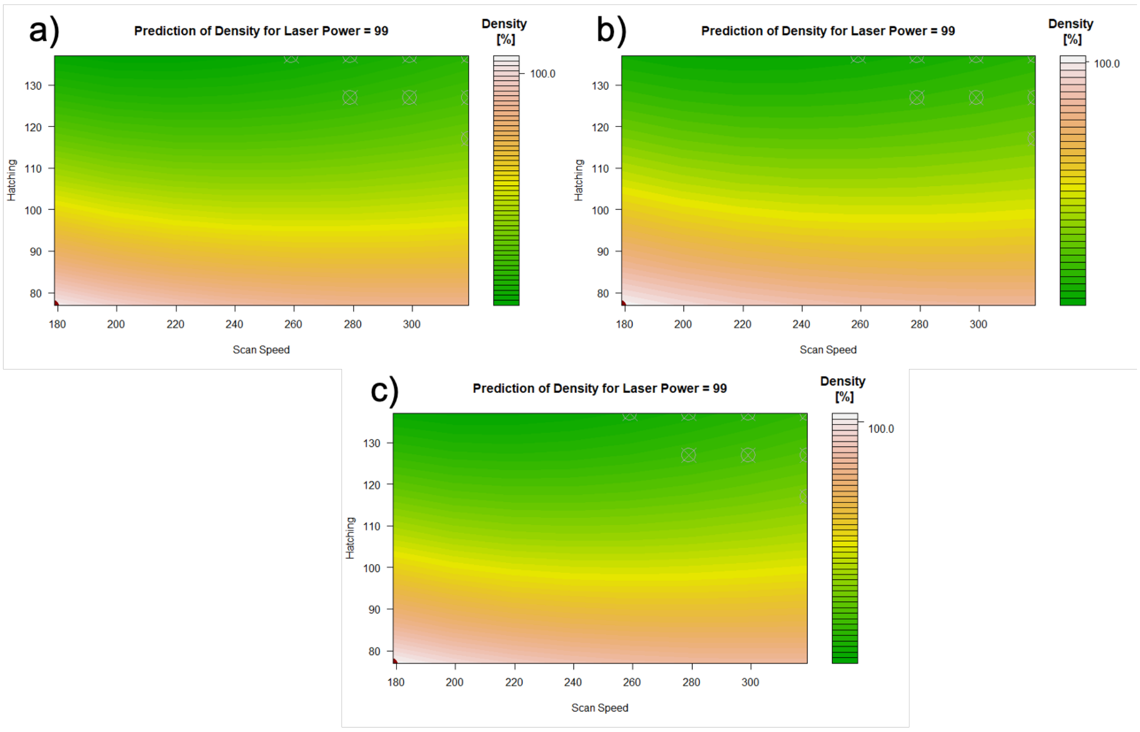

Figure 10.7: Prediction of the optimal relative density for MS1TiC mechanically alloyed for a) 2 h, b) 4 h and c) 8 h.

10.3.6 Phase analysis of the SLM specimens

In the samples of the SLM processed specimens, the phase analysis revealed some interesting behaviours of both, the matrix and the composite material. The XRD graph is given in Figure 10.8. In the samples fabricated with the 2 h and the 4 h milled powders, there were no significant changes observed. In the 4 h sample the diffraction peaks for TiC slightly decreased, which is due to the complete dissolvement of some of the TiC particles in the melt. The reduced peak intensity and the increased peak width (full width at half maximum - FWHM) furthermore indicates a refined microstructure. In Figure 10.9 it can be observed that after 4 h of milling, the peaks of the TiC shifted slightly to higher θ degrees. This usually indicates lattice distortions caused by residual stresses or by foreign atoms embedded in the crystal structure. However, the used titanium carbide had a tendency for a higher stoichiometry (i.e. $TiC_{0.97}$), which might have lead to a different crystal structure. Furthermore, the graph reveals that the strongest detected diffraction α-Fe peaks in the 2 h and the 4 h sample were measured at a higher 2θ degree in the 4 h milled sample (i.e. FWHM, or difference of 2θ). The intensity (counts) was lower in the 4 h milled sample. According to Scherrer's formula (equation 5.9) this indicates a decrease in the crystalline structure after 4 h of mechanical alloying compared to the 2 h milled sample [244]. It can therefore be said, that the crystal structure was refined as Bragg's law (equation 5.8) states that higher 2θ values indicate a shorter interplanar crystal distance of the correlated planes [12,244].

However, after 8 h of milling and SLM processing, the phases changed dramatically. The martensitic α-Fe phase diffraction peaks became weaker and instead, some high peaks of γ-Fe were visible, additionally to the, now weaker, α-Fe peaks. Obviously, there was a high amount of retained austenite in the solidified material which did not transform into martensite. If austenite reaches the martensite starting temperature, the gamma phase becomes mechanically unstable and due to the quenching mechanisms, the austenite transforms almost completely into martensite until the lower transformation temperature is reached.

It is known that carbon significantly influences the formation of martensite or austenite. A higher amount of carbon reduces the martensitic starting temperature. It can be even lower than standard room temperature, which is why there can be a lot of retained austenite in steels. In the study of Axen et al. it was reported that ceramic reinforcing particles can introduce tensile stress into the composite matrix [245]. Ceramics usually have a much lower thermal expansion coefficient than iron based alloys [12]. The martensitic transformation is therefore increased, as the particles act as a starting point for nucleation and crystal growth, which can cause a grain refinement. However, in this study it was observed that, due to the high amount of free carbon, caused by the addition and dissolvement of TiC, the alpha-Fe phase formation was hindered and the fine TiC particles did not influence the martensitic formation. The TiC particles might have acted as a starting point for crystal growth, but the thermal expansion mechanisms were too weak to transform the austenite into martensite, as the martensite starting temperature was too low. After longer milling hours, the powder was refined and agglomerations of TiC were cracked into fine particles. Therefore, there were more TiC particles dissolved completely in the melt and some carbon was bonded to the steel matrix instead of the titanium. This significantly influenced the martensitic starting temperature and therefore, caused a high amount of retained austenite.

Furthermore, the $TiC_{0.79}$ phase, which was predominant in the other samples, transformed into another form of Ti. It was not possible to identify this phase completely, but it is known that at the position of the XRD peak only TiC, TiO and WC exists. Specifically $TiO_{0.71}$ to $TiO_{0.8}$, $TiC_{0.1}O_{0.9}$ or WC_{x-1}. In the EDX analysis there were no W or O elements found. However, the used EDX detector did not have a sufficiently high resolution to detect only a few atoms and the XRD analysis was more accurate for sure. If the XRD chart peaks are representing tungsten carbide, a possible explanation would be wear caused by the ball milling equipment. However, if the peaks would represent WC_{x-1}, there would not be any peaks for TiC, which is very unlikely. The smaller the TiC particles became, the higher the chances to completely melt them. As there was some C of the TiC particles bonded to the Fe matrix, there was some free Ti in the melt. Titanium is very reactive with oxygen. Even though the SLM processing chamber was flooded with argon and the oxygen level was kept below 0.4 %, it is impossible to keep the chamber completely free of oxygen. Furthermore, while handling the powder, it is in contact with oxygen. It is very likely that some of the Ti atoms did bond to oxygen and formed a Ti-O or a Ti-C-O composite. Therefore, it is more likely that the XRD peaks did not represent WC_{x-1}, but rather represented $TiC_{0.1}O_{0.9}$. In any case, the observed phenomenon was very strange and it can not be explained with certainty.

10.3.7 Microstructural Observation and Density

The SLM processed samples were embedded and polished to analyze the microstructure, the porosity and to measure the relative density. In Table 10.4 the results of the relative density of all samples is given. Specimen no. 3 achieved the best results over all milling times, which had a laser power of 99 W, a scanning speed of 177.78 mm/s and a hatching distance of 77 μm. As a result, the energy density was 179.58 J/mm^3, as the layer thickness was set to 40 microns. However, after 8 h of milling, the particles were too deformed and therefore, the SLM process was not as stable as with lower milling times. Due to the non-spherical shape of the powder, the coating was uneven and as a result, the melt pool was unstable. This caused pores in the sample. If one compares the result of the $MS1_{90}TiC_{10}$ to the $MS1_{90}VC_{10}$, each with a similar particle size, it can be understood that there were more defects in the $MS1_{90}TiC_{10}$ samples. The overall density in the samples was comparably low. The SLM parameters were not changed for comparison reasons. Therefore, the titanium carbide influenced the melt pool even more than the vanadium carbide particles.

In Figure 10.10 specimen no. 3 is given after 10.10a 2 h, 10.10b 4 h and 10.10c 8 h of mechanical ball milling. It can be observed that the porosity increased, but also the amount of undissolved TiC particles decreases, which is an indicator for TiC particle refinement and primary formed TiC

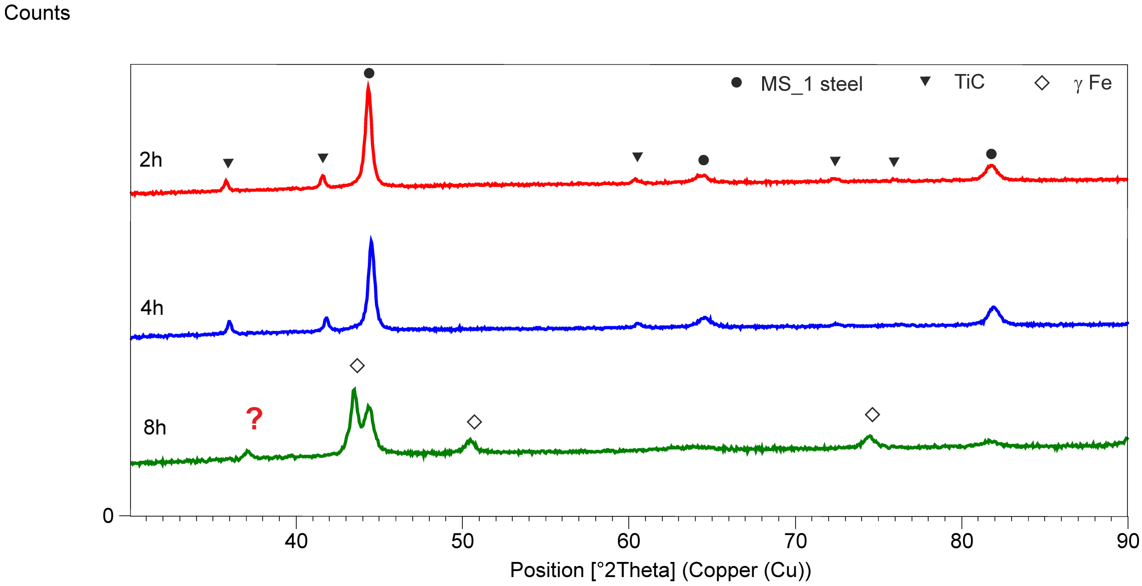

Figure 10.8: XRD graphs of the SLM processed samples after a) 2, b) 4 and c) 8 hours of milling.

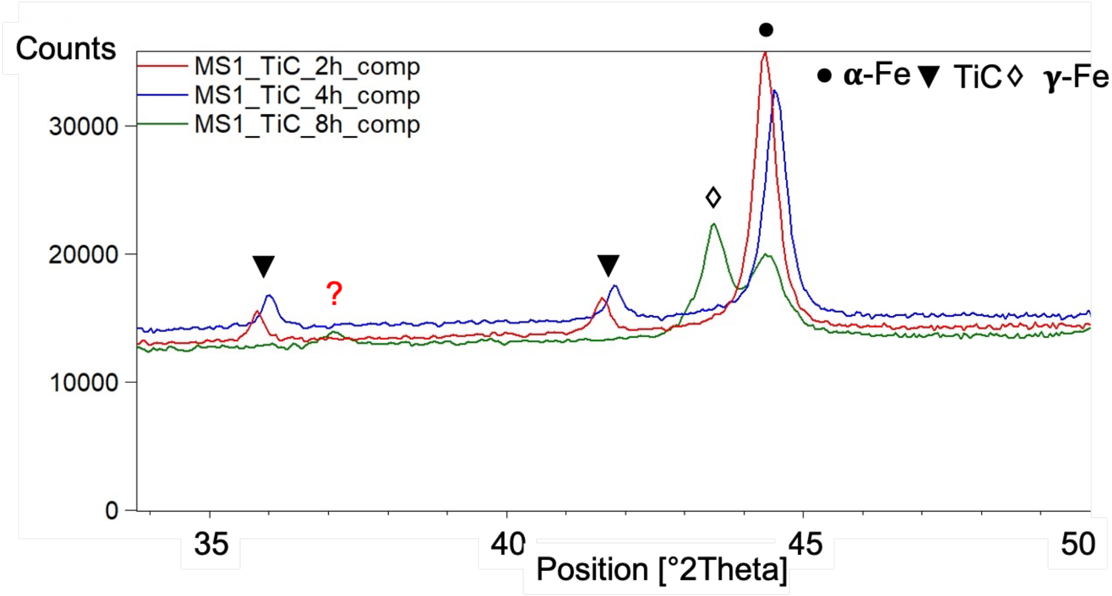

Figure 10.9: Comparison of the XRD graphs of MS1/TiC.

Table 10.4: Achieved relative densities of all SLM processed specimens.

Spec. Nr.	Energy density [J/mm^3]	Rel. D. 2 h [%]	Rel. D. 4 h [%]	Rel. D. 8 h [%]
2	117.9	94.54	78.85	88.53
3	179.57	98.52	98.59	94.54
5	67.22	72.36	78.3	77.42
6	109.33	93.5	94.2	87.29
8	84.83	72.78	86.41	78.28
10	147.09	96.12	96.32	88.03
11	60.7	64.79	72.61	62.03
18	96.69	88.72	85.95	85.43

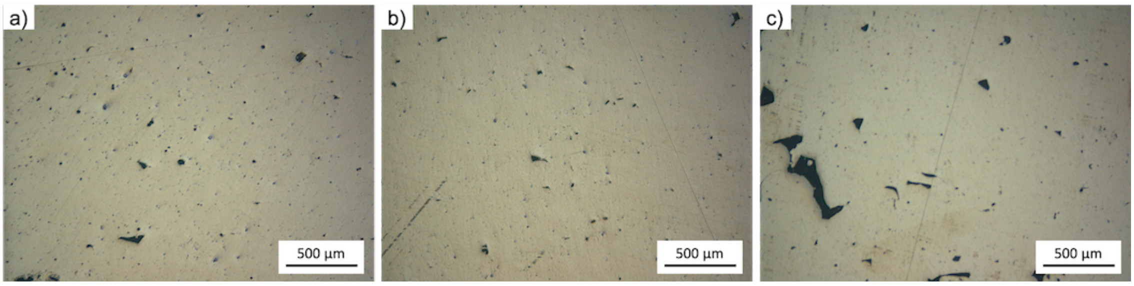

Figure 10.10: Optical images of MS1TiC SLM processed sample no. 3 after a) 2h, b) 4 h and c) 8 h of milling.

particles. The significant influence of TiC in the MS1 matrix can be seen in Figures 10.11, 10.12 and 10.13, which are presented for comparison reasons. The MMC system of maraging steel and titanium carbide is definitely a challenging composite system.

10.3.8 Microstructure analysis with SEM and EDX

In Figure 10.14 the microstructures of the 2 h (Figure 10.14a), 4 h (10.14b) and 8 h (10.14c) milled samples under a scanning electron microscope are given. There are lots of TiC particles visible in the images and obviously, there were some huge agglomerations of titanium carbide in the SLMed specimens. If one considers the initial particle size of < 2.0 μm, the agglomerations were relatively large. The mechanical milling process significantly decreased these agglomerates after longer milling times. However, in the sample processed with 179.58 J/mm^3 and with 8 h mechanically alloyed powder, it appeared as if there were some micro-blowholes in the sample, represented as black spots in Figure 10.14.

EDX analysis however revealed, that these darker spots were also formed by titanium. In Figures 10.15, 10.16 and 10.17 the EDX analyses of the SLMed samples with 2 h (10.15), 4 h (10.16) and 8 h (10.17) are shown. The yellow colour represents ferrite and blue represents the element titanium. It can be seen that the Ti was homogeneously distributed in the Fe matrix and that there were less and smaller agglomerates in the 8 h milled sample. Nevertheless, the TiC bulk powder material had a particle diameter smaller than two microns, but the EDX analysis reveals that there are still many agglomerates in the samples, even after 8 h of milling. An even longer milling could achieve even less agglomerations and more coalescences of MS1 and TiC. But as the porosity already increased, due to the non-spherical shape of the 8 h milled powder, an even longer mechanical alloying would probably cause even more defects. Al Mangour claims that a sufficiently long milling time in a planetary ball mill is needed, to attain a microstructure with nanoscale grains [12]. Furthermore, cold welded particle coalescences and broken down fragments

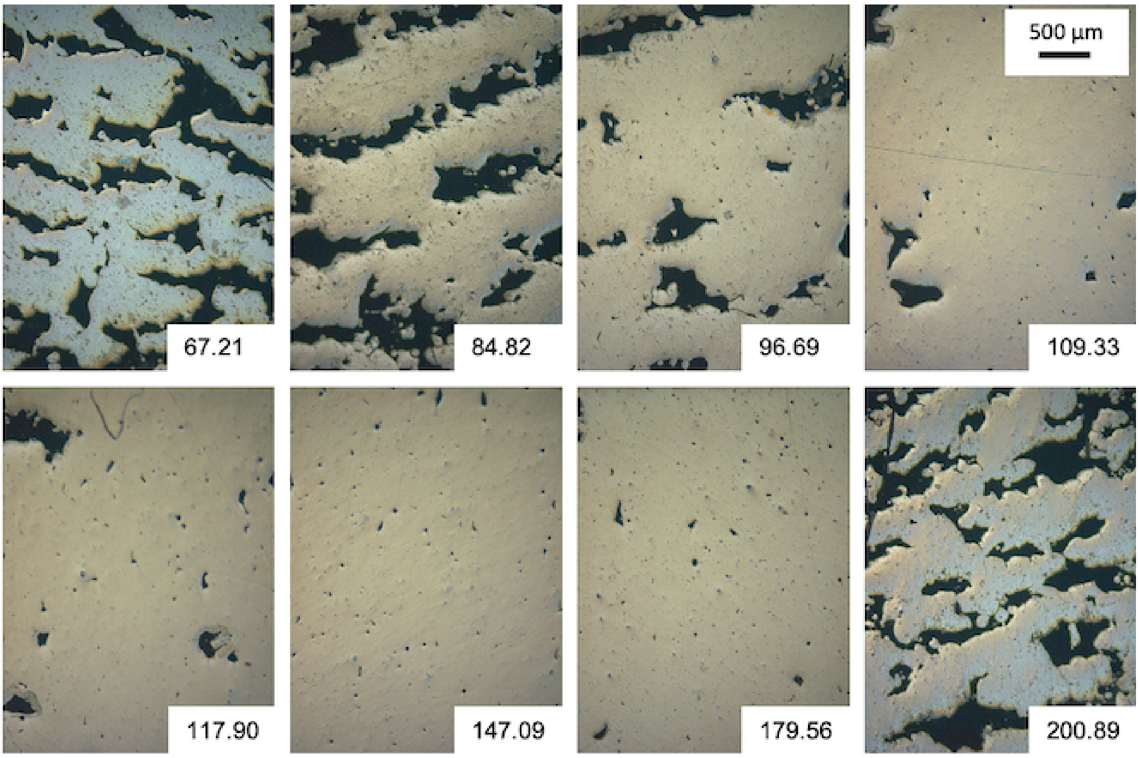

Figure 10.11: OM images of all SLMed MS1TiC specimens after 2 h of milling.

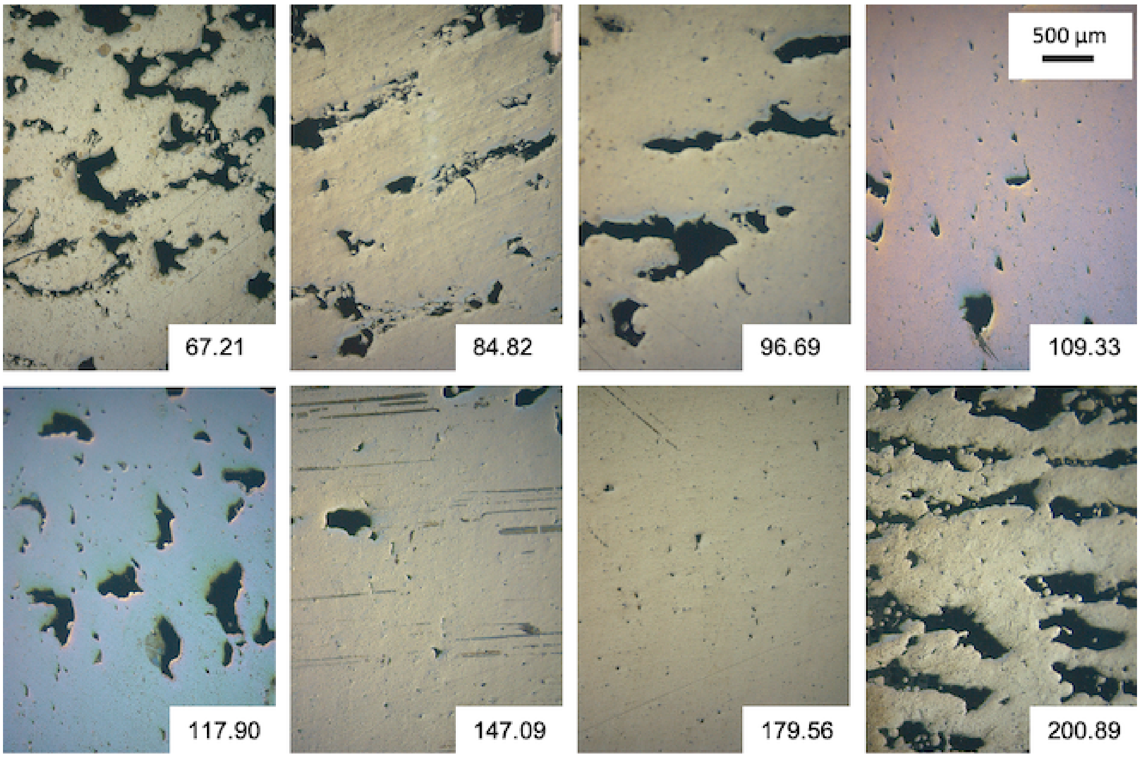

Figure 10.12: OM images of all SLMed MS1TiC specimens after 4 h of milling.

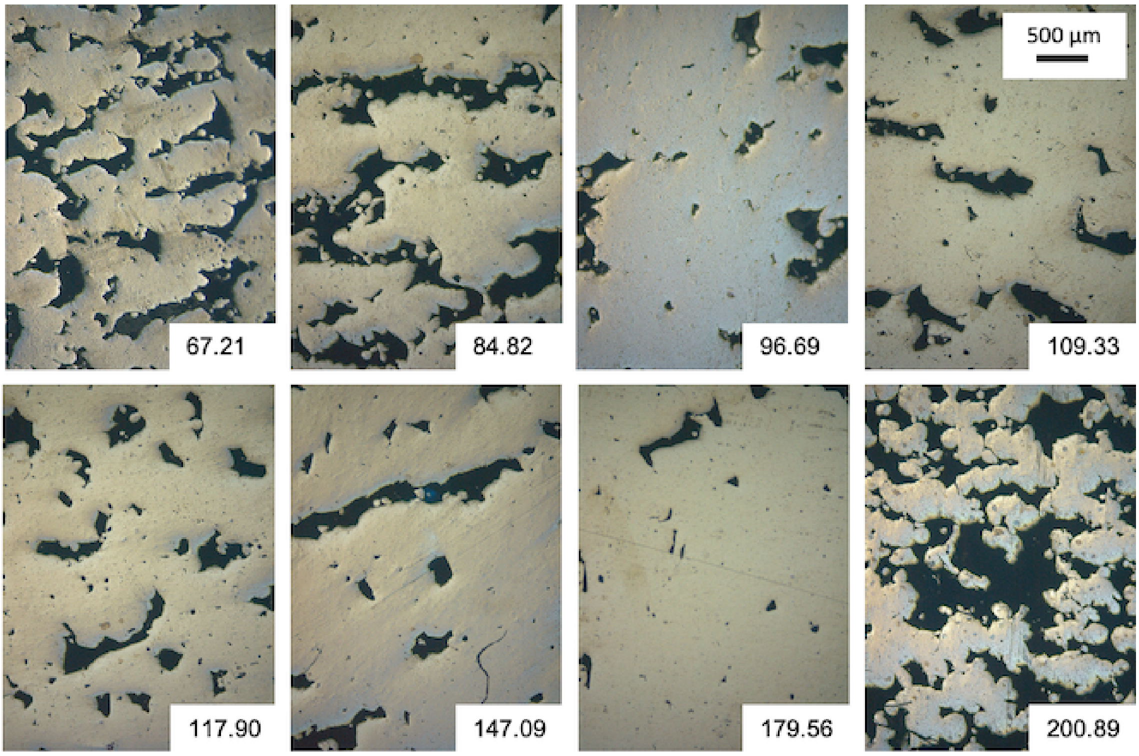

Figure 10.13: OM images of all SLMed MS1TiC specimens after 8 h of milling.

occur simultaneously during ball milling. As the used TiC powder in this study already contained a high amount of sub-micron and nano particles, the milling time is a critical factor to produce MS1/TiC coalescences with a homogeneous particle distribution and particle size distribution. The milling time for such small particles was probably not sufficiently long enough for the materials used in this study. An alternative ball milling strategy with less rounds per minute or a lower ball-to-powder weight ratio could potentially increase the density after SLM processing, but requires a more intense parameters study.

10.3.9 Microhardness

In Figure 10.18 the values of the microhardness measurements are shown and a detailed overview of the statistical data of the measurements is given in Table 10.5. The specimens are sorted ascending with increased energy density. The highest mean value for the 2 h milled powder was achieved with 60.70 J/mm^3 and was 529 HV. The highest microhardness for the 4 h milled powder was measured

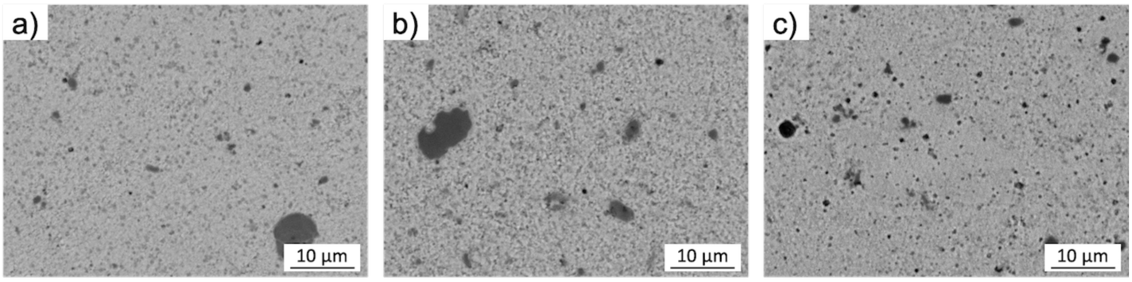

Figure 10.14: SEM images of the SLMed specimens with a) 2 h, b) 4 h and c) 8 h milled powder.

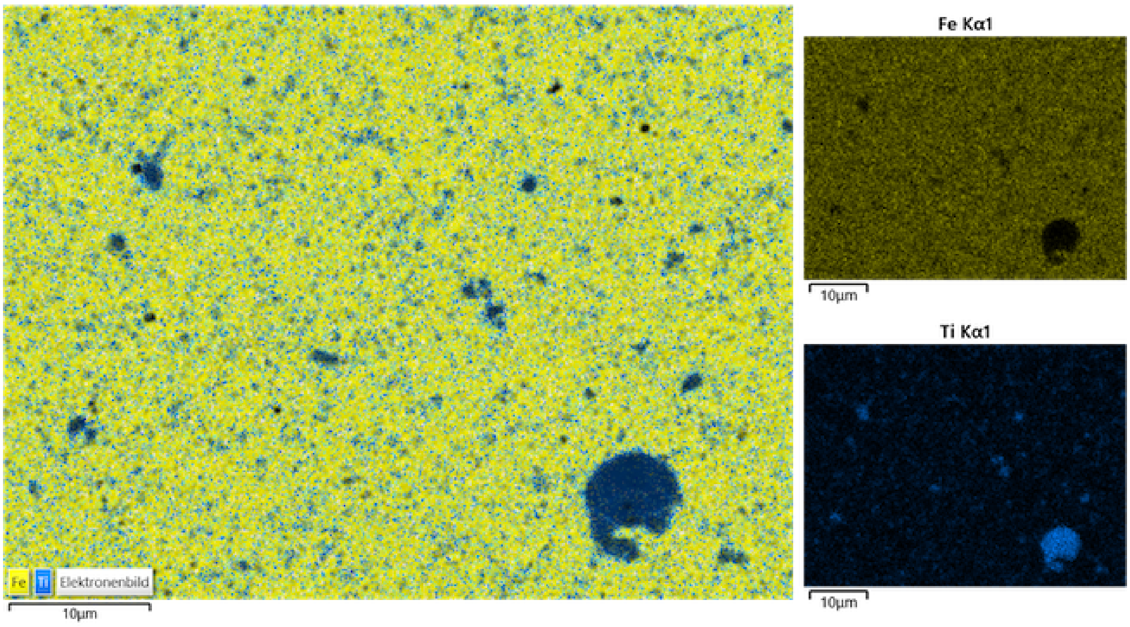

Figure 10.15: EDX image of the 2 h milled powder in which yellow represents Fe and blue Ti.

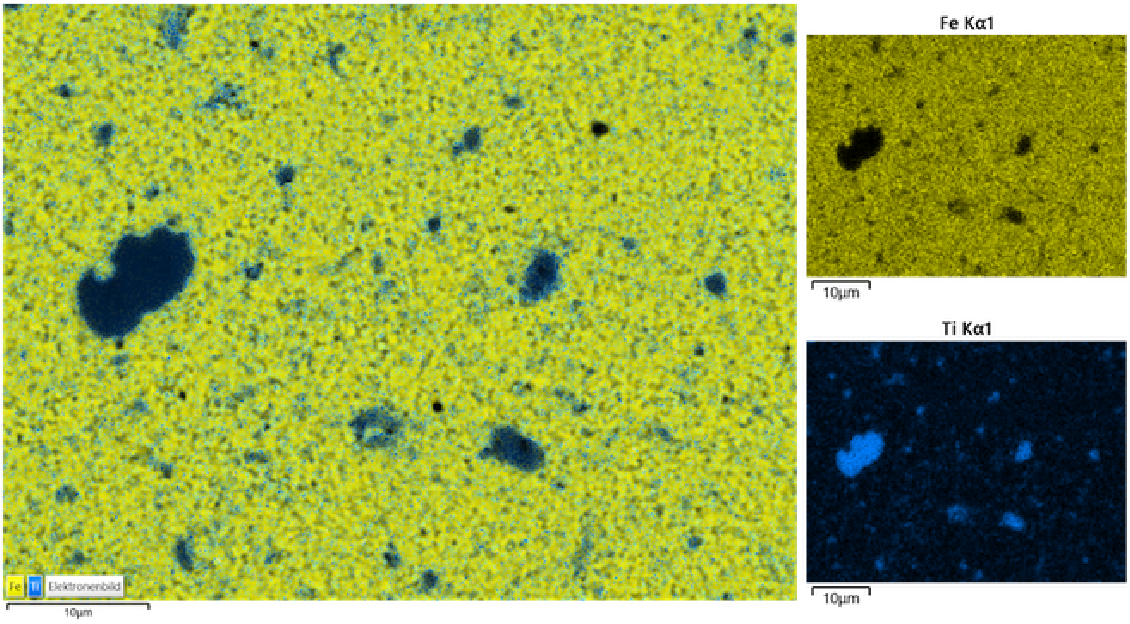

Figure 10.16: EDX image of the 4 h milled powder in which yellow represents Fe and blue Ti.

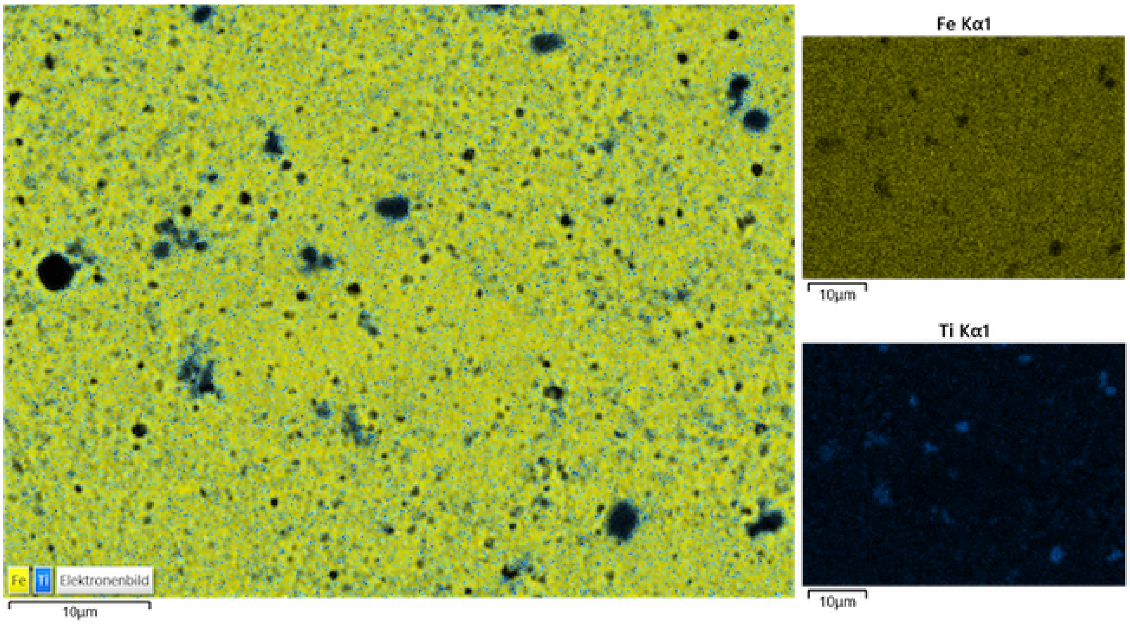

Figure 10.17: EDX image of the 8 h milled powder in which yellow represents Fe and blue Ti.

at mean 543 HV and was achieved with the sample manufactured with 179.57 J/mm^3. From all three different mechanically alloyed powders, the powder milled for 8 h was able to produce the highest Vickers hardness with an astonishing mean value of 551 HV. The value was measured at the sample which was also SLMed with 179.57 J/mm^3. The standard deviation of specimen no. 11 and 3 was very low and it is surprising that in the case of specimen no. 11, the relative part density was not related to the achieved microhardness values, as the density was comparably low at just 64.79 %. It was observed in previous studies, that the lack of fusion and the existence of blowholes significantly decreases the microhardness, as there are many imperfections underneath the surface, which can not be observed, but act as weak spots for the hardness indenter. The mean relative densities for the specimens with the highest hardness were measured at 98.59 % and 94.54 % respectively with specimen no. 3.

The outstanding values of the microhardness measurements are the proof of how significant the material properties of mechanically alloyed metal matrix composites can be, compared to non-reinforced materials. The microhardness of standard non-reinforced maraging steel MS1 is typically between 330 and 360 HV. The mechanically alloyed MS1$_{90}$/TiC$_{10}$ was able to increase these values of approximately 66.97 %.

Table 10.5: Statistical information for micro-hardness measurements of the MS1TiC samples after 2, 4 and 8 hours of milling.

Spec. Nr.	**Mean 2 h**	**R 2 h**	**V** σ^2 **2 h**	**SD** σ **2 h**	**Mean 4 h**	**R 4 h**	**V** σ^2 **4 h**	**SD** σ **4 h**	**Mean 8 h**	**R 8 h**	**V** σ^2 **8 h**	**SD** σ **8 h**
2	499	15	44,33	6,66	497	16	43,67	6,61	501	26	127	11,27
3	512	21	86	9,27	543	12	27,67	5,26	551	8	11	3,32
5	501	20	81	9	470	55	511	22,61	494	47	368,33	19,19
6	506	20	68,67	8,29	510	38	297,67	17,25	502	10	18,67	4,32
8	511	27	121,67	11,03	505	62	648,67	25,47	483	157	4792,67	69,23
10	499	12	25	5	470	72	953	30,87	502	12	27,67	5,26
11	529	58	722,67	26,88	504	41	292,67	17,11	499	59	648,33	25,46
18	502	5	4,33	2,08	431	150	4839	69,56	471	46	356,33	18,88

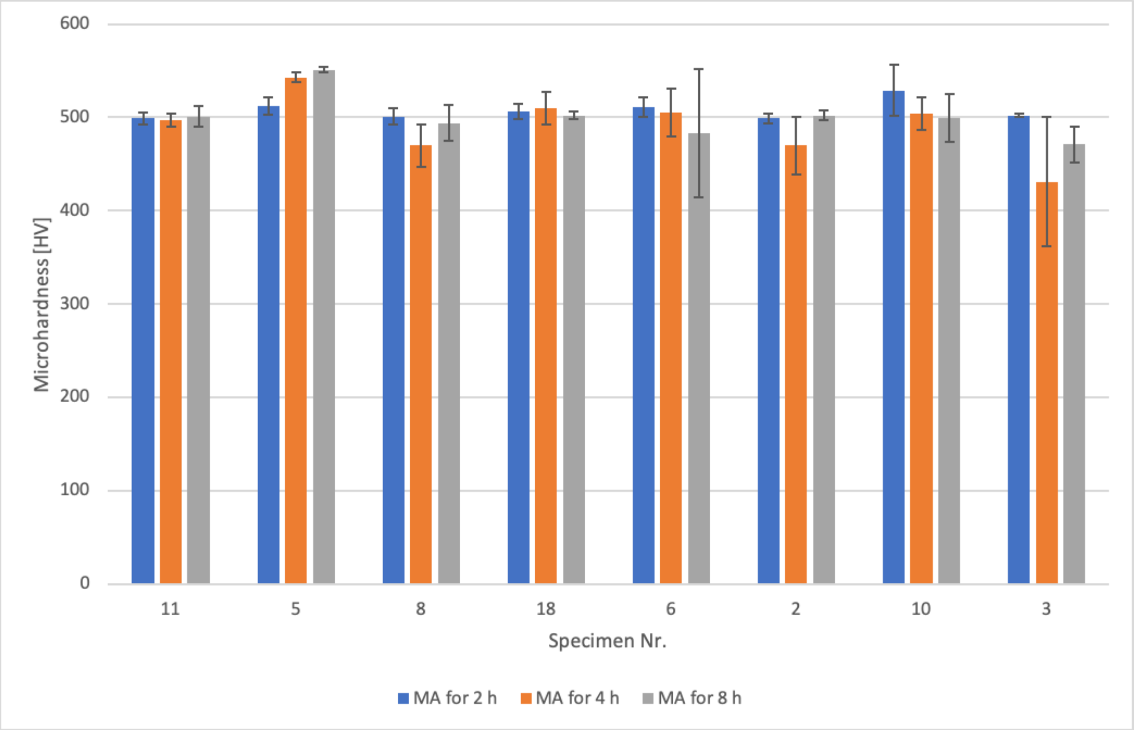

Figure 10.18: Diagram of the microhardness measurements of the SLMed MS1/TiC samples.

Table 10.6: Coefficient of friction, track wear rate and ball wear rate of MS1TiC.

Material	COF (μ)	Track Wear Rate [mm^3/Nm] x 10^{-5}	Ball Wear Rate [mm^3/Nm] x 10^{-5}
MS1	0.74	1.51	1.44
MS1TiC-2h	0.84	1.69	4.88
MS1TiC-4h	0.84	1.45	21.40
MS1TiC-8h	0.77	1.91	13.80

10.3.10 Tribological Performance

The micro scratch tester was used to analyze the wear rate and coefficient of friction of the SLM processed specimens. In Figure 10.19 the COF diagram is shown. Interestingly, the pure MS1 sample had the lowest COF value after 1000 cycles, which was $\mu = 0.382$. Figure 10.20 shows the relative penetration depth of the wear analysis and again, pure MS1 had comparably better results. The penetration depth of MS1 after 1000 cycles was 0.37 μm, whereas the penetration depth of MS1TiC - 2 h was 16.03 μm, MS1TiC - 4 h had a depth of 49.29 μm and MS1TiC - 8 h had 8.39 μm. Nevertheless, it has to be mentioned that the standard deviation of the MS1 penetration depth was very high and therefore, the actual results can differ. In Table 10.6 the COF values, the track wear rate and the ball wear rate of MS1TiC are given. The 4 h milled sample was slightly better in terms of track wear rate, but all the values were very close to each other, making an analysis difficult. If one compares the ball wear rates however, it becomes very obvious that the MMC material must have been harder and had a better wear resistance as the abrasion of the indenter was significantly higher. In Figure 10.21 the comparison is given in a graphical diagram and the differences become more obvious.

In Figure 10.22 an SEM image of the wear track and the respective EDX images are shown. It was found that the track, created by the indenter, had residues of worn material adhered in many places of the track. These residues can act as a gliding plane and cause a lower coefficient of

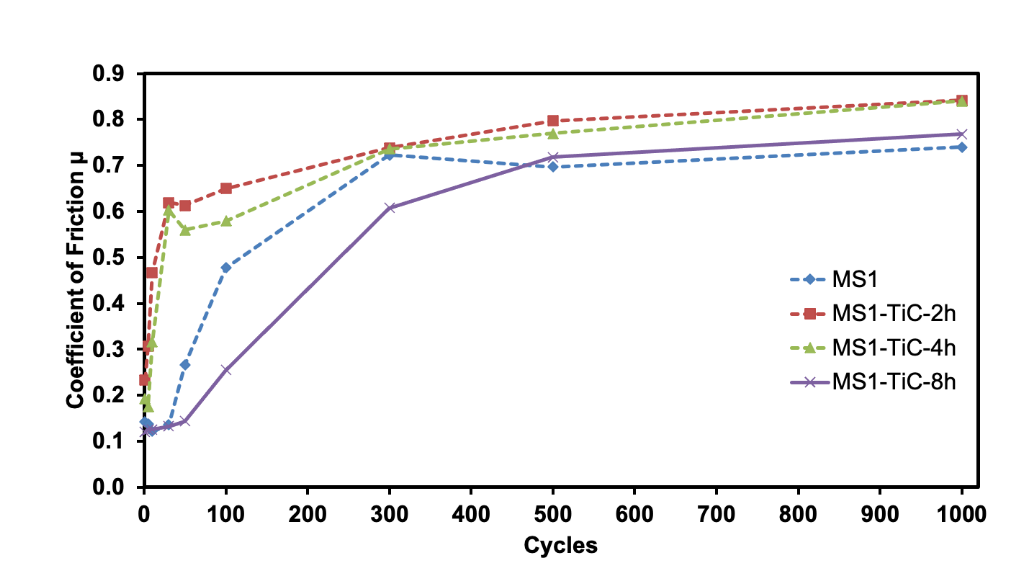

Figure 10.19: Graph of the coefficient of friction of the MS1TiC samples.

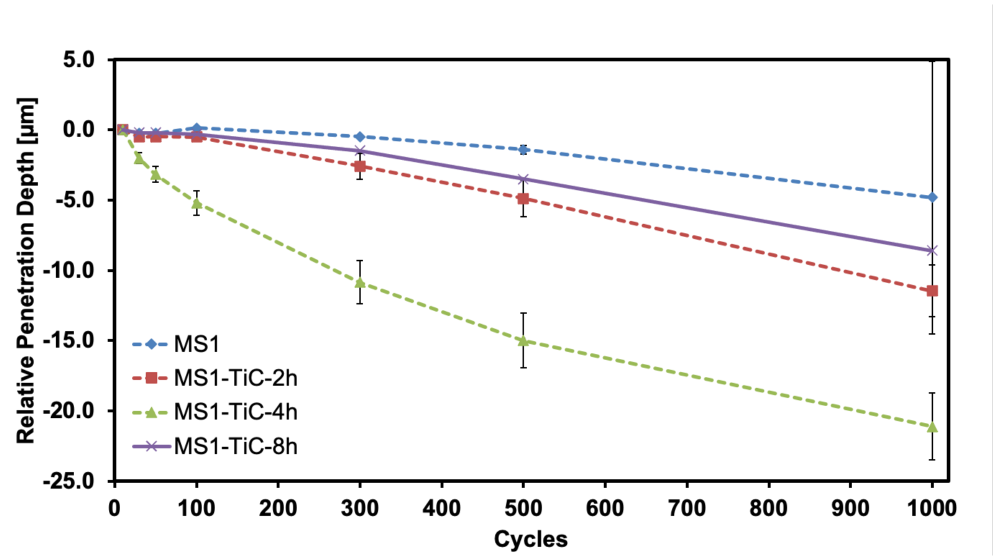

Figure 10.20: Graph of the relative penetration depth of the MS1TiC samples.

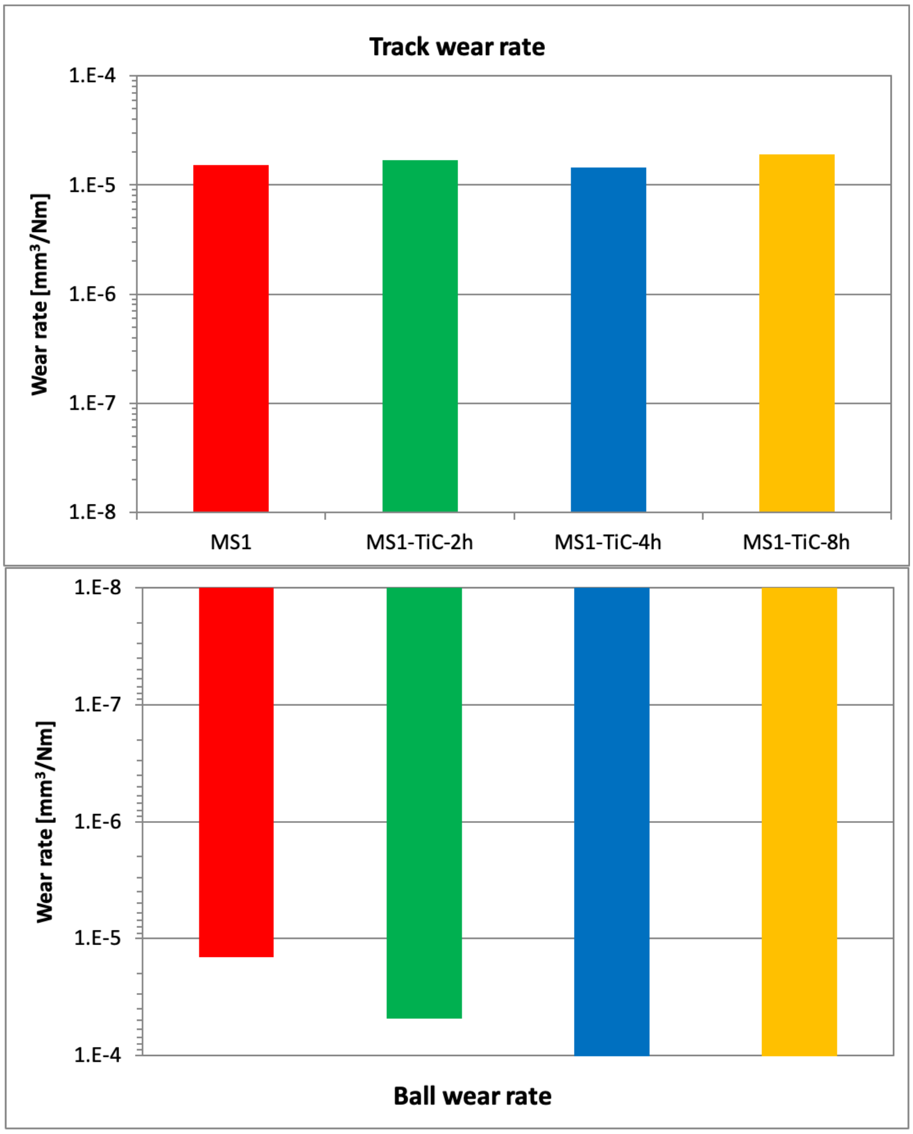

Figure 10.21: Graphs of a) the track wear rate and b) the ball wear rate of MS1TiC.

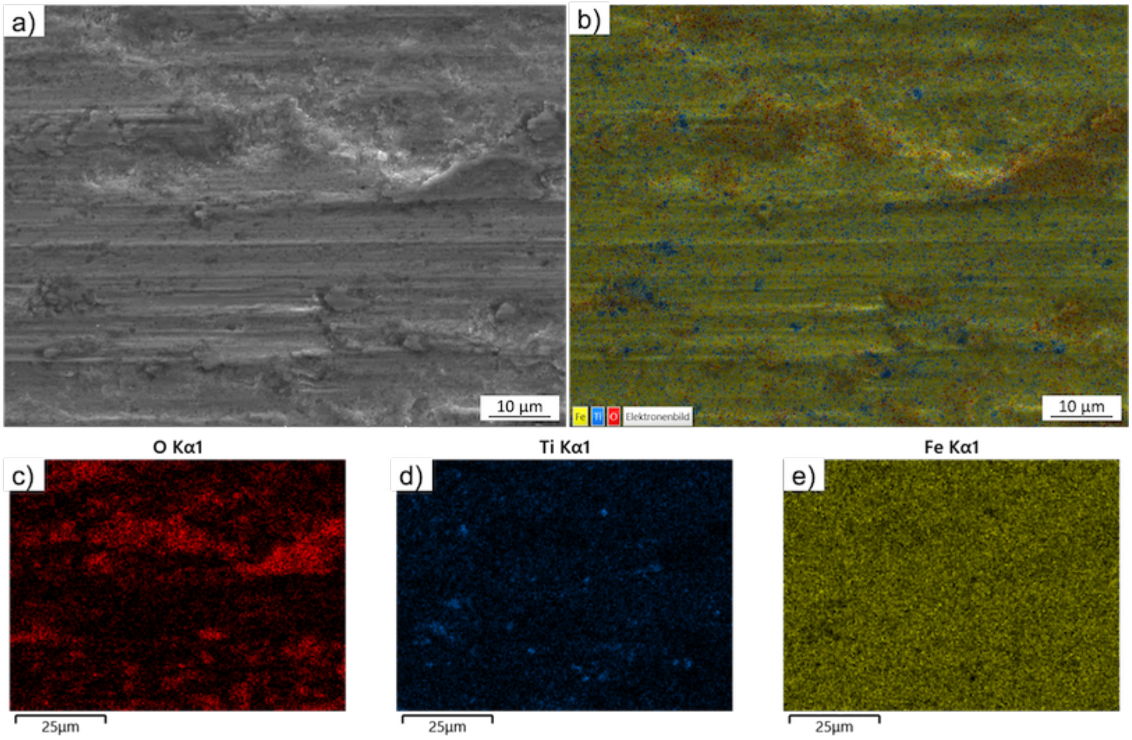

Figure 10.22: a) SEM image of the track, b) the EDX sum map and c), d) and e) the EDX maps of each element of the MS1TiC tribology test.

friction. EDX analysis also revealed a homogeneous distribution of TiC particles on the surface. The titanium carbides resist against the stainless steel indenter, but at some point they will get loose and then will act as an abrasive material while gliding between the specimen and the indenter. In Figure 10.22b the combined EDX map is given, showing the elements Fe (yellow), Ti (blue) and O (red). The image further indicates that the worn material oxidated. Due to this fact, the surface must have become very hot. As the tribological track was relatively short (i.e. 5 mm), the temperature constantly rose and did not have enough time to cool down. In Figures 10.22c, d and e the maps of each element are provided.

10.4 Conclusions

To satisfy the demand for new applications and, like in this study, new advanced materials it is inevitable to understand each relationship and process parameter. The metal matrix composite of MS1 and TiC is definitely a challenging one to understand and to control. In this chapter the powder morphology, the microstructure, the mechanical properties and the phase formation of $MS1_{90}/TiC_{10}$ was investigated. The influences of the high energy ball milling and the SLM parameters had to be understood and the effects of each parameter had to be analyzed. The powder preparation with a planetary ball mill significantly influences the powder morphology. In this MMC system, the mechanical alloying process did not drastically change the phase formation of the system. However, the TiC particle size distribution decreased and agglomerations were broken. After 8 h of milling, the formation of coalescences was observed as the cold-welding mechanisms were dominant. The particle size distribution was measured as $D_{10} = 14.10\ \mu m$, $D_{50} = 37.77\ \mu m$ and $D_{90} = 70.43\ \mu m$. After processing the powder in a planetary ball mill, the various samples were used to print specimens in a selective laser melting device. It was observed that 8 h of milling had a negative influence on the powder morphology, which was not spherical anymore. Therefore, porosities and defects occurred in the samples. Nevertheless, the microhardness was significantly improved compared to non-reinforced standard maraging steel. It was possible to increase the microhardness from 330 HV of commercially available MS1 to astonishing 551 HV. The reinforcing TiC particles were homogeneously distributed in the SLM processed metal matrix and were acting against dislocation movements. It was expected to also achieve remarkable tribological performance results, due to the high hardness. The wear resistance was hard to analyze as the results of the pure MS1 were very similar to the results of the TiC reinforced MS1. Just the ball wear rate indicated a higher wear resistance as the indenter balls were worn more than the indenter of the MS1 specimen.

The phase formation after SLM processing the 8 h milled powder was somewhat mysterious though. It was impossible to identify the peak at 2θ position of 37 ° in the XRD chart of Figure 10.8. The typical α-phase of MS1 was decreased and instead, high peaks of retained austenite were visible. It can be said that the reason for this was the dissolvement of the fine non-stoichiometric $TiC_{0.79}$ particles during SLM processing. Carbon became free and connected to ferrite. Because of this, the martensite starting temperature was lowered and the austenite was not able to transform to martensite. As a result of the decomposition of the TiC monocarbides, there was some free titanium with an extreme reactivity to oxygen left in the melt. It can not be said for certain, but it is very likely that, instead of the TiC, there was some $TiC_{0.1}O_{0.9}$ formed and precipitated. The peaks would fit according to the XRD database and there is always some oxygen left in the processing chamber.

In the tribological analysis it was found that the metal matrix composite did not outperform the pure MS1. The penetration depth of MS1 was not as deep as the depths of the MS1TiC samples or at least, they were very similar. However, the standard deviation of the MS1 sample was very high. Further, the track wear rates indicated that it was not possible to increase the tribological performance with the addition of TiC particles, even though the hardness was significantly improved. However, the ball wear rate was much higher in the MS1TiC specimens. The TiC particles were very fine distributed in the solid material and acted as a resistance against the indenter until they broke out. Then, they acted as abrasive material and this very likely caused a higher ball wear rate. For improved results, a higher part density must be achieved.

Conclusions

In the present work the influence of particle reinforcements on the microstructure, phase formation, hardness, mechanical characteristics and wear resistance of selective laser melted maraging steel MS1 was examined. Titanium carbide and vanadium carbide non-oxide carbides were used as reinforcing additives. For the first time, the behaviour of these carbides in combination with maraging steel was analyzed. The introduction of different amounts of carbides was achieved with mixing and mechanical alloying of the powder materials in a tumbler mixer and a high energy planetary ball mill, respectively. The optimal process parameters for the mechanical alloying process had to be found in order to achieve near-spherical powders. Furthermore, an embedding of carbide particles into the maraging steel matrix material was desired. Thereby, the powder morphology had to be controlled. Through a decrease of particle size of the initial carbide bulk powder material, it was possible to apply lower milling times.

For the selective laser melting process, two different machines were used. One was equipped with a 200 W fibre laser and the other one with a 100 W fibre laser. Both machines were working under argon inert gas atmosphere. For each powder batch, not just the optimal milling process parameters had to be found, but also the optimal SLM processing parameters. For this, a preliminary Design of Experiments, using the Federov operator, was performed. After measuring the density of the SLM processed specimens, the results were analyzed and the most promising parameters were used for further specimen production. One specific problem, was the sieving of the powders. Due to very fine and irregular shaped particles, the sieve can be blocked making sieving impossible. Because of this, a higher amount of carbide particles might be sieved out of the powder material, causing a different composition. This specifically applies to mixed powders, but is also applicable to mechanically alloyed powders, if there are still free carbides in the bulk powder.

Selective laser melting is - compared to other technologies like milling and casting - a relatively new production technique. It allows more degrees of freedom while designing parts and prototypes, but also has a higher capability of designing advanced materials by controlling the microstructure, and therefore, the mechanical properties. High cooling rates and a different heat distribution during SLM processing result in different grain growth and microstructures. In combination with mechanical alloying, powerful, but in the same manner very complex tools for tailored material developments are available. Phase formations and crystal structures can differ from other powder processing techniques. Sometimes these effects can be very complex to explain and understand as todays analysation tools are lacking in precision. Therefore, in some cases just experience can determine what happened exactly.

In the first phase of this thesis, maraging steel MS1 and vanadium carbide was mechanically mixed in a tumbler mixer and then SLM processed. The composition was created with 90 wt% MS1 and 10 wt% VC. The particle size of the reinforcing VC was between 1 and 33 microns and the MS1 had a particle size of 15 - 40 μm. It was found that in the VC bulk powder even smaller particles than 1 μm were found, which were immediately sticking to the bigger MS1 particles after mixing the powders together. Through the mechanical mixing, a homogeneous mixture was achieved. For comparison reasons, pure MS1 was SLM processed first and then the metal matrix composite was processed. The highest achieved relative density of pure MS1 was 98.18 % and for the MS1-VC with 1-33 μm VC particles, the maximum relative density was 97.32 %. There were some spherical and irregular shaped porosities found in the samples, indicating lack-of-fusion and gas entrapments. Furthermore, the specimens showed, after embedding the samples and polishing them, lots of unmelted VC particles. The hardness of the MS1-VC with 1-33 μm VC particles was increased by 132 HV or 37.29 % of the peak values compared to pure MS1, which had a maximum hardness of 354 HV. Even though unmolten VC can still improve the mechanical properties, it is desired to achieve molten and then precipitated primary VC particles as they are finer and more homogeneous distributed in the solidified material. Usually, these carbides are also embedded better into the matrix material and cause less stress in the matrix. Some researchers reported stress caused by strain starting at the VC particle, which is a potential source for failure. To further improve the density by stabilising the melt pool, finer VC was used for another powder batch. Instead of adding the 1-33 μm vanadium carbide, fine VC with < 2.5 μm was mixed with MS1. It was expected, to get higher part densities, because the melt pool would not be interfered by large VC particles anymore. After SLM processing and measuring the density of the samples, this expectation was confirmed. The maximum relative density was 98.02 %. However, the coating of the powder layers in the SLM process was more unstable as the fine VC powder particles agglomerated more easily, causing an uneven powder layer. This was partially compensated through a higher powder feeding rate. Through the initial particle size refinement the maximum hardness was also improved. The highest value of the MS1/VC-2.5 metal matrix composite was 597 HV. Last but not least, a double exposure scanning strategy was applied to improve the density results of the specimens. The same SLM parameters were applied, but each specimen was laser scanned twice, before the next powder layer was coated. The density results did not improve significantly, but there were more VC particles melted. This proved that melting VC in combination with MS1 in a selective laser melting machine is possible. Against expectations, the hardness was not increased with the double exposure scanning strategy though. Effects like a coarsening of the microstructure due to the scanning strategy might have had an impact, as the second exposure might have acted as a heat treatment. For this, further studies would have been advisable, but instead, a different approach was chosen.

In Chapter 7 different volume contents of VC were mixed to the MS1 powder. Again, the powders were mechanically mixed in a tumbler mixer. According to the results of Chapter 6 the large particle size of the VC bulk powder negatively influenced the part density as the melt pool was not as stable as it should be. Vanadium carbide has a significantly higher melting point and therefore, the laser induced melt pool constantly was interfered. To solve this problem, finer VC was added to the MS1 powder and four different powder batches were mixed:

- 97.5 wt% maraging steel MS1 and 2.5 wt% vanadium carbide VC-2.5 ($\mathrm{MS1}_{97.5}/\mathrm{VC}_{2.5}$),
- 95 wt% maraging steel MS1 and 5 wt% vanadium carbide VC-2.5 ($\mathrm{MS1}_{95}/\mathrm{VC}_{5}$),
- 92.5 wt% maraging steel MS1 and 7.5 wt% vanadium carbide VC-2.5 ($\mathrm{MS1}_{92.5}/\mathrm{VC}_{7.5}$),
- 90 wt% maraging steel MS1 and 10 wt% vanadium carbide VC-2.5 ($\mathrm{MS1}_{90}/\mathrm{VC}_{10}$).

The added VC powder had a particle size of < 2.5 μm. After SLM processing the cubic 10 x 10 x 10 mm samples, the part densities were evaluated. It was found that the porosity increased with the amount of VC. While the specimens with just 2.5 % of VC had astonishing part densities of > 99 %, the samples with 10 % of VC had a maximum of 98.02 %. The microstructure analysis showed that most VC particles were not molten at all and were just embedded into the matrix material. It was desired to fully melt the VC particles as they would then increase the mechanical properties better. Further, they would not be potential starting points for cracks.

The microhardness tests were very promising though, but depended on the part density as porosity notably decreased the hardness. Overall it can be said that the more reinforcing vanadium carbide was added to the MS1 material, the higher the hardness was. After finding the optimal parameters for SLM processing, further samples were manufactured for mechanical tests. It was planned to perform ultimate tensile strength, hot ultimate tensile strength and charpy impact tests. For this, several specimens were built and some were heat treated with 490 ° C for 6 hours to compare the results. However, the larger the parts were, the more difficult it was to print the parts. The composite powder caused severe spatter formation, which are a potential source for errors due to their large particle size. On one hand, a lot of energy was necessary to create parts with a high part density. On the other hand a high laser power can increase spatter formation and vaporization. These spatters were embedded into the solid part and influenced the results of the ultimate tensile and charpy tests. Both test results were comparably bad and the specimens failed way too early. Further, some lack-of-fusion areas were found after analyzing the fracture planes after ultimate tensile strength tests. An explanation for these lack-of-fusion areas was found in some interrelated factors. As some areas were built faster in Z-direction due to irregular growth, humps were created in the specimen. These humps had a negative influence on the powder layer height and in some cases it might have happened that the powder layer was too high to be completely molten and welded to the layer underneath. In these areas the humps prevented sufficient powder coating in the beginning and then after some further layers were coated, the area behind the hump was coated with too much powder at once. Another phenomenon discovered were large humps or particles, which were bonded together, that broke off of the coater and then were pushed to a surface, in which a part was created. These humps or particles then prevented the laser to sufficiently melt the powder in this area. It was also found in SEM analysis that the small VC particles had a high tendency to form agglomerations. As VC has such a high melting point, the laser was not able to fully melt these agglomerates and as a result, unmolten VC was found in the microstructure.

Another outcome of this chapter was the realization of how challenging the post-sieving of MMCs after SLM processing can be. Fine powders, like the ones of VC, started to block the sieve while using a vibrating shaker tower. To solve this sieve blocking one can use a bigger mesh, which would also result in larger particle size distribution and more spatter particles in the powder, as they were usually larger than the used MS1/VC. But a blocked sieve also results in an unknown element distribution and it can not be said, how much VC would be left after sieving. To solve these issues, mechanical alloying was applied in the next study.

In chapter 8 the focus was set on creating metal matrix composites of MS1 and VC with a planetary high energy ball mill to embed the VC particles into the MS1 powder. Mechanical alloying is a cost effective way to crack large and hard VC particles and to in-situ form coalescences with MS1 particles. In this chapter the goal was to understand the mechanical alloying process parameters and the possibilities of creating a MMC with MS1 and coarse VC. The milling parameters were set to similar parameters found in the literature. After each hour of milling, a 15 min cool-off break was set to avoid overheating. Several powder batches were produced and samples were taken after each iteration for further analysis. Powders were milled for 2, 4, 8, 12, 16, and 24 hours. Particle size analysis showed that the average PSD increased with the milling time. After 16 h of milling however, fracturing must have become predominant as the particle size distribution decreased again. Through mechanical alloying larger VC particle were cracked into smaller ones and the particles were embedded into the MS1 particles. While SLM processing the mechanically alloyed powders, it was found that the recommended energy density of 67 J/mm^3 for MS1 was not sufficient. A higher energy of 179 J/mm^3 was necessary to improve the part density and to fully melt the smaller VC particles. In the 16 h milled and SLM processed samples, there were almost no unmelted VC particles found, which indicates an optimal refinement of the VC powders and a complete melting of the composite. XRD analysis revealed that there was a phase formation change. First of all, the alpha-Fe forming MS1 was not able to completely form to alpha-Fe after SLM processing. Obviously, the high cooling rate of the surrounding VC and a possible chemical composition change hindered the martensitic phase formation process. However, it was observed that γ-Fe transformed to α-Fe after 24 hours of milling and SLM processing. The low temperature alpha-phase was the predominant phase again. This was on one hand caused by VC particle that were too small to affect the martensitic starting temperature. Furthermore, in the 24 h milled sample it was discovered that the initially used non-stoichiometric V_8C_7 has formed to precipitated primary stoichiometric VC. This indicates that some of the free C was attached to V_8C_7 and further increased the martensitic starting temperature, causing the predominant alpha-Fe phase on the other hand. Using SEM analysis, the microstructure was investigated. Some small black particles were found and it was believed that these particles were the primary precipitated VC particles. EDX analysis was used to understand the sightings, but the resolution of the detector was insufficient and therefore, it cannot be claimed for sure. However, as there were no unmelted VC particles found in the microstructure, the VC was either transformed in ultra fine or primary precipitated carbides.

Microhardness results revealed that the addition of VC had a huge impact on the hardness of the SLM processed samples. Pure MS1 usually has between 330 and 360 HV, but the mechanically alloyed MMC of MS1/VC was able to outperform these values significantly. The maximum hardness was measured at 439 HV. Some specimens had a high standard deviation, as there were pores underneath the surface and not visible with optical microscopy. One of the main aims of creating metal matrix composites is to improve their tribological performance. The sample that was mechanically milled for 16 hours had a comparably low coefficient of friction. It was discovered that worn material was adhered to the track in most samples and then polished by the indenter. Therefore, a gliding plane with a very low COF was created. This effect was discovered in all samples, but was more present in some than in others. In most cases, a VC particle was the starting point for the adhered worn material. As the 16 h sample had a very different result than the other samples, the test was repeated, but the results remained very much the same. The penetration depth did not change significantly in the MMC samples, but as the COF was very low in the 16 h sample it also had a very low penetration depth. More importantly, the track wear rate and the ball wear rate were analyzed. Especially the 16 h and the 24 h milled samples had remarkable wear rates, as they were much lower than the wear rates of pure MS1. In the 24 h milled specimen, the indenter was worn even more, but the wear rate was comparably low, which indicates a very abrasive surface. EDX analysis of the worn track revealed that the surface must have been very hot during tribological testing. The worn material consisted of mostly FeO and as expected, underneath a VC particle was found. The VC particle will act against the indenter and improve the wear performance until they break out of the sample and then act as abrasive material between the sample and the indenter. In this case, they will wear the sample even more until they are pushed away. Overall, it can be said that the wear performance was not improved with the 2 to 12 h samples, but was improved notably with the 16 and 24 h milled samples. In specific, they were able to decrease the wear rate by 93.30 % (16 h sample) and 53.80 % (24 h sample).

As it was found in Chapter 8 that VC particles have a higher tendency to fully melt, if their particle size is smaller, and that a milling time more than 4 h in most cases leads to non-spherical powders, a different approach was chosen in Chapter 9. It was decided to use vanadium carbide powder with a maximum particle size of 2.5 microns in combination with MS1. Further, two different milling equipments were chosen to compare the effects while using tungsten carbide or 440C stainless steel balls and vials. It was calculated that the temperature rise per impact was more than twice as high with WC balls and vial:

- $\Delta T_{VC_{440C}} = 32.19$ K
- $\Delta T_{VC_{WC}} = 70.52$ K

The MS1/VC mixture, containing 10 wt% of VC, was mechanically alloyed in a WC jar for 1 hour, 2 hours and 4 hours. Another powder patch of the same mixture was milled for 4 hours in a 440C jar. Afterwards, the powders were analyzed regarding their morphology and particle size distribution. In the WC milled powders, the amount of small particles was decreased the longer mechanical alloying was applied. Compared to the 4 hour milled powder with the 440C equipment, the particle size of the WC ball milled MS1/VC was still much smaller and had a smaller particle size distribution. Furthermore, the powder morphology of the WC ball milled powders was more near-spherical. After 4 hours of milling, a lot of VC particles were embedded into the MS1 matrix in both powder batches. However, the 440C ball milled powders were far-from-spherical, but were perfectly mechanically alloyed. All VC particles were embedded and almost no free VC were found in the powder. Against expectations from the beginning of the study, the 440C ball milling equipment had a much higher impact on the powder morphology than the WC ball milling equipment. As all parameters, like the radius of the main disk, the rotational speed, the diameter of the jar, and the ball-to-powder weight ratio, were kept exactly the same. The only parameters changed were the balls used for milling, due to the different material density, and the atmosphere. Mechanical alloying with the WC equipment allowed a process under argon inert gas atmosphere whereas the 440C jar was not equipped with such a valve. Even though there was slightly more oxygen found (i.e. ˜2.36 %) in the 440C milled powder batch, it is very unlikely that oxygen caused such a difference in the powder morphology. Instead, it is believed that the amount of balls had a more significant influence. As there were more balls in the 440C equipment (because the ball-to-powder weight ratio was kept similar), there were more impacts of balls in the same amount of time. This very likely caused the differences.

After SLM processing the different powders, the part density, microhardness and tribological performance was investigated. It turned out that the far-from-spherical shape of the 440C powder batch was too much deformed and the results were very bad. There were too many porosities in the samples. However, the powders processed with the WC ball milling equipment turned out to be much more promising. Compared to the more coarse VC-33 samples, the VC-2.5 specimens had a higher part density of approximately:

- 1 h milling 98.41 % relative density
- 2 h milling 99.28 % relative density
- 4 h milling 98.44 % relative density

In the SEM there were some large grains found in all processed samples. In the samples in which a lot of energy density was used, less unmelted VC particles were found. It was further discovered that some grains started to grow next to unmelted VC particles, as they can assist the nucleation process. While comparing the 4 h milled powder batches from the 440C and the WC ball milling equipment, it was found that the 440C milled powder had a much coarser microstructure and the columnar dendrites were growing very long. XRD analysis revealed that the mechanically alloyed and SLM processed samples changed their phase formation from α-Fe to γ-Fe.

The microhardness of the 1 h, 2 h and 4 h WC equipment milled and SLM processed samples was significantly improved compared to pure MS1 but also notably improved to the more coarse VC-33 samples. In fact, the hardness reached an astonishing level of 471 HV. During tribological tests it was found that the penetration depth of the 2 h and the 4 h milled samples was lower than the one of the MS1 sample.

Another approach to reinforce maraging steel was performed with titanium carbide in Chapter 10. MS1 was mechanically mixed in a tumbler shaker mixer with 10 wt% TiC for homogenisation reasons. Afterwards, the powder composition was mechanically alloyed for 2, 4 and 8 hours. After longer milling hours, the powder had a tendency to form bigger particles as the particle size distribution increased. However, after 4 hours of milling, the amount of fine particles increased again which indicates that fracturing of the large particles occurred. After 8 hours, the amount of small particles decreased again, which was due to the formation of coalescences. Selective laser melting was applied after the milling and several solid samples were produced. XRD analysis showed that after 8 h of milling and SLM processing, the martensitic phase peaks became weaker and instead, gamma-Fe was the predominant phase. This was also discovered in other studies. In some cases, this is related to the cooling capabilities of the added carbides. In other cases this effect is related to an elemental transition. In this scenario it is very likely that the $TiC_{0.79}$ transformed into $TiC_{0.1}O_{0.9}$ and some free carbon influenced the martensite start temperature. Therefore, the start temperature was decreased and the unidentified XRD peak is related to $TiC_{0.1}O_{0.9}$.

Table C.7: Uncertainties in micro-hardness measurements (based on [44]).

Uncertainty influences	Source of its determination
Uncertainty of the hardness reference plate	Calibration of the hardness reference plate
Standard uncertainty of the hardness testing device while measuring the hardness reference plate	Measurement results of the hardness reference plate
Standard uncertainty of the hardness testing device while measuring the specimen	Measurement results of the specimen
Standard uncertainty of the test specimen due to the resolution of the length measuring system	Specifications of the hardness testing device

The part density of the MS1/TiC MMC was measured at:

- 2 h milling 98.52 % relative density
- 4 h milling 98.59 % relative density
- 8 h milling 94.54 % relative density

The most astonishing result was the micro-hardness, which was increased to 551 HV in the 8 h milled and SLM processed sample. Compared to pure MS1 this value is 66.97 % higher, which is remarkable. Unfortunately, the tribological performance was not as promising as the micro-hardness was. The wear resistance was very similar to pure MS1. It was just noted that the ball wear rate was much higher, indicating a higher resistance against the indenter. But the track wear rate was not improved, which shows that the tribological test was just more abrasive.

Of course, it has to be mentioned that there are some statistical uncertainties in the results that can not be avoided. In the micro-hardness measurements for example, are several influences for uncertainties known and they are named in Table C.7. While measuring, uncertainties are inevitable. However, modern equipment can reduce measuring errors and achieve more accurate results.

In this study the metal matrix system of maraging steel was successfully reinforced with vanadium carbide and titanium carbide for the very first time using selective laser melting technologies. Even though there were some challenges to face and the overall density of the fabricated MMCs has to be improved in future works, it was proven that some material properties (i.e. hardness, wear) were significantly improved, whereas others (i.e. ultimate tensile strength) were decreased. However, the MS1VC system with 10 %wt. of fine VC (2.5 μm) was able to achieve promising results even in the ultimate tensile strength tests. The biggest issue for the specimens were SLM process related defects, rather than defects in the microstructure caused by the reinforcing particles. Further, the SLM processed and mechanically alloyed MS1TiC metal matrix composite system revealed its great capabilities and have been investigated for the first time.

Future Investigations

It is suggested that future scientific work should be performed with MS1 and TiC, but also the MS1VC system should be further improved. Specimens should be fabricated in the X-Y plane to reduce the risk of SLM related defects and binding errors caused by instabilities in the SLM machine. This way, more information about the mechanical properties could be gained. Furthermore, a preliminary refinement of the TiC and the VC particles should be considered to decrease necessary milling times and to achieve powders with an increased near-spherical shape.

On a final note it can be said that MMCs for SLM applications can outperform traditional materials, but are very complex to control. Mechanical alloying is a powerful and cost-effective technique to acquire metal matrix composites and SLM is an optimal tool for processing the powders to solid parts. However, the formation of agglomerations and coalescences, the retaining of a near-spherical shape, the melt pool stability, the phase formation and the powder sieving can be challenging while working with MMCs. Further investigations in parameter optimisation should be performed, to achieve higher part densities. This directly correlates to higher micro-hardness values and a better tribological performance.

A

Appendix

In this appendix, the symbols used in this thesis work will be explained.

α	ferrite iron
f	frequency
n	mode
v	velocity or scanning speed
L	length of a cavity
E_v	energy density
h or h_d	hatch distance
P	laser power
t	layer thickness
γ_{LV}	surface tension of the liquid-vapour
γ_{SV}	surface tension of the solid-vapour
T	temperature
m	mass
R	radius of the supporting disc
l	radius minus the diameter of a ball
ω and Ω	angular velocity
$F_{sd_{440C}}$	centrifugal force of the supporting disc with steel balls
$F_{j_{440C}}$	centrifugal force of the grinding jar with steel balls
$F_{sd_{WC}}$	centrifugal force of the supporting disc with WC balls
$F_{j_{440C}}$	centrifugal force of the grinding jar with steel balls
a_{440C}	acceleration of steel balls
a_{WC}	acceleration of WC balls
$v_{r_{440C}}$	velocity of steel balls
$v_{r_{WC}}$	velocity of WC balls
ρ_b	density of balls
ρ_p	density of powder
ρ_w	density of water
ρ_s	density of specimen
v_s	speed of a longitudinal wave
c_p	specific heat capacity of powder
F	energy heat flux
Δt	time that stress lasts
σ	stress
ΔT	temperature rise per impact
k_0	thermal conductivity
d_p	particle diameter
T_{pm}	particle melting temperature
ΔH_f	change of melting enthalpy
F_b	buoyancy force
m_a	mass in air environment
m_w	mass in water environment
V	volume
Θ	angle in X-ray diffraction
λ	X-ray wavelength
τ	mean size of ordered domains
K	Scherer form factor
$\Delta(2\theta)$	full width at the half maximum intensity (FWHM)
θ	Bragg angle
E	Young's modulus
VED	volumetric energy density
s_s	scanning speed
ϵ	strain
d_L	diameter of laser beam
w_0	laser focus point
σ_{mech}	mechanical tension

Bibliography

[1] F. Klocke, K. Arntz, M. Teli, K. Winands, M. Wegener, and S. Oliari, "State-of-the-art laser additive manufacturing for hot-work tool steels," *Procedia CIRP*, vol. 63, pp. 58 – 63, 2017. Manufacturing Systems 4.0 – Proceedings of the 50th CIRP Conference on Manufacturing Systems.

[2] A. Gebhart, *Generative Fertigungsverfahren, Rapid Prototyping - Rapid Tooling - Rapid Manufacturing.* Hanser Verlag, 2007.

[3] K. Wessam, *Die generative Fertigung mittels Laser-Sintern: Scanstrategien, Einfluesse verschiedener Prozessparameter auf die mechanischen und optischen Eigenschaften beim LS von Thermoplasten und deren Nachbearbeitungsmoeglichkeiten.* PhD thesis, University of Duesburg-Essen, 2010.

[4] G. Witt, "Moderne Produktionssysteme - Datei-Formate und Datenaufbereitung." University of Duisburg-Essen, 2008.

[5] A. Kirchheim, "Additive Fertigung von metallischen Bauteilen." Seminar 2018 der Swissmem Fachgruppe Schweiss- und Schneidtechnik.

[6] *Optimierung der Bauteileigenschaften beim Selektiven Lasersintern von Thermoplasten.* Shaker Verlag, 2005.

[7] O. Diegel, A. Nordin, and D. Motte, *A Practical Guide to Design for Additive Manufacturing.* Springer Series in Advanced Manufacturing, 2019.

[8] "Laser focus world," April 2011.

[9] D. Pitassi, E. Savoia, V. Fontanari, A. Molinari, V. Luchin, G. Zappini, and M. Benedetti, *Finite Element Thermal Analysis of Metal Parts Additively Manufactured via Selective Laser Melting.* Intech, 02 2018.

[10] M. Anam, D. Pal, and B. Stucker, "Modeling and experimental validation of nickel-based super alloy (inconel 625) made using selective laser melting." J. B. Speed School of Engineering, University of Louisville, 2013.

[11] C. Teng, D. Pal, H. Gong, and B. Stucker, "A two dimensional analytical evaluation of temperature fields in selective laser sintering," 01 2014.

[12] B. AlMangour, *Additive Manufacturing of High-Performance 316L Stainless Steel Nanocomposites via Selective Laser Melting.* PhD thesis, University of California, 2017.

[13] X. Zhou, X. Liu, D. Zhang, Z. Shen, and W. Liu, "Balling phenomena in selective laser melted tungsten," *Journal of Materials Processing Technology*, vol. 222, pp. 33–42, 2015.

[14] T. Starr, K. Rafi, B. Stucker, and C. Scherzer, "Controlling phase composition in selective laser melted stainless steel," *Power (W)*, vol. 195, p. 195, 2012.

[15] Z. Sun, X. Tan, S. Tor, and C. Chua, "Simultaneously enhanced strength and ductility for 3d-printed stainless steel 316l by selective laser melting," *NPG Asia Materials*, 04 2018.

[16] C. Pfeifer, "Technische und wirtschaftliche Bewertung von generativ gefertigten Aluminium- und Nickelbasislegierungskomponenten," Master's thesis, UAS Campus Vienna, 2016.

[17] C. Suryanaryana, “Mechanical alloying and milling,” *Progress in Materials Science*, vol. 46, pp. 1–184, 2001.

[18] “What-when-how, http://what-when-how.com/materialsparts-and-finishes/mechanical-alloying/,” March 2020.

[19] “Fritsch gmbh, https://www.fritsch-international.com/sample-preparation/milling/planetary-mills/details/product/pulverisette-6-classic-line/,” March 2020.

[20] “Willy a. bachofen ag, https://www.wab-group.com/en/mixing-technology/products/product/turbula/,” March 2020.

[21] Mikrons, “How an attritor works,” March 2020.

[22] W. Schatt, K. Wieters, and B. Kieback, *Pulvermetallurgie. Technologien und Werkstoffe.* VDI, 2007.

[23] D. Gu, Z. Wang, Y. Shen, Q. Li, and Y. Li, “In-situ tic particle reinforced ti–al matrix composites: Powder preparation by mechanical alloying and selective laser melting behavior,” *Applied Surface Science*, vol. 255, no. 22, pp. 9230 – 9240, 2009.

[24] E. Hesse and H. J. Eckstein, “Beitrag zum umwandlungsverhalten kohlenstoffarmer unlegierter staehle,” *Freiberger Forschungshefte, VEB-Verlag*, pp. 30–44, 1976.

[25] L. Swartzendruber, V. Itkin, and C. Alcock, “Phase diagrams of binary nickel alloys,” *P. Nash, Ed., ASM International*, pp. p 110–132, 1991.

[26] G. Thotakura, R. Goswami, and T. Jayaraman, “Evaluation of structure and magnetic properties of maraging steel powder feedstock for additive manufacturing of magnetic components,” *Journal of Alloys and Compounds*, vol. 814, p. 152296, 2020.

[27] K. Kempen, E. Yasa, L. Thijs, J.-P. Kruth, and J. V. Humbeeck, “Microstructure and mechanical properties of selective laser melted 18ni-300 steel,” *Physics Procedia*, vol. 12, pp. 255 – 263, 2011. Lasers in Manufacturing 2011 - Proceedings of the Sixth International WLT Conference on Lasers in Manufacturing.

[28] K. Edelstahlwerk, “Hot tool steels,” 11 2000.

[29] B. Wang, Y. Liu, and J. Ye, “Mechanical properties and electronic structures of VC, V4C3 and V8C7 from first principles,” *Physica Scripta*, vol. 88, p. 015301, jun 2013.

[30] W. Huang, “An assessment of the v-c system,” *Z. Metallkd. 82*, vol. 174, 1991.

[31] H. Okamoto, “C-ti (carbon-titanium),” *Journal of Phase Equilibria and Diffusion*, vol. 19, no. 1, pp. 89–89, 1998.

[32] H. W. Hugosson, P. Korzhavyi, U. Jansson, B. Johansson, and O. Eriksson, “Phase stabilities and structural relaxations in substoichiometric tic,” *Phys. Rev. B*, vol. 63, 04 2001.

[33] R. Mines, *Additive Manufacturing Processes and Materials for Metallic Microlattice Structures Using Selective Laser Melting, Electron Beam Melting and Binder Jetting*, pp. 17–31. Cham: Springer International Publishing, 2019.

[34] F. Girgsdies, “Peak profile analysis in x-ray powder diffraction.” Electron Microscopy Group, Department of Inorganic Chemistry, Fritz-Haber-Institut der Max-Planck-Gesellschaft, 2015.

[35] M. C. Flemings, *Solidification Processing.* American Cancer Society, 2006.

[36] I. Schruff, *Der Einfluss des Werkzeugstahles auf den Werkzeugverschleiss beim Gesenkschmieden*, vol. pp. 121-139. W. Bartz, Hrsg., Expert Verlag, 2004.

[37] N. C. . K. K. Chawla, *Metal Matrix Composites.* Springer, New York, NY, second edition ed., 2013.

[38] "Materials springer, materials.springer.com, 09/2020."

[39] H. Tulhoff, J. A. Meese-Marktscheffel, C. Oelgardt, C. Kind, M. Weinmann, and T. Säuberlich, *Carbides*, pp. 1–30. American Cancer Society, 2017.

[40] J. Hu, C. Li, F. Wang, and W. Zhang, "Thermodynamic re-assessment of the v–c system," *Journal of Alloys and Compounds*, vol. 421, no. 1, pp. 120 – 127, 2006.

[41] "V8c7 crystal structure: Datasheet from pauling file multinaries edition 2012 in springermaterials." accessed 2020-04-13.

[42] "V6c5 rt structural transitions: Datasheet from pauling file multinaries edition 2012 in springermaterials." accessed 2020-04-13.

[43] T. B. Massalski, *Binary alloy phase diagrams.* Materials Park, Ohio : ASM International, 1990.

[44] U. Brand, "Messunsicherheit in der haertemessung," tech. rep., Pyhsikalisch-Technische Bundesanstalt.

[45] I. Gibson, D. Rosen, and B. Stucker, *Additive Manufacturing Technologies.* Springer-Verlag New York, 2015.

[46] N. Hopkinson, R. Hague, and P. Dickens, *Rapid Manufacturing: An Industrial Revolution for the Digital Age.* Wiley, 2005.

[47] J. Kruth, L. Froyen, J. V. Vaerenbergh, P. Mercelis, M. Rombouts, and B. Lauwers, "Selective laser melting of iron-based powder," *Journal of Materials Processing Technology*, vol. 149, no. 1, pp. 616 – 622, 2004. 14th Interntaional Symposium on Electromachining (ISEM XIV).

[48] J. Yang, H. Ouyang, and Y. Wang, "Direct metal laser fabrication: machine development and experimental work," *The International Journal of Advanced Manufacturing Technology*, vol. 46, pp. pp 1133–1143, February 2010.

[49] A. Simchi and H. Pohl, "Effects of laser sintering processing parameters on the microstructure and densification of iron powder," *Materials Science and Engineering A*, vol. 359:119-28, 2003.

[50] A. Simchi, F. Petsoldt, and H. Pohl, "On the development of direct metal laser sintering for rapid tooling," *Journal of Materials Processing Technology*, vol. 141:319-28, 2003.

[51] A. Simchi, "Direct laser sintering of metal powders: Mechanism, kinetics and microstructural features," *Materials Science and Engineering A*, vol. 428:148-58, 2006.

[52] P. Rochus, J. Plesseria, M. van Elsen, J. Kruth, R. Carrus, and T. Dormal, "New applications of rapid prototyping and rapid manufacturing (rp/rm) technologies for space instrumentation," *Acta Astronaut*, vol. 61:352-9, 2007.

[53] E. Santos, M. Shiomi, K. Osakada, and T. Laoui, "Rapid manufacturing of metal components by laser forming," *International Journal of Machine Tools and Manufacture*, vol. 46:1459-68, 2006.

[54] S. Kumar, "Selective laser sintering: Recent advances," in *In 4th Pacific International Conference on Applications of Lasers and Optics*, (Wuhan, China), 2010.

[55] S. Kumar, "Selective laser sintering: A qualitative and objective approach," *JOM*, vol. 55:43-7, 2003.

[56] C. Wright, K. Dalgarno, and M. Dewidarin, "Processing conditions and mechanical properties of high speed steel parts fabricated using direct selective laser sintering," *Proceedings of the Institution of Mechanical Engineers, Part B*, vol. 217:1651-63, 2009.

[57] H. Niu and I. Chang, "Selective laser sintering of gas atomised m2 high speed steel," *Materials Science and Engineering A*, vol. 35:31-8, 2000.

[58] J. Kruth, P. Mercelis, J. V. Vaerenbergh, L. Froyen, and M. Rombouts, "Binding mechanisms in selective laser sintering and selective laser melting," *Rapid Prototyping Journal*, vol. 11:26-36, 2005.

[59] J. Kruth, G. Levy, F. Klocke, and T. Childs, "Consolidation phenomena in laser and powder-bed based layered manufacturing," *CIRP Annals Manufacturing Technology*, vol. 56:730-59, 2007.

[60] I. D. M. e.V., "Massivumformung - kurz und bündig," April 2013.

[61] B.-A. Behrens and T. Yilkiran, *Untersuchung zu den Verschleisseigenschaften nitrierter und beschichteter Werkzeuge fuer die Warmmassivumformung.* Bamberg: Verlag Meisenbach GmbH, 2012.

[62] S. Ocylok, *Herstellung und Eigenschaften nanopartikulär verstärkter Beschichtungen durch Laserauftragsschweißen zum Verschleißschutz von Schmiedegesenken.* PhD thesis, RWTH Aachen, 2015.

[63] P. Milonni and J. Eberly, *Laser Physics.* Wiley, 2010.

[64] E. Vaglio, *Research on Process Parameter Optimization in Selective Laser Melting.* PhD thesis, University of Udine, 2018.

[65] H. Lee, C. Lim, M. Low, N. Tham, V. Murukeshan, and Y. Kim, "Lasers in additive manufacturing: A review," *International Journal of Precision Engineering and Manufacturing-Green Technology*, 2017.

[66] M. Rajabi, A. Simchi, M. Vahidi, and P. Davami, "Effect of particle size on the microstructure of rapidly solidified al-20si-5fe-2x (x=cu, ni, cr) powder," *Journal of Alloys and Compounds*, vol. 466, pp. 111–118, 2008.

[67] T. Campbell and O. Ivanova, "3d printing of multifunctional nanocomposites," *Nano Today*, pp. 119–120, 2013.

[68] F. Chang, D. Gu, D. Dai, and P. Yuan, "Selective laser melting of in-situ al4sic4 + sic hybrid reinforced al matrix composites: Influence of starting sic particle size," *Surface and Coatings Technology*, vol. 272, pp. 15–24, 2015.

[69] T. Childs, C. Hauser, and M. Badrossamay, "Selective laser sintering (melting) of stainless and tool steel powders: experiments and modelling," *Proceedings of the Institution of Mechanical Engineers, Part B: Journal of Engineering Manufacture*, vol. 219, pp. 339–57, 2005.

[70] H. Niu and I. Chang, "Instability of scan tracks of selective laser sintering of high speed steel powder," *Scripta Materialia*, vol. 41, no. 11, pp. 1229 – 1234, 1999.

[71] E. Lavernia and T. Srivatsan, "The rapid solidification processing of materials: science, principles, technology, advances, and applications," *Journal of Materials Science*, vol. 45, p. 287, 2010.

[72] F. Scalzo, *Advanced Lattice and Porous Structures for AM Product Optimization.* PhD thesis, University of Udine, 2020.

[73] F. Abe, K. Osakada, M. Shiomi, K. Uematsu, and M. Matsumoto, "The manufacturing of hard tools from metallic powders by selective laser melting," *Journal of materials processing technology*, vol. 111, no. 210-3, 2001.

[74] R. Li, J. Liu, Y. Shi, L. Wang, and W. Jiang, "Balling behaviour of stainless steel and nickel powder during selective laser melting process," *The International Journal of Advanced Manufacturing Technology*, vol. 59, pp. 1025–35, 2012.

[75] J. S. Benjamin, "Mechanical alloying," *Scientific American*, vol. 234, no. 5, pp. 40–49, 1976.

[76] E. Arzt and L. Schultz, "New materials by mechanical alloying techniques," *Materials and Manufacturing Processes*, vol. 6, no. 4, pp. 733–736, 1991.

[77] A. E. Ermakov, E. E. Yurchikov, and V. A. Barinov, "Magnetic properties of amorphous powdered y-co system alloys obtained by mechanical grinding," 1981.

[78] C. C. Koch, O. B. Cavin, C. G. McKamey, and J. O. Scarbrough, "Preparation of "amorphous" ni60nb40 by mechanical alloying," *Applied Physics Letters*, vol. 43, no. 11, pp. 1017–1019, 1983.

[79] C. Suryanarayana, "Bibliography on mechanical alloying and milling," *Cambridge, UK: Cambridge International Science Publishing*, 1995.

[80] C. Suryanarayana, "Metals and materials," 1996.

[81] M. O. Lai and L. Lu, *Mechanical alloying.* Boston, MA: Kluwer Academic Publishers, 1998.

[82] B. S. Murty and S. Ranganathan, "Internat mat rev." 43:101-41, 1998.

[83] J. S. Benjamin, "Frontiers of high-temperature materials," in *INCO Alloys International*, (New York, NY), 1981.

[84] E. Arzt and L. Schultz, "New materials by mechanical alloying techniques," in *DGM Informationsgesellschaft*, (Oberursel, Germany), 1989.

[85] J. S. Benjamin and R. C. Benn, "Frontiers of high-temperature materials ii," in *INCO Alloys International*, (New York, NY), 1983.

[86] A. H. Clauer and J. J. deBarbadillo, "Solid state powder processing," in *TMS*, (Warrendale, PA), 1990.

[87] F. H. Froes and J. J. deBarbadillo, "Structural applications of mechanical alloying," in *ASM International*, (Materials Park, OH), 1990.

[88] R. W. Cochrane and J. O. Srom-Olsen, "Proceedings of the sixth international conference on rapidly quenched metals," in *Materials Science and Engineering*, pp. 97–9, 1988.

[89] H. Frederiksson and S. J. Savage, "Proceedings of the seventh international conference on rapidly quenched metals," in *Materials Science and Engineering*, pp. A133–134, 1991.

[90] T. Masumoto and K. Hashimoto, "Proceedings of the eighth international conference on rapidly quenched metals," in *Materials Science and Engineering*, pp. A179–182, 1994.

[91] P. Duhaj, P. Mrafko, and P. Švec, "Proceedings of the ninth international conference on rapidly quenched metals," in *Materials Science and Engineering*, pp. A226–228, 1997.

[92] A. R. Yavari, "Proceedings of the international symposium on metastable, mechanically alloyed and nanocrystalline materials (ismanam- 94)," in *Materials Science Forum*, (Zürich, Switzerland), pp. 179–81, Trans Tech Publications, 1995.

[93] R. Schulz, “Proceedings of the international symposium on metastable, mechanically alloyed and nanocrystalline materials (ismanam- 95),” in *Materials Science Forum*, (Zürich, Switzerland), pp. 225–227, Trans Tech Publications, 1996.

[94] D. Fiorani and M. Magini, “Proceedings of the international symposium on metastable, mechanically alloyed and nanocrystalline materials (ismanam- 96),” in *Materials Science Forum*, (Zürich, Switzerland), pp. 235–238, Trans Tech Publications, 1997.

[95] M. D. Baró and S. Suriñach, “Proceedings of the international symposium on metastable, mechanically alloyed and nanocrystalline materials (ismanam- 97),” in *Materials Science Forum*, (Zürich, Switzerland), pp. 269–272, Trans Tech Publications, 1998.

[96] D. Bloor, R. J. Brook, M. Flemings, and S. Mahajan, *The encyclopedia of advanced materials.* Oxford: Pergamon Press, 1994.

[97] C. Suryanaryana, *Non-equilibrium processing of materials.* Oxford: Pergamon Press, 1999.

[98] H. H. Liebermann, *Rapidly solidified alloys: Processes, structures, properties, applications.* New York, NY: Marcel Dekker, 1993.

[99] T. R. Anantharaman and C. Suryanarayana, *Rapidly solidified metals - a technological overview.* Aedermannsdorf, Switzerland: Trans Tech Publications, 1987.

[100] K. Upadhya, *Plasma synthesis and processing of materials.* Warrendale, PA: TMS, 1993.

[101] R. L. Bickerdike, D. Clark, J. Easterbrook, G. Hughes, W. Mair, P. G. Partridge, and H. C. Ranson, “Internat j rapid solidification,” 1984.

[102] D. Turnbull, “Metall trans.” 12A:695-708, 1981.

[103] P. H. Shingu, H. Henein, and T. Oki, “Processing materials for properties.” Warrendale, PA: TMS. p. 1270-80, 1993.

[104] J. Singh and S. M. Copley, eds., *Novel techniques in synthesis and processing of advanced materials*, (Warrendale, PA: TMS, p. 1-21), Minerals, Metals and Materials Society, 1994.

[105] V. Chawla, S. Prakash, and B. S. Sidhu, “State of the art: Applications of mechanically alloyed nanomaterials,” *Materials and Manufacturing Processes*, vol. 22, pp. 469–473, 2007.

[106] R. E. Schilling and M. Yang, “Attritor grinding mills and new developments,” April 2000.

[107] F. Thümmler and R. Oberacker, *Introduction to powder metallurgy.* London, UK: The Institute of Materials, 1993.

[108] S. Kaloshkin, I. Tomilin, G. Andrianov, U. Baldokhin, and E. Shelekhov, “Phase transformations and hyperfine interactions in mechanically alloyed fe-cu solid solutions,” in *Synthesis and Properties of Mechanically Alloyed and Nanocrystalline Materials*, vol. 235 of *Materials Science Forum*, pp. 565–570, Trans Tech Publications Ltd, 10 1996.

[109] R. M. Davis, B. McDermott, and C. C. Koch, “Mechanical alloying of brittle materials,” *Metallurgical Transactions A*, vol. 19, pp. 2867–2874, 1988.

[110] R. B. Schwarz and C. C. Koch, “Formation of amorphous alloys by the mechanical alloying of crystalline powders of pure metals and powders of intermetallics,” *Applied Physics Letters*, vol. 49, pp. 146–148, 1986.

[111] H. Mio, J. Kano, F. Saito, and K. Kaneko, “Optimum revolution and rotational directions and their speeds in planetary ball milling,” *International Journal of Mineral Processing*, vol. 74, pp. S85 – S92, 2004. Special Issue Supplement Comminution 2002.

[112] J. Hamilton, “Additive manufacturing materials: Fabrication of aluminum matrix composites,” Master’s thesis, Rochester Institute of Technology, 2019.

[113] K. U. Krainer, *Metal Matrix Composites.* Wiley-VCH, 2006.

[114] G. Arth, *Entwicklung von Stahl-Keramik Verbunden mit verminderter Dichte.* PhD thesis, Montanuniversität Leoben.

[115] S. Jayalakshmi and M. Gupta, “Metallic amorphous alloy reinforcements in light metal matrices.” SpringerBriefs in Materials, 2015.

[116] *Metal Matrix Composites in Industry: An Introduction and a Survey.* Springer-Verlag Berlin Heidelberg, 2003.

[117] M. Suarez, M. Alvarez-Pérez, O. Alvarez-Fregoso, and J. Juarez-Islas, “Effect of nanoprecipitates and grain size on the mechanical properties of advanced structural steels,” *Materials Science and Engineering: A*, vol. 528, no. 15, pp. 4924 – 4926, 2011.

[118] S. A. Huth, *Entwicklung neuer pulvermetallurgischer Staehle fuer Anwendungen unter Verschleiss- und Korrosionsbeanspruchung.* PhD thesis, Ruhr-Universitaet Bochum, 2009.

[119] T. Lierfeld, *Werkstoffwissenschaftliche und metallphysikalische Untersuchungen zum Einbau kleiner Keramikpartikel in dendritisch erstarrenden Metallen.* PhD thesis, Ruhr-Universitaet Bochum, 2006.

[120] W. Bleck, *Werkstoffkunde Stahl fuer Studium und Praxis*, vol. 5. Institut fuer Eisenhuettenkunde (IEHK) der RWTH Aachen, 2014.

[121] W. Smith and J. Hashemi, *Foundations of Materials Science and Engineering.* McGraw-Hill, 4 ed., 2006.

[122] Y.-L. Kang, Q.-H. Han, X.-M. Zhao, and M.-H. Cai, “Influence of nanoparticle reinforcements on the strengthening mechanisms of an ultrafine-grained dual phase steel containing titanium,” *Materials and Design*, vol. 44, pp. 331–339, 2013.

[123] K. Technical faculty of the Christian-Albrecht University, “Ausscheidungsvorgaenge diffusion,” 2012.

[124] D. Wang, Z. Tian, S. Wang, and L. Shen, “Microstructure and wear resistance of laser cladding nano-al2o3/mcraly composite graded coating on tial alloy,” *Applied Mechanics and Materials*, vol. 217-219, 2012.

[125] H. Wang, D. Zou, X. Li, M. Wang, and Y. Zhao, “Effects of nano-al2o3 on high temperature frictional wear behaviours of nicocraly cladded coatings,” *Advanced Materials Research*, vol. 426, 2012.

[126] Y. Feng, *Strengthening of steels by ceramic phases.* PhD thesis, RWTH Aachen, 2013.

[127] I. Garcia, J. Fransaer, and J. Celis, “Electrodeposition and sliding wear resistance of nickel composite coatings containing micron and submicron sic particles,” *Surface and Coatings Technology*, vol. 148, no. 2-3, pp. 171–178, 2001.

[128] L. Chang, Z. Zhang, C. Breidt, and K. Friedrich, “Tribological properties of epoxy nanocomposites: Enhancement of the wear resistance by nano-tio2 particles,” *Wear*, vol. 258, pp. 141–148, January 2005.

[129] H. Berns and W. Theisen, *Eisenwerkstoffe - Stahl und Gusseisen*, vol. 4. Springer Verlag Berlin, 2008.

[130] S. Kou, *Welding Metallurgy.* Wiley-Interscience, 2003.

[131] M. Sokoluk, C. Cao, S. Pan, and X. Li, “Nanoparticle-enabled phase control for arc welding of unweldable aluminum alloy 7075,” *Nature Communications*, vol. 10, no. 1, p. 98, 2019.

[132] J. Martin, B. Yahata, J. Hundley, J. Mayer, T. Schaedler, and T. Pollock, “3d printing of high-strength aluminium alloys,” *Nature*, vol. 549, no. 7672, pp. 365–369, 2017.

[133] B. AlMangour, D. Grzesiak, and J.-M. Yang, “In-situ formation of novel TiC-particle-reinforced 316L stainless steel bulk-form composites by selective laser melting,” *Journal of Alloys and Compounds*, vol. 706, pp. 409 – 418, 2017.

[134] B. AlMangour, D. Grzesiak, and J.-M. Yang, “In situ formation of TiC-particle-reinforced stainless steel matrix nanocomposites during ball milling: Feedstock powder preparation for selective laser melting at various energy densitiestic-particle-reinforced stainless steel matrix nanocomposites during ball milling: Feedstock powder preparation for selective laser melting at various energy densities,” *Powder Technology*, vol. 326, pp. 467–478, 2018.

[135] B. AlMangour, D. Grzesiak, T. Borkar, and J.-M. Yang, “Densification behavior, microstructural evolution, and mechanical properties of TiC/316L stainless steel nanocomposites fabricated by selective laser melting,” *Materials and Design*, vol. 138, pp. 119 – 128, 2018.

[136] D. Cormier, O. Harrysson, T. Mahale, and H. West, “Freeform fabrication of titanium aluminide via electron beam melting using prealloyed and blended powders,” *Research Letters in Materials Science*, vol. 1-4, 2007.

[137] A. Fortunato, A. Lulaj, S. Melkote, and et al., “Milling of maraging steel components produced by selective laser melting,” *Int J Adv Manuf Technol*, vol. 94, p. 1895, 2018.

[138] S. Schwarz, *Dispersionsverstaerkte Sinterstaehle hergestellt ueber Field Assisted Sintering.* PhD thesis, Karlsruher Institut fuer Technologie, 2010.

[139] X. Yan, C. Chen, R. Zhao, W. Ma, R. Bolot, J. Wang, Z. Ren, H. Liao, and M. Liu, “Selective laser melting of wc reinforced maraging steel 300: Microstructure characterization and tribological performance,” *Surface and Coatings Technology*, vol. 371, pp. 355 – 365, 2019. 8th Rencontres Internationales de la Projection Thermique.

[140] E. Pagounis, M. Talvitie, and V. K. Lindroos, “Microstructure and mechanical properties of hot work tool steel matrix composites produced by hot isostatic pressing,” *Powder Metallurgy*, vol. 40, no. 1, pp. 55–61, 1997.

[141] D. Bacon, L. Edwards, J. Moffatt, and M. Fitzpatrick, “Fatigue and fracture of a 316 stainless steel metal matrix composite reinforced with 25 percent titanium diboride,” *International Journal of Fatigue*, vol. 48, pp. 39 – 47, 2013.

[142] E. Macherauch and H. Zoch, *Martensititsche Umwandlung. In: Praktikum in Werkstoffkunde.* Vieweg Teubner, 2011.

[143] N. Takata, R. Nishida, A. Suzuki, M. Kobashi, and M. Kato, *Crystallographic Features of Microstructure in Maraging Steel Fabricated by Selective Laser Melting*, vol. 8. MDPI, 2018.

[144] D. Beckers, N. Ellendt, U. Fritsching, and V. Uhlenwinkel, “Impact of process flow conditions on particle morphology in metal powder production via gas atomization,” *Advanced Powder Technology*, vol. 31, no. 1, pp. 300 – 311, 2020.

[145] Z. Zhao, H. Zuo, Y. Liu, W. Song, S. Mao, and Y. Wang, “Effects of additives on synthesis of vanadium carbide (v8c7) nanopowders by thermal processing of the precursor,” *International Journal of Refractory Metals and Hard Materials*, vol. 27, no. 6, pp. 971 – 975, 2009.

[146] L. Yan and E. Wu, “The preparation of ultrafine v8c7 powder and its phase reactions,” *International Journal of Refractory Metals and Hard Materials*, vol. 25, no. 2, pp. 125 – 129, 2007.

[147] J. Nie, Y. Wu, P. Li, H. Li, and X. Liu, “Morphological evolution of TiC from octahedron to cube induced by Nickel element,” *CrystEngComm*, vol. 14, 05 2012.

[148] F. Binder, “Titancarbid - ein technischer hartstoff,” *Chemie Ingenieur Technik*, vol. 51, no. 5, pp. 391 – 397, 2004.

[149] D. Bandyopadhyay, R. Sharma, and N. Chakraborti, “The ti-co-c system (titanium-cobalt-carbon),” *Journal of Phase Equilibria*, vol. 21, pp. 179–185, 05 2000.

[150] R. Helmholtz, “Untersuchungen über Dämpfe und Nebel, besonders über solche von Lösungen,” *Annalen der Physik*, vol. 263, no. 4, pp. 508 – 543, 1886.

[151] F. W. Küster, *Lehrbuch der allgemeinen physikalischen und theoretischen Chemie.* Carl Winter, 1906.

[152] F. Meissner, “Mitteilungen aus dem institut für physikalische chemie der universität göttingen.,” *Zeitschrift für anorganische und allgemeine Chemie*, vol. Nr. 8 Über den Einfluß der Zerteilung auf die Schmelztemperature, no. 110 (1), pp. 169–186, 1920.

[153] R. Defay, I. Prigogine, A. Bellemans, and D. Everett, *Surface tension and adsorption.* Longmans Green and Co (London), 1966.

[154] S. Gregg and K. Sing, *Adsorption surface area and porosity.* Academic Press (London), 1967.

[155] K. K. Nanda, “Size-dependent melting of nanoparticles: Hundred years of thermodynamic model,” *Pramana*, vol. 72, no. 4, pp. 617–628, 2009.

[156] A. Calverley, “A determination of the surface tension of liquid tungsten by the drop-weight method,” *Proceedings of the Physical Society. Section B*, vol. 70, pp. 1040–1044, nov 1957.

[157] V. P. Skripov, V. P. Koverda, and V. N. Skokov, “Size effect on melting of small particles,” *physica status solidi (a)*, vol. 66, no. 1, pp. 109–118, 1981.

[158] J. Sun and S. Simon, “The melting behavior of aluminum nanoparticles,” *Thermochimica Acta*, vol. 463, no. 1, pp. 32 – 40, 2007. Chemical Thermodynamics and Thermal Analysis.

[159] C. R. M. Wronski, “The size dependence of the melting point of small particles of tin,” *British Journal of Applied Physics*, vol. 18, pp. 1731–1737, dec 1967.

[160] C. Zou, Y. Gao, B. Yang, and O. Zhai, “Melting and solidification properties of the nanoparticles of sn3.0ag0.5cu lead-free solder alloy,” *Materials Characterization 61*, vol. 61, 2010.

[161] P. Buffat and J. Borel, “Size effect on the melting temperature of gold particles,” *Physical review A*, vol. 13, no. 6, 1976.

[162] C. Solliard, “Debye waller factor and melting temperature in small gold particles - related size effects,” *Solid State Communications*, vol. 51, no. 12, 1984.

[163] R. Garrigos, P. Cheyssac, and R. Kofman, “Melting for lead particles of very small sizes; influence of surface phenomena,” *Zeitrschrift für Physik D: Atoms Molecules and Clusters*, vol. 12, no. 1-4, 1989.

[164] Y. Shibuta and T. Suzuki, “Melting and solidification point of fcc-metal nanoparticles with respect to particle size: A molecular dynamics study,” *Chemical Physics Letters*, vol. 498, 2010.

[165] M. Sadr-Lahijanya, P. Rayb, and H. Stanleya, “Melting driven by particle size-dispersity: a study in two dimensions,” *Physica A*, vol. 270, 1999.

[166] J. Borel, “Thermodynamical size effect and the structure of metallic clusters,” *Surface Science*, vol. 106, no. 1-3, 1981.

[167] J. Frenken, P. Marée, and J. van der Veen, “Observation of surface-initiated melting,” *Physical Review B*, vol. 34, 1986.

[168] V. Lipatnikov, A. Gusev, P. Ettmayer, and W. Lengauer, “Phase transformations in nonstoichiometric vanadium carbide,” *journal of Physics: Condensed Matter*, vol. 11, no. 1, pp. 163–184, 1999.

[169] P.-.-V. R. 1, *Treibacher Material Data Sheet.* Treibacher Industrie AG, 13.12.2013.

[170] A. Aversa, M. Pavese, D. Manfredi, F. Calignano, E. Ambrosio, S. Biamino, and P. Fino, “Microstructural and mechanical characterization of alsi10mg - tib2 composites produced by direct metal laser sintering technique,” in *Euro PM2015 - AM - Non-Conventional Material*, 2015.

[171] M. Tan and X. Zhang, “Powder metal matrix composites: selection and processing,” *Materials Science and Engineering A*, vol. 244, pp. 80–85, 1998.

[172] N. Kang, W. Ma, L. Heraud, M. E. Mansori], F. Li, M. Liu, and H. Liao, “Selective laser melting of tungsten carbide reinforced maraging steel composite,” *Additive Manufacturing*, vol. 22, pp. 104 – 110, 2018.

[173] J. Schneibel, P. Grahle, and J. Rösler, “Mechanical alloying of FeAl with Y2O3,” *Materials Science and Engineering A*, vol. 153, pp. 684–690, 1992.

[174] N. Kang, W. Ma, F. Li, H. Liao, M. Liu, and C. Coddet, “Microstructure and wear properties of selective laser melted wc reinforced 18ni-300 steel matrix composite,” *Vacuum*, vol. 154, pp. 69 – 74, 2018.

[175] Q. Han, R. Setchi, and S. L. Evans, “Synthesis and characterisation of advanced ball-milled al-al2o3 nanocomposites for selective laser melting,” *Powder Technology*, vol. 297, pp. 183 – 192, 2016.

[176] S. Zebarjad and S. Sajjadi, “Dependency of physical and mechanical properties of mechanical alloyed al–al2o3 composite on milling time,” *Materials and Design*, vol. 28, no. 7, pp. 2113 – 2120, 2007.

[177] F. Deirmina, B. AlMangour, D. Grzesiak, and M. Pellizzari, “H13–partially stabilized zirconia nanocomposites fabricated by high-energy mechanical milling and selective laser melting,” *Materials and Design*, vol. 146, pp. 286 – 297, 2018.

[178] E. Dreizin, “Mechanical alloying and reactive milling in a high energy planetary mill,” *Journal of Alloys and Compounds*, vol. 478, pp. 246–251, 2009.

[179] A. M. Soufiani], M. Enayati, and F. Karimzadeh, “Mechanical alloying behavior of Ti6Al4V residual scraps with addition of Al2O3 to produce nanostructured powder,” *Materials and Design*, vol. 31, no. 8, pp. 3954 – 3959, 2010.

[180] B. AlMangour, D. Grzesiak, and J.-M. Yang, “Nanocrystalline TiC-reinforced H13 steel matrix nanocomposites fabricated by selective laser melting,” *Materials and Design*, vol. 96, pp. 150 – 161, 2016.

[181] B. AlMangour, D. Grzesiak, and J.-M. Yang, “Rapid fabrication of bulk-form TiB2/316L stainless steel nanocomposites with novel reinforcement architecture and improved performance by selective laser melting,” *Journal of Alloys and Compounds*, vol. 680, pp. 480 – 493, 2016.

[182] M. Akbarpour, E. Salahi, F. A. Hesari], A. Simchi, and H. Kim, “Microstructure and compressibility of sic nanoparticles reinforced cu nanocomposite powders processed by high energy mechanical milling,” *Ceramics International*, vol. 40, no. 1, Part A, pp. 951 – 960, 2014.

[183] Q. Han, R. Setchi, F. Lacan, D. Gu, and S. L. Evans, “Selective laser melting of advanced al-al2o3 nanocomposites: Simulation, microstructure and mechanical properties,” *Materials Science and Engineering: A*, vol. 698, pp. 162 – 173, 2017.

[184] B. AlMangour, D. Grzesiak, and J.-M. Yang, “Selective laser melting of TiB2/H13 steel nanocomposites: Influence of hot isostatic pressing post-treatment,” *Journal of Materials Processing Technology*, vol. 244, pp. 344 – 353, 2017.

[185] B. AlMangour, D. Grzesiak, and J.-M. Yang, “Selective laser melting of TiB2/316L stainless steel composites: The roles of powder preparation and hot isostatic pressing post-treatment,” *Powder Technology*, vol. 309, pp. 37 – 48, 2017.

[186] D. Grzesiak, B. AlMangour, M. Krawczyk, M.-S. Baek, and K.-A. Lee, “Selective laser melting of TiC reinforced stainless steel nanocomposites: Mechanical behaviour at elevated temperatures,” *Materials Letters*, vol. 256, p. 126633, 2019.

[187] B. AlMangour, M.-S. Baek, D. Grzesiak, and K.-A. Lee, “Strengthening of stainless steel by titanium carbide addition and grain refinement during selective laser melting,” *Materials Science and Engineering: A*, vol. 712, pp. 812 – 818, 2018.

[188] R. Davis and C. Koch, “Mechanical alloying of brittle components: Silicon and germanium,” *Scripta Metallurgica*, vol. 21, no. 3, pp. 305 – 310, 1987.

[189] V. Federov, “Theory of optimal experiments (review),” *Biometrika*, vol. 59, no. 3, pp. 697–698, 1972.

[190] F. Hoffmann and M. Sartor, “The fascination of crystals and symmetriy.” Universität Hamburg, 2016.

[191] S. Gradečak, “Fundamentals of materials science and engineering part 1: Structure of materials part 1,” 2019.

[192] K. Lüders and G. von Oppen, *Lehrbuch der Experimentalphysik 1: Mechanik, Akustik, Waerme*, vol. 12. Bergmann Schaefer, 2008.

[193] “Maschinenenbau-physik,” May 2020.

[194] A. H. Cottrell and B. Bilby, “Dislocation theory of yielding and strain ageing of iron,” *Proceedings of the Physical Society London. Section A*, vol. 62, pp. 49–62, 1949.

[195] G. Gottstein, *Pyhsikalische Grundlagen der Materialkunde.* Springer-Verlag Berlin Heidelberg, 2007.

[196] J. Goldstein, D. Newbury, D. Joy, P. Echling, C. Lyman, *et al.*, *Scanning Electron Microscopy and X-Ray Microanalysis: Third Edition.* Scanning Electron Microscopy and X-ray Microanalysis, Springer US - Springer Science + Business Media, 2003.

[197] A. G. dos Reis, D. A. P. Reis, A. J. Abdalla, and J. Otubo, “High-temperature creep resistance and effects on the austenite reversion and precipitation of 18 ni (300) maraging steel,” *Materials Characterization*, vol. 107, pp. 350 – 357, 2015.

[198] R. Casati, J. Lemke, A. Tuissi, and M. Vedani, “Aging behaviour and mechanical performance of 18-ni 300 steel processed by selective laser melting,” *Metals*, vol. 6, p. 218, 09 2016.

[199] L. Kučerová, I. Zetková, A. Jandová, and M. Bystrianský, “Microstructural characterisation and in-situ straining of additive-manufactured x3nicomoti 18-9-5 maraging steel,” *Materials Science and Engineering: A*, vol. 750, pp. 70 – 80, 2019.

[200] E. A. Jägle, P.-P. Choi, J. Van Humbeeck, and D. Raabe, "Precipitation and austenite reversion behavior of a maraging steel produced by selective laser melting," vol. 29, no. 17, pp. 2072–2079, 2014.

[201] I. Chang and Y. Zhao, *Advances in Powder Metallurgy*, vol. 1st Edition. Woodhead Publishing, 2013.

[202] M. A. Smirnov, M. A. Kaplan, and M. A. Sevostyanov, "Receiving finely divided metal powder by inert gas atomization," *IOP Conference Series: Materials Science and Engineering*, vol. 347, p. 012033, apr 2018.

[203] U. Fritsching and V. Uhlenwinkel, *Hybrid gas atomization for powder production*, ch. 5, pp. 99–124. University of Bremen, 2012.

[204] C. Pfeifer, D. Grzesiak, P. Figiel, E. Brandstätter, B. Meier, O. Harrysson, M. Sortino, G. Totis, and A. Biedunkiewicz, "Microstructural characterization of vanadium carbide reinforced maraging steel obtained by selective laser melting." submitted for publication in 3D printing and additive manufacturing, 2021.

[205] T. Hermann Becker and D. Dimitrov, "The achievable mechanical properties of slm produced maraging steel 300 components," vol. 22, pp. 487–494, 2020/05/21 2016.

[206] A. Dalmau, W. Rmili, C. Richard, and A. Igual-Muñoz, "Tribocorrosion behavior of new martensitic stainless steels in sodium chloride solution," *Wear*, vol. 368-369, pp. 146 – 155, 2016.

[207] A. Dalmau, C. Richard, and A. I. Muñoz], "Degradation mechanisms in martensitic stainless steels: Wear, corrosion and tribocorrosion appraisal," *Tribology International*, vol. 121, pp. 167 – 179, 2018.

[208] N. Chawla and Y. L. Shen, "Mechanical behavior of particle reinforced metal matrix composites," *Advanced Engineering Materials*, vol. 3, pp. 357–370, 2019/09/24 2001.

[209] S. Strouf, "Herstellung und Charakterisierung von Stahl-Kupfer Legierungen aus Pulvermischungen mittels Laserstrahl Pulverbett Schmelzen," Master's thesis, Montanuniversität Leoben, 2018.

[210] A. Iveković, N. Omidvari, B. Vrancken, K. Lietaert, L. Thijs, K. Vanmeensel, J. Vleugels, and J.-P. Kruth, "Selective laser melting of tungsten and tungsten alloys," *International Journal of Refractory Metals and Hard Materials*, vol. 72, pp. 27 – 32, 2018.

[211] B. Song, S. Dong, P. Coddet, G. Zhou, S. Ouyang, H. Liao, and C. Coddet, "Microstructure and tensile behavior of hybrid nano-micro sic reinforced iron matrix composites produced by selective laser melting," *Journal of Alloys and Compounds*, vol. 579, pp. 415 – 421, 2013.

[212] C. Tan, K. Zhou, M. Kuang, W. Ma, and T. Kuang, "Microstructural characterization and properties of selective laser melted maraging steel with different build directions," *Science and Technology of Advanced Materials*, vol. 19, no. 1, pp. 746–758, 2018.

[213] J.-P. Choi, G.-H. Shin, S. Yang, D.-Y. Yang, J.-S. Lee, M. Brochu, and J.-H. Yu, "Densification and microstructural investigation of inconel 718 parts fabricated by selective laser melting," *Powder Technology*, vol. 310, 01 2017.

[214] B. Zhang, Y. Li, and Q. Bai, "Defect formation mechanisms in selective laser melting: A review," *Chinese Journal of Mechanical Engineering*, vol. 30, no. 3, pp. 515–527, 2017.

[215] H. Gong, H. Rafi, H. Gu, T. Starr, and B. Stucker, "Analysis of defect generation in ti-6al-4 v parts made using powder bed fusion additive manufacturing processes," *Additive Manufacturing*, vol. 1-4, 08 2014.

[216] B. Liu, B.-Q. Li, and Z. Li, “Selective laser remelting of an additive layer manufacturing process on alsi10mg,” *Results in Physics*, vol. 12, pp. 982 – 988, 2019.

[217] T. Gustmann, H. Schwab, U. Kühn, and S. Pauly, “Selective laser remelting of an additively manufactured cu-al-ni-mn shape-memory alloy,” *Materials and Design*, vol. 153, pp. 129 – 138, 2018.

[218] S. Griffiths, M. Rossell, J. Croteau, N. Vo, D. Dunand, and C. Leinenbach, “Effect of laser rescanning on the grain microstructure of a selective laser melted al-mg-zr alloy,” *Materials Characterization*, vol. 143, pp. 34 – 42, 2018. Metal Additive Manufacturing: Microstructures and Properties.

[219] H. Chen, D. Gu, D. Dai, M. Xia, and C. Ma, “A novel approach to direct preparation of complete lath martensite microstructure in tool steel by selective laser melting,” *Materials Letters*, vol. 227, pp. 128 – 131, 2018.

[220] A. G. Demir and B. Previtali, “Investigation of remelting and preheating in slm of 18ni300 maraging steel as corrective and preventive measures for porosity reduction,” *The International Journal of Advanced Manufacturing Technology*, vol. 93, no. 5, pp. 2697–2709, 2017.

[221] N. B. Dahotre and S. Harimkar, *Laser Fabrication and Machining of Materials*, vol. 1. Springer-Verlag US, 2008.

[222] R. Xiao and X. Zhang, “Problems and issues in laser beam welding of aluminum–lithium alloys,” *Journal of Manufacturing Processes*, vol. 16, 01 2013.

[223] T. Rong, D. Gu, Q. Shi, S. Cao, and M. Xia, “Effects of tailored gradient interface on wear properties of wc/inconel 718 composites using selective laser melting,” *Surface and Coatings Technology*, vol. 307, pp. 418 – 427, 2016.

[224] R. Khmyrov, V. Safronov, and A. Gusarov, “Obtaining crack-free wc-co alloys by selective laser melting,” *Physics Procedia*, vol. 83, pp. 874 – 881, 2016. Laser Assisted Net Shape Engineering 9 International Conference on Photonic Technologies Proceedings of the LANE 2016 September 19-22, 2016 Fürth, Germany.

[225] H. Wang and D. Gu, “Nanometric tic reinforced alsi10mg nanocomposites: Powder preparation by high-energy ball milling and consolidation by selective laser melting,” *Journal of Composite Materials*, vol. 49, no. 13, pp. 1639–1651, 2015.

[226] B. AlMangour, D. Grzesiak, and J.-M. Yang, “Scanning strategies for texture and anisotropy tailoring during selective laser melting of tic/316l stainless steel nanocomposites,” *Journal of Alloys and Compounds*, vol. 728, pp. 424 – 435, 2017.

[227] M. Lorusso, A. Aversa, D. Manfredi, F. Calignano, E. P. Ambrosio, D. Ugues, and M. Pavese, “Tribological behavior of aluminum alloy alsi10mg-tib2 composites produced by direct metal laser sintering (dmls),” *Journal of Materials Engineering and Performance*, vol. 25, no. 8, pp. 3152–3160, 2016.

[228] D. Gu, Y.-C. Hagedorn, W. Meiners, K. Wissenbach, and R. Poprawe, “Nanocrystalline tic reinforced ti matrix bulk-form nanocomposites by selective laser melting (slm): Densification, growth mechanism and wear behavior,” *Composites Science and Technology*, vol. 71, no. 13, pp. 1612 – 1620, 2011.

[229] N. J. Harrison, I. Todd, and K. Mumtaz, “Reduction of micro-cracking in nickel superalloys processed by selective laser melting: A fundamental alloy design approach,” *Acta Materialia*, vol. 94, pp. 59 – 68, 2015.

[230] M. Garibaldi, I. Ashcroft, M. Simonelli, and R. Hague, “Metallurgy of high-silicon steel parts produced using selective laser melting,” *Acta Materialia*, vol. 110, pp. 207 – 216, 2016.

[231] R. Canali, *Study, development and characterization of aluminium based materials by additive manufacturing.* PhD thesis, Politecnico di Torino, 2015.

[232] A. Bhattacharya and E. Arzt, "Temperature rise during mechanical alloying," *Scripta Metallurgica et Materialia*, vol. 27, no. 6, pp. 749 – 754, 1992.

[233] A. Dass and A. Moridi, "State of the art in directed energy deposition: From additive manufacturing to materials design," *Coatings*, vol. 9, p. 418, 06 2019.

[234] E. Olakanmi, R. Cochrane, and K. Dalgarno, "Densification mechanism and microstructural evolution in selective laser sintering of al–12si powders," *Journal of Materials Processing Technology*, vol. 211, no. 1, pp. 113 – 121, 2011.

[235] J. Hashim, L. Looney, and M. Hashmi, "Particle distribution in cast metal matrix composites," *Journal of Materials Processing Technology*, vol. 123, pp. 251–257, 04 2002.

[236] F. He, Q. Han, and M. Jackson, "Nanoparticulate reinforced metal matrix nanocomposites - a review," *International Journal of Nanoparticles*, vol. 1, no. 4, pp. 301–9, 2008.

[237] P. A. Hooper, "Melt pool temperature and cooling rates in laser powder bed fusion," *Additive Manufacturing*, vol. 22, pp. 548 – 559, 2018.

[238] A. Farid, S. Guo, F. Cui, P. Feng, and T. Lin, "Tib2 and tic stainless steel matrix composites," *Materials Letters*, vol. 61, pp. 189–91, 2007.

[239] F. Akhtar, "Microstructure evolution and wear properties of in situ synthesized tib2 and tic reinforced steel matrix composites," *Journal of Alloys and Compounds*, vol. 459, pp. 491–7, 2008.

[240] M. Sheikhzadeh and S. Sanjabi, "Structural characterization of stainless steel/tic nanocomposites produced by high-energy ball-milling method at different milling times," *Materials and Design*, vol. 39, pp. 366–72, 2012.

[241] K. Parashivamurthy, R. Kumar, S. Seetharamu, and M. Chandrasekharaiah, "Review on tic reinforced steel composites," *Journal of Materials Science*, vol. 36, pp. 4519–30, 2001.

[242] F. Akhtar, S. GUO, P. FENG, S. Khadijah Ali, and A. Syed Javid, "Tic-maraging stainless steel composite: microstructure, mechanical and wear properties," *Rare Metals*, vol. 25, no. 6, pp. 630 – 635, 2006.

[243] S. Wei, L. Huang, Y. Zhu, Z. Shi, X. Li, and L. Geng, "Sub-stoichiometry-facilitated oxidation kinetics in a delta-tixc-doped ti-based alloy," *npj Materials Degradation*, vol. 3, no. 1, p. 3, 2019.

[244] C. Suryanaryana and M. G. Norton, *X-ray diffraction: a practical approach.* Springer Science and Business Media, 2013.

[245] N. Axen and K.-H. Zum-Gahr, "Abrasive wear of tic-steel composite clad layers on tool steel," *Wear*, no. 157, pp. 189–201, 1992.